Université catholique de Louvain
Institute of Condensed Matter and Nanosciences (IMCN)
Bio- and Soft Matter (BSMA)

Polymer Brushes and AFM Cantilevers for Nanosensing and Nanocatalysis

Bertrand Mathy

Supervisors: Prof. B. Nysten & Prof. A.M. Jonas

Thesis submitted to obtain
the degree of Docteur en Sciences de l'Ingénieur

Louvain-la-Neuve, 2012

Université catholique de Louvain
Institute of Condensed Matter and Nanosciences (IMCN)
Bio- and Soft Matter (BSMA)

Polymer Brushes and AFM Cantilevers for Nanosensing and Nanocatalysis

Examining Committee:

Professor Bernard Nysten (UCL), supervisor
Professor Alain Jonas (UCL), supervisor
Professor Sophie Demoustier (UCL), chairperson
Professor Olivier Riant (UCL)
Professor Anne-Sophie Duwez (ULg)
Professor Jean-Pierre Aimé (Université Bordeaux 1)

Louvain-la-Neuve, 2012

Remerciements

Tout d'abord, je tiens à remercier mes promoteurs, les professeurs Alain Jonas et Bernard Nysten, de m'avoir proposé ce sujet de thèse innovant et très stimulant. Merci également d'avoir suivi l'évolution de ma thèse de façon régulière et d'avoir toujours répondu présents lorsque les problèmes (et il y en a eu pas mal!) se sont présentés.

Je voudrais ensuite remercier tous les membres du jury, les professeurs Sophie Demoustier, Anne-Sophie Duwez, Jean-Pierre Aimé et Olivier Riant pour avoir accepté de lire ce manuscrit et de le commenter.

Merci à tous les membres de l'équipe "Dynanomove" pour l'aide qu'ils ont pu m'apporter à un moment ou à un autre, notamment pour tout ce qui concerne la chimie organique. Merci à Olivier, Peter et Antony. Merci aussi à Xavier pour avoir débuté cette grande aventure qu'est la thèse à mes côtés!

Merci également à tous les membres du feu laboratoire POLY et du nouveau pôle BSMA que j'ai pu cotoyer pour leur contribution à l'excellente ambiance qui y régnait. Un merci tout particulier à mes collègues de bureau Colette, Fanny, Jo, François C. et T., aux comités d'organisation de festivités en tous genres qui se sont succédés au cours de ces 4 années (à savoir le COGF dirigé notamment par Anne-Christine et

Colette et la Team BBQ composée de Dimitry, François, Pascal, Edwin et Rémi) ainsi qu'à Cécile, Guido, Xavier D., Céline, Houssein, Delphine, Laurianne, Vincent, Lucas, Julian, Pascale, Cédric,... et bien sûr à Aurore.

Je voudrais aussi remercier les membres du Melville Laboratory for Polymer Synthesis à Cambridge de m'avoir si bien accueilli pendant les quelques mois que j'ai eu la chance d'y passer. Merci à Gesine, Johanna, Einat, Khooi Yeei, Steve, Urs, César et Bettina et merci aux professeurs Alain Jonas et Wilhelm Huck d'avoir rendu cela possible.

Merci à mes partenaires de sport pour les nombreuses heures passées à transpirer côte à côte! Merci à mes partenaires de volley, de mini-foot, de badminton, de natation, d'indoor-training (je compte sur toi Guido pour continuer l'année prochaine!) et de squash.

Merci à toute la bande des "dîners-filles": Cécile, Sébastien, Xavier H., Anne-Pascale, Simon, Philippe, Krystel, Véronique et Suzanne. Les jeudis midis ne seront plus jamais pareils!

Merci à toutes les personnes qui devraient figurer ici mais que j'ai oublié de citer.

Je voudrais terminer en exprimant toute ma reconnaissance et mon affection à mes parents, mes grands-parents, mes frères, Céline ainsi que tous ceux qui ont fait de moi ce que je suis aujourd'hui pour leur soutien dans tous les moments importants de ma vie qu'ils soient bons ou mauvais.

Abstract

The Atomic Force Microscope is a powerful tool for probing the surface of a sample at the nanoscopic scale. Indeed it can give information about the sample topography and map various physical or chemical surface properties. But in parallel to these "classical" applications, there exist other very interesting techniques. They include sensing applications in which the adsorption of molecules on the cantilever is quantitatively monitored and surface engineering applications in which the tip is used as a pen to write chemical features on a substrate.

The aim of this thesis was to develop innovative ways to go further in these two series of applications and to improve their performances. The main strategy was to increase the number of reactive sites on the cantilevers in order to interact faster and with more sensitivity. To reach this objective, AFM cantilevers were functionalized with polymer brushes which provide stable surfaces that can contain a large amount of reactive side groups per unit area.

First, the study of the kinetics of (physico)chemical reactions at the submicrometric scale was undertaken with cantilevers bearing reactive brushes. Two different methods were investigated: the frequency shift method and the deflection method. The first method was based on the fact that the resonance frequency of a lever is inversely proportional to

its mass which was increased upon adsorption of analytes by the reactive brushes while the second one was based on the variation of the surface stress of the cantilever upon adsorption of molecules by the reactive brushes.

Second, a surface-confined "click" reaction was catalyzed at the nanoscopic scale with functionalized polymer brushes bearing ligands for metals that were grafted from an AFM tip. The scan speed was a determining parameter and in every case, the patterns were thicker than a monolayer of the grafted molecules. The proposed mechanism of the lithography involves two steps: the formation of crystal seeds by the catalysis of the reaction and the subsequent pi stacking of aggregates that were absorbed in the brush.

Contents

Abbreviations **x**

List of Figures **xi**

List of Tables **xvii**

1 General Introduction **1**
1.1 Objectives and Strategies 4
1.2 Methodology 5

2 Functionalization of AFM Cantilevers with Polymer Brushes **9**
2.1 Introduction 11
2.2 Theoretical Aspects 13
2.2.1 Functionalization of AFM Probes 13
2.2.2 Self-Assembled Monolayers on Gold and Silicon . . 15
2.2.3 Polymer Brushes 22
2.3 Results and Discussion 35
2.3.1 Thiol Monolayers on Gold 35
2.3.2 Silane Monolayers on Silicon 41
2.3.3 Polymer Brush Growth 45
2.4 Conclusion 55

3 Studying Local Reactions with AFM: The "Frequency Shift" Method **65**

3.1 Introduction 67
3.2 Theoretical Aspects 69
3.2.1 Measurement of the Grafted Mass on a Vibrating Sensor 72
3.2.2 Thermoresponsive Polymer Brushes 78
3.3 Results and Discussion 81
3.3.1 Measurement of the kinetics of a chemical reaction 82
3.3.2 Measurement of the collapse transition temperature of a thermoresponsive brush 89
3.4 Conclusion 97

4 Studying Local Reactions with AFM: The "Deflection" Method 105
4.1 Introduction 107
4.2 Theoretical Aspects 109
4.2.1 Measurement of the Grafted Mass on a Flexible Sensor 110
4.2.2 pH-Responsive Polymer Brushes 117
4.2.3 Click Chemistry 119
4.3 Results and Discussion 123
4.3.1 pH Sensor Based on PEL Brushes 123
4.3.2 Chemical Sensor Based on Reactive Brushes 126
4.4 Conclusion 131

5 Local Catalysis of "Click" Reactions with Functionalized AFM Probes 139
5.1 Introduction 141
5.2 Theoretical Aspects 143
5.2.1 Nanopatterning Techniques 143
5.2.2 Local Heterogeneous Catalysis 152
5.3 Results and Discussion 154
5.3.1 Preliminary Study 155
5.3.2 Local Catalysis 164

5.4 Conclusion 175

6 Experimental Part 189

6.1 Materials 191
6.1.1 Self-Assembled Monolayers on Silicon and Gold . . 191
6.1.2 Polymer brush growth 192
6.1.3 Resonance frequency shifts experiments 193
6.1.4 Deflection experiments 194
6.1.5 Local catalysis experiments 196
6.2 Methods 197
6.2.1 Self-assembled monolayers on silicon and gold . . . 197
6.2.2 Polymer brush growth 198
6.2.3 Resonance frequency shifts experiments 201
6.2.4 Deflection experiments 204
6.2.5 Local catalysis experiments 206
6.3 Characterization 211
6.3.1 X-Ray Reflectivity (XRR) 211
6.3.2 Ellipsometry 215
6.3.3 X-Ray Photoelectron Spectroscopy (XPS) 219
6.3.4 Fourier Transform Infrared Spectrometry (FTIR) . 224
6.3.5 Atomic Force Microscopy (AFM) 227
6.3.6 Quartz Crystal Microbalance with Dissipation Monitoring (QCM-D) 232
6.3.7 Front-Face Fluorimetry (FFF) 234
6.3.8 Scanning Electron Microscopy (SEM) 235

7 General Conclusions and Perspectives 239

Abbreviations

MEO_2MA	Di(Ethylene glycOl)Methyl ether MethAcrylate
AFM	Atomic Force Microscopy
AM-AFM	Amplitude Modulated AFM
ATRP	Atom Transfer Radical Polymerization
C-AFM	Contact AFM
CuAAC	Cu^{I}-Catalyzed Alkyne-Azide Cycloaddition
FFF	Front-Face Fluorimetry
FM-AFM	Frequency Modulated AFM
FMM	Force Modulation Microscopy
FTIR	Fourier Transform Infrared Spectrometry
HEMA	2-HydroxyEthyl MethAcrylate
IC-AFM	Intermittent Contact AFM
KPFM	Kelvin Probe Force Microscopy
LCST	Lower Critical Solution Temperature
LFM	Lateral Force Microscopy
MAA	MethAcrylic Acid
MES	mono-2-(Methacryloyloxy) Ethyl Succinate
MFM	Magnetic Force Microscopy
NC-AFM	Non-Contact AFM
NEMS	Nano Electro-Mechanical System

NMP	Nitroxide-Mediated Polymerization
PFT-AFM	Peak Force Tapping AFM
PSD	Position Sensitive Detector
QCM-D	Quartz Crystal Microbalance with Dissipation monitoring
RAFT	Reversible Addition-Fragmentation Chain Transfer
ROMP	Ring Opening Metathesis Polymerization
ROP	Ring Opening Polymerization
SAM	Self-Assembled Monolayer
SEM	Scanning Electron Microscopy
SIP	Surface-Initiated Polymerization
SPM	Scanning Probe Microscopy
STM	Scanning Tunneling Microscopy
TEM	Transmission Electron Microscopy
TON	TurnOver Number
UHV	Ultra High Vacuum
XPS	X-Ray Photoelectron Spectroscopy
XRD	X-Ray Diffraction
XRR	X-Ray Reflectometry

List of Figures

1.1 Scheme of a nanofactory. 6

2.1 Main kinetic steps during the growth of thiol-SAMs. 18
2.2 Scheme of a thiol-SAM on gold. 19
2.3 Scheme of a covalently-bound monochlorosilane-SAM on silicon. 20
2.4 Scheme of a crosslinked trichlorosilane-SAM on silicon. . . 20
2.5 Main kinetic steps during the growth of trichlorosilane-SAMs. 21
2.6 "Mushroom" regime vs "Brush" regime. 23
2.7 "Grafting to" approach. 26
2.8 "Grafting from" approach. 27
2.9 Kinetics of poly(MES) brush growth on gold. 37
2.10 Kinetics of place-exchange reactions between different inert thiols and the initiator. 39
2.11 Kinetics of the place-exchange reaction at -78°C. 39
2.12 XRR spectrum of a silane-initiator SAM on silicon. 42
2.13 Electron density profiles obtained from the fits of the XRR data. 43
2.14 XPS survey scan of the silane-initiator SAM on silicon. . . 44
2.15 XPS high resolution C_{1s} scan of the silane-initiator SAM on silicon. 44
2.16 Kinetics of poly(MES) brush growth on silicon and gold. . 45
2.17 Kinetics of poly(MEO_2MA) brush growth on silicon. . . . 47

2.18 Kinetics of poly(MAA) brush growth on silicon. 49
2.19 FTIR spectrum of a poly(MEO_2MA) brush after neutralization. 51
2.20 FTIR spectrum of a poly(MAA) brush after neutralization. 52
2.21 FTIR spectrum of a poly(MEO_2MA_{42}-*co*-MAA_{58}) brush after neutralization. 53
2.22 Evolution of the molar fraction of MEO_2MA in the copolymer brush as a function of the composition of the feed solution. 55
2.23 Evolution of the average block length in the copolymer brush as a function of the composition of the feed solution. 56

3.1 Description of the "Resonance Frequency Shift" method for the measurement of the kinetics of a local reaction. . . 68
3.2 Frequency spectrum of a bare silicon cantilever in water. . 77
3.3 Frequency spectrum of a magnetically driven silicon cantilever with a magnetic coating in water. 78
3.4 Scheme of the collapse transition of a thermoresponsive polymer brush. 79
3.5 Impact of the collapse transition of a thermoresponsive brush grafted on a cantilever on its resonance frequency. . 80
3.6 Resonance frequency curves of an AFM cantilever in air or in water upon silane-initiator functionalization and subsequent brush growth. 83
3.7 Mass change of AFM cantilevers coated with poly(MAA) brushes and conversion of the carboxylic acid functions inside these brushes when dipped in a 0.2 M EDC solution or a 0.2 M/0.2 M EDC/NHS solution. 88
3.8 Derivative of QCM-D data (frequency shift, third overtone) for a poly(MEO_2MA) brush grafted from a quartz sensor upon heating or cooling. 90

3.9 Comparison between the resonance frequency curves for a poly(MEO_2MA) brush grafted from AFM cantilevers obtained in different solutions. 92
3.10 Comparison of three different T_{CT} measurements for the same AFM cantilever coated with a poly(MEO_2MA) brush. 94
3.11 Frequency spectra in water of an AFM cantilever grafted with a poly(MEO_2MA) brush obtained at 25℃ and 7℃. . 96

4.1 Description of the "Deflection" method for the measurement of the kinetics of a local reaction. 108
4.2 Some examples of sensors based on the measurement of the deflection of cantilevers. 111
4.3 Lateral view of a stressed beam. 112
4.4 Link between the radius of curvature of a beam and its deflection. 114
4.5 Conformation change of pH-responsive polymer brushes upon changing the pH. 118
4.6 Impact of a change of pH on the deflection state of a cantilever grafted with a pH-responsive polymer brush. . . 119
4.7 Thermal Huisgen 1,3-dipolar cycloaddition of azides and alkynes. 121
4.8 Proposed mechanism for the Cu^{I}-catalyzed alkyne-azide cycloaddition. 122
4.9 Deflection measurements and corresponding surface stress difference for a bare cantilever and a cantilever grafted with a poly(MES) brush when dipped in buffer solutions of different pH. 124
4.10 XPS measurements for the intermediate steps leading to azido-modified brushes. 127
4.11 Front-Face Fluorimetry spectrum obtained for an azido-brush clicked with propargyl-sulforhodamine and comparison with the spectrum of a bare substrate. 128

4.12 Deflection measurements for a bare cantilever and for a lever grafted with an azido-brush when dipped in a saturated propargyl-sulforhodamine solution. 129

5.1 Description of the "Local Catalysis" experiment. 142
5.2 Some conventional lithography techniques. 145
5.3 Some examples of force-assisted AFM nanolithography techniques. 151
5.4 Energetic diagram showing the progress of a chemical reaction with and without catalyst. 153
5.5 In preliminary tests, the catalytic complexes were in solution. 155
5.6 Description of the steps involved in the preparation of the samples used in the preliminary study. 157
5.7 Density of initiator and relative thicknesses of the subsequent brush as a function of the azidation time measured for two different silanes. 158
5.8 Front-Face Fluorimetry spectra obtained for azido-SAMs reacted with alkyne (9) for 60 minutes. 160
5.9 Conversion of azide molecules to 1,2,3-triazoles by reaction with alkyne (11). 161
5.10 XPS survey scans of a poly(HEMA) brush coupled with ligand (12) and of a poly(MES) brush coupled with ligand (12) after complexation with $CuSO_4 \cdot 5\,H_2O$. 163
5.11 3D structure of the catalytic complex. 165
5.12 In local catalysis experiments, the catalytic complexes were grafted on AFM tips. 166
5.13 AFM images obtained after the local catalysis experiment in a saturated solution of alkyne (9). 169
5.14 Height profile of the thicker catalyzed line. 170
5.15 Influence of the scan speed on the thickness of the patterned lines for a constant contact force of 17 nN. 171

6.1 Chemical structures of the silanes and thiol used as SAMs. 192
6.2 Chemical structures of the monomers. 193
6.3 SEM images of a non contact silicon cantilever. 194
6.4 SEM images of the V-shaped Si_3N_4 cantilevers. 196
6.5 Chemical structures of the alkynes and the ligand. 197
6.6 Poly(HEMA) brush growth from a silanized silicon wafer with initiator (1). 201
6.7 Teflon holder for the manipulation of AFM cantilevers. . . 202
6.8 Activated ester intermediates obtained by activating carboxylic acids with EDC and NHS. 202
6.9 Modification of poly(HEMA) brushes to obtain N_3 pendant groups. 205
6.10 Patterning of the substrates for the local catalysis. 207
6.11 Silanization of silicon wafers with silane (3). 208
6.12 S_N2 substitution of the terminal Cl atoms on silane (3) with N_3. 208
6.13 Attachment of the catalytic complex to V-shaped cantilevers. 209
6.14 Description of the local catalysis of an alkyne-azide cycloaddition reaction with catalytic complexes grafted on an AFM tip. 210
6.15 Scheme of the XRR apparatus. 212
6.16 Description of the interference phenomenon. 213
6.17 Definition of the angles at play in ellipsometric measurements. 217
6.18 Definition of the information depth in a XPS experiment. 221
6.19 Scheme of the XPS apparatus. 222
6.20 Vibrational degrees of freedom of a CH_2 moiety in ethylene. 225
6.21 Morse potential model and harmonic approximation. . . . 226
6.22 Scheme of the AFM apparatus. 228
6.23 Lennard-Jones potential. 229
6.24 Definition of the working frequency in an AFM experiment. 231

List of Tables

2.1 Experimental conditions used in Figure 2.9 for the synthesis of poly(MES) brushes. 36
2.2 Experimental conditions used in Figure 2.17 for the synthesis of poly(MEO_2MA) brushes. 46
2.3 Experimental conditions used in Figure 2.18 for the synthesis of poly(MAA) brushes. 48

3.1 Numerical data for the resonance frequency experiments shown in Figure 3.6(1). 83
3.2 Numerical data for the resonance frequency experiments shown in Figure 3.6(2). 84
3.3 Comparison of the T_{CT} of poly(MEO_2MA) brushes measured by QCM-D and AFM in water and in aqueous solutions of Na_2SO_4 and NaSCN. 93

5.1 Parameters for the first local catalysis experiment. 168
5.2 Summary of the different tests made to investigate the mechanisms of the local catalysis. 171

6.1 Typical quantities for the ATRP of MES (5). 199
6.2 Typical quantities for the ATRP of MEO_2MA (6). 199
6.3 Typical quantities for the ATRP of MAA (7). 200
6.4 Typical quantities for the ATRP of HEMA (8). 200
6.5 Typical quantities for the ATRP of MAA-*co*-MEO_2MA. . 200

Chapter 1

General Introduction

Since the famous lecture that Richard Feynman gave on December 29th 1959 at the annual meeting of the American Physical Society ("There's plenty of room at the bottom"), the scientific community entered the "Nanoworld": nanotechnology was born [1]. This breakthrough completely changed the way of making science. One of the most thrilling perspectives about nanotechnology is the design of nanofactories in which swarms of nanorobots would assemble atoms or molecules to form products ranging from new molecules to macroscopic objects with an atomic precision. Whereas the ethical and economical implications are still under debate, lots of applications could benefit from that. For instance, one could think of nanodevices that would be implanted in a human body to track any source of disease such as cancer and synthesize the appropriate drug *in situ*. This is still a dream nowadays but according to some theories, this dream could come true in the not-too-distant future [2].

K. Eric Drexler spent a lot of effort in developing the concepts of nanotechnology from the theoretical point of view, giving a detailed analysis of molecular machinery and the way to design, analyze and build it [3, 4]. His main conclusion is that there seems to be no insurmountable problem to translate these theories into practice. Other authors agree with his visions [5–7] but the debate is still open. Anyway, while it is clear that his dream nanofactory will not be realized anytime soon, more pragmatic examples of physicochemical devices working at the nanoscale can be found in the literature such as nanomachines or molecular motors based for instance on catenanes and rotaxanes [8–10], carbon nanotubes [11, 12], Nano Electro-Mechanical Systems (NEMS) [13] or stimuli-responsive materials such as polymer brushes [14].

As it will be further described in the following paragraphs, this thesis aimed to develop new tools for these future nanofactories.

1.1 Objectives and Strategies

This thesis was embedded in a larger project called DYnanoMOVe whose purpose was to develop the constitutive elements of a nanometric chemical factory such as nanochemical reactors or nanoconveyor belts and to increase the understanding of the behavior of such elements at the nanoscopic scale (Figure 1.1(1)). In that respect, two series of tools were fabricated. The first one was developed in order to precisely monitor the kinetics of the chemical reactions arising in each of the nanoreactors and to measure the efficiency of the molecular transport between them (Figure 1.1(2)). The second tool was built to locally modify the kinetics of a reaction taking place inside a particular reactor or between molecules on the substrate and molecules in solution (Figure 1.1(3)). The development of these tools is the purpose of this thesis.

Atomic Force Microscopy (AFM) cantilevers were chosen as the probes because, on the one hand, these micro-levers are commercially available, relatively cheap and equipped with sharp tips and, on the other hand, the piezoresistive tube of the microscope nose on which the cantilever is mounted allows its precise positioning on the substrate under study. These cantilevers have widely been used in the literature for sensing applications and as lithographic tools. However, their sensitivity is generally well below the one of dedicated probes.

The aim of this thesis was thus to improve the performances of these AFM cantilevers for such applications. The main strategy was to increase the number of reactive sites on the cantilevers in order to interact faster and with more sensitivity. To reach this objective, AFM cantilevers were functionalized with polymer brushes. Indeed, polymer brushes, as assemblies of macromolecules densely grafted on a substrate, provide stable surfaces that can contain a large amount of reactive side groups per unit area.

1.2 Methodology

The present work is divided into three main parts. The first part (Chapter 2) is dedicated to polymer brushes and their synthesis as they will be used as the basic material for all the subsequent applications. The preparation of polymerization-initiator-SAMs either on gold or on silicon will also be discussed as well as the study of the kinetics of their growth.

The second part (Chapters 3 and 4) deals with the analysis of the kinetics of (physico)chemical reactions at the submicrometric scale using modified AFM cantilevers as the sensing probes. Two different methods will be examined: the frequency shift method (Chapter 3) and the deflection method (Chapter 4). The first method is based on the fact that the resonance frequency of a cantilever is inversely proportional to its mass while the second one is based on the variation of the surface stress of the cantilever upon selective adsorption of target molecules on one of its faces. The kinetics of the activation reaction of weak polyacid brushes and the collapse transition temperature of thermo-responsive brushes will be measured by the first method while the pH-responsive behavior of polyelectrolyte brushes and the kinetics of a "click" reaction will be studied with the second method.

The third part (Chapter 5) concerns the catalysis of surface-confined "click" reactions at the nanoscopic scale with functionalized polymer brushes grafted from an AFM tip. Before determining the mechanism of this lithographic technique, the grafted catalytic complexes as well as the reactive surfaces will be fully characterized.

Finally, the experimental details related to every undertaken experiment will be given in a dedicated chapter for the sake of clarity (Chapter 6) and this will be followed by some concluding remarks and some suggestions for a future work (Chapter 7).

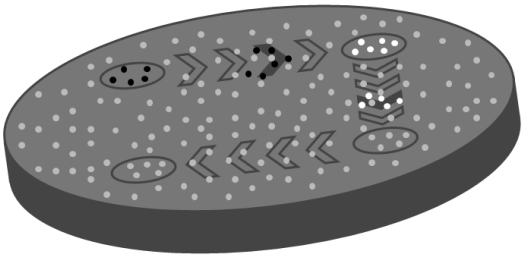

(1) A nanofactory contains nanoreactors and nanoconveyor belts among other things

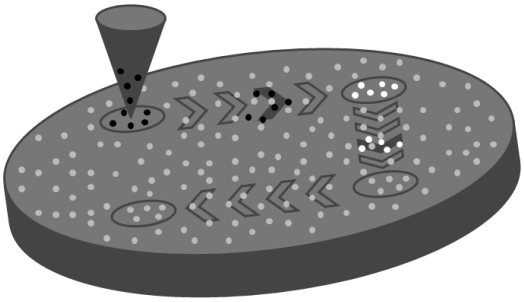

(2) Probes can be used to monitor the kinetics of the reactions

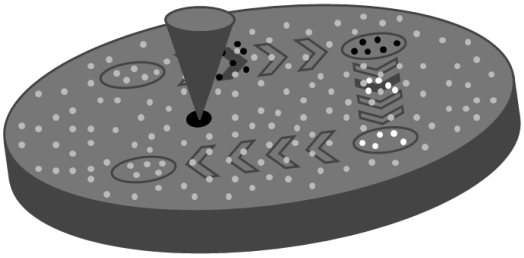

(3) Probes can be used to locally catalyze a reaction

Figure 1.1: A nanofactory is composed, among other things, of nanoreactors and nanoconveyor belts. Then, to characterize the progress of the reactions arising on the nanoreactors or to increase the kinetics of a specific reaction, nanoprobes are needed.

References

[1] Feynman, R. P. There's Plenty of Room at the Bottom. In *Miniaturization*; Gilbert, H. D., Ed.; Reinhold, 1961; pp 282–296.

[2] Ozin, G. A.; Manners, I.; Fournier-Bidoz, S.; Arsenault, A. *Adv. Mater.* **2005**, *17*, 3011–3018.

[3] Drexler, K. *Nanosystems: molecular machinery, manufacturing, and computation*; John Wiley and Sons, Inc., 1992.

[4] Drexler, K. E. *Annu. Rev. Biophys. Biomol. Struct.* **1994**, *23*, 377–405.

[5] Krummenacker, M.; Lewis, J. *Prospects in nanotechnology: toward molecular manufacturing*; John Wiley and Sons, Inc., 1995.

[6] Freitas, R. *Nanomedicine, Volume I: Basic Capabilities*; Landes Bioscience Georgetown, TX, 1999; Vol. 509.

[7] Hall, J. *Nanofuture: What's next for nanotechnology*; Prometheus Books, 2005; Vol. 284.

[8] Balzani, V.; Credi, A.; Silvi, S.; Venturi, M. *Chem. Soc. Rev.* **2006**, *35*, 1135–1149.

[9] Kay, E.; Leigh, D.; Zerbetto, F. *Angew. Chem., Int. Ed.* **2007**, *46*, 72–191.

[10] Sauvage, J.-P. *Acc. Chem. Res.* **1998**, *31*, 611–619.

[11] Lozovik, Y. E.; Minogin, A. V.; Popov, A. M. *Phys. Lett. A* **2003**, *313*, 112–121.

[12] Lozovik, Y.; Popov, A. *Fullerenes, Nanotubes, Carbon Nanostruct.* **2004**, *12*, 485–492.

[13] Craighead, H. G. *Science* **2000**, *290*, 1532–1535.

[14] Santer, S.; Ruhe, J. *Polymer* **2004**, *45*, 8279–8297.

Chapter 2

Functionalization of AFM Cantilevers with Polymer Brushes

2.1 Introduction

As mentioned in the general introduction, the two main objectives of this thesis were first, the measurement of the kinetics of local reactions and second, the local catalysis of surface reactions. For both objectives, AFM cantilevers and tips were used. Then, in order to increase the sensitivity and the reactivity of these probes, polymer brushes were grafted from their surface. Indeed, polymer brushes offer a good coverage of the substrate and provide a high density of desired functional groups per unit surface area.

This chapter will thus focus on polymer brushes since they were used as the basic material throughout this whole thesis. Prior to the polymerization step, it is necessary to coat the substrate with a polymerization initiator. The most common route is to use a self-assembled monolayer (SAM) of the desired initiator.

Depending on the nature of the substrate, different monolayers can be used. The two most frequent systems are, on the one hand, silane monolayers on silicon and, on the other hand, thiol monolayers on gold. In this work, two different types of cantilevers were needed depending on the considered application. Indeed, the measurement of the kinetics of a local reaction with the resonance frequency shift method necessitated stiff cantilevers to increase the fundamental resonance frequency and thus the sensitivity whereas the measurement of the kinetics of a local reaction with the deflection method as well as the local catalysis of a reaction necessitated flexible cantilevers to increase the sensitivity of the detection in the first case and to not damage the surface during the lithography in the second case. Commercially-available stiff cantilevers usually have a rectangular cross-section and are made of silicon while commercially-available flexible cantilevers are usually V-shaped, made of silicon nitride and coated with a thin layer of gold. Both kinds of cantilevers can be functionalized with silanes since these molecules can

self-assemble on silicon and silicon nitride. However, to get rid of the thermal drift in the deflection curves of the V-shaped cantilevers (as they are made of Au/Si_3N_4 bilayers), the idea was to coat the Au-side of the cantilevers with an inert thiol monolayer, to evaporate a thin layer of gold on the Si_3N_4-side and to coat it with a thiol-initiator monolayer. In that case, the system would have been symmetrical and should not have suffered from thermal drift. So, the formation of both types of monolayers will be investigated.

Since the thiol molecules form weak covalent bonds with the substrate, thiol SAMs are less stable and exchange with other thiols in solution can occur. The kinetics of place-exchange reactions of thiols on gold was thus investigated since it would not be desirable that the inert thiol molecules exchanged with thiol-initiator molecules. To measure this kinetics, the strategy was to self-assemble an inert thiol monolayer on a gold-coated silicon substrate, then to immerse it in a solution containing the thiol-initiator for various amounts of time, to grow a polymer brush on the resulting samples and to measure the thickness of these brushes. It will be shown that this particular exchange between inert and initiator thiols is very fast so that the above mentioned strategy could not be followed. Then, whenever the thermal drift was limiting, the temperature had to be controlled.

Regarding silane-initiator-SAMs, they were characterized in terms of thickness, grafting density, chemical composition and activity.

Throughout this work, four different monomers were used: the mono-2-(methacryloyloxy) ethyl succinate (MES) (5), the di(ethylene glycol)-methyl ether methacrylate (MEO_2MA) (6), the methacrylic acid (MAA) (7) and the 2-hydroxyethyl methacrylate (HEMA) (8) (Figure 6.2 on page 193 in the Experimental Part). A full study of the growth kinetics of poly(MEO_2MA) and poly(MAA) brushes will be presented for different experimental conditions and the parameters that influence this kinetics will be described. The purpose of this part will be to deter-

mine the optimal conditions in order to get rapidly growing brushes in a controlled fashion. The parameters that will be varied are mainly the monomer concentration, the amounts of catalyst and of deactivator and the water content of the solution. We will see that the optimal conditions for growing poly(MEO_2MA) and poly(MAA) brushes are quite different from each other. Then, intermediate conditions will be selected for the copolymerization of these two monomers and the composition of the resulting copolymer brushes will be determined depending on the relative concentration of each comonomer in the feed solution. This will allow the calculation of the reactivity ratios of these two monomers. With these ratios, the *a priori* determination of the composition and of the structure of the copolymer as well as of the average block length inside the copolymer will be possible for any comonomer ratios in the feed solution.

Prior to the presentation and the discussion of these results, some theoretical aspects concerning the functionalization of AFM probes, the self-assembly of monolayers on gold and silicon and the synthesis of polymer brushes will be presented. Finally, a conclusion will be drawn in the last section.

2.2 Theoretical Aspects

2.2.1 Functionalization of AFM Probes

When AFM probes are used for sensing applications, their functionalization is often necessary to allow the selective adsorption of target molecules. There exist various ways to functionalize AFM cantilevers or tips and different kinds of materials can be deposited/grafted such as metals, semiconductors, polymers, biomolecules, SAMs, etc [1, 2].

When only one probe is to be functionalized (or multiple probes but with the same coating), standard methods can be used. For instance, thermal or electron beam-assisted evaporation of metals [3, 4] was used to coat AFM probes. The metal layers can be used as such, e.g. for gas or ion detection [5–7], or as substrates to anchor successive layers such as polymers and SAMs [8, 9]. Similarly, sputtering can also be used to coat the cantilevers with metals [6] for aforementioned applications or with other kinds of materials such as ZnO [10]. In this precise case, ZnO was not used as a sensing layer but as a piezoelectric material to detect the bending of the cantilever. Sputtering and evaporation allow the formation of controlled thickness of the deposited layers.

Monolayer functionalization through the self-assembly of molecules (typically thiols on gold and silanes on silicon) is a widely used technique for obtaining dense, ordered and stable monolayers of molecules with specific chemical properties. The formation of these self-assembled monolayers (SAMs) will be described in the next section. To summarize, these molecules can be deposited either from the liquid phase or from the vapor phase and due to specific interactions between the endgroups of these molecules and the substrate, the formation of dense monolayers is promoted. These SAMs were used for instance to anchor biomolecules for the fabrication of biosensors [11–14], or as initiating layers for the polymerization of various monomers [8, 15–18] in order to measure the behavior of these polymers under different experimental conditions or to create efficient sensing layers.

Polymers can also be deposited via other methods such as spray coating [3, 19] or spin coating [20] while layers of organic and biological molecules can be created without the intermediary of SAMs, by layer-by-layer nanoassembly (LBL) [21] or by Langmuir-Blodgett (LB) deposition for instance.

When cantilever arrays have to be functionalized with different sensing layers, two different approaches can be developed. Either the previ-

ous standard methods can be applied but with some modifications such as the use of shadow masks [3] or the focused ion beam milling of the undesired material [20], or specific techniques can be used. In that case, simple methods can be employed such as the manual placement of particles [22–24] or direct pipetting of solutions onto the cantilevers [7] but these techniques are rather time consuming and have a limited reproducibility. More advanced techniques are thus often preferred. These include the use of microfluidic networks [25], arrays of dimension-matched capillaries [26, 27] and inkjet spotting [28, 29].

In this thesis, the AFM cantilevers were functionalized with polymer brushes. This necessitated the coating of the cantilevers with initiator-SAMs prior to the polymerization step. In the next two sections, the theory of SAMs and of polymer brushes will thus be presented.

2.2.2 Self-Assembled Monolayers on Gold and Silicon

Self-assembled monolayers (SAMs) are monolayers of molecules that form specific interactions between one of their ends and the substrate on which they are deposited. It induces the formation of a stable layer even after the removal from the reactive medium.

It is often written that the concept of self-assembled monolayers was first described by Zisman et al. in 1946 [30]. They first showed that some organic molecules can be adsorbed from solutions to form well-oriented monolayers on solid surfaces. They concluded from their experiments that the studied films were made of close-packed molecules that were almost vertically oriented. But it is only in the early 1980s that this concept definitively entered the scientific consciousness thanks to the works of Nuzzo & Allara [31] and Maoz & Sagiv [32]. Nuzzo & Allara dealt with thiols on gold while Maoz & Sagiv were interested in silanes

on silicon. Interest in these two systems has been continuously growing since that time. These are now by far the two most popular families of SAMs and are used in many different applications.

The formation of SAMs was reviewed in 1996 by Ulman [33] and more recently by Schwartz [34]. Basically, the formation of a monolayer is a stepwise phenomenon. Generally and to simplify, there are at least three steps that can be compared to an isothermal path through a quasi-equilibrium 2D-phase diagram. During the first step there is only one phase considered as the "vapor" phase and made of single mobile molecules adsorbed on the substrate in a disordered and random fashion. For intermediate concentrations at the interface, there is a coexistence between randomly-oriented, low density domains and higher-density condensed domains. Finally, there is the "solid" phase for high concentrations where the molecules are well ordered and closely packed.

There exist two methods to self assemble monolayers on a substrate: one can either deposit these layers from the vapor phase or from the liquid phase. In this study, the liquid phase method was mainly used as it was easier to handle when dealing with AFM probes. Moreover the monolayers obtained from these two methods gave similar results. The substrates of interest were, on the one hand, silicon as it is the main material used for AFM cantilevers production and, on the other hand, gold as it is easily evaporated to form controlled layers of desired thicknesses. The liquid phase deposition technique for thiols on gold and silanes on silicon will thus be described into more details. These two families of monolayers are quite different from each other because thiols form reversible bonds with gold which enables them to move on the surface and to rearrange themselves whereas silanes form irreversible covalent links on silicon which makes them immobile. So the monolayer formation responds to rather different mechanisms.

Thiols on gold

There are multiple processes at play during the growth of a thiol-based SAMs. Indeed, contact angle measurements and ellipsometry by Bain et al. [35] on quenched thiols monolayers on gold indicated that the contact angle and the thickness of these films reached around 90% of their final values in only 1 minute for typical conditions. However, the last 10% were attained only after a few hours meaning that a second phenomenon with a much longer time scale intervened. Lots of studies drew the same conclusions and showed that there were at least two main kinetic steps involved in the growth process for regular conditions [36–38].

The solvent and the chain length were shown to influence the kinetics of the film growth in a great fashion. Schneider and Buttry [39] established that the better the solvent is, the faster is the kinetics but the lower is the final quality of the monolayer. Interestingly, it was shown by Peterlinz et al. that the kinetics of the first step increases with decreasing chain lengths while this is the opposite for the second step [40]. In their model, the first step consists in the transport of molecules to the substrate through a physisorbed film on top of the chemisorbed molecules (Figure 2.1(1)) while in the second, islands growth happens via molecular motion within the chemisorbed film (Figure 2.1(2)). So in the first step, as the length of the chain increases, the transport is slowed down due to higher interchain interactions. Then during the second step, islands growth is favored for higher interchain interactions thus for longer thiols. They also showed that for strong solvents such as heptane, the formation of the physisorbed film is inhibited and only one fast kinetic step is observed while for weaker solvents such as ethanol, a third kinetic step can be observed for longer thiols (C_{16}-C_{18}) and multilayer formation is promoted as also mentioned by other studies [41]. Finally, they noticed a decrease of the overall film growth as the concentration decreases.

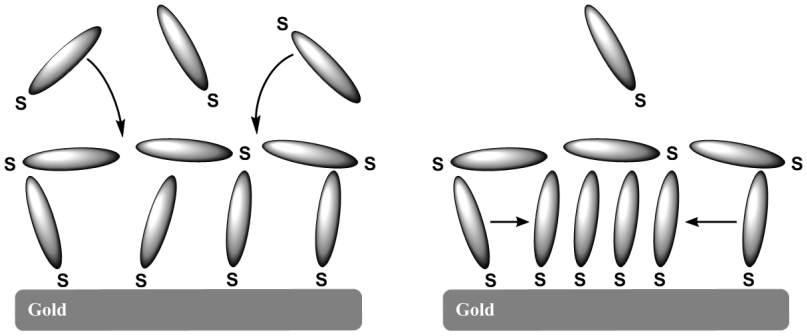

(1) Step 1 (2) Step 2

Figure 2.1: Main kinetic steps during the growth of thiol-SAMs. Left : Step 1: Transport of molecules through a physisorbed film on top of the chemisorbed molecules. Right : Step 2: Molecular motion inside the chemisorbed film.

All these observations are coherent with the mechanism involving patches of lying and disordered molecules and islands of vertically oriented molecules that grow to cover the surface. This has been supported by spectroscopic studies [42, 43] and by more recent scanning probe microscopy studies [44–46]. These also showed that the thiol molecules follow the hexagonal pattern of the gold surface in their final arrangement. So at the end of the SAM formation, thiol molecules are densely packed and well oriented in a crystalline fashion as schematized in Figure 2.2.

Due to the nature of the chemical Au–S bond, there can be various stability issues such as place-exchange reactions between thiols adsorbed on a gold surface and thiols in solution. Thiols-based SAMs can be stabilized by increasing the length of the thiols or by introducing specific groups in order to enhance lateral interactions between shorter chains. Anyway it is often reported that the exchange process is a matter of hours [47–50]. However, depending on the quality of the gold surface,

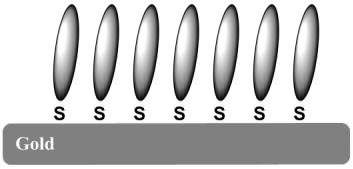

Figure 2.2: Scheme of a thiol-SAM on gold.

this process can be sped up. Indeed, it is well known that the defects, such as grain boundaries, are sites where the exchange is faster [51–53]. So for systems where gold surfaces are produced by thermal evaporation for example, this phenomenon can have dramatic consequences.

Silanes on silicon

Silane-based SAMS are very interesting in the field of monolayers because of the irreversible covalent bonds that these molecules form with the substrate as underlined in Figure 2.3. It is even truer for trichlorosilanes (or trimethoxy- and triethoxysilanes) because they can cross-link on the surface to form a siloxane network as depicted on Figure 2.4. It leads to layers that have good mechanical and chemical tenues. In parallel, this prevents the layer from having long-range molecular order as opposed to thiol SAMs where the Au lattice dictates the arrangement.

During the self-arrangement of the monolayer on the surface, there is a competition between the immobilization of the molecules and their hydrolysis. The relative kinetics of these two phenomena depends on the experimental conditions such as the pH, the temperature and the water content. Of course, this is a critical point for the kinetics of the monolayer formation itself. It can have a dramatic influence on the morphology and

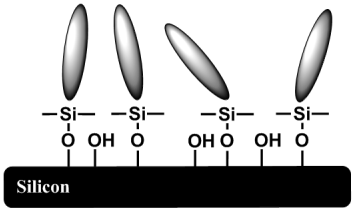

Figure 2.3: Scheme of a covalently-bound monochlorosilane-SAM on silicon.

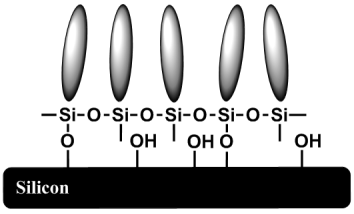

Figure 2.4: Scheme of a crosslinked trichlorosilane-SAM on silicon.

the final properties of the monolayer [34].

The Hoffmann group spent lots of efforts in investigating the growth mechanisms of silane-SAMs for various experimental conditions [54–56]. *In situ* AFM measurements of octadecyltrichlorosilane (OTS) SAMs [57] showed that quite large islands are observed during the first few moments of the silanization meaning that the growth is first initiated by the adsorption of polysiloxane oligomers formed in solution in the presence of traces of water (Figure 2.5(1)). So oligomers adsorb much faster on the active sites than the monomeric units. These islands were 2.5 nm-thick which is comparable to the molecular length of OTS molecules. This suggests that molecules are perpendicularly oriented on the surface. In a second and much slower step, the islands grow by the adsorption of

monomers from the solution (Figure 2.5(2)). However, in previous AFM studies on quenched OTS films, they simultaneously observed both islands and a continuous phase. But, although a lot of authors proposed to quench the reaction at early stages to study the mechanisms of the silane-based monolayer formation, it has been proved by Richter and coworkers [58, 59] that there exist systematic differences between monolayers studied by *in situ* experiments and quenched partial monolayers. They observed by X-Ray Reflectivity (XRR) studies that quenching OTS films leads to an irreversible decrease of their density and thickness even after reimmersion in the solvent. Since the density was more affected than the thickness, they suggested that molecules closely packed inside the growing islands were not much affected while molecules on the perimeter were removed or allowed to tilt. In conclusion, while quenching experiments provide an interesting overview of the growing mechanisms of the silane-SAMs, they should be looked at carefully.

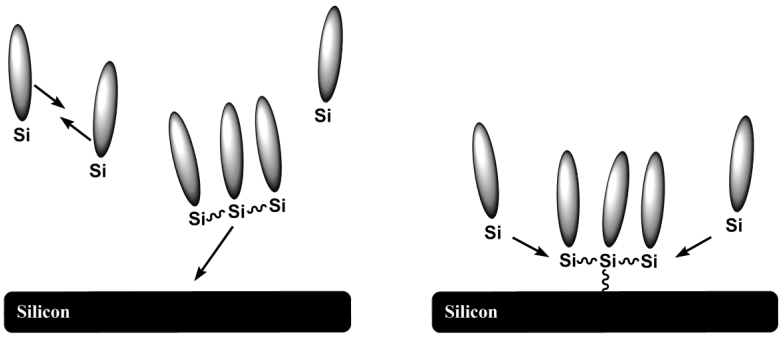

(1) Step 1 (2) Step 2

Figure 2.5: Main kinetic steps during the growth of trichlorosilane-SAMs. Left : Step 1: Oligomers form in solution in the presence of traces of water and adsorb on the surface. Right : Step 2: Islands grow by adsorption of monomers from the solution.

Hoffmann and coworkers also showed that the water content in the solution is a crucial parameter for the kinetics and the mechanisms of

the growth as well as for the final properties of the films. Indeed, for higher water contents, the islands grow faster because water speeds up the oligomer formation in solution (called "solution polymerization") and induces the adsorption of longer oligomers. These oligomers were found by Zhao et al. to form only a few chemical bonds with the surface [60]. Moreover, even higher water contents results in polysiloxane gel deposition on the surface. A more recent review from Sander et al. [61] showed that water can also interact with the silane in another way: when water is adsorbed on the surface instead of being mixed with the solution, the silane molecules polymerize directly on the surface ("surface polymerization") providing a higher final grafting density than for solution polymerization. Finally, in the absence of water, the trifunctional silanes react similarly to monofunctional ones and "monomeric synthesis" is favored. This kind of synthesis also arise for low silane concentrations. In this case, the units adsorb one at a time on the surface and the final density is decreased.

2.2.3 Polymer Brushes

Generalities

When polymer chains are grafted on a substrate, different regimes can be observed depending on the grafting density. For low grafting densities, the chains do not influence one another. They thus roughly occupy the volume of a half-sphere whose radius in comparable to the radius of gyration, R_g, of the chain in solution. This regime is called the "Mushroom" regime (Figure 2.6(1)). For higher grafting densities, i.e. when the interchain distance is much smaller than twice the radius of gyration, the chains tend to extend from the substrate due to the high sterical hindrance and are in the "Brush" regime (Figure 2.6(2)). Polymer brushes are thus defined as dense layers of macromolecules densely grafted on a

substrate [62, 63].

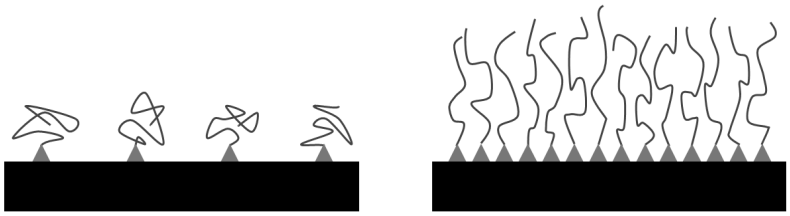

(1) "Mushroom" regime (2) "Brush" regime

Figure 2.6: There exist two limiting regimes for the conformation of polymer chains grafted on a surface in function of the grafting density: (1) the "Mushroom" regime for low grafting densities and (2) the "Brush" regime for high grafting densities.

This latter conformation leads to many very interesting properties. For example, surfaces with a high density of given chemical functionalities can be obtained [64]. This can enhance the reactivity of the substrate. Alternatively, this dense layer can be used as a protective coating against fouling or corrosion [65–67]. But their most used set of properties lies in their ability to respond to external stimuli [68]. Brushes possessing this property are called "stimuli-responsive polymer brushes" [69]. It is well known since the work of Flory and Huggins in the early 1940's [70, 71] that macromolecular chains adapt their conformation due to environmental changes. They developed a thermodynamic model to calculate the Gibbs free energy change ΔG_m accompanying the mixing of a polymer and a solvent. Generally, the Gibbs free energy change upon mixing is the difference between the enthalpy change ΔH_m and the product of the temperature and the entropy change $T\Delta S_m$:

$$\Delta G_m = \Delta H_m - T\Delta S_m \tag{2.1}$$

When the relative sizes of the mixed components do not match, which is the case when dissolving a polymer in a solvent, this equation becomes:

$$\Delta G_m = RT\left(n_1 \ln \phi_1 + n_2 \ln \phi_2 + n_1 \phi_2 \chi_{12}\right) \tag{2.2}$$

So the free energy change depends on the number of moles n_1 and volume fraction ϕ_1 of the solvent, the number of moles n_2 and the volume fraction ϕ_2 of the polymer and the polymer-solvent interaction parameter χ_{12}. This parameter depends on the nature of the solvent and of the polymer.

By extension, one finds that the end-to-end distance of a free polymer chain $\left\langle r^2 \right\rangle^{1/2}$ depends on the balance between monomer-solvent interaction, monomer-monomer interaction and solvent-solvent interaction, notions embedded in the definition of χ_{12}. This equilibrium can be displaced by modifying the environment (e.g. the pH, the temperature,...) and the chain can swell or shrink accordingly. Since polymer brushes are macromolecules densely grafted by one end to a substrate, the chains can expand or collapse but the movement is restricted to the dimension perpendicular to the substrate and the amplitude of this movement is hence increased.

Thus, literally speaking, every polymer is responsive to external stimuli. But when we talk about stimuli-responsive polymers (or here stimuli-responsive polymer brushes), we refer more to the applications of these polymers. A polymer will be considered responsive if a change in its environment modifies its properties in a noticeable way regarding the considered application. Talking of stimuli-responsive polymer brushes, these can then be considered as smart coatings with applications in actuation [16, 72], motion control [73], tuning of biointeractions [74, 75], stimuli-gated filtration [76] and sensing [15].

Ideally, a good polymer brush is highly monodisperse, its thickness is finely controllable and is constituted of linear chains. There exist two strategies of polymer brush grafting, the "grafting to" approach and the "grafting from" approach:

1. "Grafting to"

   In this approach, fully grown polymer chains are grafted to the substrate (Figure 2.7). In order to do so, the chain ends [77] and/or the substrate [78] are functionalized. Depending on these endgroups, the polymers are subsequently grafted onto the surface by chemical bond formation or physisorption [63]. In the latter case, the anchor points can move on the substrate. This is not suitable for some applications e.g. when the brushes have to withstand high shear rates. Aside from that, some functional groups can not be used in this approach due to parasitic chemical or physical adsorption. Moreover, this method limits the maximum achievable grafting density. Indeed, at a certain point of the grafting, the surface becomes unreachable for the chains still in solution due to steric hindrance. Finally, the thickness of the brush is limited by the degree of polymerization in solution. This induces thicknesses usually much lower than 100 nm. While these two last facts can be drawbacks for some applications, low grafting densities and thicknesses are not necessarily detrimental for sensing applications as it will be seen in the following.

2. "Grafting from"

   To circumvent some of these limitations and to obtain a more versatile system, the "grafting from" method was selected. This technique, also called surface-initiated polymerization (SIP) requires the self assembly of a polymerization initiator. The most used substrates are gold and silicon but other substrates, such as aluminum and stainless steel, can be used as well [79]. Here, the

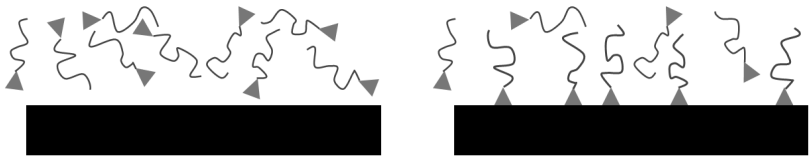

(1) Initial step (2) Intermediate step

(3) Final step

Figure 2.7: In the "grafting to" approach, functionalized, fully grown polymer chains are immersed in solution in the presence of the substrate (top-left). The chains are progressively chemi- or physisorbed (top-right). This method leads to quite low grafting densities (bottom).

monomers are added one at a time on the growing chains which allows high grafting densities (Figure 2.8) although lower densities are also reachable by decreasing the surface concentration of initiators. This method is compatible with a huge collection of different monomers either in aqueous or organic solvents [63].

Living Polymerizations

Living polymerization is the common choice for the grafting from of polymer brushes. Indeed, it allows the fine control of their polydispersity, their thickness and their composition. In this kind of polymerizations, the initiation step is fast in comparison with the propagation step, all chains grow simultaneously and there is ideally no termination or transfer reactions. The reaction steps are described by:

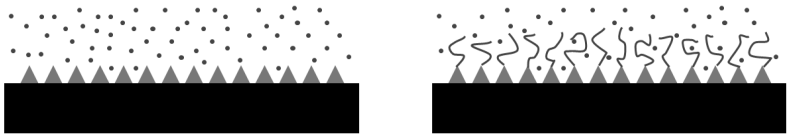

(1) Initial step (2) Intermediate step

(3) Final step

Figure 2.8: In the "grafting from" approach, a substrate covered with polymerization initiators is immersed in the solution containing the monomers (top-left). The monomers add one at a time on the growing chains (top-right). This method can lead to high grafting densities (bottom).

$$\text{Activation} \quad : \quad \sim M_n - R \xrightarrow{k_a} \sim M_n^{\bullet} + R^{\bullet} \tag{2.3}$$

$$\text{Propagation} \quad : \quad \sim M_n^{\bullet} + M \xrightarrow{k_p} \sim M_{n+1}^{\bullet} \tag{2.4}$$

$$\text{Deactivation} \quad : \quad \sim M_n^{\bullet} + R^{\bullet} \xrightarrow{k_d} \sim M_n - R \tag{2.5}$$

$$\text{Termination} \quad : \quad \sim M_n^{\bullet} + \sim M_m^{\bullet} \xrightarrow{k_t} \sim M_{n+m} \tag{2.6}$$

Equation (2.6) suggests that it is better to work with low radical concentrations to avoid termination reactions. To achieve this, it is necessary to form dormant species. The conversion rate of the monomer is given by:

$$-\frac{d[M]}{dt} = k_p[M_n^\bullet][M] \tag{2.7}$$

This is a first order polymerization rate regarding the monomer concentration. If the amount of radicals remains constant, we can integrate equation (2.7):

$$\ln\left(\frac{[M]}{[M]_0}\right) = -k_p[M_n^\bullet]t \tag{2.8}$$

We can see that there exists a linear dependence between the logarithm of the monomer concentration and the time. Polymerizations that have rates approaching equation (2.8) are called "living polymerizations". In real life, they are limited by progressive saturation of the growth due to termination reactions or chain transfers. There exist many different kinds of living polymerizations. Some of the most frequently used ones are listed below:

- Anionic Polymerization allows a good control of the polymer thickness. However, it needs drastic purification and drying conditions. This polymerization is very sensitive to impurities. Moreover, there is only a limited amount of monomers that permits it and its rate is quite low [80].
- Cationic Polymerization needs a cationic species as initiator that transfers a positive charge on the monomer. Most Lewis acids used to induce the polymerization are water intolerant and there is thus a need to thoroughly dry the medium. However, recent developments made possible the cationic polymerization of styrene in presence of water [81].
- Ring Opening Polymerization (ROP) is limited to cyclic monomers

whose rings are opened during the polymerization process. It can be either anionic or cationic depending on the monomer and the initiator. It was shown that the propagation may proceed without termination and irreversible transfer reactions [82].

- Ring Opening Metathesis Polymerization (ROMP) is limited to cyclic olefins. The mechanism of the polymerization is based on olefin metathesis thanks to a metal catalyst. In this polymerization, the double bonds of the monomers are conserved in the polymer which leads to interesting properties [83].

- Reversible Addition-Fragmentation chain Transfer (RAFT) consists in a free radical polymerization in the presence of dithioesters. These esters transfer between active and dormant chains to give the living character to the polymerization. This method can be used with a wide range of monomers and reaction conditions and provides a good control of the molecular weight of the polymers and narrow polydispersities [84].

- Nitroxide-Mediated Polymerization (NMP) is a living radical polymerization where the active sites are protected by the reversible addition of nitroxide end groups. This polymerization needs high temperatures (ca. 120°C) which may not be suitable for all applications [85].

- Atom Transfer Radical Polymerization (ATRP) is the most commonly used polymerization technique for growing brushes. It is well controlled. The initiator synthesis is easier than for surface-initiated RAFT or NMP [62]. Some of them are commercially available. Moreover the synthesis conditions are not restrictive. It is possible to carry out this polymerization at room temperature in aqueous solutions. This is the route that we chose to synthesize our polymer brushes. The ATRP reaction scheme is given by:

$$M_n - X + Mt^z LY \underset{k_d}{\overset{k_a}{\rightleftharpoons}} \quad M_n^\bullet \quad + X Mt^{z+1} LY \qquad (2.9)$$

$$\circlearrowleft$$

$$M_{n+1}^\bullet$$

Mt^z is the transition metal, usually Cu, at oxidation state z, L is the ligand, Y and X are halogen atoms. Activation of the dormant species is due to bond breaking between the growing chain and the protective terminal halogen atom. This is catalyzed by the oxidation of a metallic complex. Propagation can then occur. Deactivation is the reverse process when the halogen atom recombines with the chain [86]. ATRP kinetics is highly influenced by many parameters such as the solvent, the ligand, the monomer(s), the quality of the initiator, the pH, the temperature, the ionic force, etc [87].

We have seen that due to the living aspect of the polymerization, the thickness of a polymer brush is directly proportional to the monomer concentration in solution and from equation (2.8), it is possible to directly link the monomer concentration with the reaction time provided that the radical concentration remains constant. However, nonlinearities can arise after some time due to termination reactions [86]. Moreover, some reactive sites can be engulfed inside the brush and become no longer accessible for the catalytic complexes [88]. So in many cases, the radical concentration is not constant. In 1999, Fischer proposed an equation that gives the time variation of the radical concentration [89]:

$$\frac{d[M_n^\bullet]}{dt} = k_a[M_n - X] - k_d[M_n^\bullet] - k_t[M_n^\bullet][M_m^\bullet] \qquad (2.10)$$

The equilibrium constant K_{eq} between activation and deactivation is given by:

$$K_{eq} \doteq \frac{k_a}{k_d} = \frac{[M_n^\bullet][\mathrm{Cu^{II}}LY_2]}{[M_n - X][\mathrm{Cu^{I}}LY]} \tag{2.11}$$

This suggests that the ratio between $[\mathrm{Cu^{II}}]$ and $[\mathrm{Cu^{I}}]$ is critical to maintain a controlled polymerization and to decrease the rate of termination reactions.

In the case of surface-initiated ATRP (or SI-ATRP), the amount of initiator molecules is very small and equation (2.8) becomes:

$$\frac{[M]}{[M]_0} \approx 1 - k_p[M_n^\bullet]t \tag{2.12}$$

Making the approximation that a change in $[M_n^\bullet]$ only comes from termination reactions, equation (2.10) rewrites:

$$\frac{d[M_n^\bullet]}{[dt]} = -k_t[M_n^\bullet][M_m^\bullet] \tag{2.13}$$

By integration of equation (2.13) and substitution in equation (2.12), we have:

$$[M]_0 - [M] = \frac{[M]_0 k_p [M_n^\bullet]_0 t}{1 + [M_n^\bullet]_0 k_t t} \tag{2.14}$$

Since the thickness of the brush is proportional to $[M]_0 - [M]$, we

can see that termination reactions induce a non linear dependence of the thickness as a function of time [90].

Copolymer brushes

Growing copolymer brushes is somewhat tricky because one has to find a common set of parameters that allows the controlled polymerization of both comonomers with an appropriate kinetics. But this is not enough. Indeed, the composition of the copolymer is usually not the same as the composition of the solution. Moreover, the architecture of the copolymer brush (statistical or block copolymer) can also vary according to different factors.

The work of F. Mayo and F. Lewis in 1944 allows solving these two issues [91]. Indeed, they developed an equation to describe the composition of a copolymer at every stage of the reaction. Considering two monomers M_1 and M_2, four propagation reactions can take place:

$$\sim M_1^\bullet + M_1 \xrightarrow{k_{11}} \sim M_1^\bullet \tag{2.15}$$

$$\sim M_1^\bullet + M_2 \xrightarrow{k_{12}} \sim M_2^\bullet \tag{2.16}$$

$$\sim M_2^\bullet + M_1 \xrightarrow{k_{21}} \sim M_1^\bullet \tag{2.17}$$

$$\sim M_2^\bullet + M_2 \xrightarrow{k_{22}} \sim M_2^\bullet \tag{2.18}$$

The reactivity ratios are given by:

$$r_1 \doteq \frac{k_{11}}{k_{12}} \tag{2.19}$$

$$r_2 \doteq \frac{k_{22}}{k_{21}} \tag{2.20}$$

The Mayo-Lewis equation gives the instantaneous composition of the copolymer as a function of the composition of the feed solution:

$$\frac{d[M_1]}{d[M_2]} = \frac{[M_1](r_1[M_1] + [M_2])}{[M_2]([M_1] + r_2[M_2])} \tag{2.21}$$

This equation is valid in the quasi-stationary state approximation that considers that the rate of radicals formation is equal to the rate of their destruction ($d[M_1^\bullet]/dt = d[M_2^\bullet]/dt \simeq 0$). Other reasonable hypotheses have to be accepted in this model such as no hydrolysis, homogeneous reactive medium, no effect of chain length on the reactivity of the radicals, etc.

The most common way to determine the reactivity ratios of a comonomer couple is to express r_2 as a linear function of r_1 by linearizing equation (2.21):

$$r_2 = \frac{([M_1]/[M_2])^2}{d[M_1]/d[M_2]} r_1 - \left(\frac{[M_1]}{[M_2]} - \frac{[M_1]/[M_2]}{d[M_1]/d[M_2]} \right) \tag{2.22}$$

So, analyzing the composition of some copolymer brushes for given solution concentrations gives straight lines whose intersection is the couple (r_1,r_2) of these comonomers for these particular conditions. Indeed, the reactivity ratios vary according to experimental parameters such as the temperature, the solvent, the pH,... Not only these ratios serve to

predict the composition of a copolymer for given concentrations in solution but depending on their relative values, they give an insight into the copolymer structure:

- If $r_1 = r_2 = 1$, the copolymer is statistical. The final composition of the copolymer is the same as the composition of the solution.
- If $r_1, r_2 << 1$, the copolymer is alternating. The monomer 1 preferentially reacts with monomer 2 and inversely.
- If $r_1, r_2 > 1$, the copolymer is blocky. Each monomer tends to react with itself but they still can react with the other one leading to block copolymers.
- If $r_1, r_2 >> 1$, we have a mixture of two homopolymers. The monomers only react with their own kind.
- If $r_1 > 1 > r_2$, we have a drift in the composition of the copolymers. At first, the copolymer is rich in monomer 1 and when it is completely consumed, more monomers 2 are added leading to a variation in the composition along the chain.

Going further into the analysis of these equations allows us to calculate the average length of each block in the final copolymer. Indeed, considering that the composition of the feed solution does not change with the conversion in SI-ATRP, we can calculate the probability for a monomer 1 to react with itself (W_{11}) [92]:

$$W_{11} = \frac{r_1 f_1}{f_1(r_1 - 1) + 1} \tag{2.23}$$

with $f_1 = [M_1]/([M_1] + [M_2])$. Then, the average number of monomers 1 per block, $\langle N_1 \rangle$ is given by:

$$\langle N_1 \rangle = \frac{1}{1 - W_{11}} \tag{2.24}$$

2.3 Results and Discussion

2.3.1 Thiol Monolayers on Gold

Generally, to characterize a monolayer on a solid substrate, one of the best tools that can be used is X-Ray Reflectometry (XRR). Indeed, this gives precious information on the thickness and the density of the layer. However, here a thin monolayer of thiol (ca. 1 nm) on top of a thicker and denser gold layer (ca. 20 nm) evaporated on a silicon substrate with a thin layer of chromium (ca. 2 nm) as the adhesive layer has to be characterized. In this case, the system is quite complex. Nevertheless, as previously said, thiol-SAMs can suffer from a lack of stability. Therefore, the stability and the activity of these SAMs were investigated by the following strategy: a polymer brush was grafted from this monolayer to account for its activity and the kinetics of place-exchange reactions between an inert thiol and the initiator was studied to account for its stability. For this part of the work, mono-2-(methacryloyloxy)ethyl succinate (MES) was used as the monomer. More information about the materials and methods involved in this section are given on pages 191 and 197.

First, the kinetics of poly(MES) brush growth from gold surfaces previously covered with the thiol-initiator (2) was studied. The thicknesses of brushes grown in different experimental conditions (Table 2.1) are displayed in Figure 2.9 as a function of time. The polymerization is not well controlled for the initial concentrations (MES/bipy/CuCl/$CuCl_2$ = 95/5/1.6/0.08 mmol, □ in Figure 2.9): after a few minutes, the brush

is already 100 nm-thick and its thickness does not increase much after 2 hours of reaction (around 130 nm). This can be due to a very high amount of free radicals on the substrate arising either from the high reactivity of the monomer, from a too large amount of catalyst CuCl or from a too small amount of deactivator $CuCl_2$ [62, 63]. Indeed, if there are too many free radicals at the end of the growing chains, they can terminate by pairing. So, first the amount of catalyst was decreased by 50% (■). Unexpectedly the thickness of this brush is even higher and the growth is also not controlled. This could be explained by the combined action of a decrease of the termination reactions and a high reactivity of the monomer: in this case, the growth is very fast and terminates quickly (but slower than with the previous conditions, which gives higher thicknesses). This is confirmed by the next experiment where the amount of catalyst has been increased by 100% in comparison with the initial concentration (▲). In that case, the thicknesses are highly reduced as expected. Another way to improve the control is to increase the amount of deactivator (▶). In that case, a decrease of the thickness is observed as expected but the control is not really improved. The last experiment of this series is the synthesis of a brush without any pH adjustment (▼). In that last case, hardly any growth is observed as in [93].

	EtOH (ml)	H_2O (ml)	MES (mmol)	bipy (mmol)	CuCl (mmol)	$CuCl_2$ (mmol)	pH (-)
□	15	30	95	5	1.6	0.08	9
■	15	30	95	5	0.8	0.08	9
▲	15	30	95	5	3.2	0.08	9
▶	15	30	95	5	1.6	0.32	9
▼	15	30	95	5	1.6	0.08	<5

Table 2.1: Conditions used in Figure 2.9.

From these experiments it can be concluded that it is possible to select the thickness of the brush *a priori* by adjusting the quantities of catalyst and deactivator; however, it is useless to play with the polymerization time as the growth is not well controlled. It could be possible

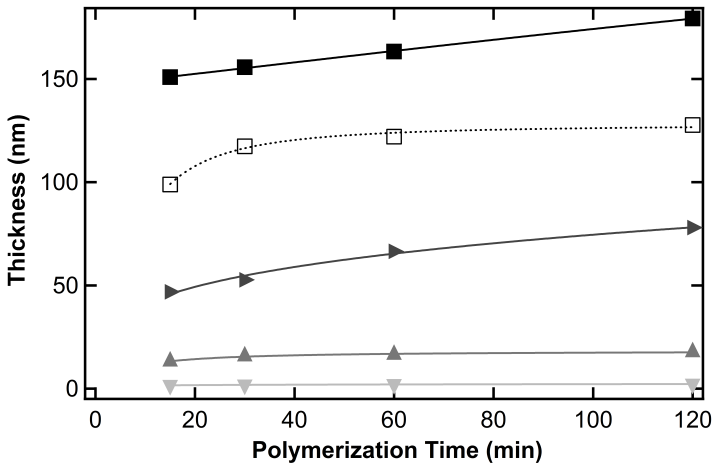

Figure 2.9: Kinetics of poly(MES) brush growth for the different polymerization conditions listed in Table 2.1. The lines are drawn to guide the eye.

to somehow improve the control by finely tuning the relative amounts of each chemicals but it would cost a lot of time and this is not necessary in the framework of this study as the purpose is to assess the validity of the thiol-initiator SAM.

Having this in mind, it was possible to start the study of the stability of the thiol monolayers. The kinetics of desorption or exchange are supposed to be relatively slow [47–50] and the rate of these reactions can be further decreased by increasing the packing density of the first thiol monolayer, i.e. by increasing the chain length, or by introducing groups capable of forming lateral interactions. However, this phenomenon was investigated into more details in order to be sure that it will not be limiting for the following experiments.

As a first test, monolayers of undecanethiol (UDT) were grown overnight in ethanol on gold wafers. After rinsing with ethanol and water,

they were dried under a flow of N_2. Then they were placed in a solution containing the initiator for respectively 2, 5, 30 and 120 minutes along with bare gold substrates used as references. They were subsequently rinsed with ethanol and water and then dried under a flow of N_2. As small amounts of molecules are supposed to have been exchanged in such short periods of time, poly(MES) brushes were grown from these surfaces for 1 hour to increase the signal. Then, the thicknesses were measured by ellipsometry (see section 6.3.2 on page 215 for more information on this technique). Figure 2.10 shows that even after only 2 minutes of place-exchange reaction, the resulting brush is already approximately 40 nm thick (▶). This thickness should be compared to that of a brush grown from an initiator-SAM for 2 minutes, i.e. 110 nm (□). Making the assumption that the thickness of the brush is directly correlated with the initiator coverage as suggested by Huck et al. [94], this would mean that around a third of the inert thiol molecules previously deposited on the substrate were exchanged in only 2 minutes. After 5 minutes of place-exchange reaction, this ratio becomes 55%, then 90% for 30 minutes to finally reach 100% after 2 hours. This was totally unexpected. To increase the stability of the inert thiol layer, a longer thiol (hexadecanethiol, HDT) with a low (< 1 mM, ▲) and a higher concentration (10 mM, ■) and a more hydrophilic thiol (mercaptoundecanol, UDTOH, ▼) were tested. In every case, no major improvement was made and the lowest thickness obtained for 2 minutes exchange was around 30 nm.

To go further into the understanding of this phenomenon, the place-exchange reaction was performed at -78°C in a mixture of acetone and dry ice. As can be seen in Figure 2.11, the resulting thicknesses of the brushes are quite high with a 27 nm-thick brush for a 2 minutes exchange. At this point, we had to conclude that the replacement of inert thiols by the thiol initiator (2) is very fast.

When doing the reverse exchange where the initiator is the first

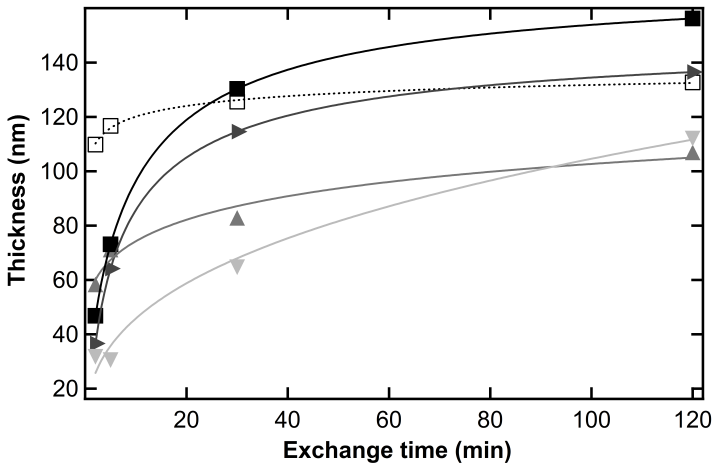

Figure 2.10: Kinetics of place-exchange reactions between different inert thiols and the initiator - □ : Reference experiment (initiator only); ■ : 10 mM HDT; ▶ : UDT; ▲ : HDT; ▼ : UDTOH.

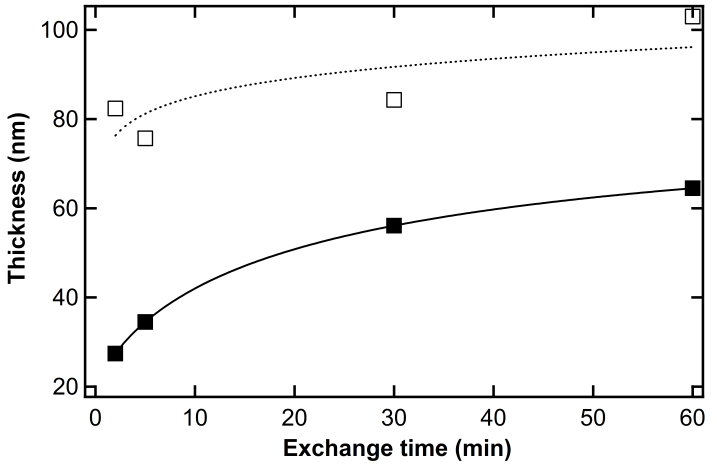

Figure 2.11: Kinetics of the place-exchange reaction at -78°C - □ : Reference experiment (initiator only); ■ : HDT.

species grafted on the gold substrate, no drastic change in the thick-

nesses of the subsequent brushes is monitored (results not shown). This would mean that either the initiator is very stable or that there is not a direct correlation between the polymer brush thicknesses and the actual proportion of each thiol on the surface. This seems to contrast with the previously mentioned paper by Huck et al. [94] which showed that although only 1 out of 10 initiators bound to the surface is expected to initiate a polymer brush, there is a linear relationship between the initiator density and the growth rate of the polymer brush formed. This would mean that the probability for a thiol to initiate the polymerization does not change with its amount on the surface. But if the thiol molecules are exchanged in patches rather than randomly, it would mean that the final surface is composed of two phases: one with unreacted inert thiols (low thickness) and one containing densely packed chains (high thickness) leading to an average decrease of the thickness. This hypothesis is supported by the facts that on the one hand, the morphology of evaporated gold layers is made of spherical grains of about 25 nm diameter [95] and that on the other hand, the exchange reaction is highly favored at defect sites [51–53].

Another plausible explanation could come from the lack of control on the polymerization kinetics. For example, the growth could proceed not only from thiol initiators, but that hydrogen abstraction, radical transfers, etc. would lead to further initiation from the alkane layer and/or to the formation of heavily branched chains. This would extend the influence of a single exchanged thiol initiator molecule well beyond its location, which would explain why a very small amount of exchanged thiol molecules could already lead to a relatively high film thickness.

Anyway, these results show that working with thiol-initiators should be avoided in the following of this study due to their quick exchange against neutral thiols.

2.3.2 Silane Monolayers on Silicon

Since it has been demonstrated in the previous section that thiol monolayers are not suitable to be used as initiator-SAMs for our brushes, silane-based-initiator-SAMs were used (more information to be found in the Experimental Part on section 6.1.1, page 191 and section 6.2.1, page 197 about the materials and methods involved). Before studying the growth of polymer brushes, these silane-SAMs were studied in more details.

The quality of the silane monolayer was evaluated by XRR. As mentioned in the Experimental Part (section 6.3.1 on page 211), a first approximation of the thickness d of the silane layer can be made from the value of $k_{z,min}$ in the reflectogram (Figure 2.12) according to $d = \pi/2k_{z,min}$. In the present case, a thickness, d, of 10.5 Å is measured. This value is reasonable though a bit too large for a densely packed layer of this silane.

A further analysis can be made by computing the autocorrelation function of the electron density gradient (i.e. the Patterson function). The maximum of the last peak of this function gives an accurate, parameter-free estimation of the thickness which is close to our first approximation (data not shown). Finally, the reflectivity curve was fitted to obtain the vertical profile of electron density of the surface of our sample as shown by the continuous black line on Figure 2.13. By subtraction of the profile of a bare silicon wafer (dotted black line), the electron density profile of the silane monolayer (gray continuous line) was obtained. Integrating the area under this curve provides the number of electrons of the layer per unit surface area ζ_g which is 311 electron/nm^2. Since one molecule of silane contains 119 electrons (not taking into account the reactive Cl atoms as they are removed during the grafting), the grafting density of the silane molecules σ_g is 2.6 molecule/nm^2. This grafting density is

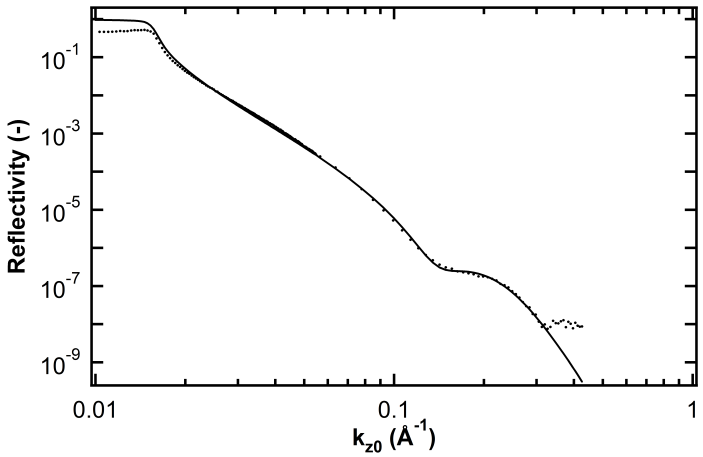

Figure 2.12: XRR spectrum of a silane-initiator SAM on silicon (dots: data; line: fit). The local minimum of this curve, $k_{z,min}$ gives a first approximation of the layer thickness (ca. 10.5 Å).

about 50% lower than the values found for very densely packed alkane chains; for instance, crystalline alkanes have a packing density of about 5-5.5 chain/nm^2 measured in planes perpendicular to the chain axes, depending on their sub-cell [96]. This relatively low grafting density results from the bulky end of the silane which prevents a close packing of the chains and from the amorphous nature of the native layer of silicon oxide on silicon wafers. However, in our case, the packing density is sufficient to allow a dense packing of polymer chains.

The chemical characterization of the silane layer was provided by X-ray Photoelectron Spectroscopy (XPS) (cf. section 6.3.3 on page 219). Figures 2.14 and 2.15 show the survey scan and the high-resolution elemental C_{1s} scan of a silane-initiator monolayer on silicon. The Si_{2s} and Si_{2p} peaks come from the substrate, whereas the C_{1s} and the Br_{3d} peaks come from the silane layer. Analyzing a monolayer presents two major difficulties: first, the substrate (composed of silicon and oxygen in

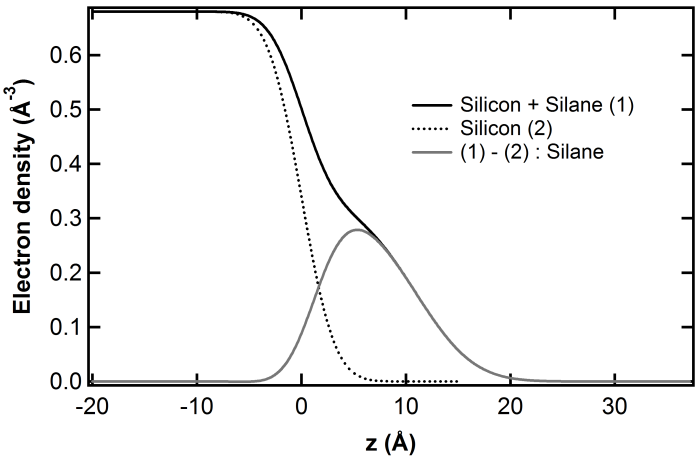

Figure 2.13: Electron density profiles obtained from the fits of the XRR data. The Si/monolayer interface is located at 0 Å. The electron density profile of the silane layer (gray line) is computed by subtraction of the Si profile (dotted black line) from the Si+monolayer profile (continuous black line).

unknown proportions) prevents from extracting quantitative ratios between the C_{1s} and O_{1s} peaks; second, the relative proportion between the actual silane layer and the unavoidable organic contaminants prevents from comparing the different contributions to the carbon spectrum in a quantitative fashion. As an example, for the three components of the carbon peak at 284.8, 286.4 and 289 eV corresponding to C–(C,H), C–O and O=C–O, a ratio of around 5:1:1 was expected (assuming that the carbon linked to the terminal bromine atom is included in the C–C component since the electronegativity of bromine is not far from the one of carbon). However, the measured ratio is close to 10:3:1. This proves the presence of a quite large contamination coming from hydrocarbonaceous adsorbed molecules. The ratio between C_{1s} and Br_{3d} cannot be accounted for since it is well known that the bromine atoms are expelled from the surface through x-ray radiation. But the fact that bromine is visible in the spectrum (even in small proportions), proves that the silane

was successfully grafted on the surface.

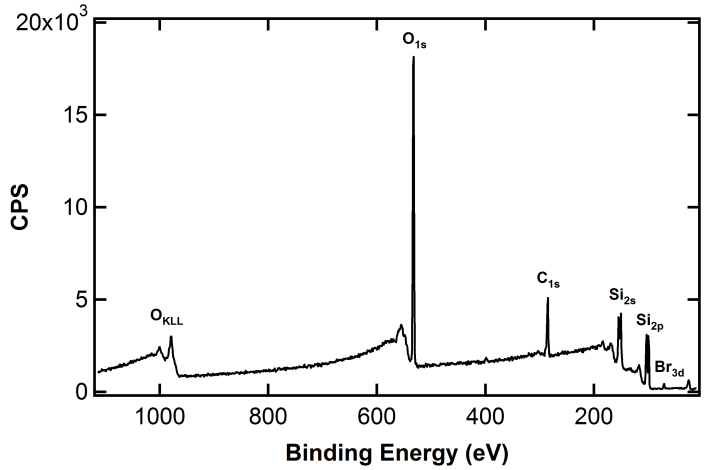

Figure 2.14: XPS survey scan of the silane-initiator SAM on silicon.

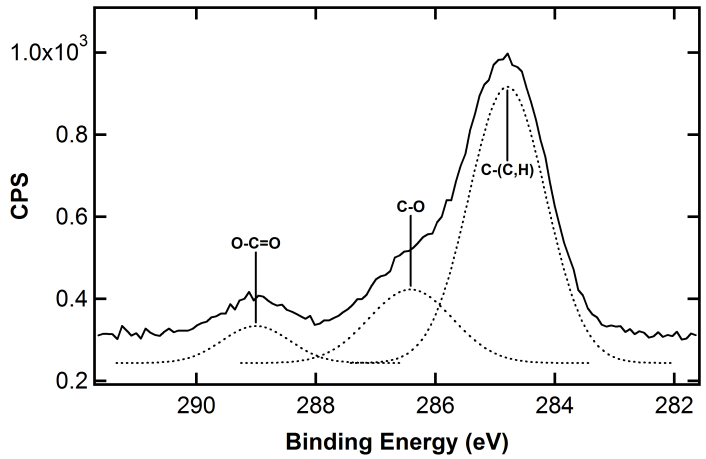

Figure 2.15: XPS high resolution C_{1s} scan of the silane-initiator SAM on silicon. The spectrum is composed of three peaks: the C–(C,H) peak at 284.8 eV, the C–O peak at 286.4 eV and the O=C–O peak at 289 eV. These peaks are fitted with Gaussian curves as guides for the eye.

Finally, the silane-initiator SAM activity regarding the polymer brush

growth was tested. Figure 2.16 compares the growth of poly(MES) brush growth on a silane-initiator-covered silicon surface (■) and on a thiol-initiator-covered gold surface (▶). These two curves look very similar. The thickness of the brush grown on gold seems to saturate sooner than the one grown on silicon but in both cases the growth is not well controlled as discussed in the previous section. It is also noteworthy that this gives the final proof that a monolayer of the ATRP initiator was grafted on silicon.

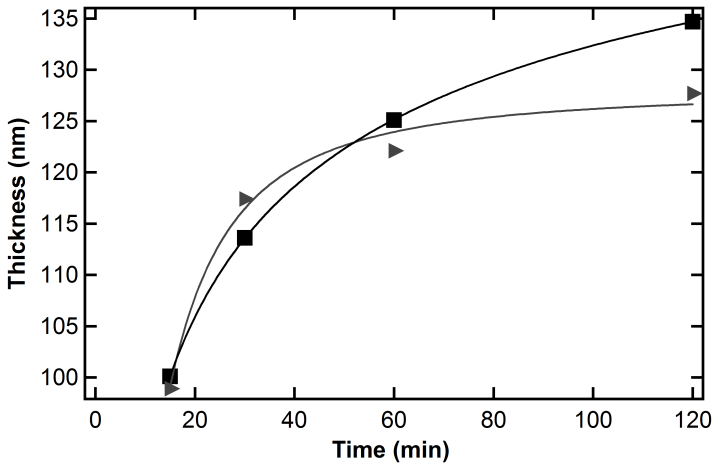

Figure 2.16: Kinetics of poly(MES) brush growth on silicon (■) and gold (▶) for standard conditions. The lines are drawn to guide the eye.

2.3.3 Polymer Brush Growth

A lot of parameters can have an influence on the growth kinetics of polymer brushes. Some parameters can modify the polymerization rate such as the monomer concentration, the water content and the temperature, while others have an impact on the control of the growth such as the catalytic complex or deactivator concentrations. Of course, these two kinds of parameters are linked because when the control of the reaction

is enhanced, the growth kinetics is often slowed down.

Our goal here was to determine the appropriate set of parameters in order to obtain brushes which could grow rapidly and in a controlled fashion. Then, by copolymerization with a reactive comonomer, the synthesis of copolymer brushes whose composition and structure can be determined *a priori* was considered. These brushes were intended to be further post-functionalized in a reproducible way to develop sensing or catalytic layers for our AFM probes. Section 6.1.2 on page 192 presents the monomers used in this thesis as well as the materials involved in their polymerization and section 6.2.2 on page 198 describes the protocol used for the synthesis of polymer brushes.

First, the polymerization kinetics of di(ethylene glycol)methyl ether methacrylate (MEO_2MA) brushes was studied. The amount of monomer or of the deactivator $CuCl_2$, the nature of the solvent and the pH (since it could be anticipated that the pH has to be raised to 9 in order to polymerize acidic monomers [93]) were varied (Table 2.2).

	MeOH (ml)	H_2O (ml)	MEO_2MA (mmol)	bipy (mmol)	CuCl (mmol)	$CuCl_2$ (mmol)	pH (-)
□	30	15	95	5	1.6	0.08	~ 6
■	15	30	95	5	1.6	0.08	9
▲	15	30	95	5	1.6	0.64	9
▼	15	30	142.5	5	1.6	0.64	9
▶	15	30	142.5	5	1.6	0.32	9

Table 2.2: Conditions used in Figure 2.17.

The open squares (□) in Figure 2.17 show the kinetics curve for concentrations of $MEO_2MA/bipy/CuCl/CuCl_2$ = 95/5/1.6/0.08 mmol. This first result shows that a poly(MEO_2MA) brush can be grown in a quite well controlled fashion since the growth is linear in a bilogarithmic graph. However, after approximately 24 hours of polymerization, the thickness is only around 40 nm which is not enough for our objectives.

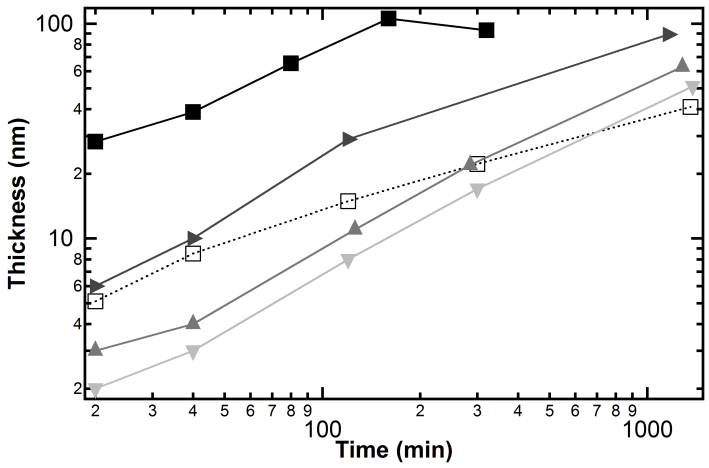

Figure 2.17: Kinetics of poly(MEO_2MA) brush growth on silicon for the different conditions listed in Table 2.2. The lines are drawn to guide the eye.

Since water increases the rate of ATRP, the proportion between water and methanol was modified from 1:2 to 2:1 holding the total volume of solvent constant and raising the pH to 9 for the reason evoked earlier. The resulting curve (■) shows that the brush grows quickly in the early stages of the polymerization, reaching around 30 nm in 2 minutes. Then, the polymerization slows down but the thickness continues to increase in a linear way. However, the control is decreased with these conditions and some heterogeneities appear on the wafer after a few hours of reaction. So, to minimize the initial thickness and to enhance the control on the reaction, the concentration of $CuCl_2$ was increased up to 800% (▲). In this case, the initial thickness is lowered to only 3 nm, the polymerization is well controlled and the final thickness is close to 60 nm. In order to further increase the final thickness of the brush, the monomer concentration was increased by 50% (▼). This does not lead to modifications compared to the previous curve. To get an intermediate behaviour between good control and good final thickness, the $CuCl_2$ concentration

was decreased down to 400% (▶). These conditions lead to a low initial thickness (around 6 nm) and a high final thickness of around 90 nm for 20 hours of polymerization. So depending on the use of these brushes, different sets of conditions providing brushes with nicely controlled thicknesses are available.

This first kind of polymer brushes is interesting because they are thermo-responsive. This means that the polymer undergoes a conformation change in water at a given temperature of ca. 27°C. For temperatures below this transition temperature, the brush is swollen because enthalpy is the dominant term in the Gibbs free energy of the system: the chains repel each other due to steric forces, water molecules form hydrogen bonds with the polymer chains and the brush is hydrated. For higher temperatures, the entropy is dominant and the chains tend to adopt their statistical coil conformation leading to a collapsed state. Much more details about the transition mechanisms are given in [69]. Now, it would also be interesting to introduce reactive groups inside the polymer brush while keeping its responsive behavior. Therefore, reactive monomers were introduced inside the brushes, i.e. methacrylic acid (MAA). Besides the reactivity, poly(MAA) brushes are hydrophilic and responsive to a change of pH [97] or ionic force [98].

	MeOH (ml)	H_2O (ml)	MAA (mmol)	bipy (mmol)	CuCl (mmol)	$CuCl_2$ (mmol)	pH (-)	NaCl (g)
□	15	30	95	5	1.6	0.08	9	0
▼	15	30	95	5	1.6	0.16	9	2.8
■	15	30	190	5	1.6	0.08	9	0
▶	15	30	190	5	1.6	0.64	9	0
▲	15	30	142.5	5	1.6	0.64	9	0

Table 2.3: Conditions used in Figure 2.18.

As for poly(MEO_2MA) brushes, the growth kinetics of poly(MAA) brushes was studied for the different conditions listed in Table 2.3. First, the conditions yielding the highest thicknesses of poly(MEO_2MA) bru-

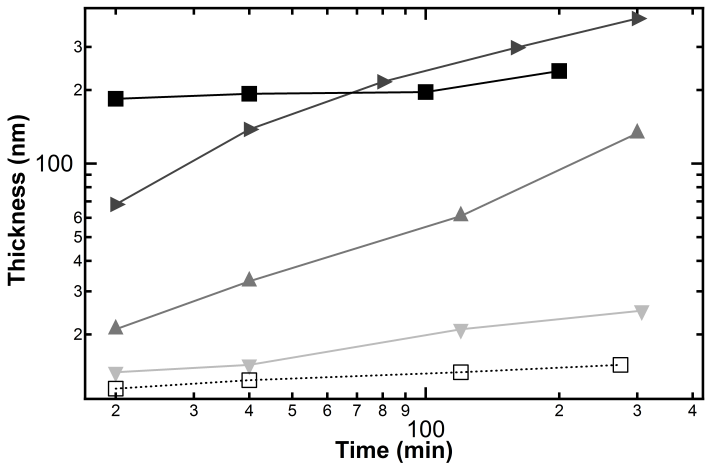

Figure 2.18: Kinetics of poly(MAA) brush growth on silicon for the different conditions listed in Table 2.3. The lines are drawn to guide the eye.

shes were used (■ in Figure 2.17). These conditions are not suitable for this monomer because the kinetics is very slow as can be seen in Figure 2.18 (□). In order to increase the kinetics, NaCl was added in the solution. Indeed, NaCl has two advantages. First, it can have a shielding effect on the charges borne by the monomers [98]. Second, NaCl can prevent complexation reactions of methacrylic acid with Cu^{I} and Cu^{II}, yielding a better control of the polymerization [99]. The $CuCl_2$ concentration was also doubled to counterbalance these foreseen effects of NaCl. The kinetics is increased but only to a small extent (▼). The MAA concentration was thus also doubled since the monomer concentration plays a major role in the polymerization kinetics for acidic monomers [98]. In this case (■), the kinetics is highly increased but the control is completely lost: a 200 nm-thick brush is obtained in 2 minutes. The $CuCl_2$ concentration was thus increased up to 800% (▶). This increased the control but this was insufficient as the brush was around 70 nm thick in 2 minutes which is still too high. Finally, maintaining this high $CuCl_2$

concentration but lowering the MAA concentration to an intermediate value of 150% (▲) gave brushes with a low initial thickness of 20 nm and a high thickness of more than 100 nm for 5 hours of polymerization with a very nice control.

It can be concluded from this exploratory work that the two studied systems obey to rather different rules. Indeed, the conditions issuing the highest thickness for poly(MEO_2MA) gave very thin poly(MAA) brushes. In order to increase the thickness of poly(MAA) brushes, the monomer concentration can be increased whereas this has no major influence on the kinetics of poly(MEO_2MA) brushes. For this latter, the amount of water in the solution seems to be of importance.

Based on these conclusions, growing copolymer brushes according to different conditions should give thick brushes with various amounts of each monomer. However, it was more interesting to find a common set of parameters with the relative proportions of each monomer being the only variable. This was not straightforward because a solvent compatible with each monomer and parameters that allow a controlled and fast polymerization for every composition had to be found. This set of parameters is: monomers/bipy/CuCl/$CuCl_2$ = 190/5/1.6/0.08 mmol in H_2O/EtOH = 15/10 ml.

Copolymer brushes were grown with different proportions of monomers and their composition was investigated by Fourier Transform InfraRed spectroscopy (FTIR) (cf. section 6.3.4 on page 224). In a first step, the FTIR spectra of the two homopolymer brushes were studied. Poly(MEO_2MA) brushes exhibit a strong isolated peak at 1728 cm^{-1}. This peak corresponds to the asymmetrical stretching of the C=O groups ($\delta_{as}^{PMEO2MA}$) (Figure 2.19). Two smaller peaks are also visible and correspond to the asymmetrical bending of the CH_3 groups and to the symmetrical stretching of the CH_2 groups. The infrared spectrum of

the poly(MAA) brushes depends on their protonation state [100, 101]. At low pH, the acid units of poly(MAA) brushes are protonated and form dimers involving intra- or intermolecular H-bonds. The asymmetrical stretching of the C=O groups associated with this configuration is located at 1704 cm^{-1} and cannot be used to determine easily the copolymer composition because it overlaps with the $\delta_{as}^{\mathrm{PMEO2MA}}$ peak. At high pH, the acid groups of poly(MAA) brushes are deprotonated, and the asymmetric stretching of the C=O shifts to ca. 1500 cm^{-1} and splits into five peaks [101] (Figure 2.20). Here, the strong peak at 1554 cm^{-1} of deprotonated brushes ($\delta_{as}^{\mathrm{PMAA}}$) was selected to be the main characteristic peak of poly(MAA). A typical infrared spectrum of a deprotonated poly(MEO_2MA_{42}-*co*-MAA_{58}) is shown in Figure 2.21. The two major components coming from each comonomer, $\delta_{as}^{\mathrm{PMEO2MA}}$ and $\delta_{as}^{\mathrm{PMAA}}$ can be clearly observed.

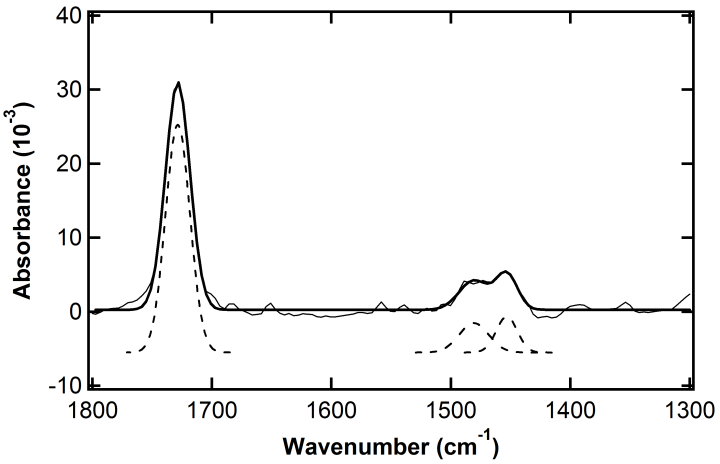

Figure 2.19: FTIR spectrum of a 90 nm-thick poly(MEO_2MA) brush on glass after 30 minutes immersion in a neutralization bath at pH=10. The dashed lines represent the decomposition of the signal in Voigt components.

The areas of those characteristic peaks had then to be linked to the

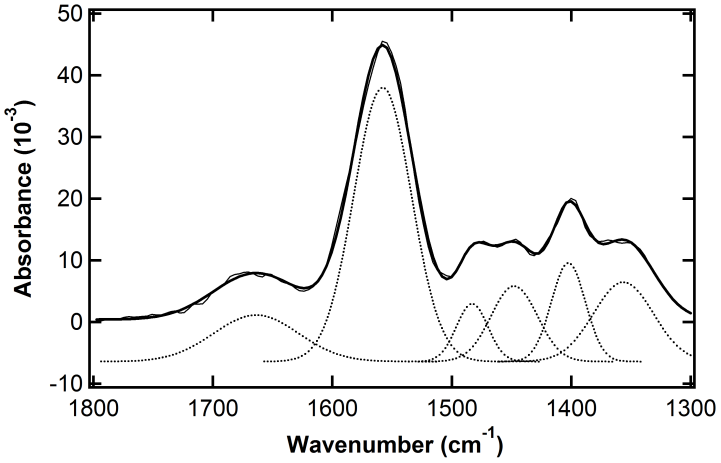

Figure 2.20: FTIR spectrum of a 200 nm-thick poly(MAA) brush on glass after 30 minutes immersion in a neutralization bath at pH=10. The dotted lines represent the decomposition of the signal in Voigt components.

actual relative amounts of each comonomer inside the brush. The absorbance of these peaks was thus calibrated. This was done taking into account the Lambert-Beer equation that linearly links the absorbance (A) to the thickness of the dry brush (h^{dry}):

$$A = \epsilon \cdot c \cdot h^{dry} \doteq a \cdot h^{dry} \tag{2.25}$$

with ϵ being the extinction coefficient of the brush and c, the molar concentration in monomer units. So for a given peak, the parameter a is constant and will be used as the calibration parameter. This parameter was estimated by measuring the absorbance of the two characteristic peaks for various thicknesses of homopolymer brushes. This gave a_{PMEO2MA} (1728 cm^{-1}) = 0.008 ± 0.001 nm^{-1} and a_{PMAA} (1554 cm^{-1}) = 0.03±0.007 nm^{-1}. Knowing this parameter allows to calculate a virtual

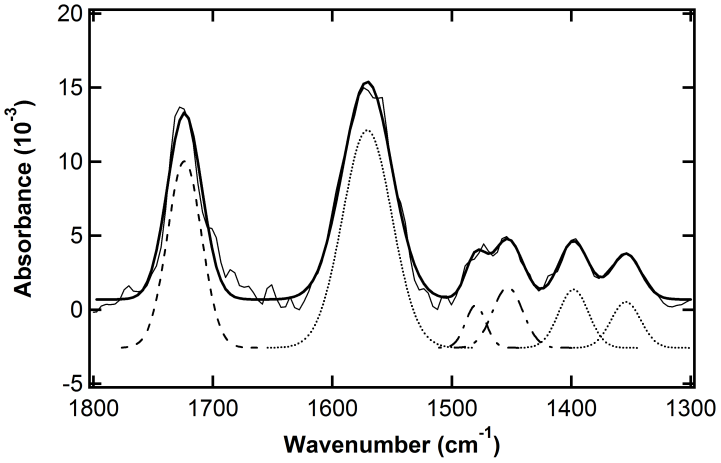

Figure 2.21: FTIR spectrum of a 66 nm-thick poly(MEO_2MA_{42}-*co*-MAA_{58}) brush after 15 minutes in a neutralization bath at pH=9 and decomposition of the signal in Voigt components (dashed lines refer to MEO_2MA units, dotted lines to MAA units and dash dotted lines come from both MEO_2MA and MAA units.

thickness of each of the two homopolymer brushes forming the copolymer brush:

$$h^{dry}_{\mathrm{PMEO2MA}} = \frac{A_{1728}}{a_{\mathrm{PMEO2MA}}} \quad \text{and} \quad h^{dry}_{\mathrm{PMAA}} = \frac{A_{1554}}{a_{\mathrm{PMAA}}} \tag{2.26}$$

These virtual dry thicknesses had then to be linked with the molar ratio of the two constituents. This can be done by taking into account the molar volume of each comonomer ($\bar{V}_i$):

$$\frac{n_{\mathrm{MAA}}}{n_{\mathrm{MEO2MA}}} = \frac{h^{dry}_{\mathrm{PMAA}}}{h^{dry}_{\mathrm{PMEO2MA}}} \cdot \frac{\bar{V}_{\mathrm{MEO2MA}}}{\bar{V}_{\mathrm{MAA}}} \tag{2.27}$$

$$\simeq \frac{h^{dry}_{\mathrm{PMAA}}}{h^{dry}_{\mathrm{MEO2MA}}} \cdot \frac{\bar{M}_{\mathrm{MAA}}}{\bar{M}_{\mathrm{MEO2MA}}} \cdot \frac{\rho_{\mathrm{MEO2MA}}}{\rho_{\mathrm{MAA}}} \tag{2.28}$$

with $\bar{M}_i$ and ρ_i the molar mass and the density of component i respectively. Then, the molar fraction of MEO_2MA in the brush (f_{MEO2MA}) writes:

$$f_{\mathrm{MEO2MA}} = \frac{n_{\mathrm{MEO2MA}}}{n_{\mathrm{MEO2MA}} + n_{\mathrm{MAA}}} = \left(1 + \frac{n_{\mathrm{MAA}}}{n_{\mathrm{MEO2MA}}}\right)^{-1} \tag{2.29}$$

Figure 2.22 shows the evolution of f_{MEO2MA} as a function of the composition of the feed solution. The copolymer has a tendency to contain more MEO_2MA units than the feed solution meaning that, for these conditions, MEO_2MA polymerizes preferentially compared to MAA. The reactivity ratios were extracted from the linearized Mayo-Lewis equation (2.22) applied to these data, providing $r_{\mathrm{MEO2MA}} = 3.7$ and $r_{\mathrm{MAA}} = 1$. This is fairly close to the values obtained for free radical copolymerization in solution where $r_{\mathrm{MEO2MA}} = 3.6$ and $r_{\mathrm{MAA}} = 2$ [102]. The black line on Figure 2.22 is the Mayo-Lewis equation (2.21) in which the values of the calculated reactivity ratios were injected. It nicely fits the data points.

From these reactivity ratios, the average block length inside the copolymer was calculated as a function of the composition of the feed solution according to equation (2.24) (Figure 2.23). For a 50/50 ratio of the two monomers in the solution, the average length of MAA segments

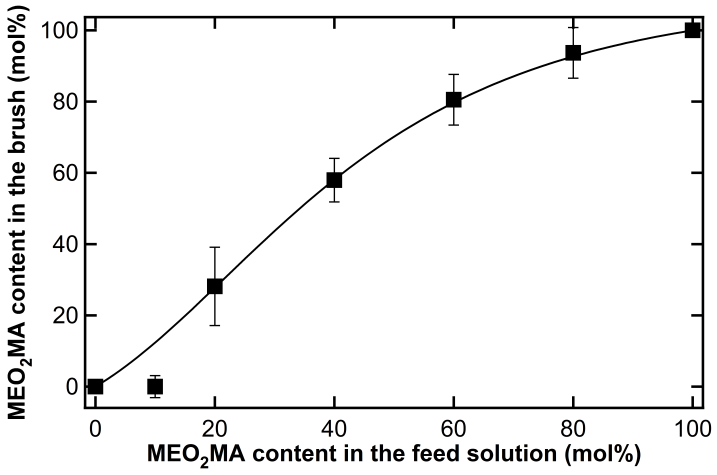

Figure 2.22: Evolution of the molar fraction of MEO_2MA in the copolymer brush as a function of the composition of the feed solution. The black line corresponds to the Mayo-Lewis equation (2.21) with r_{MEO2MA} = 3.7 and r_{MAA} = 1.

is 2 while it is close to 5 for MEO_2MA.

2.4 Conclusion

In this chapter, the growth kinetics of polymer brushes grafted from solid substrates by ATRP was studied. In a first part, it was shown that ATRP-initiator silane SAMs on silicon were better suited than their thiols counterparts on gold because these latter exchange rapidly. This was demonstrated by proceeding to place-exchange reactions of inert thiols with initiator thiols and grafting poly(MES) brushes from the resulting surfaces. The growth was significant even after a few minutes of exchange. So, the strategy consisting of having an inert thiol on one side and an initiator-thiol on the other side of a gold-coated cantilever to avoid thermal drifts during the experiments, could not be used. The

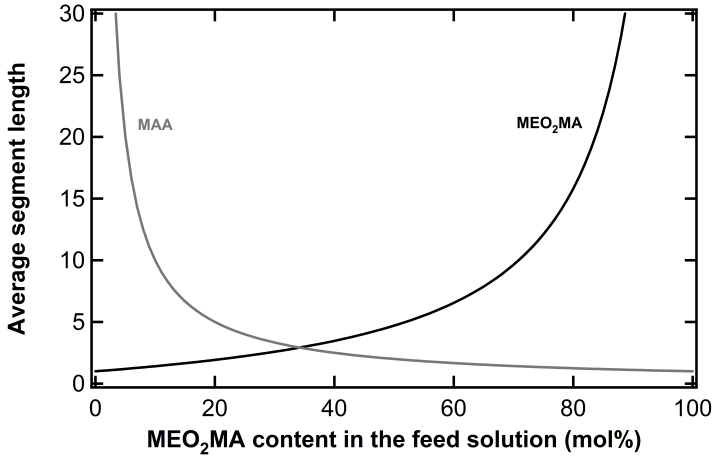

Figure 2.23: Evolution of the average block length in the copolymer brush as a function of the composition of the feed solution. The black line corresponds to the MEO_2MA and the gray line to MAA.

precise control of the temperature was used instead whenever this effect was limiting.

Then, the growth kinetics of two homopolymer brushes, i.e. the poly(MEO_2MA) brush and the poly(MAA) brush, was investigated for different experimental conditions. Different sets of parameters were found in order to produce thick polymer brushes with a nicely controlled kinetics. Finally, the behavior of these two monomers upon mixing into the same polymerization solution was studied. The resulting copolymer brushes contained more MEO_2MA units than the feed solution. This is to be related with the larger reactivity ratio of MEO_2MA as compared to MAA as was already found in the literature for radical polymerization of these two comonomers in solution.

References

[1] Raiteri, R.; Grattarola, M.; Berger, R. *Materials Today* **2002**, *5*, 22–29.

[2] Lang, H.; Hegner, M.; Gerber, C. Nanomechanical Cantilever Array Sensors. In *Springer Handbook of Nanotechnology*; Bhushan, B., Ed.; Springer Berlin Heidelberg, 2007; pp 443–460.

[3] Baller, M. K.; Lang, H. P.; Fritz, J.; Gerber, C.; Gimzewski, J. K.; Drechsler, U.; Rothuizen, H.; Despont, M.; Vettiger, P.; Battiston, F. M.; Ramseyer, J. P.; Fornaro, P.; Meyer, E.; Guntherodt, H. J. *Ultramicroscopy* **2000**, *82*, 1–9.

[4] Paxton, W. F.; Spruell, J. M.; Stoddart, J. F. *J. Am. Chem. Soc.* **2009**, *131*, 6692–6694.

[5] Cherian, S.; Mehta, A.; Thundat, T. *Langmuir* **2002**, *18*, 6935–6939.

[6] Chou, Y.-I.; Chiang, H.-C.; Wang, C.-C. *Sens. Actuators, B* **2008**, *129*, 72–78.

[7] Lang, H. P.; Berger, R.; Battiston, F.; Ramseyer, J. P.; Meyer, E.; Andreoli, C.; Brugger, J.; Vettiger, P.; Despont, M.; Mezzacasa, T.; Scandella, L.; GÃijntherodt, H. J.; Gerber, C.; Gimzewski, J. K. *Appl. Phys. A: Mater. Sci. Process.* **1998**, *66*, S61–S64.

[8] Zhou, F.; Shu, W.; Welland, M. E.; Huck, W. T. S. *J. Am. Chem. Soc.* **2006**, *128*, 5326–5327.

[9] Kohale, S.; Molina, S. M.; Weeks, B. L.; Khare, R.; Hope-Weeks, L. J. *Langmuir* **2007**, *23*, 1258–1263.

[10] Itoh, T.; Suga, T. *Appl. Phys. Lett.* **1994**, *64*, 37–39.

[11] Shin, S.; Kim, J. P.; Sim, S. J.; Lee, J. *Appl. Phys. Lett.* **2008**, *93*, 102902–3.

[12] Lee, J. H.; Kim, T. S.; Yoon, K. H. *Appl. Phys. Lett.* **2004**, *84*, 3187–3189.

[13] Raiteri, R.; Grattarola, M.; Butt, H.-J.; Skladal, P. *Sens. Actuators, B* **2001**, *79*, 115–126.

[14] Moulin, A. M.; O'Shea, S. J.; Welland, M. E. *Ultramicroscopy* **2000**, *82*, 23–31.

[15] Abu-Lail, N. I.; Kaholek, M.; LaMattina, B.; Clark, R. L.; Zauscher, S. *Sens. Actuators, B* **2006**, *114*, 371–378.

[16] Zhou, F.; Biesheuvel, P. M.; Choi, E. Y.; Shu, W.; Poetes, R.; Steiner, U.; Huck, W. T. *Nano Lett.* **2008**, *8*, 725–730.

[17] Bumbu, G.-G.; Wolkenhauer, M.; Kircher, G.; Gutmann, J. S.; Berger, R. *Langmuir* **2007**, *23*, 2203–2207.

[18] Lenz, S.; RuĬĹhm, A.; Major, J.; Berger, R.; Gutmann, J. S. *Macromolecules* **2011**, *44*, 360–367.

[19] Vidic, A.; Then, D.; Ziegler, C. *Ultramicroscopy* **2003**, *97*, 407–416.

[20] Betts, T. A.; Tipple, C. A.; Sepaniak, M. J.; Datskos, P. G. *Anal. Chim. Acta* **2000**, *422*, 89–99.

[21] Yan, X.; Ji, H.-F.; Lvov, Y. *Chem. Phys. Lett.* **2004**, *396*, 34–37.

[22] Berger, R.; Gerber, C.; Lang, H. P.; Gimzewski, J. K. *Microelectron. Eng.* **1997**, *35*, 373–379.

[23] Gimzewski, J. K.; Gerber, C.; Meyer, E.; Schlittler, R. R. *Chem. Phys. Lett.* **1994**, *217*, 589–594.

[24] Berger, R.; Gerber, C.; Gimzewski, J. K.; Meyer, E.; Guntherodt, H. J. *Appl. Phys. Lett.* **1996**, *69*, 40–42.

[25] Cesaro-Tadic, S.; Dernick, G.; Juncker, D.; Buurman, G.; Kropshofer, H.; Michel, B.; Fattinger, C.; Delamarche, E. *Lab Chip* **2004**, *4*, 563–569.

[26] Fritz, J.; Baller, M. K.; Lang, H. P.; Strunz, T.; Meyer, E.; Guntherodt, H. J.; Delamarche, E.; Gerber, C.; Gimzewski, J. K. *Langmuir* **2000**, *16*, 9694–9696.

[27] Arntz, Y.; Seelig, J. D.; Lang, H. P.; Zhang, J.; Hunziker, P.; Ramseyer, J. P.; Meyer, E.; Hegner, M.; Gerber, C. *Nanotechnology* **2003**, *14*, 86.

[28] Braun, T.; Ghatkesar, M. K.; Backmann, N.; Grange, W.; Boulanger, P.; Letellier, L.; Lang, H.-P.; Bietsch, A.; Gerber, C.; Hegner, M. *Nat. Nanotechnol.* **2009**, *4*, 179–185.

[29] Snow, D.; Weeks, B. L.; Kim, D. J.; Loui, A.; Hart, B. R.; Hope-Weeks, L. J. *J. Colloid Interface Sci.* **2007**, *316*, 687–693.

[30] Bigelow, W. C.; Pickett, D. L.; Zisman, W. A. *J. Colloid Sci.* **1946**, *1*, 513–538.

[31] Nuzzo, R. G.; Allara, D. L. *J. Am. Chem. Soc.* **1983**, *105*, 4481–4483.

[32] Maoz, R.; Sagiv, J. *J. Colloid Interface Sci.* **1984**, *100*, 465–496.

[33] Ulman, A. *Chem. Rev.* **1996**, *96*, 1533–1554.

[34] Schwartz, D. K. *Annu. Rev. Phys. Chem.* **2001**, *52*, 107–137.

[35] Bain, C. D.; Troughton, E. B.; Tao, Y. T.; Evall, J.; Whitesides, G. M.; Nuzzo, R. G. *J. Am. Chem. Soc.* **1989**, *111*, 321–335.

[36] Shimazu, K.; Yagi, I.; Sato, Y.; Uosaki, K. *Langmuir* **1992**, *8*, 1385–1387.

[37] Debono, R. F.; Loucks, G. D.; Manna, D. D.; Krull, U. J. *Can. J. Chem.* **1996**, *74*, 677–688.

[38] Shao, H. B.; Yu, H. Z.; Cheng, G. J.; Zhang, H. L.; Liu, Z. F. *Ber. Bunsen-Ges. Phys. Chem.* **1998**, *102*, 111–117.

[39] Schneider, T. W.; Buttry, D. A. *J. Am. Chem. Soc.* **1993**, *115*, 12391–12397.

[40] Peterlinz, K. A.; Georgiadis, R. *Langmuir* **1996**, *12*, 4731–4740.

[41] Kim, Y. T.; McCarley, R. L.; Bard, A. J. *Langmuir* **1993**, *9*, 1941–1944.

[42] Haehner, G.; Woell, C.; Buck, M.; Grunze, M. *Langmuir* **1993**, *9*, 1955–1958.

[43] Truong, K. D.; Rowntree, P. A. *J. Phys. Chem.* **1996**, *100*, 19917–19926.

[44] Yamada, R.; Uosaki, K. *Langmuir* **1997**, *13*, 5218–5221.

[45] Yamada, R.; Uosaki, K. *Langmuir* **1998**, *14*, 855–861.

[46] Xu, S.; Cruchon-Dupeyrat, S. J. N.; Garno, J. C.; Liu, G.-Y.; Jennings, G. K.; Yong, T.-H.; Laibinis, P. E. *J. Chem. Phys.* **1998**, *108*, 5002–5012.

[47] Chung, C.; Lee, M. *J. Electroanal. Chem.* **1999**, *468*, 91–97.

[48] Hong, R.; Fernandez, J. M.; Nakade, H.; Arvizo, R.; Emrick, T.; Rotello, V. M. *Chem. Commun.* **2006**, 2347–2349.

[49] Montalti, M.; Prodi, L.; Zaccheroni, N.; Baxter, R.; Teobaldi, G.; Zerbetto, F. *Langmuir* **2003**, *19*, 5172–5174.

[50] Kassam, A.; Bremner, G.; Clark, B.; Ulibarri, G.; Lennox, R. B. *J. Am. Chem. Soc.* **2006**, *128*, 3476–3477.

[51] Ionita, P.; Caragheorgheopol, A.; Gilbert, B. C.; Chechik, V. *Langmuir* **2004**, *20*, 11536–11544.

[52] Hostetler, M. J.; Templeton, A. C.; Murray, R. W. *Langmuir* **1999**, *15*, 3782–3789.

[53] Baralia, G. G.; Duwez, A.-S.; Nysten, B.; Jonas, A. M. *Langmuir* **2005**, *21*, 6825–6829.

[54] Brunner, H.; Vallant, T.; Mayer, U.; Hoffmann, H.; Basnar, B.; Vallant, M.; Friedbacher, G. *Langmuir* **1999**, *15*, 1899–1901.

[55] Vallant, T.; Brunner, H.; Mayer, U.; Hoffmann, H.; Leitner, T.; Resch, R.; Friedbacher, G. *J. Phys. Chem. B* **1998**, *102*, 7190–7197.

[56] Vallant, T.; Kattner, J.; Brunner, H.; Mayer, U.; Hoffmann, H. *Langmuir* **1999**, *15*, 5339–5346.

[57] Resch, R.; Grasserbauer, M.; Friedbacher, G.; Vallant, T.; Brunner, H.; Mayer, U.; Hoffmann, H. *Appl. Surf. Sci.* **1999**, *140*, 168–175.

[58] Richter, A. G.; Yu, C. J.; Datta, A.; Kmetko, J.; Dutta, P. *Phys. Rev. E* **2000**, *61*, 607–615.

[59] Richter, A. G.; Durbin, M. K.; Yu, C. J.; Dutta, P. *Langmuir* **1998**, *14*, 5980–5983.

[60] Zhao, X.; Kopelman, R. *J. Phys. Chem.* **1996**, *100*, 11014–11018.

[61] Sander, L. C.; Lippa, K. A.; Wise, S. A. *Anal. Bioanal. Chem.* **2005**, *382*, 646–668.

[62] Pyun, J.; Kowalewski, T.; Matyjaszewski, K. *Macromol. Rapid Commun.* **2003**, *24*, 1043–1059.

[63] Edmondson, S.; Osborne, V. L.; Huck, W. T. S. *Chem. Soc. Rev.* **2004**, *33*, 14–22.

[64] Edmondson, S.; Huck, W. T. S. *J. Mater. Chem.* **2004**, *14*, 730–734.

[65] Glinel, K.; Jonas, A. M.; Jouenne, T.; Leprince, J.; Galas, L.; Huck, W. T. S. *Bioconjugate Chem.* **2008**, *20*, 71–77.

[66] Bernards, M. T.; Cheng, G.; Zhang, Z.; Chen, S.; Jiang, S. *Macromolecules* **2008**, *41*, 4216–4219.

[67] Kruszewski, K. M.; Gawalt, E. S. *Langmuir* **2011**, *27*, 8120–8125.

[68] Minko, S. *J. Macromol. Sci., Polym. Rev.* **2006**, *46*, 397–420.

[69] Laloyaux, X.; Mathy, B.; Nysten, B.; Jonas, A. M. *Langmuir* **2009**, *26*, 838–847.

[70] Flory, P. J. *J. Chem. Phys.* **1942**, *10*, 51–61.

[71] Huggins, M. L. *J. Chem. Phys.* **1941**, *9*, 440.

[72] Huck, W. T. S. *Materials Today* **2008**, *11*, 24–32.

[73] Santer, S.; Ruhe, J. *Polymer* **2004**, *45*, 8279–8297.

[74] Ebara, M.; Yamato, M.; Aoyagi, T.; Kikuchi, A.; Sakai, K.; Okano, T. *Biomacromolecules* **2004**, *5*, 505–510.

[75] Laloyaux, X.; Fautre, E.; Blin, T.; Purohit, V.; Leprince, J.; Jouenne, T.; Jonas, A. M.; Glinel, K. *Adv. Mater.* **2010**, *22*, 5024–5028.

[76] Alem, H.; Duwez, A.-S.; Lussis, P.; Lipnik, P.; Jonas, A. M.; Demoustier-Champagne, S. *J. Membr. Sci.* **2008**, *308*, 75–86.

[77] Liu, G.; Yan, L.; Chen, X.; Zhang, G. *Polymer* **2006**, *47*, 3157–3163.

[78] Ostaci, R.-V.; Damiron, D.; Capponi, S.; Vignaud, G.; Leger, L.; Grohens, Y.; Drockenmuller, E. *Langmuir* **2008**, *24*, 2732–2739.

[79] Minet, I.; Delhalle, J.; Hevesi, L.; Mekhalif, Z. *J. Colloid Interface Sci.* **2009**, *332*, 317–326.

[80] Zhang, H.; Ruckenstein, E. *Macromolecules* **1998**, *31*, 7575–7580.

[81] Radchenko, A. V.; Kostjuk, S. V.; Vasilenko, I. V.; Ganachaud, F.; Kaputsky, F. N. *Eur. Polym. J.* **2007**, *43*, 2576–2583.

[82] Penczek, S.; Cypryk, M.; Duda, A.; Kubisa, P.; Slomkowski, S. *Prog. Polym. Sci.* **2007**, *32*, 247–282.

[83] Bielawski, C. W.; Grubbs, R. H. *Prog. Polym. Sci.* **2007**, *32*, 1–29.

[84] Chiefari, J.; Chong, Y. K.; Ercole, F.; Krstina, J.; Jeffery, J.; Le, T. P. T.; Mayadunne, R. T. A.; Meijs, G. F.; Moad, C. L.; Moad, G.; Rizzardo, E.; Thang, S. H. *Macromolecules* **1998**, *31*, 5559–5562.

[85] Couvreur, L.; Lefay, C.; Belleney, J.; Charleux, B.; Guerret, O.; Magnet, S. *Macromolecules* **2003**, *36*, 8260–8267.

[86] Tang, W.; Nanda, A. K.; Matyjaszewski, K. *Macromol. Chem. Phys.* **2005**, *206*, 1171–1177.

[87] Zhou, F.; Huck, W. T. S. *Phys. Chem. Chem. Phys.* **2006**, *8*, 3815–3823.

[88] Topham, P. D.; Howse, J. R.; Crook, C. J.; Parnell, A. J.; Geoghegan, M.; Jones, R. A. L.; Ryan, A. J. *Polym. Int.* **2006**, *55*, 808–815.

[89] Fischer, H. *J. Polym. Sci., Part A: Polym. Chem.* **1999**, *37*, 1885–1901.

[90] Xiao, D.; Wirth, M. J. *Macromolecules* **2002**, *35*, 2919–2925.

[91] Mayo, F. R.; Lewis, F. M. *J. Am. Chem. Soc.* **1944**, *66*, 1594–1601.

[92] Catalgil-Giz, H.; Giz, A.; Alb, A. M.; OnculKoc, A.; Reed, W. F. *Macromolecules* **2002**, *35*, 6557–6571.

[93] Ashford, E. J.; Naldi, V.; O'Dell, R.; Billingham, N. C.; Armes, S. P. *Chem. Commun.* **1999**, *14*, 1285–1286.

[94] Jones, D. M.; Brown, A. A.; Huck, W. T. S. *Langmuir* **2002**, *18*, 1265–1269.

[95] Semaltianos, N. G.; Wilson, E. G. *Thin Solid Films* **2000**, *366*, 111–116.

[96] Segerman, E. *Acta Cryst.* **1965**, *19*, 789–796.

[97] VanCamp, W.; DuPrez, F. E.; Bon, S. A. F. *Macromolecules* **2004**, *37*, 6673–6675.

[98] Tugulu, S.; Barbey, R.; Harms, M.; Fricke, M.; Volkmer, D.; Rossi, A.; Klok, H. A. *Macromolecules* **2007**, *40*, 168–177.

[99] Sankhe, A. Y.; Husson, S. M.; Kilbey, S.; Michael, I. *J. Polym. Sci., Part A: Polym. Chem.* **2007**, *45*, 566–575.

[100] Hu, H.; Saniger, J.; Garcia-Alejandre, J.; Castano, V. M. *Mater. Lett.* **1991**, *12*, 281–285.

[101] Konradi, R.; Ruhe, J. *Macromolecules* **2004**, *37*, 6954–6961.

[102] Smith, B. L.; Klier, J. *J. Appl. Polym. Sci.* **1998**, *68*, 1019–1025.

Chapter 3

Studying Local Reactions with AFM
The "Frequency Shift" Method

3.1 Introduction

The first objective of this thesis was to develop a tool that could monitor the kinetics of a localized chemical reaction. Two methods were considered: the first method was based on the resonance frequency shifts that accompany the adsorption of some molecules on a cantilever. Stiff AFM silicon cantilevers with a resonance around 160 kHz were used. These cantilevers were selected because they met a compromise between a high resonance frequency and a high surface area both being important for the sensitivity of the detection. In order to further increase this sensitivity, reactive polymer brushes were grafted from their surface to increase the surface density of reactive sites. This first method will be studied in the present chapter. The second considered method was based on the deflection of flexible cantilevers upon adsorption of molecules on one of its sides and will be investigated in the next chapter.

The basic principle of the technique to be developed is depicted in Figure 3.1. Considering a reaction between molecules on a substrate and molecules in solution and an AFM cantilever coated with a reactive polymer brush (Figure 3.1(1)), when the product is formed (Figure 3.1(2)), the product molecules will diffuse in the solution and eventually, some of them will be caught by the brush. Then, due to the mass increase of the system, the resonance frequency will shift towards lower values (Figure 3.1(3)). If the system is well calibrated, it will lead to the precise monitoring of the kinetics of this localized reaction.

In a preliminary study, the resonance frequency shifts obtained in air and in water for AFM cantilevers after their silanization with initiator-SAMs and after the subsequent polymerization step were measured to evaluate the sensitivity of the technique.

Then, as a model reaction, the activation of the functional side groups

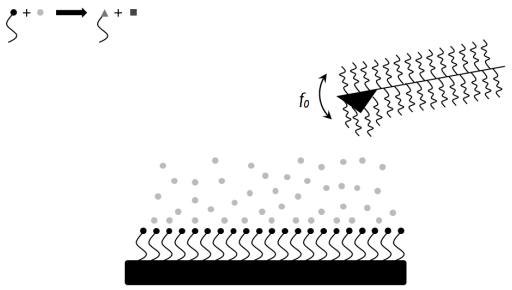

(1) Initial stage

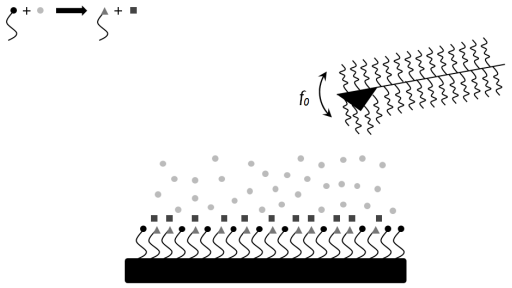

(2) Reaction

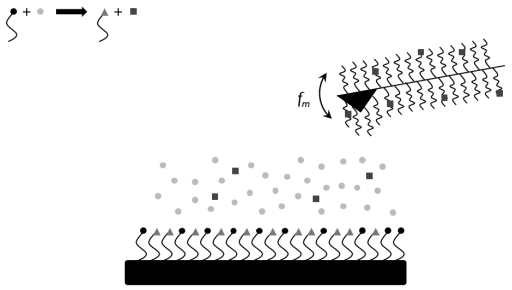

(3) Final stage

Figure 3.1: When molecules from the surface and reagents in solution react with each other, some product molecules are caught by the brush that is grafted on the AFM cantilever. The initial resonance frequency of the cantilever, f_0, shifts towards lower values due to this mass increase and becomes f_m.

of poly(methacrylic acid) (poly(MAA)) brushes with N-(3-Dimethyl-aminopropyl)-N'-ethylcarbodiimide hydrochloride (EDC) and N-Hydroxysuccinimide (NHS) was followed. This reaction converts the carboxylic acid functional groups to activated esters and was selected because it is fast and well known. Both the mass increase during the reaction and the conversion of the reactive side groups inside the brush were recorded as a function of time.

This method was also used for the characterization of changes in the conformation of the grafted brush. To this respect, the collapse transition of a thermoresponsive brush was studied. These brushes exhibit a transition from a swollen to a collapsed state upon heating. So, the collapse transition temperature (T_{CT}) of poly(di(ethylene glycol)methyl ether methacrylate) (poly(MEO_2MA)) brushes was measured. This temperature is linked to the Lower Critical Solution Temperature (LCST) of free chains in solution. In water, poly(MEO_2MA) has a LCST around 27°C. This LCST can be modified by adding specific salts to water. The variation of the T_{CT} was thus investigated upon the addition of two salts, Na_2SO_4 and NaSCN, which have opposite effects on the T_{CT}: Na_2SO_4 lowers it while NaSCN increases it.

Before the presentation and the discussion of the results, the theoretical aspects of the quantitative determination of a grafted mass on a vibrating sensor and the concept of thermoresponsive polymer brushes will be presented.

3.2 Theoretical Aspects

The story of Scanning Probe Microscopies (SPM) began in 1981 by the first experimental evidence by G. Binnig and H. Rohrer of the exponen-

tial distance dependence of the tunneling current between a conductive tip and a surface [1]. A few months later, they revealed the first topographic pictures of Au and $CaIrSn_4$ surfaces with atomic resolution using this technique [2]. The Scanning Tunneling Microscope (STM) was born. The experimental setup consisted in a tungsten tip fixed to a support that could move in the three directions of space thanks to a piezoelectric plate placed on three metallic feet that could be clamped independently. Another piezoelectric device enabled the sample to be displaced towards the tip very precisely. To reduce the internal vibrations, the system was maintained under static magnetic levitation over a superconducting bowl of lead cooled by liquid helium. The vertical resolution of this STM was below 1 Å and the lateral resolution was below 10 Å. This technique was so powerful that its inventors received the Nobel Prize in 1986.

Knowing the structure of materials and see their atomic arrangements is of course of tremendous use for all aspects of material science. However, the operating principle based on the tunneling current prevents STM from being used on insulator samples. For this category of materials, some other techniques were used such as the stylus profilometer. Its concept is rather simple. It consists in a stylus mounted on a cantilever beam that is scanned on a sample. The deflection of the cantilever is recorded to produce three dimensional images. Teague et al. [3] recorded 3D images with a lateral resolution of 1000 Å and a vertical resolution of 10 Å. Due to the high contact force between the tip and the surface (between 10^{-2} and 10^{-5} N, leading to pressures up to 3 GPa), the sample can suffer from plastic deformation or other kinds of damages. This is of course not suited for the observation of soft materials or organic samples. In order to solve this issue and to improve the resolution, Binnig et al. proposed in 1986 to couple these two powerful techniques in a single instrument that they called the Atomic Force Microscope (AFM) [4]. Here, the cantilever with the attached diamond stylus was sandwiched between the sample and an STM tip. This tip was used to record the position of

the stylus. The small force between the AFM tip and the sample was maintained constant via two feedback loops, one on the STM and one on the stylus. The AFM was then operated in four different modes depending on the interconnection between the two feedback loops. In one of these modes, the cantilever was oscillated at its resonance frequency while scanning the sample. The force between the stylus and the sample changed the resonance frequency of the cantilever which induced a change in both the amplitude and the phase of the tunnel current. These signals were then used to drive the feedback circuit. With this setup, they could achieve a lateral resolution of 30 Å and a vertical resolution of less than 1 Å.

Since this discovery, the experimental setup has constantly been updated. For instance, the deflection and the amplitude of the cantilever vibration are no more recorded with a STM but by a system composed of a laser reflecting on the apex of the cantilever towards a position sensitive detector (PSD). Nowadays, a huge variety of applications have been developed. The AFM can give information about the sample topography (AM-AFM, C-AFM), it can map different physical properties like the elastic modulus (PFT-AFM), the viscosity (LFM, FMM), the electrical conductivity (CS-AFM), the surface potential (KPFM), the magnetic domains (MFM)... or chemical properties like interatomic bond strength thanks to functionalized tips.

But this discovery also developed a huge interest for these microfabricated cantilevers that can be used as sensors [5]. Previously, some authors already had the idea to use silicon beams as sensors. The first example dates from 1968 when Wilfinger et al. studied the detection of resonances with large silicon structures (50 × 30 × 8 mm) [6]. However, the availability of commercial, relatively cheap AFM cantilevers fabricated in a reproducible way boosted the frequency of such reports. Moreover, the reduced size of these cantilevers induces a low spring con-

stant (and thus a high sensitivity to applied forces) and a high resonance frequency (for fast response) [7]. The first chemical application was proposed by Gimzewski et al. in 1994 who detected chemical reactions by the means of a bimetallic cantilever [8]. From there, these cantilever sensors have been widely used in a lot of different applications such as gas sensing [9, 10], chemistry [11, 12], mechanics [13, 14] and biology [15–18]. The operating principle of all these applications is based either on the measurement of the resonance frequency shifts of the cantilever coming from mass adsorption (or loss) or on the measurement of its deflection resulting from differential adsorption on each side of the cantilever. This chapter will only focus on this first aspect while next chapter will concentrate on the second one. Apart from these two kinds of detection, we can cite the work by Vancso et al. who developed the Inverted Chemical Force Microscopy (ICFM) [19, 20]. Here, the surface of the AFM tip is covered with reagents and the chemical reactions involving these reagents are probed *in situ* by force-distance measurements on a solid substrate on a scale of less than 100 molecules.

3.2.1 Measurement of the Grafted Mass on a Vibrating Sensor

The AFM literature provides extensive details about the mechanics of cantilever vibrations [21–23]. The objective of this introduction is not to go into deep details, but to provide the main developments.

The cantilevers usually used for vibrational studies are rectangular cantilevers with a uniform cross section. For this kind of beams, the equation of flexural motion is given by the Euler-Lagrange equation [24]:

$$EI\frac{\partial^4 y}{\partial x^4} + \rho A\frac{\partial^2 y}{\partial t^2} = 0 \tag{3.1}$$

In this equation, E is the Young's modulus of the material constituting the beam, I is the area moment of inertia, $y(x)$ is the deflection of the beam at point x along the longitudinal axis, ρ is the mass density and $A = a \cdot b$ is the cross section of the cantilever with a and b, the width and the thickness respectively. In the case of rectangular cross sections, which is usually the case for commercial cantilevers, $I = ab^3/12$. The general solution of this equation is of the type:

$$y(x,t) = \left(a_1 e^{kx} + a_2 e^{-kx} + a_3 e^{ikx} + a_4 e^{-ikx}\right) e^{-i\omega t} \tag{3.2}$$

with $k = 2\pi/\lambda$, the wavenumber and $\omega = 2\pi f$, the angular frequency. By replacing equation (3.2) into equation (3.1), we obtain the dispersion relation linking ω and k:

$$EI \cdot k^4 - \rho A \cdot \omega^2 = 0 \tag{3.3}$$

The solutions (3.2) must satisfy the following boundary conditions:

$$\begin{aligned} y|_{x=0} = 0 \quad , \quad \left.\frac{\partial y}{\partial x}\right|_{x=0} = 0 \\ \left.\frac{\partial^2 y}{\partial x^2}\right|_{x=L} = 0 \quad , \quad \left.\frac{\partial^3 y}{\partial x^3}\right|_{x=L} = 0 \end{aligned} \tag{3.4}$$

When equation (3.2) is injected in these conditions, it can be solved for the coefficients a_i if the conditions given in (3.5) are fulfilled:

$$\cos k_n L \cdot \cosh k_n L + 1 = 0 \tag{3.5}$$

From this equation, the wavenumbers k_n corresponding to the different flexural modes n can be calculated and the resonance frequencies of the cantilever are given by:

$$f_n = \frac{(k_n L)^2}{c_c^2} \quad \text{with} \quad c_c = L\sqrt{2\pi} \cdot \sqrt[4]{\frac{\rho A}{EI}} \tag{3.6}$$

Finally, the deflection $y_n(x)$ for each flexural mode can be written as:

$$\begin{aligned} y_n(x) = y_0\Big(& (\cos k_n x - \cosh k_n x) \\ & - \frac{\cos k_n L + \cosh k_n L}{\sin k_n L + \sinh k_n L}(\sin k_n x - \sinh k_n x)\Big) \end{aligned} \tag{3.7}$$

with y_0, the amplitude of the vibration.

Usually, the authors do not use these formulas to calculate the grafted mass on a cantilever but instead use a derivation of the point-mass model. In this model, a point mass m is attached to a massless spring with stiffness k_c. The resonance frequency of the system is then:

$$f_0 = \frac{1}{2\pi}\sqrt{\frac{k_c}{m}} \quad \text{or} \quad \omega_0 = \sqrt{\frac{k_c}{m}} \tag{3.8}$$

This model can be slightly modified in order to take the constraints of the real system into account. The idea is to replace the mass m in equation (3.8) with the effective mass m^* of the system in such a way that the resonance frequency of the model is equal to the lowest flexural vibration frequency f_1 of the cantilever. The stiffness of a rectangular

cantilever is given by:

$$k_c = \frac{3EI}{L^3} = \frac{Eab^3}{4L^3} \tag{3.9}$$

The lowest flexural vibration frequency is given by equation (3.6) with $n = 1$. Knowing from equation (3.5) that $k_1 L = 1.875$, m^* can be calculated as:

$$m^* = \frac{k_c}{\omega_1^2} = \frac{3\rho Lab}{1.875^4} \simeq 0.24 \cdot m \tag{3.10}$$

So the final expression of the resonance frequency of the first flexural mode in the modified point-mass model is:

$$f_0 = \frac{1}{2\pi}\sqrt{\frac{k_c}{m^*}} = \frac{1}{2\pi}\sqrt{\frac{k_c}{nm}} \quad \text{with} \quad n \simeq 0.24 \tag{3.11}$$

Now if the mass of the beam slightly changes due to a removal or an addition of material, the resonance frequency becomes:

$$f_m = \frac{1}{2\pi}\sqrt{\frac{k_c}{m^* + n\Delta m}} \tag{3.12}$$

where Δm is the change in mass. It can be derived from equations (3.11) and (3.12):

$$\Delta m = -\frac{k_c}{4\pi^2 n}\left(\frac{1}{f_0^2} - \frac{1}{f_m^2}\right) \tag{3.13}$$

This equation is a basic model that does not account for the resulting surface stress change, the effect of temperature or variation in the beam stiffness. Indeed it was shown that the surface stress coming from the adsorption of molecules modifies the resonance frequency even if this adsorption occurs on both sides of the cantilever [25–27]. However, for a typical silicon cantilever, this variation is small and of the order of 10 ppm for the adsorption of an atomic monolayer. The influence of temperature is a bit more important since it is of the order of -30 ppm/K for the same kind of cantilevers [9]. This effect is mainly due to the fact that the Young's modulus of the beam varies with temperature [28]. Effects of the stiffness variation can be dramatic as was shown by Thundat et al. in 1994 [29]. In their study, they coated a cantilever with gelatin and observed an increase in the resonance frequency upon water absorption which is in contradiction with equation (3.13).

Moreover, the medium has a huge influence on the behavior of the cantilever. For example, in water, large damping of the cantilever motion happens due to the higher density and viscosity of water as compared to air [5, 7]. This leads to a decrease of both the resonance frequency and the quality factor Q which is the ratio between the stored energy in the beam and the energy loss of the system and can be estimated by the ratio between the resonance frequency and the full width of the peak at an amplitude $A = A_{max}/\sqrt{2}$ where A_{max} is the amplitude of the vibrations at the resonance. The effect of the medium on the resonance frequency of the cantilever can be calculated by using equation (3.11) with a modified expression for m^* taking into account the mass of the fluid in contact with the lever [30]:

$$m^* = 0.24 \cdot m + 0.144\rho_w(La)^{3/2} \tag{3.14}$$

with ρ_w, the mass density of water.

The direct consequence of this fact is that the mass sensitivity is lowered. Some authors proposed different methods to increase Q and thus the resolution [31, 32] but these techniques involve the use of expensive modification of the experimental setup and/or specifically microfabricated cantilevers.

In addition, when operated in acoustic mode, the nose of the AFM oscillates at the same frequency as the cantilever which induces large vibrations of the surrounding liquid and produces parasitic effects in the resonance spectra as can be seen in Figure 3.2 [33]. To circumvent this issue, authors propose to use magnetically driven cantilevers [9, 30]. However, the magnetic coating of these cantilevers oxidizes rapidly and it can lead to a lack of precision in the measurement. Moreover, for commercial cantilevers, the resonance peak is not well defined and located at small frequencies (Figure 3.3).

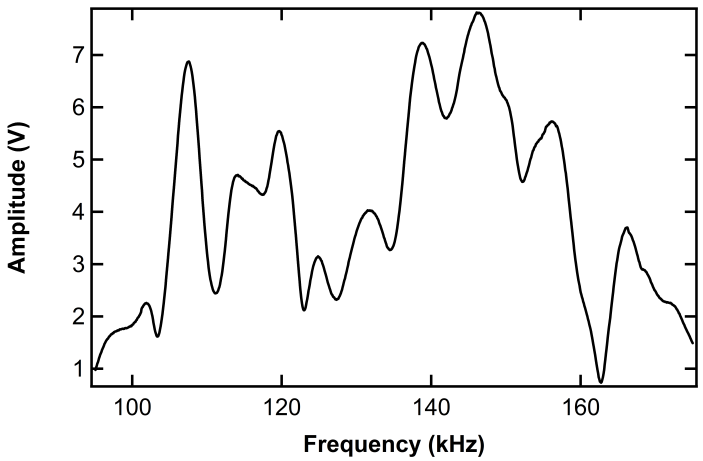

Figure 3.2: Frequency spectrum of a bare silicon cantilever in water. The noise comes from coupling between the vibration of the cantilever and of the surrounding liquid.

So far, the best sensitivities were obtained either for specifically de-

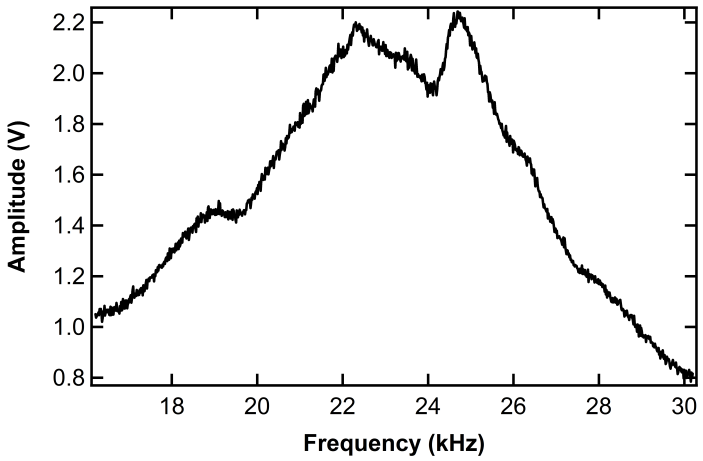

Figure 3.3: Frequency spectrum of a magnetically driven silicon cantilever with a magnetic coating in water.

signed cantilevers [11, 34–38] with mass sensitivities up to 2.7 ag [39] or for cantilever arrays [10, 15, 27, 40, 41] for the simultaneous sensing of different species or for getting rid of the static noise. However, here we want to use basic and commercially available AFM cantilevers in a concern to be reproducible and cost effective. Moreover, the AFM has another advantage concerning the final application: its piezoelectric nose allows the precise positioning of the cantilever at a desired spot on the surface and the semi-continuous monitoring of its resonance frequency.

3.2.2 Thermoresponsive Polymer Brushes

Polymers (as well as some smaller molecules) can exhibit a reversible phase transition in solvent from solubility to insolubility upon heating [42]. These materials are thus called thermoresponsive since their behavior is modified when the temperature changes. These "smart" materials have applications in adaptive coatings [43–46], sensors and actuators

[47–51], chromatographic separation [52, 53], drug delivery [54–56], etc. The temperature at which the phenomenon is observed is called "Lower Critical Solution Temperature" or LCST. Below the LCST, the polymer chains interact preferentially with the solvent and are thus soluble. Above the LCST, the polymer chains become more solvophobic and thus insoluble. If these polymers are synthesized as dense brushes, a transition between two states is observed: a swollen state below the collapse transition temperature (T_{CT}) where the polymer chains stretch away from the surface and a collapsed state over the T_{CT} when the brush expels the solvent. This is schematized in Figure 3.4.

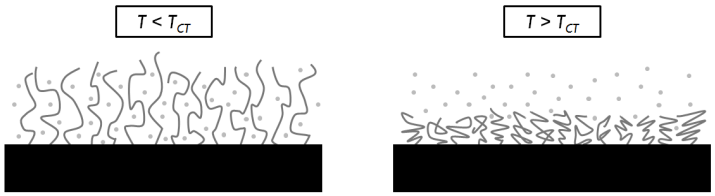

Figure 3.4: Below the collapse transition temperature (T_{CT}), the brush is hydrated while it is collapsed above.

This transition has been widely studied by Quartz Crystal Microbalance with Dissipation monitoring (QCM-D) measurements [57–61]. Two different and opposite phenomenons have been remarked by authors from these studies. Authors from [57] observed a continuous decrease of the effective mass on the sensor upon heating while authors from [58] observed that this decrease is precessed by a sudden increase of this effective mass. The first finding is easy to understand. Below the transition temperature, the brush is hydrated. While the temperature rises, the brush progressively dehydrates and this loss of water molecules explains the observed mass loss. In the second case, the authors explain their observation by considering that before the transition, the brush poorly transmits energy to the surrounding fluid as the sensor oscillates while after the collapse, the brush couples much more effectively to the sensor.

If this effect overcompensates the mass loss due to the dehydration of the brush then the result is an increase of the effective mass.

The mechanism of the collapse transition is thus not easy to study and the detailed pathway of this transition is still under debate. Recently, we proposed to study this transition by coupling equilibrium water contact angles measurements for probing the outer surface of the brush during the transition and QCM-D measurements which are sensitive to the bulk transition [62]. We concluded that the bulk of the brush collapses over a broad temperature interval (ca. 25°C) and that the end of this process is characterized by a sharp first-order transition of the surface of the brush.

If this transition can be followed by QCM-D, it should be possible to measure this collapse transition by grafting a thermoresponsive polymer brush from an AFM cantilever and following the resonance frequency shifts as a function of the temperature in a similar approach to the one explained earlier for the study of the grafted mass on an AFM cantilever. Figure 3.5 depicts this idea.

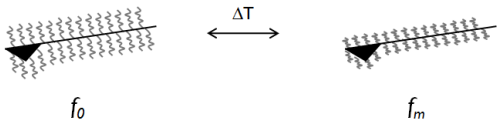

Figure 3.5: If a thermoresponsive brush is grafted from an AFM cantilever, the collapse transition of the brush above the T_{CT} is expected to modify the resonance frequency of the system.

The polymer selected for this study is poly(di(ethylene glycol)methyl ether methacrylate) or poly(MEO_2MA). This polymer has a LCST at about 27°C [44]. This temperature can be tuned by copolymerization with methacrylic acid or oligo(ethyleneglycol) methacrylates [42, 63–65] or by modifying the experimental conditions such as the pressure [66]

or the solvent [67–69]. This latter parameter was studied by adding specific salts to the water. Indeed, some solutes can change the structure of water: chaotropic species are less polar than water and break the hydrogen bonds between water molecules which prevents the formation of an ordered structure while kosmotropic species are more polar than water and reinforce the structuration by forming hydrogen bonds with water [70, 71].

F. Hofmeister was the first in 1888 to classify these species based on their ability to reinforce the structuration of water [72]. For example, for anions, the classification is: $CO_3^{2-} > SO_4^{2-} > H_2PO_4^- > F^- > Cl^- > Br^- > NO_3^- > I^- > ClO_4^- > SCN^-$. The anions on the left are strong kosmotropes while anions on the right are strong chaotropes. Here, the effects of Na_2SO_4 and NaSCN on the T_{CT} of poly(MEO_2MA) brushes were studied.

3.3 Results and Discussion

This section is divided into two parts: the first one dealing with the results obtained for the measurement of the kinetics of a chemical reaction and the second one dealing with the results obtained for the measurement of the collapse transition temperature of a thermoresponsive brush. The materials and methods involved in each part are briefly described in the following and more information can be found in the Experimental Part (section 6.1.3, page 193 for materials and section 6.2.3, page 201 for methods).

3.3.1 Measurement of the kinetics of a chemical reaction

Preliminary study

As a first test, the resonance frequency shifts obtained in air and in water upon functionalization of AFM cantilevers with polymer brushes were studied. Silanization and polymerization steps were conducted simultaneously on rectangular silicon cantilevers and on silicon squares for the characterization of the organic layers. In order to estimate the masses grafted after each step, the exact geometric dimensions of the considered cantilevers were first measured by Scanning Electron Microscopy (SEM) (Figure 6.3 on page 194). The section of the beam is not exactly rectangular but is of hexagonal shape. Its dimensions are: length (L) = 202 μm, width (a) = 50.7 μm and thickness (b) = 10.4 μm.

Then, the thickness of the silane-initiator self-assembled monolayer (SAM) was measured by X-Ray Reflectometry (XRR) (cf. section 6.3.1 on page 211) on the corresponding silicon square making the assumption that this layer is of the same thickness as the one covering the cantilever since the reaction was executed in the same batch. The reflectogram is available in Figure 2.12 and its corresponding electronic density profile in Figure 2.13. The number of silane molecules per nm^2 estimated from this profile was around 2.6. Knowing this grafting density, the geometric dimensions of the cantilever and the molecular weight of the silane (236 g/mol not taking into account the reactive Cl atoms), the grafted mass on the cantilever after this silanization step was estimated to be around 20.9 pg.

The same scheme was reproduced for the estimation of the mass of the poly(MEO_2MA) brush. After an hour of polymerization, ellipsometric measurements (cf. section 6.3.2 on page 215) showed that the dry thickness of the final brush was 35 nm. Knowing that the mass den-

sity of a dry polymer layer can be estimated as 1 g/cm^3, the mass of the polymer brush grafted from the cantilever was estimated at around 717 pg.

These values were compared with those obtained from the resonance frequency shifts measurements. Figure 3.6 presents these shifts measured in air (left) and in water (right). The black line shows the resonance peak of the bare cantilever, the dark gray line, the peak after the silanization and the light gray curve, the peak after the brush growth. The numerical data are given in Tables 3.1 and 3.2 respectively.

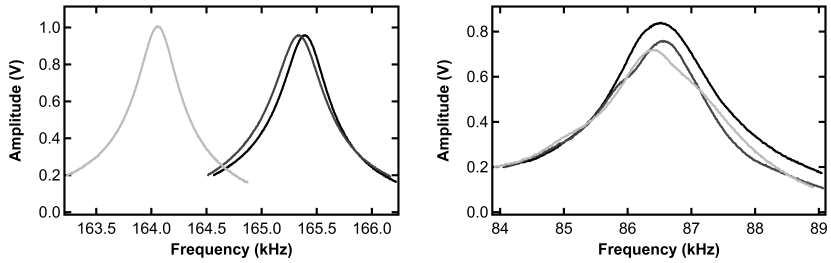

(1) Air (2) Water

Figure 3.6: Resonance frequency curves of an AFM cantilever in air (left) or in water (right) upon silane-initiator functionalization (dark gray) and subsequent brush growth (light gray). The black line shows the initial resonance frequency of the cantilever.

Step	f_0 (kHz)	Δm (pg)	Q (-)
Bare cantilever	165.39	-	460
Silanization	165.33	120	420
Brush growth	164.06	2570	495

Table 3.1: Numerical data for the resonance frequency experiments shown in Figure 3.6(1).

These curves were fitted with equation (6.1) (page 203) to obtain the values of the resonance frequencies f_0 (rounded to the nearest 10 Hz)

Step	f_0 (kHz)	Δm (pg)	Q (-)
Bare cantilever	86.53	-	70
Silanization	86.55	-100	75
Brush growth	86.41	540	65

Table 3.2: Numerical data for the resonance frequency experiments shown in Figure 3.6(2).

and of the quality factors Q (rounded to the nearest 5) while the grafted masses Δm were calculated with equation (3.13) (page 75).

The first immediate observation that can be done is that the resonance frequencies in water are lower than those obtained in air by a factor of two. This is due to the higher density and viscosity of this medium compared to air as already discussed in the introduction. The direct consequence of this fact is that the mass sensitivity is decreased. Indeed, equation (3.13) shows that the higher the resonance frequency is, the higher the shift in the resonance frequency is for a given mass change. The second observation is the broadening of the peaks in water. This is linked to the decrease by a factor of 6-8 of the quality factor Q of the resonator. This leads to an increased uncertainty in the measured resonance frequency and this has of course an impact on the accuracy of the calculated mass change. The reason for this broadening is the same as already evoked. It is also a bit surprising that the quality factor does not always decrease when increasing the amount of organic matter on the lever. It is believed that such small quantities of soft matter do not have a huge impact on Q and that other effects such as the position of the cantilever on the nose and its interaction with the surrounding medium have a stronger influence on it. Finally, the peaks are not well defined in water. This is due to the fact that all the piezoelectric system oscillates in the liquid cell giving rise to vibrational patterns and artifacts in our graphs.

On the quantitative point of view, in air, the measured mass on the cantilever after the silanization step is 120 pg while it further increases to 2570 pg after the polymerization step[1]. These values are much larger than the theoretical masses that were calculated (respectively 21 and 720 pg). This was observed in all the experiments made to confirm these results. To explain that, some hypothesis can be drawn:

1. The surface properties of the cantilevers were different from those of the wafers.
2. The n factor for the effective mass of the cantilever was derived for a rectangular cantilever while the real one had an hexagonal cross-section.
3. More materials were grafted on the cantilever than expected due to gel formation or bad rinsing.
4. The stiffness k_c of the cantilever was modified by the organic layers.
5. The surface tension of the cantilever was modified by the organic layers.

The first hypothesis could explain a slight variation in the observed values but certainly not the factor 4-5 regularly recorded. The second one could maybe explain part of this difference but a rapid calculation of the stiffness of the bare cantilever with equation (3.11) gave a k_c of ca. 43 N/m which is within the range given by the manufacturer. Hypothesis 3 is plausible because some gel was sometimes observed on the edges of the cantilever with the optical microscope. This is maybe due to a bad rinsing of the cantilevers after each step. Indeed, it is not possible to wash them with a flow of solvent then to dry them with a stream of

[1]For information, the UV/O_3 activation usually increases the resonance frequency of the cantilever meaning that the surface is cleaned by removal of the organic contaminants. The estimated weight loss is around a few tens of pg.

nitrogen. They were in fact dipped in successive rinsing baths for a few minutes then let at air for drying. This method was maybe not sufficient to remove the excess of initiator or some polymer gel on the cantilever. Hypothesis 4 and 5 have been discussed in the introduction. For this system, the exact effect of the thick polymer brush layer on the stiffness or on the surface tension of the cantilever is not known. However, it is expected that these variations could lead to a shift of the measured frequencies by a few hertz but could not explain the quite huge difference that is observed.

In water, the grafted mass deduced from the resonance frequency shift after the silanization step is negative which is impossible. Moreover, other experiments gave opposite results and the values obtained after the polymerization step were not reproducible. This is due on the one hand to the decrease of Q inducing a broadening of the peaks and on the other hand, to the coupling effect between the vibration of the cantilever and of the surrounding liquid (Figure 3.2) inducing a deformation of the peaks. These two effects lead to an increase of the uncertainty of the measured values. Moreover, it was observed that the resonance frequency of the cantilever also slightly changes by up to 10 Hz as a function of its position on the AFM nose. This is not too dramatic for measurements in air because the mass sensitivity is around 1 pg/Hz which leads to an uncertainty of 10 pg but in water, since the resonance frequency is lower, the mass sensitivity is around 8 pg/Hz leading to an uncertainty of 80 pg, larger than the mass of the silane layer. For higher grafted masses, the relative error is reduced but is still large in the case of water measurements.

To decrease this error, averages over a series of experiments could be calculated. This solution would not be very cost/time effective. The suggested approach is to make the measurements *in situ* during the mass increase. This will be the object of the next section.

Activation reaction of a poly(MAA) brush with EDC/NHS

In this section are presented the results obtained for the study of the kinetics of a chemical reaction by the measurement of the resonance frequency shifts of an AFM cantilever grafted with a reactive polymer brush. However, instead of probing a reaction arising on a nanocatalytic islet which was the final goal, the reagents were here in solution to test the feasibility of the technique. The reaction that was selected is the activation reaction of a poly(methacrylic acid) (poly(MAA)) brush by EDC alone or by the couple EDC/NHS. These species convert the carboxylic acid functions into activated esters (Figure 6.8 on page 202). This reaction is quite fast and well-known in organic chemistry and biochemistry, e.g. for the cross-linking of collagen [73–77].

Poly(MAA) brushes were grown from both AFM cantilevers and silicon squares. These cantilevers were then dipped in the reactive medium and their resonance frequencies were measured for different reaction times. Then, the frequency shifts were converted in masses using equation (3.13). Figure 3.7 (left) shows the results obtained for three different cantilevers. The first one (■) was grafted with a 110 nm-thick poly(MAA) brush and immersed in a 0.2 M aqueous solution of EDC. The second one (▲) was grafted with a 22 nm-thick poly(MAA) brush and dipped in a 0.2 M EDC/0.2 M NHS aqueous solution. The last curve (□) is the reference curve for a bare cantilever dipped in the 0.2 M solution of EDC.

On the reference curve (□), we see that after 8 to 10 minutes, the resonance frequency stabilizes around a constant value roughly corresponding to $\Delta m = -400$ pg. This stabilization time can be explained by the progressive change of the viscosity of the medium as water is replaced by the reactive solution.

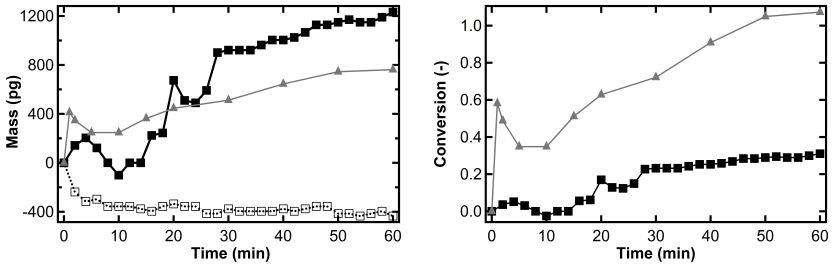

(1) Grafted mass (2) Conversion

Figure 3.7: Mass change of AFM cantilevers coated with poly(MAA) brushes (left) and conversion of the carboxylic acid functions inside these brushes (right) when dipped in a 0.2 M EDC solution (■) or a 0.2 M/0.2 M EDC/NHS solution (▲). The masses were calculated by *in situ* resonance frequency shifts measurements. The black dotted line on the left figure shows the reference experiment where a bare cantilever was dipped in a 0.2 M EDC solution (□).

For the 0.2 M solution of EDC (■), the grafted mass first increases, then decreases after 4 minutes and finally steadily increases again after 10 minutes of reaction. These 10 minutes correspond to the stabilization time where there is a competition between the exchange of solution inside the brush and the grafting of EDC molecules on its reactive side chains. After this period, the grafted mass steadily increases to reach a final value of 1200 pg after 1 hour of reaction.

Finally, for the EDC/NHS solution (▲), the same behavior was observed: after a stabilization time of a around 10 minutes, the grafted mass increases continuously. The final grafted amount is only 800 pg. This is not too surprising given the fact that the polymer brush on this lever is much thiner (23 nm vs 110 nm). Moreover, the molar mass of NHS is lower than that of EDC.

To compare these two different experiments more easily (right graph

in Figure 3.7), the number of reactive functions on each polymer brush was estimated by calculating the polymer mass (cf. above) and by dividing it by the molecular weight of the MAA monomer. Then, the mass of EDC or EDC/NHS (1:1) needed to convert 100% of these functions was calculated. Finally, by dividing the grafted masses in Figure 3.7(1) by this total mass, the conversion of the reactive –COOH groups was obtained. It can clearly be seen that the conversion is close to 1 after one hour for the thin polymer brush in EDC/NHS (▲) while it is only ca. 0.3 for the thick polymer brush in EDC (■). At this point, it would have been interesting to compare these results with those for a thin brush in EDC and for a thick brush in EDC/NHS. However, the observed difference was expected because first, the couple EDC/NHS is more reactive than EDC alone and second, the proportion of the accessible reactive groups inside the brush increases as its thickness decreases.

3.3.2 Measurement of the collapse transition temperature of a thermoresponsive brush

In this part, the results obtained for the study of the collapse transition of thermoresponsive polymer brushes grafted from AFM cantilevers are described. Usually, the collapse of the bulk of the brush is followed by QCM-D [57–61]. Recently, we published results for the study of the surface and bulk collapse transitions of these brushes allowing to obtain more information on the physics of the process [62]. Some details on this technique are given in the Experimental Part (section 6.3.6 on page 232). First, the collapse transition temperature of a poly(MEO_2MA) brush grafted from a quartz sensor was studied for different experimental conditions with QCM-D.

A poly(MEO_2MA) brush was grafted from a quartz sensor and from a silicon square used as reference. The thickness of this brush was 106 nm

on the reference and 130 nm on the sensor. Figure 3.8 displays the results obtained with QCM-D for different solutions: water (top left), 0.2 M Na_2SO_4 aqueous solution (top right) and 0.1 M NaSCN aqueous solution (bottom) upon heating (black curves) or cooling (gray curves) the system. As the collapse transition implies a change in the slopes of the QCM-D raw data, they were differentiated so that the maxima of the subsequent curves directly give the transition temperatures. Na_2SO_4 (kosmotrope) and NaSCN (chaotrope) have been chosen because of their antagonistic effect on the collapse transition temperature as discussed in the introduction. Indeed, these salts modify the structure of water by either enhancing or diminishing the cohesion between water molecules.

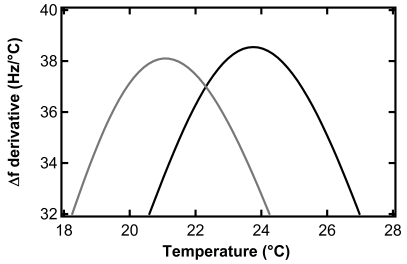

(1) Water

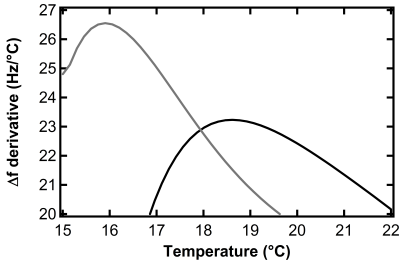

(2) 0.2 M Na_2SO_4 aqueous solution

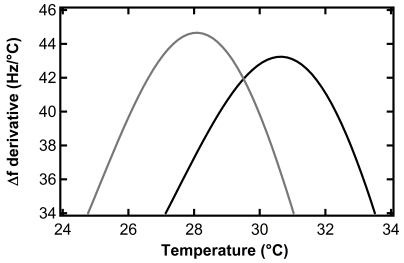

(3) 0.1 M NaSCN aqueous solution

Figure 3.8: Derivative of QCM-D data (frequency shift, third overtone) for a poly(MEO_2MA) brush grafted from a quartz sensor upon heating (black curves) or cooling (gray curves). The maxima of these curves give the collapse transition temperature.

In Figure 3.8(1), it is observed that the collapse transition temperature of the poly(MEO_2MA) brush lies between 21 and 24°C in water as expected. In Na_2SO_4, T_{CT} is decreased by 5°C and ranges between 16 and 19°C (Figure 3.8(2)). This is in agreement with results from Zhang et al. on poly(NIPAM) [69]. It means that the solubility of the polymer brush was decreased by addition of Na_2SO_4. This is because this salt polarizes the water molecules that are adjacent to the polymer chains and hence weakens the hydrogen bonds between the polymer and these water molecules.

Finally, the addition of NaSCN increases T_{CT} by 7°C compared to pure water (Figure 3.8(3)). Indeed, in this medium, T_{CT} is comprised between 28 and 31°C. This increase is explained by the polarization of the polymer chains by the anion SCN^- which enhances the hydrogen bonding with the surrounding water molecules. The polymer brush is then more soluble.

Two cantilevers were then grafted with poly(MEO_2MA) brushes. The thickness of brushes grown in the same conditions on Si wafers was measured by ellipsometry to be 74 nm. The variation of the resonance frequency of the AFM levers were then recorded in water and in the two different aqueous solutions.

Figure 3.9 shows the results obtained for the first lever in water (upper left) and in a 0.2 M Na_2SO_4 aqueous solution (upper right). The black curve (■) was acquired during heating while the gray one (▲) was during cooling.

On the two top graphs in Figure 3.9, the heating and cooling curves present a change in their slopes around T_{CT}. This slope variation mostly arises between 19 and 24°C in water and between 15 and 20°C in Na_2SO_4. These values are in agreement with the QCM-D results. Here, it is

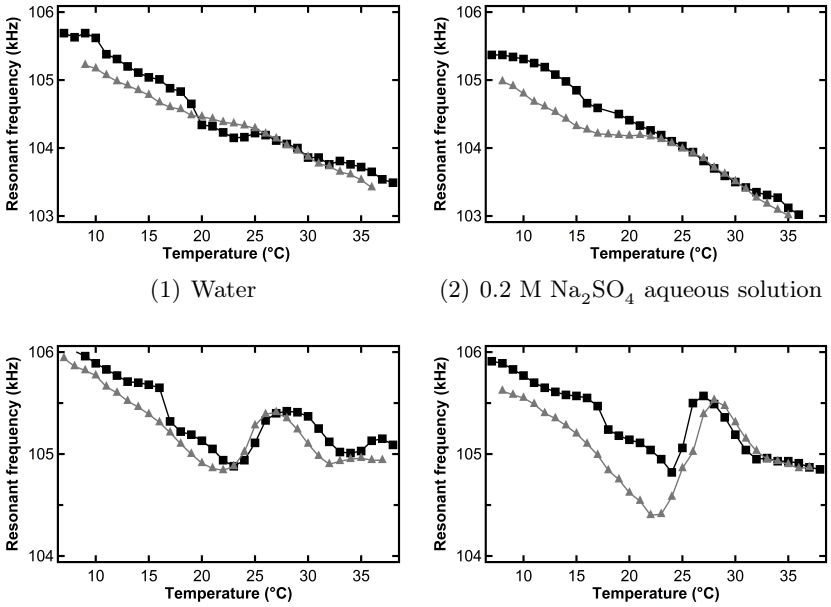

(1) Water (2) 0.2 M Na_2SO_4 aqueous solution

(3) Water (4) 0.1 M NaSCN aqueous solution

Figure 3.9: Comparison between the resonance frequency curves for a poly(MEO_2MA) brush grafted from AFM cantilevers obtained in different solutions: water (upper left) vs 0.2 M Na_2SO_4 aqueous solution (upper right) and water (lower left) vs 0.1 M NaSCN aqueous solution (lower right) upon heating (■) or cooling (▲). The change in the slope of these curves indicates the range of the collapse transition.

interesting to remark that the transition does not happen at a specific temperature but over a quite broad range of temperatures. This is due to the distribution in chain lengths [42] and in grafting densities inside the brush: where the chains are closer to each other, the enthalpic term is more important compared to zones where the chains spread more and the transition temperature is higher. This was observed by Laloyaux et al. through QCM-D measurements on poly(MEO_2MA) brushes [62]. In their paper, the authors studied the sequence of events occurring during the collapse transition of thermoresponsive (co)polymer brushes. They showed that the bulk of such brushes collapses over a large range of

temperatures, and the end of the process is signaled by a sharp first-order transition of the surface of the brush. This is thus a confirmation that what is probed here is the bulk collapse transition of the brush. Moreover, the transition is not a sharp event. However, the heating and cooling curves overlap quite well which means that the effect of the heating/cooling rate is limited in our case. The decrease in the resonance frequency when the temperature increases is due to the decrease of the Young's modulus of silicon [28]. The slope of the curve is less steep during the transition meaning that the system looses weight. As previously said this is because the brush expels water when it collapses.

The two bottom graphs in Figure 3.9 show the results obtained for the second lever in water (lower left) and in a 0.1 M NaSCN aqueous solution. The aspect of these curves are quantitatively very different from the previous ones. Nevertheless, an increase in the resonance frequency of the lever during the transition can still be observed as in the two top graphs. Here, this leads to a change in the sign of the slopes while it was not the case for the previously measured lever. In water, the slope change appears between 22 and 26℃ while it is comprised between 22 and 28℃ in NaSCN. These values are quite in disagreement with the previous measurements with QCM-D and T_{CT} does not seem to increase significantly when NaSCN is added. The results are summarized in Table 3.3 where the T_{CT} were averaged over the range of the transition.

	QCM-D	AFM
Water	22.5℃	22.8℃
Na_2SO_4 0.2 M	17.5℃	17.5℃
NaSCN 0.1 M	29.5℃	25.0℃

Table 3.3: Comparison of the T_{CT} of poly(MEO_2MA) brushes measured by QCM-D and AFM in water and in aqueous solutions of Na_2SO_4 and NaSCN.

These results are consistent with each others except in NaSCN where

a 4.5℃ difference between QCM-D and AFM measurements is observed. To better understand that, the same experiment was reproduced three times on the same lever within a few days. The resulting curves can be found in Figure 3.10.

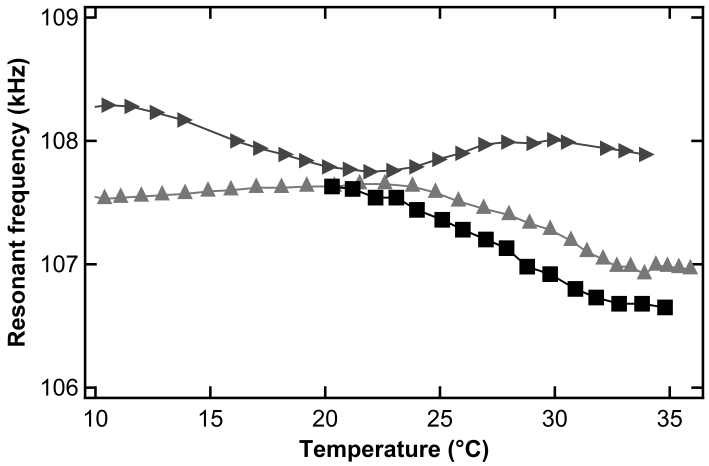

Figure 3.10: Comparison of three different T_{CT} measurements in water for the same AFM cantilever coated with a poly(MEO_2MA) brush. (■ : first experiment; ▶ : second experiment; ▲ : third experiment.

The three curves appear very different. On the one hand, the resonance frequency of this lever at a fixed temperature varies a lot (up to 1.3 kHz at 35℃) and, on the other hand, the change of slope during the transition does not seem to obey the same rules. However, this change happens in the same range of temperatures (between 22 and 32℃). On the black curve (■), a continuous decrease of the resonance frequency is observed as a function of the temperature. During the transition, this slope increases (in absolute value) which is in disagreement with the previous results. This could come from a change in the coupling between the brush and the lever as previously discussed. On the dark gray curve (▶), the slope becomes positive during the transition. Apart from this region, the general tendency of the curve is a global decrease of the resonance

frequency with increasing temperatures just as the first curve. Finally, on the light gray curve (▲), the resonance frequency slightly increases as a function of temperature before the transition. This is surprising compared to the previous observations. The rest of the curve is nevertheless quite similar to the first curve.

The conclusion of this study is that doing the same experiment with the same lever can lead to different results. It is thus difficult to draw some generalities concerning the mechanisms of the transition. The process seems quite complex.

In the last examples, it is astonishing to observe a resonance frequency of more than 100 kHz while it should be around 80 kHz. In all the experiments, the peak with the highest amplitude and the best quality factor Q in the frequency spectrum was selected. But as we can see on Figure 3.11, selecting the right peak is not always easy.

In this figure, the frequency spectra obtained for a standard cantilever grafted with a poly(MEO_2MA) brush at 25 (black curve) and 7°C (gray curve) are presented. At 7°C, there are lots of peaks with the most intense one around 80 kHz and a series of smaller peaks around 100 kHz. The peak with the highest intensity should be the resonance peak. But this peak is asymmetric and not well defined (low Q). In addition, at 25°C, the shape of the spectrum changes completely. The peak at 80 kHz splits in at least four different contributions that moved in opposite directions. This is due to a coupling between the oscillations of the lever and the surrounding fluid. It is then nearly impossible to select the correct resonance peak. Fortunately, whatever the peak selected, its frequency value always changes during the collapse transition but in an unpredictable way as seen on Figure 3.10.

At this point, different suggestions can be done to improve the sys-

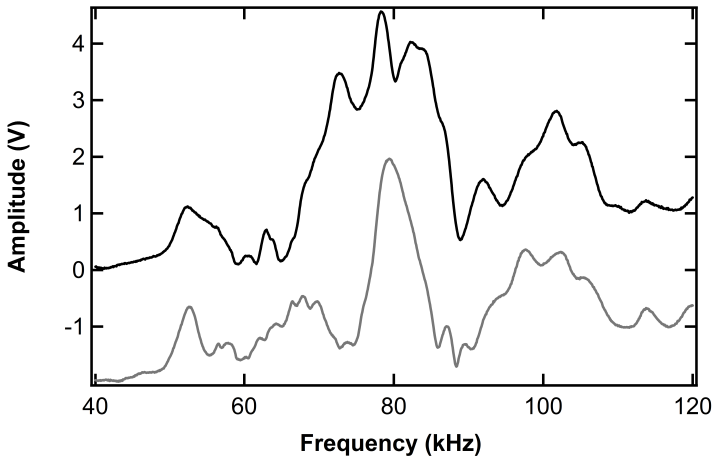

Figure 3.11: Frequency spectra in water of an AFM cantilever grafted with a poly(MEO_2MA) brush obtained at 25℃ (black curve) and 7℃ (gray curve). The apparent resonance frequency peak of the cantilever that is seen at 7℃ splits into at least 4 different peaks moving in opposite directions upon heating the solution.

tem. The length and the width of the lever could be decreased (or similarly, its stiffness could be increased) to increase its resonance frequency and the quality factor of the resonance peak in order to be more sensitive and to lower coupling effects. Indeed, if the lateral dimensions of a cantilever are reduced by a scaling factor α, the sensing area decreases by a factor of α^2 but the sensitivity increases by a factor of α^4 [41]. However, some tests for low values of α ($\alpha < 2$) showed that the resonance frequency was not easier to detect in the spectrum. In addition, for higher values of α, the resonance frequencies are shifted towards the MHz range and other methods have to be used to measure them such as the measurement of the capacitance of the cantilever by an impedance analyzer.

Magnetically driven cantilevers could also be used to reduce the parasitic effects of the oscillating liquid. But as discussed in the introduction

on the basis of Figure 3.3, the peak is situated at low frequencies and is not well defined for commercially available magnetic cantilevers.

Finally, it would be very interesting to study another way of detecting a change in mass on an AFM cantilever. This will be done in the next chapter where the deflection of an AFM cantilever grafted on one side with polymer brushes will be studied under different conditions.

3.4 Conclusion

In this chapter, it was shown that an AFM cantilever grafted with a polymer brush can be used as a mass sensor by measuring the variation of its resonance frequency.

Two different applications concerning this techniques were investigated. The first one was the measurement of the kinetics of a chemical reaction. Reactive polymer brushes were grafted from AFM cantilevers. When they were dipped in the reaction mixture, a decrease of their resonance frequency, compatible with an increase of their mass, was observed. The conversion of the reactive side groups inside the polymer brushes was estimated. For a thin polymer brush immersed in a EDC/NHS solution, the conversion was close to 1 after one hour while it was only 0.3 for a thick polymer brush after a 1 hour-immersion in a EDC solution. This was explained by a higher reactivity of the EDC/NHS couple compared to EDC alone and by the larger proportion of accessible reactive groups inside the thin brush compared to the thick one.

The second considered application was the study of the collapse transition temperature of a thermoresponsive brush. Here, the variation in the resonance frequency of a cantilever grafted with such brushes was

followed in different salt solutions as a function of the temperature. The slopes of the resulting curves showed variations in the expected ranges of temperatures which were previously determined by QCM-D measurements. Although the selection of the right resonance peaks was not always straightforward due to coupling between the oscillations of the cantilever and the surrounding liquid, the slope changes were always located in the same range of temperatures. Nevertheless, this study indicates clearly that this first method is not precise enough for quantitative determinations, which is intrinsic to its conditions of use (water). Therefore, we will not pursue further this track in the sequel.

References

[1] Binnig, G.; Rohrer, H.; Gerber, C.; Weibel, E. *Appl. Phys. Lett.* **1982**, *40*, 178–180.

[2] Binnig, G.; Rohrer, H.; Gerber, C.; Weibel, E. *Phys. Rev. Lett.* **1982**, *49*, 57.

[3] Teague, E. C.; Scire, F. E.; Baker, S. M.; Jensen, S. W. *Wear* **1982**, *83*, 1–12.

[4] Binnig, G.; Quate, C. F.; Gerber, C. *Phys. Rev. Lett.* **1986**, *56*, 930.

[5] Lang, H.; Hegner, M.; Gerber, C. Nanomechanical Cantilever Array Sensors. In *Springer Handbook of Nanotechnology*; Bhushan, B., Ed.; Springer Berlin Heidelberg, 2007; pp 443–460.

[6] Wilfinger, R. J.; Bardell, P. H.; Chhabra, D. S. *IBM J.* **1968**, *12*, 113–118.

[7] Raiteri, R.; Grattarola, M.; Berger, R. *Materials Today* **2002**, *5*, 22–29.

[8] Gimzewski, J. K.; Gerber, C.; Meyer, E.; Schlittler, R. R. *Chem. Phys. Lett.* **1994**, *217*, 589–594.

[9] Vidic, A.; Then, D.; Ziegler, C. *Ultramicroscopy* **2003**, *97*, 407–416.

[10] Lang, H. P.; Baller, M. K.; Berger, R.; Gerber, C.; Gimzewski, J. K.; Battiston, F. M.; Fornaro, P.; Ramseyer, J. P.; Meyer, E.; Guntherodt, H. J. *Anal. Chim. Acta* **1999**, *393*, 59–65.

[11] Lavrik, N. V.; Datskos, P. G. *Appl. Phys. Lett.* **2003**, *82*, 2697–2699.

[12] Betts, T. A.; Tipple, C. A.; Sepaniak, M. J.; Datskos, P. G. *Anal. Chim. Acta* **2000**, *422*, 89–99.

[13] Cherian, S.; Mehta, A.; Thundat, T. *Langmuir* **2002**, *18*, 6935–6939.

[14] Sushko, M. L. *Faraday Discuss.* **2009**, *143*, 63–80.

[15] Braun, T.; Ghatkesar, M. K.; Backmann, N.; Grange, W.; Boulanger, P.; Letellier, L.; Lang, H.-P.; Bietsch, A.; Gerber, C.; Hegner, M. *Nat. Nanotechnol.* **2009**, *4*, 179–185.

[16] Raiteri, R.; Grattarola, M.; Butt, H.-J.; Skladal, P. *Sens. Actuators, B* **2001**, *79*, 115–126.

[17] Frometa, R., N. *Biotecnologica Aplicada* **2006**, *23*, 320–323.

[18] Moulin, A. M.; O'Shea, S. J.; Welland, M. E. *Ultramicroscopy* **2000**, *82*, 23–31.

[19] Schonherr, H.; Chechik, V.; Stirling, C. J. M.; Vancso, G. J. *J. Am. Chem. Soc.* **2000**, *122*, 3679–3687.

[20] Dordi, B.; Pickering, J. P.; Schonherr, H.; Julius Vancso, G. *Eur. Polym. J.* **2004**, *40*, 939–947.

[21] Sarid, D. *Scanning Force Microscopy With Applications to Electric, Magnetic and Atomic Forces*; Oxford University Press: Oxford, 1994; Vol. 5.

[22] Nonnenmacher, N. Ph.D. thesis, 1990.

[23] Rabe, U.; Janser, K.; Arnold, W. *Rev. Sci. Instrum.* **1996**, *67*, 3281.

[24] Timoshenko, S. *History of strength of materials*; McGraw-Hill: New-York, 1953.

[25] Lu, P.; Lee, H. P.; Lu, C.; O'Shea, S. J. *Phys. Rev. B: Condens. Matter Mater. Phys.* **2005**, *72*, 085405–5.

[26] Cherian, S.; Thundat, T. *Appl. Phys. Lett.* **2002**, *80*, 2219.

[27] Lee, J. H.; Kim, T. S.; Yoon, K. H. *Appl. Phys. Lett.* **2004**, *84*, 3187–3189.

[28] Lee, J.; Goericke, F.; King, W. P. *Sens. Actuators, A* **2008**, *145-146*, 37–43.

[29] Thundat, T.; Warmack, R. J.; Chen, G. Y.; Allison, D. P. *Appl. Phys. Lett.* **1994**, *64*, 2894–2896.

[30] Herruzo, E. T.; Garcia, R. *Appl. Phys. Lett.* **2007**, *91*, 143113–3.

[31] Tamayo, J.; Humphris, A. D. L.; Malloy, A. M.; Miles, M. J. *Ultramicroscopy* **2001**, *86*, 167–173.

[32] Mehta, A.; Cherian, S.; Hedden, D.; Thundat, T. *Appl. Phys. Lett.* **2001**, *78*, 1637–1639.

[33] Okajima, T.; Sekiguchi, H.; Arakawa, H.; Ikai, A. *Appl. Surf. Sci.* **2003**, *210*, 68–72.

[34] Hosaka, S.; Chiyoma, T.; Ikeuchi, A.; Okano, H.; Sone, H.; Izumi, T. *Current Applied Physics* **2006**, *6*, 384–388.

[35] Forsen, E.; Abadal, G.; Ghatnekar-Nilsson, S.; Teva, J.; Verd, J.; Sandberg, R.; Svendsen, W.; Perez-Murano, F.; Esteve, J.; Figueras, E.; Campabadal, F.; Montelius, L.; Barniol, N.; Boisen, A. *Appl. Phys. Lett.* **2005**, *87*, 043507–3.

[36] Kehrbusch, J.; Ilin, E. A.; Hullin, M.; Oesterschulze, E. *Appl. Phys. Lett.* **2008**, *93*, 023102–3.

[37] Sarioglu, A. F.; Solgaard, O. *Appl. Phys. Lett.* **2008**, *93*, 023114–3.

[38] Yu, H.; Li, X. *Appl. Phys. Lett.* **2009**, *94*, 011901–3.

[39] Ilic, B.; Craighead, H. G.; Krylov, S.; Senaratne, W.; Ober, C.; Neuzil, P. *J. Appl. Phys.* **2004**, *95*, 3694–3703.

[40] Spletzer, M.; Raman, A.; Sumali, H.; Sullivan, J. P. *Appl. Phys. Lett.* **2008**, *92*, 114102–3.

[41] Shin, S.; Kim, J. P.; Sim, S. J.; Lee, J. *Appl. Phys. Lett.* **2008**, *93*, 102902–3.

[42] Becer, C. R.; Hahn, S.; Fijten, M. W. M.; Thijs, H. M. L.; Hoogenboom, R.; Schubert, U. S. *J. Polym. Sci., Part A: Polym. Chem.* **2008**, *46*, 7138–7147.

[43] Nagase, K.; Kobayashi, J.; Kikuchi, A.; Akiyama, Y.; Kanazawa, H.; Okano, T. *Langmuir* **2007**, *23*, 9409–9415.

[44] Jonas, A. M.; Glinel, K.; Oren, R.; Nysten, B.; Huck, W. T. S. *Macromolecules* **2007**, *40*, 4403–4405.

[45] Zou, Y.; Rossi, N. A. A.; Kizhakkedathu, J. N.; Brooks, D. E. *Macromolecules* **2009**, *42*, 4817–4828.

[46] Laloyaux, X.; Fautre, E.; Blin, T.; Purohit, V.; Leprince, J.; Jouenne, T.; Jonas, A. M.; Glinel, K. *Adv. Mater.* **2010**, *22*, 5024–5028.

[47] Mitsuishi, M.; Koishikawa, Y.; Tanaka, H.; Sato, E.; Mikayama, T.; Matsui, J.; Miyashita, T. *Langmuir* **2007**, *23*, 7472–7474.

[48] Pelah, A.; Jovin, T. M. *ChemPhysChem* **2007**, *8*, 1757–1760.

[49] Pelah, A.; Seemann, R.; Jovin, T. M. *J. Am. Chem. Soc.* **2007**, *129*, 468–469.

[50] Harmon, M. E.; Tang, M.; Frank, C. W. *Polymer* **2003**, *44*, 4547–4556.

[51] Moya, S.; Azzaroni, O.; Farhan, T.; Osborne, V. L.; Huck, W. T. S. *Angew. Chem., Int. Ed.* **2005**, *44*, 4578–4581.

[52] Maharjan, P.; Woonton, B. W.; Bennett, L. E.; Smithers, G. W.; DeSilva, K.; Hearn, M. T. W. *Innovat. Food Sci. Emerg. Tech.* **2008**, *9*, 232–242.

[53] Kanazawa, H.; Sunamoto, T.; Matsushima, Y.; Kikuchi, A.; Okano, T. *Anal. Chem.* **2000**, *72*, 5961–5966.

[54] Schmaljohann, D. *Adv. Drug Delivery Rev.* **2006**, *58*, 1655–1670.

[55] Twaites, B. R.; de las Heras Alarcon, C.; Cunliffe, D.; Lavigne, M.; Pennadam, S.; Smith, J. R.; Gorecki, D. C.; Alexander, C. *J. Controlled Release* **2004**, *97*, 551–566.

[56] Eeckman, F.; Moes, A. J.; Amighi, K. *Int. J. Pharm.* **2002**, *241*, 113–125.

[57] Annaka, M.; Yahiro, C.; Nagase, K.; Kikuchi, A.; Okano, T. *Polymer* **2007**, *48*, 5713–5720.

[58] Ishida, N.; Biggs, S. *Langmuir* **2007**, *23*, 11083–11088.

[59] Domack, A.; Prucker, O.; Ruhe, J.; Johannsmann, D. *Phys. Rev. E* **1997**, *56*, 680.

[60] Zhang, Y.; Du, B.; Chen, X.; Ma, H. *Anal. Chem.* **2008**, *81*, 642–648.

[61] Liu, G.; Zhang, G. *J. Phys. Chem. B* **2005**, *109*, 743–747.

[62] Laloyaux, X.; Mathy, B.; Nysten, B.; Jonas, A. M. *Langmuir* **2009**, *26*, 838–847.

[63] Jones, J. A.; Novo, N.; Flagler, K.; Pagnucco, C. D.; Carew, S.; Cheong, C.; Kong, X. Z.; Burke, N. A. D.; Stover, H. D. H. *J. Polym. Sci., Part A: Polym. Chem.* **2005**, *43*, 6095–6104.

[64] Yamamoto, S.-I.; Pietrasik, J.; Matyjaszewski, K. *J. Polym. Sci., Part A: Polym. Chem.* **2008**, *46*, 194–202.

[65] Yamamoto, S.-i.; Pietrasik, J.; Matyjaszewski, K. *Macromolecules* **2008**, *41*, 7013–7020.

[66] Kunugi, S.; Takano, K.; Tanaka, N.; Suwa, K.; Akashi, M. *Macromolecules* **1997**, *30*, 4499–4501.

[67] Freitag, R.; Garret-Flaudy, F. *Langmuir* **2002**, *18*, 3434–3440.

[68] Magnusson, J.; Khan, A.; Pasparakis, G.; Saeed, A. O.; Wang, W.; Alexander, C. *J. Am. Chem. Soc.* **2008**, *130*, 10852–10853.

[69] Zhang, Y.; Furyk, S.; Bergbreiter, D. E.; Cremer, P. S. *J. Am. Chem. Soc.* **2005**, *127*, 14505–14510.

[70] Hua, Z. *J. Chem. Technol. Biotechnol.* **2006**, *81*, 877–891.

[71] Moelbert, S.; Normand, B.; De Los Rios, P. *Biophys. Chem.* **2004**, *112*, 45–57.

[72] Hofmeister, F. *Naunyn-Schmiedeberg's Arch. Pharmacol.* **1888**, *24*, 247–260.

[73] Ligaj, M.; Jasnowska, J.; Musial, W. G.; Filipiak, M. *Electrochim. Acta* **2006**, *51*, 5193–5198.

[74] Tengvall, P.; Jansson, E.; Askendal, A.; Thomsen, P.; Gretzer, C. *Colloids and Surfaces B: Biointerfaces* **2003**, *28*, 261–272.

[75] Wissink, M. J. B.; Beernink, R.; Pieper, J. S.; Poot, A. A.; Engbers, G. H. M.; Beugeling, T.; van Aken, W. G.; Feijen, J. *Biomaterials* **2001**, *22*, 151–163.

[76] Lahiri, J.; Isaacs, L.; Tien, J.; Whitesides, G. *Anal. Chem.* **1999**, *71*, 777–790.

[77] Richert, L.; Boulmedais, F.; Lavalle, P.; Mutterer, J.; Ferreux, E.; Decher, G.; Schaaf, P.; Voegel, J.; Picart, C. *Biomacromolecules* **2004**, *5*, 284–294.

Chapter 4

Studying Local Reactions with AFM
The "Deflection" Method

4.1 Introduction

In the previous chapter, it was shown that the measurement of a grafted mass by the resonance frequency shift method is much less effective in water than in air with standard AFM cantilevers. This is due, on the one hand, to the large decrease of both the resonance frequency and the quality factor of the resonance peak because of the damping effect of the liquid and, on the other hand, to the parasitic effects in the frequency spectra due to a coupling between the oscillations of the cantilever and the surrounding fluid. These two drawbacks have major consequences on the mass sensitivity of this technique in liquids. This is the reason why authors usually prefer working with sensors based on the surface stress detection when working in liquid environments. This chapter will thus focus on AFM cantilever sensors based on the static measurement of their deflection.

The operating principle of this kind of sensors is presented in Figure 4.1. Considering a reaction between molecules on a substrate and molecules in solution and a flexible AFM cantilever coated on one side with a reactive polymer brush (Figure 4.1(1)), when the product is formed (Figure 4.1(2)), the product molecules will diffuse in the solution and eventually, some of them will be caught by the brush. Then, due to the surface stress change on the cantilever, it will bend (Figure 4.1(3)). If the system is well calibrated, it will lead to the precise monitoring of the kinetics of this localized reaction.

Two different types of sensors based on this technique were studied. First, a pH-sensor was developed by grafting a poly(mono-2-(methacryloyloxy) ethyl succinate) (poly(MES)) brush from on side of an AFM cantilever. Poly(MES) is a weak polyacid (PEL) and hence its charge varies with pH. When it is grafted in the form of a dense brush on a flexible substrate, the brush progressively swells upon increasing the pH due

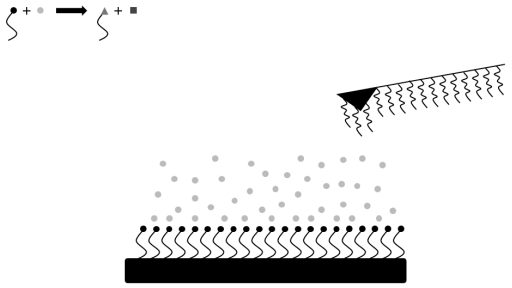

(1) Initial stage

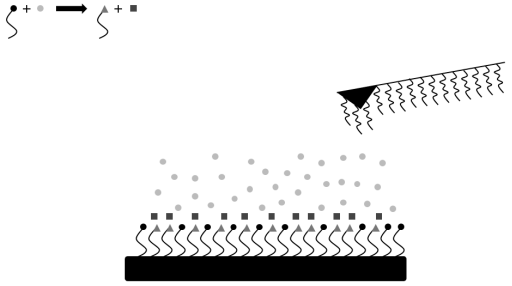

(2) Reaction

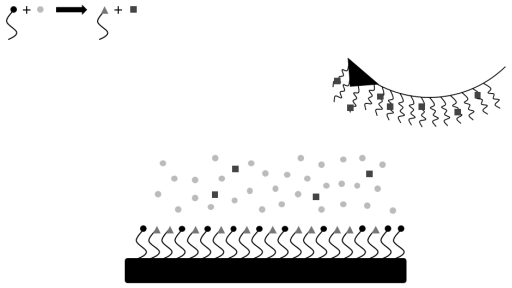

(3) Final stage

Figure 4.1: When molecules from the surface and reagents in solution react with each other, some product molecules are caught by the brush that is grafted on one side of the AFM cantilever. This cantilever bends due to a change in the surface stress difference between its two sides.

to electrostatic repulsion between the chains as it becomes deprotonated. This repulsion induces a compressive stress on the substrate which bends to release this stress. So by measuring the deflection of the cantilever, the pH of a solution can be determined. This sensor was developed to test the feasibility of this sensing method since it was expected that large deflections would arise during the modification of the pH.

Second, a chemical sensor was developed to probe the kinetics of a "click" reaction between an azidated brush grafted on an AFM cantilever and alkyne molecules in solution. A poly(2-hydroxyethyl methacrylate) (poly(HEMA)) brush was thus grafted from one side of an AFM cantilever and functionalized with 2-azidoethylamine in order to obtain N_3 side groups. So by recording the deflection of the cantilever upon immersion in a solution containing alkyne-modified sulforhodamine molecules, the kinetics of the reaction can be deducted. This "click" reaction between azides and alkynes was selected because it is fast, quantitative and does not produce byproducts that could be absorbed by the brush.

Before presenting and discussing the results, some theoretical aspects concerning deflection sensors, pH-responsive polymer brushes and the notion of "click chemistry" will be presented.

4.2 Theoretical Aspects

There exist a lot of techniques exploiting the bending of micro-cantilevers under external stimuli (Figure 4.2). For example, bimetallic cantilevers can be used to sense temperature (Figure 4.2(1)) [1]. Indeed, the thermal expansion difference between the two layers of the cantilever induces a bending of the beam when the temperature changes. This effect was first used by Gimzewski et al. in 1994 when they built a micro-calorimeter to

measure heat fluxes in a sample coated on a bimetallic cantilever during a chemical reaction (Figure 4.2(2)) [2]. Later examples can be found in [3, 4]. A similar approach consists in measuring the heat produced by light irradiation of a sample to perform photothermal spectroscopy (Figure 4.2(3)) [5–7]. Electrostatic force sensors (Figure 4.2(4)) or magnetic force sensors could also be based on this concept (Figure 4.2(5)). In this chapter, we will concentrate on stress sensors (Figure 4.2(6)). Ibach first used this method in 1994 to study surface stresses induced by the adsorption of different atoms on a nickel cantilever [8]. A few years later, Berger et al. reported the surface-stess-induced bending of a gold coated cantilever upon functionalization with an alkanethiol [9]. Now, stress sensors based on cantilevers are widely used in different applications such as viscosity sensors [10], pH sensors [11, 12], (bio)molecule recognition [13–16], gas sensors [17, 18],...

4.2.1 Measurement of the Grafted Mass on a Flexible Sensor

The deflection of a cantilever is not directly linked with the variation of its mass as it was the case for the resonance frequency shift (cf. equation (3.13) on page 75). However, there is a link between this deflection and a change in the surface stress of the sensor.

The Stoney equation is used to convert the curvature of the sensor, R (or similarly its deflection Δz), to the differential surface stress, $\Delta\sigma$, which is the surface stress difference between the two opposite sides of the cantilever as shown in Figure 4.3.

The original version of this equation was derived by Stoney in 1909 for metallic thin films deposited on rectangular steel rules by electrolysis [19]. It writes:

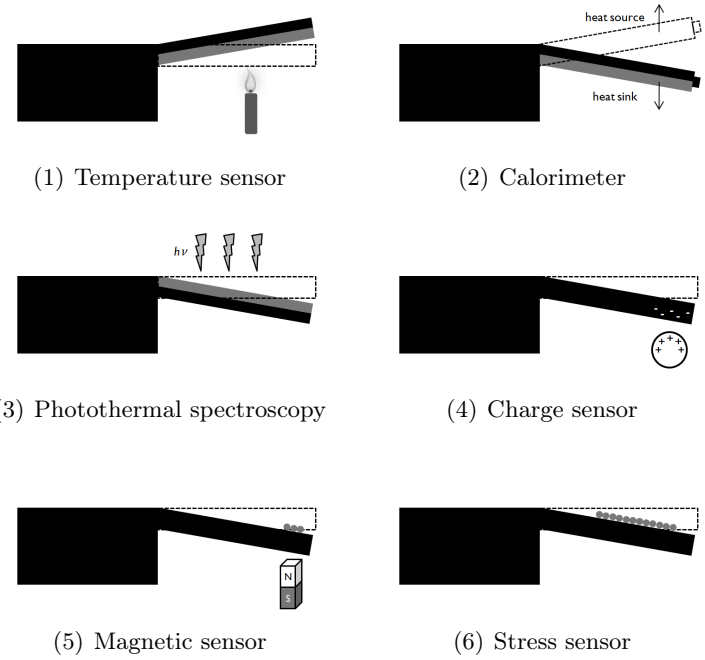

(1) Temperature sensor (2) Calorimeter

(3) Photothermal spectroscopy (4) Charge sensor

(5) Magnetic sensor (6) Stress sensor

Figure 4.2: Some examples of sensors based on the measurement of the deflection of cantilevers.

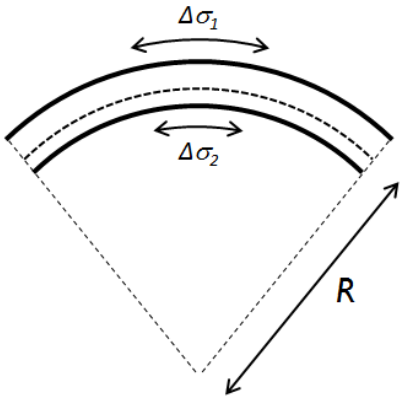

Figure 4.3: Lateral view of a stressed beam. The differential surface stress $\Delta\sigma$ is defined as the difference between the surface stress changes $\Delta\sigma_1$ and $\Delta\sigma_2$ acting on each side of the beam. R is the radius of curvature of the beam induced by this differential stress.

$$\Delta\sigma = \sigma_f \cdot t_f = \frac{E_s t_s^2}{6R} \tag{4.1}$$

where σ_f is the in-plane stress in the film[1], t_s and t_f are the thicknesses of the substrate and of the film respectively and E_s is the Young's modulus of the substrate.

In his paper, Stoney assumed an uniaxial stress in the film instead of a biaxial one. Indeed, since the width of the strip is much larger than the thickness of the film, the stress in the film is biaxial [20]. In this case, the elastic behavior of the strip is $E_s/(1-\nu_s)$, with ν_s the Poisson's ratio of the substrate, instead of E_s. The corrected version of the Stoney equation is thus:

[1]The surface stress σ and the in-plane stress in the film σ_f are commonly referred as σ in the literature which can confuse the reader.

$$\Delta\sigma = \frac{E_s t_s^2}{6R(1-\nu_s)} \tag{4.2}$$

Equation (4.2) is valid for films that are thin in comparison to the substrate but thick enough to bend the substrate as a result of their internal stress. Another requirement is that this stress has to be isotropic in the plane of the film.

The proof of this equation is quite simple. From the Euler-Bernoulli beam equation, we can find that the bending moment $M(x)$ of a beam is [21]:

$$M(x) = -E^* I \frac{d^2 z}{dy^2} \simeq \frac{E^* I}{R} \Longrightarrow \frac{1}{R} = \frac{M(x)}{E^* I} \tag{4.3}$$

where $E^* = E/(1-\nu)$. In the case of an elastically bent rectangular cantilever [22]:

$$I_{\text{rect}} = \frac{wt^3}{12} \quad \text{and} \quad M_{\text{rect}} = \frac{\Delta\sigma wt}{2} \tag{4.4}$$

where w is the width of the cantilever. Substituting these values into equation (4.3) yields equation (4.2).

Although equation (4.2) was derived for rectangular levers, the radius of curvature R is independent on the lateral shape, size and method of holding the lever [23]. For instance, in the case of the triangular cantilevers that were used here:

$$I_{\text{tri}} = \begin{cases} \frac{wt^3}{6} & \text{for } 0 \le y \le L_1 \\ \frac{(1-\frac{y}{L})Bt^3}{12} & \text{for } L_1 \le y \le L \end{cases} \quad \text{and} \quad M_{\text{tri}} = \begin{cases} \Delta\sigma wt & \text{for } 0 \le y \le L_1 \\ \frac{(1-\frac{y}{L})\Delta\sigma Bt}{2} & \text{for } L_1 \le y \le L \end{cases} \tag{4.5}$$

where w is the width of one leg of the cantilever and B, the length of the cantilever base as shown on Figure 6.4. Again, putting these values in equation (4.3) gives equation (4.2).

The link between the radius of curvature R and the deflection Δz can be deducted from geometric considerations [24] (Figure 4.4).

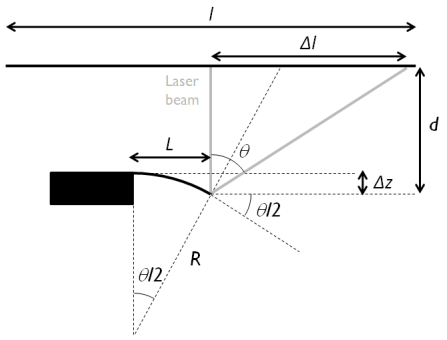

Figure 4.4: Definition of the geometric constants needed to link the observed laser displacement on the photodiodes Δl to the radius of curvature R and to the deflection Δz. l is the length of the photodiode, d is the distance between the cantilever and the photodiodes, θ is the angle between the reflected and incident beams from the laser and L is the length of the cantilever.

For small deformations, the relation between the angle of curvature $\frac{\theta}{2}$ and the radius of curvature R is:

$$R\frac{\theta}{2} = L \tag{4.6}$$

while the deflection is in turn related to the angle $\frac{\theta}{2}$ with:

$$\Delta z = L\frac{\theta/2}{2} \tag{4.7}$$

Combining equations (4.6) and (4.7) yields:

$$R = \frac{L^2}{2\Delta z} \tag{4.8}$$

Substituting R in equation (4.2) with this last result gives the relation between $\Delta\sigma$ and Δz:

$$\Delta\sigma = \frac{E_s t_s^2}{3(1-\nu_s)L^2}\Delta z \tag{4.9}$$

To measure this actual deflection, different techniques exist such as piezoresistive [25], piezoelectric [26], capacitive [27], interferometric [28] and optical readouts [29]. In most commercial AFM, a laser beam is reflected on the tip towards a detector made of 4 photodiodes. By measuring the current in the 4 different diodes, the position of the laser spot can be determined. The deflection signal, read in volts, has to be converted in an actual deflection in nanometers by measuring force curves on a hard surface.

Equation (4.9) is only valid for thin layers coated on a thick substrate. It can be shown from the general theory of elastic interactions in multilayer laminates that the corrective factor which has to be applied to Stoney's equation is small if the ratio δ between the thicknesses of the substrate and of the film is less than 0.1 [30]. The thickness of used cantilevers is around 600 nm while the thickness of the grafted brush

is around 80 nm. This is above the limit of the equation. More recent models take into account the relative thicknesses of both layers as well as the mechanical properties of both materials. Among them, the Atkinson equation [31, 32], derived in 1995, provides an improved approximation up to $\delta \simeq 0.4$ [30]:

$$\frac{1}{R} = \frac{6t_f\left(1+\frac{t_s}{t_f}\right)(1-\nu_s)}{E_s t_s^3}\Delta\sigma \tag{4.10}$$

It is clear that equation (4.10) can be approximated by equation (4.2) for small values of δ. A more complete model based on the aforementioned general theory of multilayers can be expressed as:

$$\frac{1}{R} = \frac{6E_f^* E_s^*(t_f+t_s)t_f t_s}{E_f^{*2}t_f^4 + 4E_f^* E_s^* t_f^3 t_s + 6E_f^* E_s^* t_f^2 t_s^2 + 4E_f^* E_s^* t_f t_s^3 + E_s^{*2} t_s^4}\Delta\varepsilon_0 \tag{4.11}$$

where $\Delta\varepsilon_0$ is the mismatch strain between the substrate and the film prior to bending. For $t_f << t_s$, this equation becomes:

$$\frac{1}{R} = \frac{6(1-\nu_s)}{E_s t_s^2}E_f^* t_f \Delta\varepsilon_0 \tag{4.12}$$

and given that $\Delta\sigma = E_f^* t_f \Delta\varepsilon_0$ in the thin-films approximation, the Stoney equation (4.2) is recovered.

Another interesting model was proposed by Godin et al. [23]. Their motivation was to eliminate the Young's modulus from the equation as it is not always easy to determine, especially for silicon nitride canti-

levers with a metallic coating. In the case of triangular cantilevers, this equation writes:

$$\Delta\sigma = \frac{2}{3(1-\nu_s)} \frac{L^2}{\left[wt_s L_1 + \frac{tB}{4L}(L-L_1)^2\right]} k\Delta z \tag{4.13}$$

with k, the stiffness of the beam and L_1 as described in Figure 6.4.

A lot of other derivations of Stoney's equation as well as other theories exist [12, 18, 33–36].

4.2.2 pH-Responsive Polymer Brushes

pH-responsive polymer brushes are made of weak polyelectrolytes (PEL) whose charge varies with pH. PEL are macromolecules with ionizable side groups. In solution in polar solvents, they carry charges. If the side chains are weak acids or bases, their degree of dissociation f depends on the local pH whereas it is not the case for strong acids or bases for which f is equal to 1 [37].

In the case of weak polyacid brushes, the chains are fully protonated at low pH. They are thus less soluble and are in a collapsed state. When the pH increases, f increases and the brush swells accordingly due to electrostatic repulsion between the chains as shown on Figure 4.5. Another important parameter is the ionic strength of the solution. Actually, salt has an impact on the screening of electrostatic interactions and on the regulation of the charge. But these two parameters are not the only ones at play for determining f. The degree of dissociation of a PEL brush depends also on the local density of the chains, the pK_a of the functional groups, the solvent quality and the number of counterions [38]. So the

local degree of dissociation in the brush can be very different from the degree of dissociation of the polymer in solution. Recently it was shown that the transition pH of a poly(methacrylic acid) brush can be tuned by copolymerization with di(ethylene glycol) methyl ether methacrylate [39]. More information on the theory of PEL brushes can be found in [38, 40, 41] for planar substrates and in [42, 43] for curved substrates.

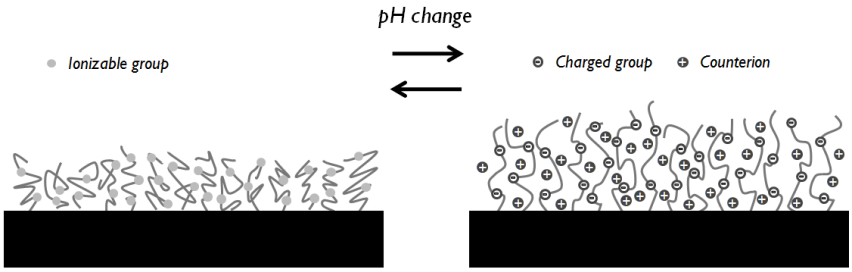

Figure 4.5: The charge density of weak polyelectrolyte brushes changes with pH. This induces a change in the conformation of such brushes. They are thus called pH-responsive.

When grafted onto compliant structures, the change in the swelling state of the brush translates into a change in the surface stress of the structure. This has been studied for uncharged polymer brushes upon changing the solvent/non-solvent mixing ratio [12, 32] and for PEL brushes upon changing the pH or the ionic strength of the solvent [11, 12, 44] or upon applying a bias on the cantilever [35, 45]. Two deflection stages were observed for all experiments dealing with uncharged polymers. When the brush collapses, it induces a compressive surface stress on the cantilever and when it swells, the stress is released. In the case of polyacid brushes, two or three deflection stages were distinguished. For example, for experiments in which the pH of the solvent is changed, either the authors only observed a continuous bending of the cantilever when increasing the pH or they monitored a first bending, then a plateau and finally a second bending in the opposite direction. This latter case is schematized on Figure 4.6. At low pH (acidic conditions), the brush

is collapsed which generates a compressive surface stress because the footprint of each polymer chain is too small to accommodate this state and the cantilever bends. Then for intermediate pH values, the polymer chains begin to swell and the stress is released. At high pH (basic conditions), the chains are fully deprotonated and the electrostatic repulsion between the chains produces again a high compressive stress. This behavior was observed for poly(methacryloyl ethylene phosphate) (poly(MEP)) brushes by Huck et al [46]. The phosphate side groups have two dissociation constants (one between RH_2PO_3 and $RHPO_3^-$ and one between $RHPO^-$ and RPO_3^{2-}). So at high pH, each side groups bears two negative charges which explains the large observed deflection.

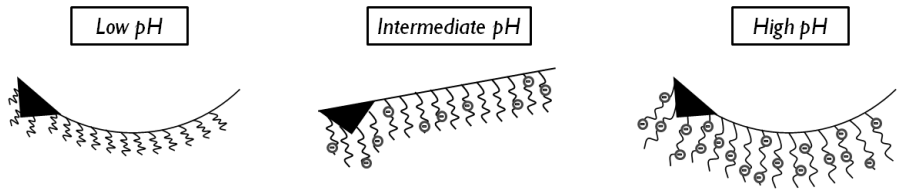

Figure 4.6: When polyacid brushes are grafted onto compliant structures, three deflection stages can be observed: at low pH, the brush is collapsed and the cantilever bends due to compressive surface stress (left); at intermediate pH, the brush begins to swell and the stress is released (center); at high pH, the electrostatic forces between the chains once again produce a compressive stress (right).

In this study, the deflection behavior of an AFM cantilever grafted with a poly(MES) brush will be studied. This polymer bears carboxylic acid functional groups which have only one dissociation constant.

4.2.3 Click Chemistry

By observing how Nature synthesizes its basic chemical compounds (such as polysacharrides, polynucleotides, polypeptides,...), Sharpless et al.

proposed a new chemical philosophy which tends to simplify organic chemistry (in the field of drug discovery for example) by linking small units together via heteroatom bond formation (C–X–C) instead of building tough C–C bonds [47]. They argued that: "all searches must be restricted to molecules that are easy to make". They thus proposed a concept that they called "Click Chemistry". The "click" reactions must:

- be modular,
- be wide in scope,
- give very high yields,
- generate only inoffensive byproducts that can be removed by non-chromatographic methods,
- be stereospecific,
- yield stable products under physiological conditions.

The required process characteristics include:

- simple reaction conditions (ideally it should be insensitive to oxygen and water),
- readily available starting materials and reagents,
- the use of no solvent or of a solvent that is benign (such as water) or easily removed,
- simple product isolation by nonchromatographic methods.

Among the different reactions identified by Sharpless, the Huisgen 1,3-dipolar cycloaddition was promising. Indeed, it can be applied to

alkynes and azides which are very stable under different conditions and can easily be introduced into molecules. The products obtained with Huisgen 1,3-dipolar cycloaddition of azides and alkynes are presented in Figure 4.7. Both 1,4- and 1,5-regioisomers of the 1,2,3-triazole are obtained in a 1:1 ratio for the majority of alkynes.

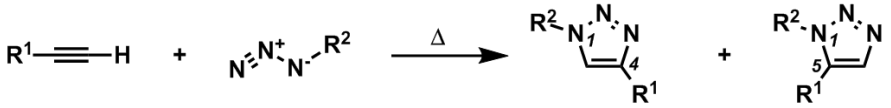

Figure 4.7: The thermal Huisgen 1,3-dipolar cycloaddition of azides and alkynes usually affords mixtures of the 1,4- and 1,5-regioisomers.

However, due to their high kinetic stability, the cycloaddition of azides and alkynes is relatively slow and requires elevated temperatures. Nevertheless, the Sharpless and Meldal groups continued to investigate ways to accelerate this reaction and in 2002, they simultaneously and independently discovered the Cu^{I}-catalyzed alkyne-azide coupling [48, 49]. This copper catalysis exclusively provides the 1,4-regioisomer with high yields at a (up to) 10^7-fold higher rate and is compatible with lots of different functional groups [50]. This is thus one of the best click reactions. Its catalytic cycle is still under debate but Figure 4.8 shows one likely mechanism [51, 52].

It is generally accepted that this reaction is stepwise and starts with the formation of Cu^{I} acetylides via the deprotonation of π-complex **1**. Kinetic studies show that different Cu^{I} acetylides might coexist in solution but their exact nature is not known with certainty [53]. However, there are indications that they require two metal centers, one or two alkyne ligands and other labile ligands that allow for competitive azide binding. The first copper atom is linked to the alkyne moiety while the second one seems to activate the azide as in **2**. Then, cyclization occurs by nucleophilic attack of acetylide carbon C4 at N3 of the activated

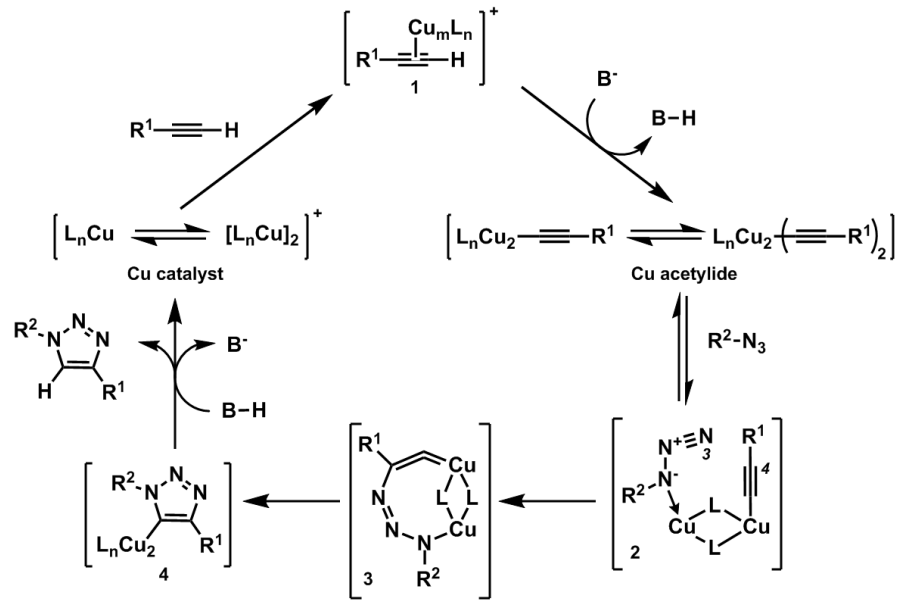

Figure 4.8: Proposed mechanism for the Cu^{I}-catalyzed alkyne-azide cycloaddition (adapted from refs [51] and [52]).

azide. This was shown to be the rate-determining step [52]. In the next step, ring contraction follows to give the triazole-copper derivative **4**. Finally, the protonation of this derivative is followed by the dissociation of the product and the regeneration of the catalyst.

This reaction is sometimes referred to as the Cu^{I}-catalyzed Huisgen 1,3-dipolar cycloaddition but as we have just seen from the mechanism, it is not formally a 1,3-dipolar cycloaddition. That is why some authors prefer using the name Cu^{I}-catalyzed azide-alkyne cycloaddition (CuAAC).

There have been numerous reports of CuAAC reactions performed on silicon surfaces. Both alkyne and azide moieties can be grafted on the surface depending on whether the molecules to be clicked are more

easily functionalized with one or the other. The most common route is to silanize the surfaces with a brominated silane and to proceed to the nucleophilic displacement (S_N2) of these bromine atoms with azides by immersion in a saturated NaN_3 solution in DMF for periods up to 72 h [54, 55]. But this is only one of the multiple methods to yield clickable surfaces. For example, the silanization step can be avoided and replaced by the grafting of azidated or alkylated molecules bearing double or triple bonds on passivated silicon surfaces [56]. Such clickable surfaces can have applications in biological arrays [57], catalysis [58], biosensors [59, 60], drug delivery [61], molecular motors [62], optical filters [63], microfluidic devices [64], surface engineering [65–68], material engineering [69–71], etc.

4.3 Results and Discussion

In this section are presented the results concerning the pH and the chemical sensors, both based on the deflection of flexible AFM cantilevers grafted with polymer brushes. The temperature and the volume of the solution inside the liquid cell of the AFM were kept constant during all experiments to avoid drifts in the deflection curves. More information concerning this fact as well as details on the materials and methods involved in this part are given in the Experimental Part (sections 6.1.4 and 6.2.4 on pages 194 and 204).

4.3.1 pH Sensor Based on PEL Brushes

Figure 4.9 shows the results obtained for the deflection measurements of an AFM cantilever grafted with a 80 nm-thick pH-responsive polymer brush when dipped into different buffer solutions. Both the pH and the

ionic strength of the solutions play a role in the response of the polymer. Here, the ionic strength was fixed at 200 mM so that the pH was the only influential parameter.

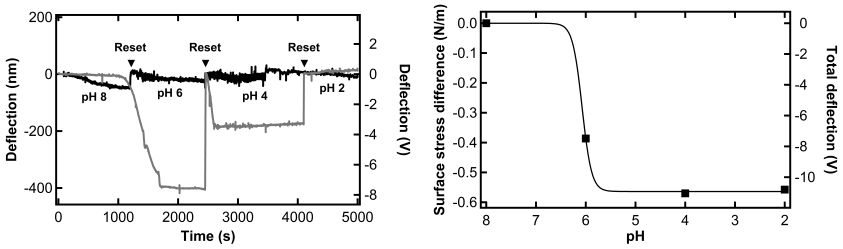

(1) Deflection

(2) Surface stress difference $\Delta\sigma$

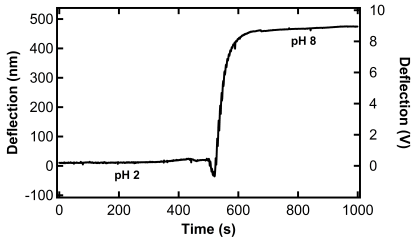

(3) Reversibility

Figure 4.9: Deflection measurements (top left) and corresponding surface stress difference (top right) for a bare cantilever (black line) and a cantilever grafted with a poly(MES) brush (gray line) when dipped in buffer solutions of different pH. The bottom graph shows the reversibility of the phenomenon.

The top-left graph in Figure 4.9 compares the variations in the deflection of a bare (black line) and of a grafted lever (gray line) in different buffer solutions ranging from pH 8 to pH 2. The laser was re-centered on the position sensitive detector (PSD) between each solution change in order to reset the deflection to zero to have the most linear signal possible. For our PSD, the linear region is comprised between ca. -4 V and +4 V (which roughly corresponds to deflection values in the range [-200;200] nm). Outside this range, the relation between the signal from the PSD and the actual deflection is no more linear. It can be seen that

the signal obtained for the bare lever is noisy but anyway that its deflection is very small in comparison to the one of the grafted lever. For that lever, a sharp decrease of the deflection value was observed when going from pH 8 to pH 6. This means that the lever was subject to a compressive stress at pH 8 due to electrostatic interactions in the brush and that this stress was partially released by lowering the pH to 6. Then the deflection continued to decrease between pH 6 and 4 but to a smaller extent and finally, it reached a plateau between pH 4 and 2. So here, only two deflection stages were observed as opposed to [11]. It seems that here, the collapsed brush at low pH does not induce a sufficient force to bend the lever.

On the top-right graph in Figure 4.9, the measured deflection values were translated into surface stress differences thanks to the Atkinson equation (4.10). For even more accurate values, it would have been necessary to measure the wet thickness of the brush in each buffer solution. As surface stress is equivalent to surface tension for liquids, these values can be compared with the surface tension of water for instance. The surface stress difference that was observed for the grafted lever between pH 8 and pH 2 (ca. 600 mN/m) is one order of magnitude higher than the surface tension of water (72 mN/m) [72]. So the stresses at play are relatively high.

Finally, the reversibility of the deflection was tested. The pH of the solution was changed from pH 2 to pH 8. The results are given on the bottom graph in Figure 4.9. This time, the deflection value of the cantilever increased, meaning that the cantilever bent towards its initial deflection state as the brush became deprotonated. The initial deflection value was not fully recovered because the signal approached its saturation value (10 V).

4.3.2 Chemical Sensor Based on Reactive Brushes

In a second experiment, the kinetics of a "click" reaction between azidated brushes and propargyl-sulforhodamine (9) in solution was measured. Cantilevers were prepared as follows: they were grafted with poly(HEMA) brushes which were subsequently activated with N,N'-Disuccinimidyl carbonate (DSC) and 4-(Dimethylamino)pyridine (DMAP) before being reacted with 2-azidoethylamine. XPS measurements (cf. section 6.3.3 on page 219) were performed after each reaction step and the spectra are displayed on Figure 4.10.

The poly(HEMA) brush is essentially constituted of C, O and H. The C_{1s} core-level spectrum (Figure 4.10(1)) shows the presence of three components having binding energies at about 284.8, 286 and 288.4 eV, corresponding to $\underline{C}$–C, C–O and O=$\underline{C}$–O carbons, respectively. Their relative intensity is 3:2.3:1 and is fairly close to the 3:2:1 theoretical ratio. During the activation, two different reactions can arise depending on the activating species that reacts with the brush (Figure 4.10(2)). A new peak appears on the C_{1s} spectrum for the activated brush at 290.3 eV (Figure 4.10(3)), corresponding to the O=$\underline{C}$–O_2 carbon from DSC or to the O=$\underline{C}$–ON^+ carbon from DMAP. The relative amounts of each activating species in the brush can be estimated by interpreting the N_{1s} spectrum (Figure 4.10(3)). Two components are present with binding energies of around 399.8 and 401.6 eV which correspond to $\underline{N}$–C and N^+. The ratio of their intensities is 1:6.1. DSC and DMAP contribute for 1 N each to the peak at higher energies (considering that the N from the imide function of DSC is nearly positively charged) while only 1 N from DMAP contributes to the other peak. This yields to an overall DSC/DMAP ratio of 5:1. After the coupling with azidoethylamine (AEA), the characteristic peak from DSC and DMAP at 290.3 eV disappears from the C_{1s} spectrum (Figure 4.10(5)) while the peak at 286 eV increases and the peak at 284.8 eV decreases. This has two meanings: first, the ac-

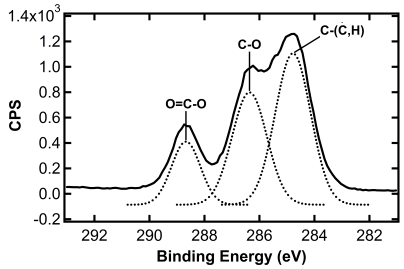

(1) Poly(HEMA) brush (C_{1s} peak)

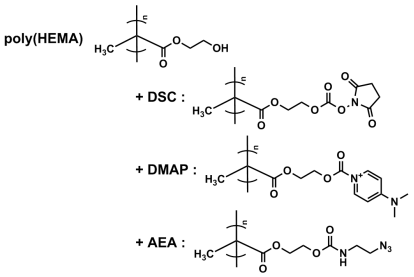

(2) Molecules and reaction pathways

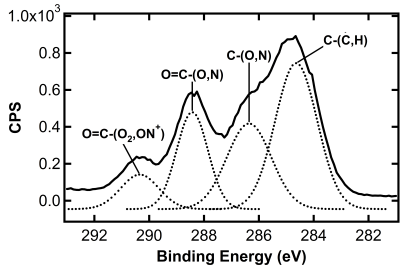

(3) Activated brush (C_{1s} peak)

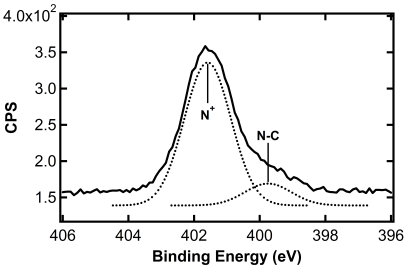

(4) Activated brush (N_{1s} peak)

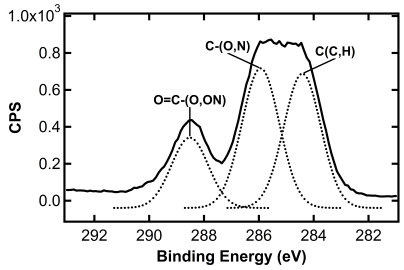

(5) Azido-brush (C_{1s} peak)

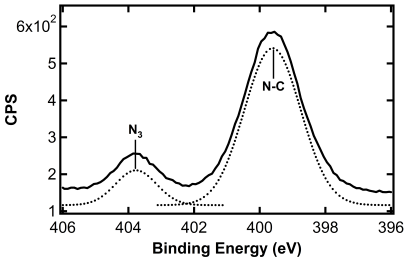

(6) Azido-brush (N_{1s} peak)

Figure 4.10: XPS measurements for the intermediate steps leading to azido-modified brushes. Top: C_{1s} peak for the initial poly(HEMA) brush (left) and presentation of the molecules and the reaction pathways (right); middle: C_{1s} (left) and N_{1s} (right) peaks for the activated poly(HEMA) brush with DSC and DMAP; bottom: C_{1s} (left) and N_{1s} (right) peaks for the final azido-brush.

tivating species seem to be completely removed from the brush during the reaction and second, there is a relative increase of the C–N carbons

attesting for the incorporation of azidoethylamine in the brush. This is fully confirmed by the N_{1s} spectrum where, on the one hand, the N^+ peak has disappeared meaning that the activating moieties from DMAP and DSC were fully removed and, on the other hand, another peak shifted to higher binding energies (around 403.8 eV) has appeared coming from N_3 functions incorporated in the brush [62, 64, 68, 70, 71].

The reaction between surface-confined azido functions and propargyl-sulforhodamine (9) in solution was then characterized in the presence of a copper complex in solution. Therefore, the emission spectrum of a sample was measured with a Front-Face Fluorimeter (cf. section 6.3.7 on page 234) after the reaction with propargyl-sulforhodamine (9) (Figure 4.11).

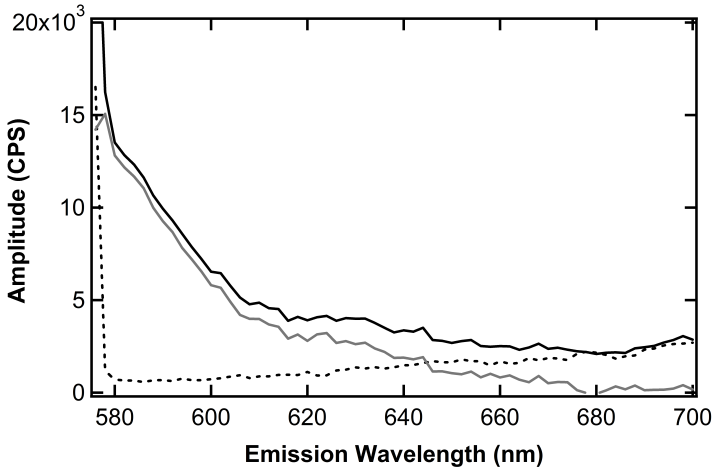

Figure 4.11: Front-Face Fluorimetry spectrum obtained for an azido-brush clicked with propargyl-sulforhodamine (9) (black line) and comparison with the spectrum of a bare substrate (dashed line). The gray line is the difference between these two curves. The excitation wavelength was 566 nm.

In this figure, the emission spectra from the aforementioned sample (continuous black line) and from a bare substrate (interrupted line) are

compared. No signal is measured on the bare substrate while a broad peak is observed for the grafted samples. This proves the successful grafting of propargyl-sulforhodamine (9) in the brushes.

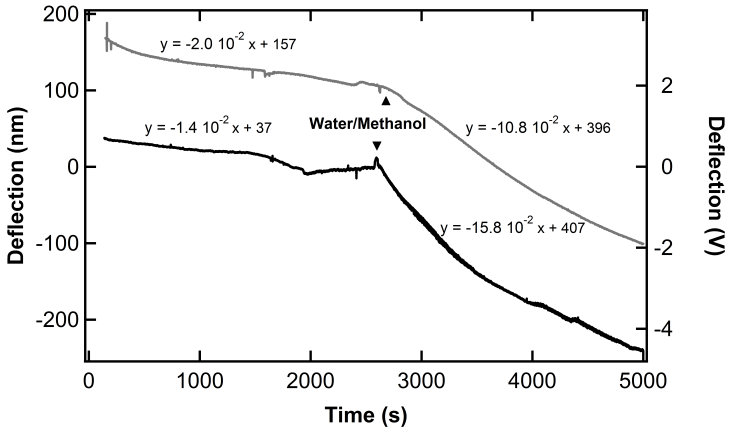

Figure 4.12: Deflection measurements for a bare cantilever (black line) and for a lever grafted with an azido-brush (gray line) when dipped in a saturated propargyl-sulforhodamine (9) solution containing copper complexes. The black triangles indicate the replacement of the reactive solution with the pure solvent (H_2O/MeOH 1:1).

Figure 4.12 presents the deflection measurements for a bare cantilever (black line) and for a lever grafted with an azido-modified poly(HEMA) brush when immersed in a saturated propargyl-sulforhodamine (9) solution containing copper complexes. At the initiation of the experiment, the reactive solution was injected in the liquid cell of the AFM and the deflection signal was recorded. Then, after around 2600 s (as indicated by the black triangles), the reactive solution was replaced with the pure solvent in order to remove the propargyl-sulforhodamine molecules that were not covalently grafted.

Only a very small difference between the two levers is observed. In the reactive solution, the slope of the curve for the grafted lever is slightly

steeper than the one for the bare lever ($-2.0 \cdot 10^{-2}$ vs $-1.4 \cdot 10^{-2}$ nm/s). When this solution is replaced with the solvent, the opposite phenomenon is observed as the adsorbed alkyne molecules are rinsed away from the cantilevers ($-10.8 \cdot 10^{-2}$ vs $-15.8 \cdot 10^{-2}$ nm/s). As the slope is steeper for the bare cantilever, it can be suggested that the molecules are more easily removed from it than from the grafted one. It would mean that the molecules that were only adsorbed on the levers or absorbed in the brush are removed while some covalently grafted molecules still remain inside the brush. But, as the difference between the two curves is very small, these results should be interpreted carefully.

The weak difference between the bare and the grafted cantilever could be due to the low penetration depth of the sulforhodamine molecules inside the brush. Indeed, these molecules are quite large and it is not sterically favorable for them to enter the brush. If they only react with the outer surface of the brush, their impact on the surface stress is highly limited. It could also be due to the sensitivity of the system. When the whole brush undergoes a transition, the system responds well. But when a small change happens, the surface stress is only slightly affected and the deflection signal cannot clearly overtake the dynamic noise coming from the environment.

To solve this issue, a softer cantilever could be used to improve the sensitivity of the detection. Moreover, while brushes offer a convenient way to increase the amount of reactive sites per unit surface area, they should not be too thick nor too dense. Indeed, if the brush is too thick, molecules that will interact with the top part of the brush will not influence the surface stress on the lever and will further impede the diffusion of other molecules towards the bottom of the brush. If the brush is too dense, molecules in solution will only see the reactive sites that are at the surface of the brush and the benefit of having a brush instead of a SAM will be lost. The density and the thickness of the brushes could

then be optimized as a function of the size of the reactive molecules to detect. Finally, other kinds of reactions that could enhance the signal could be tested, for example, a reaction which detaches some polymer chains from the brush as proposed in [73].

4.4 Conclusion

In this chapter, it was shown that an AFM cantilever with a polymer brush grafted on one side can be used as a sensor to detect some changes in the environment by measuring its deflection due to differential variation of surface stress.

First, in the case of pH-responsive polymer brushes, the deflection decreased when lowering the pH of the solution from 8 to 2. The final observed deflection was around 600 nm which corresponds to a surface stress difference of around 600 mN/m. In this experiment, only two stages were observed: at high pH, the brush is fully deprotonated and the cantilever bends to accommodate the compressive stress coming from the electrostatic forces between the polymer chains. When the pH is decreased, this stress is released and the cantilever recovers its original state. This phenomenon was reversible.

In a second set of experiments, a reactive polymer brush was grafted on these levers and functionalized with azidoethylamine to have N_3 end-groups. XPS measurements proved the successful azidation of the brushes. However, when the cantilever was immersed in a reactive solution containing the alkyne molecules, the deflection signal was not very different from the signal coming from a bare cantilever in the same conditions. This could be due to the fact that the penetration depth of the reactive molecules inside the brush was too low. This could be solved by using

smaller molecules or by decreasing both the thickness and the grafting density of the brush. For the kind of molecules that were presented here, it is believed that a 50% more diluted brush with a thickness of around 10 nm would give a satisfactory sensitivity.

References

[1] Nezhadian, S. K.; Rezazadeh, G.; Arya, S. K. *Sensors and Transducers Journal* **2007**, *84*, 1660–1668.

[2] Gimzewski, J. K.; Gerber, C.; Meyer, E.; Schlittler, R. R. *Chem. Phys. Lett.* **1994**, *217*, 589–594.

[3] Berger, R.; Gerber, C.; Gimzewski, J. K.; Meyer, E.; Guntherodt, H. J. *Appl. Phys. Lett.* **1996**, *69*, 40–42.

[4] Jung, M.-Y.; Kim, D.-W.; Choi, S. S.; Kang, C. J.; Kuk, Y. *Jpn. J. Appl. Phys.* **1999**, *38*, 6555–6557.

[5] Barnes, J. R.; Stephenson, R. J.; Welland, M. E.; Gerber, C.; Gimzewski, J. K. *Nature* **1994**, *372*, 79–81.

[6] Li, G.; Burggraf, L. W.; Baker, W. P. *Appl. Phys. Lett.* **2000**, *76*, 1122–1124.

[7] Krecmer, P.; Moulin, A. M.; Stephenson, R. J.; Rayment, T.; Welland, M. E.; Elliott, S. R. *Science* **1997**, *277*, 1799–1802.

[8] Ibach, H. *J. Vac. Sci. Technol., A* **1994**, *12*, 2240–2245.

[9] Berger, R.; Delamarche, E.; Lang, H. P.; Gerber, C.; Gimzewski, J. K.; Meyer, E.; Guntherodt, H.-J. *Science* **1997**, *276*, 2021–2024.

[10] Vidic, A.; Then, D.; Ziegler, C. *Ultramicroscopy* **2003**, *97*, 407–416.

[11] Zhou, F.; Shu, W.; Welland, M. E.; Huck, W. T. S. *J. Am. Chem. Soc.* **2006**, *128*, 5326–5327.

[12] Abu-Lail, N. I.; Kaholek, M.; LaMattina, B.; Clark, R. L.; Zauscher, S. *Sens. Actuators, B* **2006**, *114*, 371–378.

[13] Yan, X.; Ji, H.-F.; Lvov, Y. *Chem. Phys. Lett.* **2004**, *396*, 34–37.

[14] Raiteri, R.; Grattarola, M.; Berger, R. *Materials Today* **2002**, *5*, 22–29.

[15] Frometa, R., N. *Biotecnologica Aplicada* **2006**, *23*, 320–323.

[16] Moulin, A. M.; O'Shea, S. J.; Welland, M. E. *Ultramicroscopy* **2000**, *82*, 23–31.

[17] Baller, M. K.; Lang, H. P.; Fritz, J.; Gerber, C.; Gimzewski, J. K.; Drechsler, U.; Rothuizen, H.; Despont, M.; Vettiger, P.; Battiston, F. M.; Ramseyer, J. P.; Fornaro, P.; Meyer, E.; Guntherodt, H. J. *Ultramicroscopy* **2000**, *82*, 1–9.

[18] Betts, T. A.; Tipple, C. A.; Sepaniak, M. J.; Datskos, P. G. *Anal. Chim. Acta* **2000**, *422*, 89–99.

[19] Stoney, G. G. *Proc. R. Soc. London, A* **1909**, *82*, 172–175.

[20] Janssen, G. C. A. M.; Abdalla, M. M.; van Keulen, F.; Pujada, B. R.; van Venrooy, B. *Thin Solid Films* **2009**, *517*, 1858–1867.

[21] Gere, J. M.; Timoshenko, S. *Mechanics of Materials*; PWS Publishing Company: New-York, 1997.

[22] Chen, G. Y.; Thundat, T.; Wachter, E. A.; Warmack, R. J. *J. Appl. Phys.* **1995**, *77*, 3618–3622.

[23] Godin, M.; Tabard-Cossa, V.; Grutter, P.; Williams, P. *Appl. Phys. Lett.* **2001**, *79*, 551–553.

[24] Lang, H.; Hegner, M.; Gerber, C. Nanomechanical Cantilever Array Sensors. In *Springer Handbook of Nanotechnology*; Bhushan, B., Ed.; Springer Berlin Heidelberg, 2007; pp 443–460.

[25] Itoh, T.; Suga, T. *Appl. Phys. Lett.* **1994**, *64*, 37–39.

[26] Lee, C.; Itoh, T.; Ohashi, T.; Maeda, R.; Suga, T. *J. Vac. Sci. Technol., B* **1997**, *15*, 1559–1563.

[27] Goddenhenrich, T.; Lemke, H.; Hartmann, U.; Heiden, C. *J. Vac. Sci. Technol., A* **1990**, *8*, 383–387.

[28] Schonenberger, C.; Alvarado, S. F. *Rev. Sci. Instrum.* **1989**, *60*, 3131–3134.

[29] Meyer, G.; Amer, N. M. *Appl. Phys. Lett.* **1988**, *53*, 2400–2402.

[30] Klein, C. A. *J. Appl. Phys.* **2000**, *88*, 5487–5489.

[31] Atkinson, A. Generation and relief of stress in ceramic films. In *Ceramic Films and Coatings*; Lee, W., Ed.; Institute of Materials, Minerals and Mining, 1995; p 1.

[32] Bumbu, G.-G.; Wolkenhauer, M.; Kircher, G.; Gutmann, J. S.; Berger, R. *Langmuir* **2007**, *23*, 2203–2207.

[33] Cherian, S.; Mehta, A.; Thundat, T. *Langmuir* **2002**, *18*, 6935–6939.

[34] Cherian, S.; Thundat, T. *Appl. Phys. Lett.* **2002**, *80*, 2219.

[35] Zhou, F.; Biesheuvel, P. M.; Choi, E. Y.; Shu, W.; Poetes, R.; Steiner, U.; Huck, W. T. *Nano Lett.* **2008**, *8*, 725–730.

[36] Utz, M.; Begley, M. R. *J. Mech. Phys. Solids* **2008**, *56*, 801–814.

[37] Minko, S. *J. Macromol. Sci., Polym. Rev.* **2006**, *46*, 397–420.

[38] Gong, P.; Genzer, J.; Szleifer, I. *Phys. Rev. Lett.* **2007**, *98*, 018302.

[39] Laloyaux, X.; Mathy, B.; Nysten, B.; Jonas, A. M. *Macromolecules* **2010**, *43*, 7744–7751.

[40] Lyatskaya, Y. V.; Leermakers, F. A. M.; Fleer, G. J.; Zhulina, E. B.; Birshtein, T. M. *Macromolecules* **1995**, *28*, 3562–3569.

[41] Zhulina, E. B.; Birshtein, T. M.; Borisov, O. V. *Macromolecules* **1995**, *28*, 1491–1499.

[42] Zhulina, E. B.; Borisov, O. V. *Macromolecules* **1996**, *29*, 2618–2626.

[43] Zhulina, E. B.; Birshtein, T. M.; Borisov, O. V. *Eur. Phys. J. E* **2006**, *20*, 243–256.

[44] Kelby, T. S.; Huck, W. T. S. *Macromolecules* **2010**, *43*, 5382–5386.

[45] Huck, W. T. S. *Materials Today* **2008**, *11*, 24–32.

[46] Zhou, F.; Huck, W. T. S. *Chem. Commun.* **2005**, *2005*, 5999–6001.

[47] Kolb, H. C.; Finn, M. G.; Sharpless, K. B. *Angew. Chem., Int. Ed.* **2001**, *40*, 2004–2021.

[48] Tornoe, C. W.; Christensen, C.; Meldal, M. *J. Org. Chem.* **2002**, *67*, 3057–3064.

[49] Rostovtsev, V. V.; Green, L. G.; Fokin, V. V.; Sharpless, K. B. *Angew. Chem., Int. Ed.* **2002**, *41*, 2596–2599.

[50] Appukkuttan, P.; Dehaen, W.; Fokin, V. V.; Van der Eycken, E. *Org. Lett.* **2004**, *6*, 4223–4225.

[51] Bock, V. D.; Henk, H.; van Maarseveen, J. H. *Eur. J. Org. Chem.* **2006**, *2006*, 51–68.

[52] Sun, S.; Wu, P. *J. Phys. Chem. A* **2010**, *114*, 8331–8336.

[53] Rodionov, V. O.; Fokin, V. V.; Finn, M. G. *Angew. Chem., Int. Ed.* **2005**, *44*, 2210–2215.

[54] Fryxell, G. E.; Rieke, P. C.; Wood, L. L.; Engelhard, M. H.; Williford, R. E.; Graff, G. L.; Campbell, A. A.; Wiacek, R. J.; Lee, L.; Halverson, A. *Langmuir* **1996**, *12*, 5064–5075.

[55] Marrani, A. G.; Dalchiele, E. A.; Zanoni, R.; Decker, F.; Cattaruzza, F.; Bonifazi, D.; Prato, M. *Electrochim. Acta* **2008**, *53*, 3903–3909.

[56] Ciampi, S.; Bocking, T.; Kilian, K. A.; James, M.; Harper, J. B.; Gooding, J. J. *Langmuir* **2007**, *23*, 9320–9329.

[57] Rozkiewicz, D. I.; Janczewski, D.; Verboom, W.; Ravoo, B. J.; Reinhoudt, D. N. *Angew. Chem., Int. Ed.* **2006**, *45*, 5292–5296.

[58] Haensch, C.; Ott, C.; Hoeppener, S.; Schubert, U. S. *Langmuir* **2008**, *24*, 10222–10227.

[59] Ciampi, S.; LeÂăSaux, G.; Harper, J.; Gooding, J. J. *Electroanalysis* **2008**, *20*, 1513–1519.

[60] Qing, G.; Xiong, H.; Seela, F.; Sun, T. *J. Am. Chem. Soc.* **2010**, *132*, 15228–15232.

[61] Britcher, L.; Barnes, T. J.; Griesser, H. J.; Prestidge, C. A. *Langmuir* **2008**, *24*, 7625–7627.

[62] London, G.; Carroll, G. T.; Fernandez Landaluce, T.; Pollard, M. M.; Rudolf, P.; Feringa, B. L. *Chem. Commun.* **2009**, 1712–1714.

[63] Ciampi, S.; Bocking, T.; Kilian, K. A.; Harper, J. B.; Gooding, J. J. *Langmuir* **2008**, *24*, 5888–5892.

[64] Prakash, S.; Long, T. M.; Selby, J. C.; Moore, J. S.; Shannon, M. A. *Anal. Chem.* **2006**, *79*, 1661–1667.

[65] Lummerstorfer, T.; Hoffmann, H. *J. Phys. Chem. B* **2004**, *108*, 3963–3966.

[66] Ostaci, R.-V.; Damiron, D.; Capponi, S.; Vignaud, G.; Leger, L.; Grohens, Y.; Drockenmuller, E. *Langmuir* **2008**, *24*, 2732–2739.

[67] Gassensmith, J. J.; Erne, P. M.; Paxton, W. F.; Valente, C.; Stoddart, J. F. *Langmuir* **2010**, *27*, 1341–1345.

[68] Haensch, C.; Hoeppener, S.; Schubert, U. S. *Nanotechnology* **2008**, *19*, 035703.

[69] Oguchi, K.; Nagao, M.; Umeyama, H.; Katayama, T.; Yamashita, Y.; Mukai, K.; Yoshinobu, J.; Akagi, K.; Tsuneyuki, S. *J. Am. Chem. Soc.* **2007**, *129*, 1242–1245.

[70] Daugaard, A. E.; Hvilsted, S.; Hansen, T. S.; Larsen, N. B. *Macromolecules* **2008**, *41*, 4321–4327.

[71] Chen, R. T.; Muir, B. W.; Such, G. K.; Postma, A.; Evans, R. A.; Pereira, S. M.; McLean, K. M.; Caruso, F. *Langmuir* **2009**, *26*, 3388–3393.

[72] Lange, N. A.; Dean, J. A. *Lange's Handbook of chemistry*; McGraw-Hill: New York, 1973.

[73] Liu, J.; Yang, W.; Zareie, H. M.; Gooding, J. J.; Davis, T. P. *Macromolecules* **2009**, *42*, 2931–2939.

Chapter 5

Local Catalysis of "Click" Reactions with Functionalized AFM Probes

5.1 Introduction

In this chapter, the second objective of the thesis, i.e. the local catalysis of a chemical reaction with functionalized AFM tips, will be pursued. The reaction that will be catalyzed is a reaction from the "click" chemistry: the Cu^{I}-Catalyzed Azide-Alkyne Cycloaddition (CuAAC). It was chosen because it is a quick reaction whose kinetics is effectively increased by the copper catalyst and because it leads to very high yields without byproducts. Moreover, azide or alkyne functionalities can easily be introduced in many molecules of interest or grafted on surfaces.

To reach this goal, the idea was to functionalize a surface with an azidated monolayer, to immerse it in a reactive solution containing the molecules with the alkyne moiety and to scan an AFM tip bearing Cu complexes at specific locations on the surface to locally catalyze the reaction according to a predetermined pattern (Figure 5.1).

In the next section, some concepts will be developed from a theoretical point of view. Several existing lithography techniques and more particularly scanning probe lithography techniques will be listed before defining the notion of (local) catalysis[1]. Then, some interesting results will be highlighted about, first, the preparation of the substrates, the functionalization of the AFM tips and the characterization of the click reaction and, second, the local catalysis experiments in themselves. Finally, a few conclusions will be drawn.

[1]The concept of "click" chemistry was introduced in the previous chapter (Section 4.2.3 on page 119) and will not be rediscussed here.

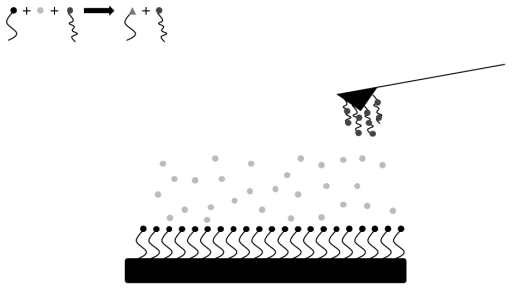

(1) Initial stage

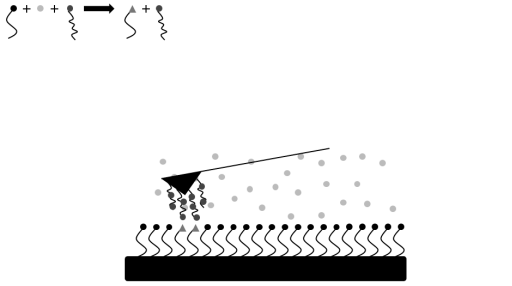

(2) Catalysis at a specified location on the surface

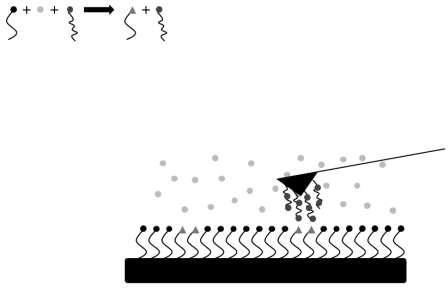

(3) Catalysis at another location

Figure 5.1: When an AFM tip bearing catalytic complexes is scanned along a predetermined pattern, it locally catalyzes the reaction between molecules in solution and molecules on the substrate.

5.2 Theoretical Aspects

5.2.1 Nanopatterning Techniques

Generalities

Interest for the miniaturization of devices has dramatically increased these past years. Nowadays, nanotechnology is present in the everyday life, mostly in microelectronics, for the fabrication of integrated circuits, memories, display units, sensors, processors, etc [1]. The challenge of this emerging technology is to build functional units that have typical sizes of less than 100 nm. It is usually considered that two approaches exist for the fabrication of such nanostructures: the top-down approach and the bottom-up approach. The top-down approach starts from a bulk material which is nanopatterned thanks to different lithography techniques while the bottom-up approach starts from molecules or clusters whose interaction and self-assembly lead to the desired nanostructures. The most widely used techniques in the industry are based on the top-down approach. For example, photolithography consists of irradiating a polymer film through a mask with a UV beam to modify its structure in order to obtain a replica of the mask (positive or negative) after a revealing step [2, 3] (Figure 5.2(1)). The resolution of this technique is ca. 100 nm. For better resolutions (but lower throughputs and higher costs), the UV beam can advantageously be replaced with a scanning electron or ion beam. These techniques are thus called Electron Beam Lithography (EBL) [4, 5] or Focused Ion Beam (FIB) [6, 7]. The resolution reaches 20 nm for EBL and 5 nm for FIB. Apart from these conventional techniques, newer methods have been developed in a purpose to achieve a better time/cost efficiency. Among them, the Nano-Imprint Lithography can be cited [8–10]. It consists of controllably pressing a hard mold in a resist upon heating or UV irradiating to induce the transfer of the pat-

tern (Figure 5.2(2)). In a similar fashion, Soft Lithography techniques [11, 12] have emerged. The best-known example is the Microcontact Printing (μCP) [13, 14]. These techniques are easier to undertake but usually lead to lower lateral resolutions. They consist of pressing a previously inked elastomeric stamp on a solid substrate to transfer molecules from the protrusions of the mold to the surface (Figure 5.2(3)). Finally, Scanning Probe Lithography (SPL) techniques offer new possibilities and are of great interest in many applications [15, 16]. These techniques take advantage of the scanning capabilities of the microscope, of the very small radius of curvature of the probes and of the strong interactions between this tip and the surface to achieve high resolution patterns on a wide range of substrates. Moreover, the resulting patterns can be directly imaged by the same SPM probe which is a great benefit. The next section will give some examples of SPL techniques.

Scanning Probe Lithography Techniques

Since the discovery of the STM [17, 18] and more recently of the AFM by Binnig et al. [19], these scanning probe microscopies have not only been used for imaging or sensing applications (as seen in previous chapters) but they opened the way to a completely new set of lithography techniques. In this section, a rapid review of STM-based techniques will be given before going into more details about AFM-based ones.

STM has been used to manipulate individual atoms. For instance, Crommie et al. constructed circular quantum corrals by individually positioning iron adatoms on a Cu surface with a STM tip [20]. A famous paper by Manoharan et al. [21] reported the apparition of a "quantum mirage" at the empty focus when they placed a single Co atom at one focal point of an elliptical quantum corral. Gaseous and organic molecules can also be manipulated by an STM tip. Heinrich et al. arranged CO mo-

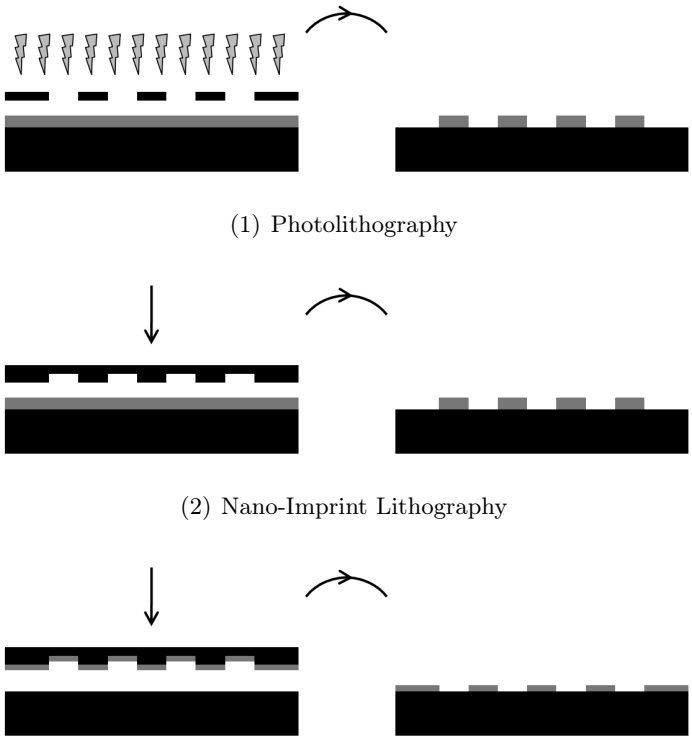

(1) Photolithography

(2) Nano-Imprint Lithography

(3) Microcontact Printing

Figure 5.2: Some conventional lithography techniques.

lecules in an atomically precise position to study the domino-like motion of these molecules as a function of temperature [22]. In addition, STM nanomanipulation was used to initiate some chemical reaction by moving reactive molecules close to each other and/or by exchanging electrons with these molecules. For instance, it was possible to form individual covalent bonds between Fe and O atoms on a surface by electron injection through an STM tip [23]. Multi-step reactions have also been reported where two C_5H_5I molecules were reacted together to from one $C_{12}H_{10}$ molecule [24]. Finally, it was also possible to perform STM-based nanolithography by, for instance, emitting an electron beam [25] or voltage

pulses [26, 27] on a surface while scanning.

All these STM-based techniques are very powerful but have nevertheless some flaws. For instance, they are time consuming, they often require high vacuum and/or low temperatures which increases the operating costs and they can only be used on conductive surfaces. That is why some authors turned to AFM-based techniques. Indeed, these techniques can be used in air or in liquids at room temperature and can be used to pattern organic and biological molecules on nearly all kinds of substrates. Although by nature they are operated in serial processes, parallel patterning can be achieved by using cantilever arrays [28, 29].

Lots of AFM nanolithography techniques have been developed in the last 20 years. They can be divided into two main groups: techniques involving electron transfer between the tip and the surface and techniques involving mechanical interactions. Many reviews are available in the literature [1, 30–33]. That is why only some examples of both series of techniques are listed below:

1. Bias-assisted AFM nanolithography

    - Scanning Probe Oxidation: In this method, the localized electric field produced by the negatively-biased tip dissociates the water meniscus present between the tip and the surface in OH^- and H^+ leading to the local oxidation of the underlying substrate [34, 35]. This substrate can be a semiconductor such as Si [36–38] or SiC [39, 40] or a metal [41, 42]. It can also be covered with an organic coating used as a mask for a subsequent wet etching of the formed oxide [43, 44] or for another self-assembly of molecules [45, 46]. If the water meniscus is replaced with an organic solvent, other electrochemical reactions can take place. For example, it can lead to the formation of carbonaceous species [47, 48].

- Field-Induced Evaporation: Here, the application of bias or voltage pulses on a gold-coated cantilever leads to the field evaporation of gold from the tip and its deposition on the substrate in the form of dots [49–51] or lines [52]
- Electrochemical Dip Pen Nanolithography (EDPN): This is the electrochemical version of the DPN technique that will be discussed below. As in DPN, the tip is dipped in a solution (the "ink") and this ink is deposited on a substrate (the "paper") during the scan. But here, a bias is applied during the deposition which induces an electrochemical reaction. For instance, a H_2PtCl_6 ink can be reduced to Pt(0) [53], or a local polymerization can happen [54].
- Electro-Oxidative Lithography: In this technique, inert SAMs are electrochemically modified by a biased tip to initiate subsequent reactions. For example, the inert $–CH_3$ endgroups of alkyl SAMs can be oxidized into reactive –COOH groups [45, 55, 56].
- Scanning Electrochemical Microscopy (SECM): This scanning probe microscopy technique [57, 58] can be used to locally perform electrochemical reactions near a surface. For instance, it can locally reduce Cu^{II} to Cu^{I} to induce the local catalysis of CuAAC reactions [59]. We will come back to this reaction later on.
- Electrical Cutting: Nanostructures such as carbon nanotubes can be cut by electrically biased AFM tips to change their electronic properties [60–62].
- AFM Electrostatic Nanolithography (AFMEN): The principle of this technique is to apply an electric field between the tip and the surface to locally heat the underlying material by Joule heating. For instance, this can induce the deformation of polymers [63] or the crystallization of phase change materials [64]. If high voltages (30-40 V) are applied on poly-

mers, Taylor cones are observed due to electrohydrodynamic instabilities in the melt [65, 66].

- Nanoexplosion: If a biased tip induces an electric field that exceeds the breakdown strength of an underlying dielectric, an explosive discharge is produced in the tip/sample gap. In this case, a central conic structure is observed as well as a depressed outer ring [67].
- Charge Deposition and Nanomanipulation: Here, charge patterns are written on a surface by a negatively biased AFM tip [68, 69]. Then, charged particles can be electrostatically attracted by these charges to form the final pattern [70].

2. Force-assisted AFM nanolithography

   - Nanoindentation, Nanoplowing and Nanoshaving: Nanoindentation is the simplest AFM lithography technique. A high force is applied on a static tip to indent the surface. If the tip is scanned on the substrate during the application of this force, authors speak of plowing lithography (Figure 5.3(1)). This can be done in contact (static plowing) or intermittent contact (dynamic plowing) modes and on various types of substrates such as polymers [31, 71], metals [72–74] and semiconductors [75, 76]. For polymers, typical applied forces are around 100 nN and they can rise up to 30 mN for metals. This technique can also be used to plow a resist coated on top of a substrate of interest. Then by wet-etching [77, 78] or by lift-off techniques [79], nanostructures can be fabricated according to the initial pattern. In nanoshaving, the substrates are covered with inactive SAMs and lower forces are applied between the tip and the substrate (around 5-10 nN). This enables the removal of the SAMs without damaging the surface. Then, the holes can be filled for instance with active SAMs [80–82].

- Thermomechanical Writing: Thermomechanical writing was invented by the IBM research group of Zurich [83]. The process is quite simple: a resistive tip is heated up to 500-700°C via an electrical current and is pressed on the polymer substrate with a high loading force (Figure 5.3(2)). Applying this principle to a cantilever array (32 × 32 probes), it was possible to make a fast and reliable data writing/reading device for memory applications [84]. The same group also used these heated tips to locally induce the polymerization of diazides and diynes precursors [85].

- Nanomanipulation: In nanomanipulation, the tip is used as a tweezer to catch and release materials to form patterns (Figure 5.3(3)). Particles as small as single atoms can be handled by AFM tips [86]. But this technique is also suitable for bigger objects such as nanoparticles [87], nanocrystals [88], carbon nanotubes [89] or even DNA strands [90]. However, both the surface and the cantilever can be heavily damaged during the process [91].

- Dip-Pen Nanolithography (DPN): DPN was invented in 1999 by Mirkin et al. [92]. It uses the AFM tip as a "nib" to deposit molecules (the "ink") on a solid-state substrate (the "paper") (Figure 5.3(4)). This generated a huge enthusiasm in the scientific community because this technique is complementary to microcontact printing or nanoimprint lithography (among others) since it can selectively place different types of molecules at specific sites even on already patterned surfaces with a high resolution (ca. 30 nm). However, although recent developments allow the parallel DPN with arrays containing 55000 pens [93], it generally has a lower throughput because each pattern (or series of patterns) has to be drawn individually by the tip(s) while a lot of different patterns can be imprinted at once with nanocontact printing. The transport of molecu-

les to the substrate is made through the water meniscus that is formed between the tip and the surface at a controlled relative humidity. It is somehow similar to the Nano Fountain Pen (NFP) technique that uses a nanopipet integrated in an AFM to deliver minute amounts of liquid on a substrate [94, 95] but it does not necessitate a complex and costly cantilever. This technique was used to deposit gold nanoparticles on silicon [96, 97], to change the reactivity of molecules on a substrate thanks to an oxidant ink [98], to perform localized chemical reactions [99], etc.

- Dip-Pen Nanodisplacement Lithography (DNL): This technique pioneered by Zheng et al. [100, 101], combines DPN and nanoshaving and consists in inking an AFM probe and bringing the tip into contact with a surface previously modified with a dense SAM (Figure 5.3(5)). Under high loads, this SAM is then shaved by the scanning AFM tip and the ink is simultaneously deposited on the uncovered areas of the surface. In their papers, Zheng et al. used this technique with polymerization initiators as the ink to obtain polymer brushes with a very good control on their spatial arrangement.

- Local Catalysis: This method is the one that will be used in this chapter. Here, a catalyst is coated on AFM tips to locally catalyze a reaction involving molecules grafted on a substrate and, in most cases, molecules in solution (Figure 5.3(6)). So the basic difference with DPN is that here, the chemical species on the tip do not transfer to the surface but stay on it. For example, Stoddart et al. catalyzed a CuAAC reaction between azide-moieties on a surface and alkyne-moieties in solution with a Cu-coated AFM tip [102] while others used a Pd-coated tip to catalyze a Suzuki reaction [103] or other kinds of reactions [104]. All the previously mentioned studies were undertaken in liquid solutions containing the reactive

molecules to be selectively grafted on the substrate. But in some cases, there is no need of such solutions. For example, Pt-covered tips were used to perform a Pt-catalyzed transfer hydrogenation resulting in the reduction of grafted azide molecules to form amines [105], a powder of reducing agent was attached to an AFM tip to reduce a monolayer of imines to amines [106], acidic molecules were grafted on tips to induce the local hydrolysis of surface-bound moieties [107], etc.

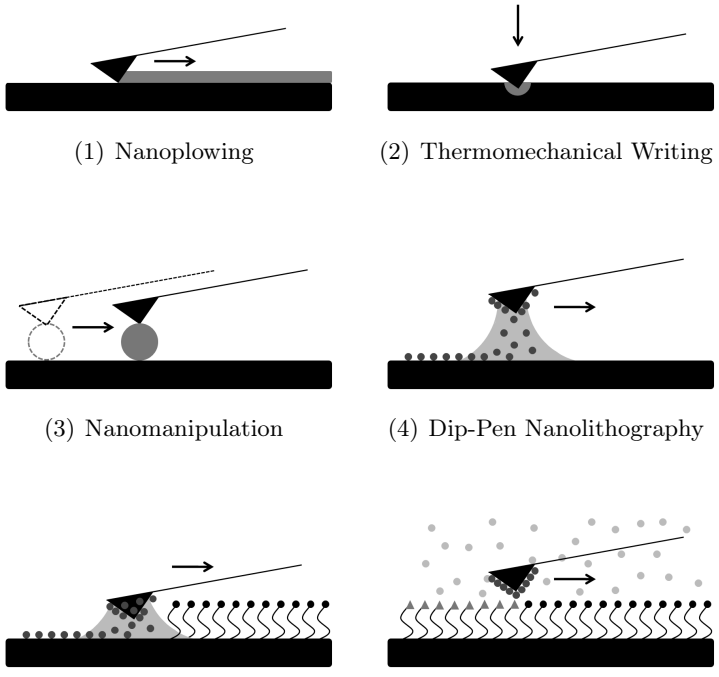

(1) Nanoplowing (2) Thermomechanical Writing

(3) Nanomanipulation (4) Dip-Pen Nanolithography

(5) Dip-Pen Nanodisplacement Lithography (6) Local Catalysis

Figure 5.3: Some examples of force-assisted AFM nanolithography techniques.

In this chapter, we will focus on the technique developed by Stoddart et al. for the local catalysis of the azide-alkyne cycloaddition as mentioned above [102]. The minimum line width that they could reach was around 50 nm which is well below the ones of similar studies based on DPN (ca. 300 nm) [99], microcontact printing (ca. 1 μm) [108–110] or SECM (ca. 500 μm) [59]. The best results they got for the direct-write click chemistry of 4-pentynoic acid (50 mM in ethanol) were obtained with a 2 μm/s scan speed and a contact force of 300 nN. In this case, the height of the pattern was 1.4 nm (slightly more than the thickness of a monolayer).

In this study, attempts were made to improve this technique. First, fluorescent alkyne molecules will be used in order to have supplementary tools for the characterization of the substrates after the CuAAC reaction, i.e. fluorescence spectroscopy and microscopy. Second, instead of coating a tip with copper, Cu-ligands will be attached through a polymer brush grafted from the tip. It is believed that this will lead to a better control on the catalysis because of the higher flexibility of the Cu-ligands as compared to bulk copper. Moreover, due to the nature of the brush itself, the number of copper atoms available for the catalysis will be relatively high.

5.2.2 Local Heterogeneous Catalysis

Catalysis is the action of modifying the rate of a chemical reaction that is performed by a substance (called the catalyst) which is not consumed in the reaction [111]. The catalyst lowers the activation energy (E_a) needed to transform the initial reagents into the product without modifying the global enthalpy change (ΔH) of the system (Figure 5.4). It can also promote the stabilization of intermediate products.

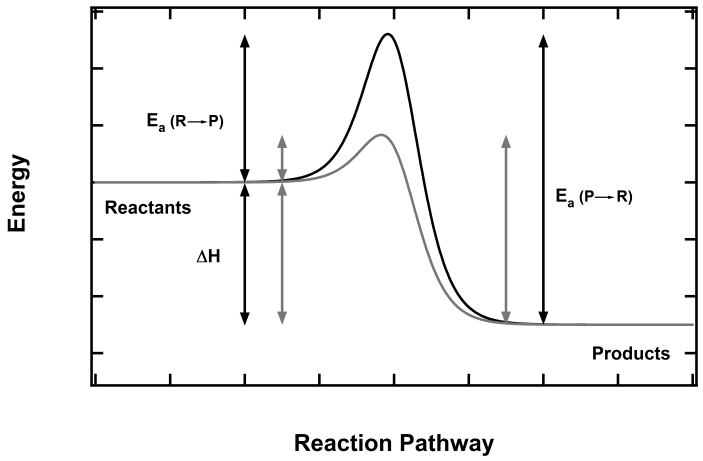

Figure 5.4: Energetic diagram showing the progress of a chemical reaction with (gray line) and without (black line) catalyst.

The term "catalysis" was first introduced by Jöns Jacob Berzelius in his annual report of 1835 [112] where he reviewed the findings of the scientific community concerning apparently very different domains ranging from the conversion of starch to sugar by acids to the hastening of gas combustion by platinum [113]. He deducted that all these processes had something in common which he called catalysis.

There exist basically two types of catalysis:

1. Homogeneous catalysis
   In homogeneous catalysis, the reagents and the catalyst are in the same phase [114]. In this case, the instantaneous composition is the same in the whole medium and the rate of the reaction only depends on temperature, pressure and concentrations.

2. Heterogeneous catalysis
   In heterogeneous catalysis, the phase of the catalyst differs from

that of the reagents [115, 116]. Lots of industrial reactions use solid catalysts and liquid or gaseous reagents. In this kind of catalysis, other parameters influence the rate of the reaction such as the diffusion of the constituents, the stirring and the specific surface area of the catalyst. Some researchers who substantially contributed to the rise of the heterogeneous catalysis were awarded with Nobel Prizes: Fritz Haber and Carl Bosch in 1918 for the catalytic formation of ammonia [117, 118], Irving Langmuir in 1932 for his work on surface chemistry [119], and Gerhard Ertl in 2007 for his studies of chemical processes on solid surfaces [120].

Aside from these two types of catalysis, we can add the local catalysis which is an extension of the heterogeneous catalysis where a supported catalyst is brought in close contact to the reagents to locally activate their reaction [59, 102, 103, 109].

Further reading concerning catalysis can be found in [121–123].

5.3 Results and Discussion

This section is divided into two parts. The first part concerns the results obtained for a preliminary study dedicated to the characterization of all the constitutive parts of the system while the second part presents the results obtained for the actual local catalysis experiments. The materials involved here are described in section 6.1.5 on page 196 whereas the preparation of the surfaces, of the tips and of the solution is detailed in section 6.2.5 on page 206. Finally, all the characterization techniques used in this chapter are presented in section 6.3 from page 211.

5.3.1 Preliminary Study

Before performing the local catalysis experiments, preliminary tests were undertaken to settle down each part of the reaction, i.e. the preparation of the substrate, the functionalization of the AFM tips and the click reaction in itself. In these tests, the catalytic complexes were in solution and 3 different alkynes were used (Figure 5.5).

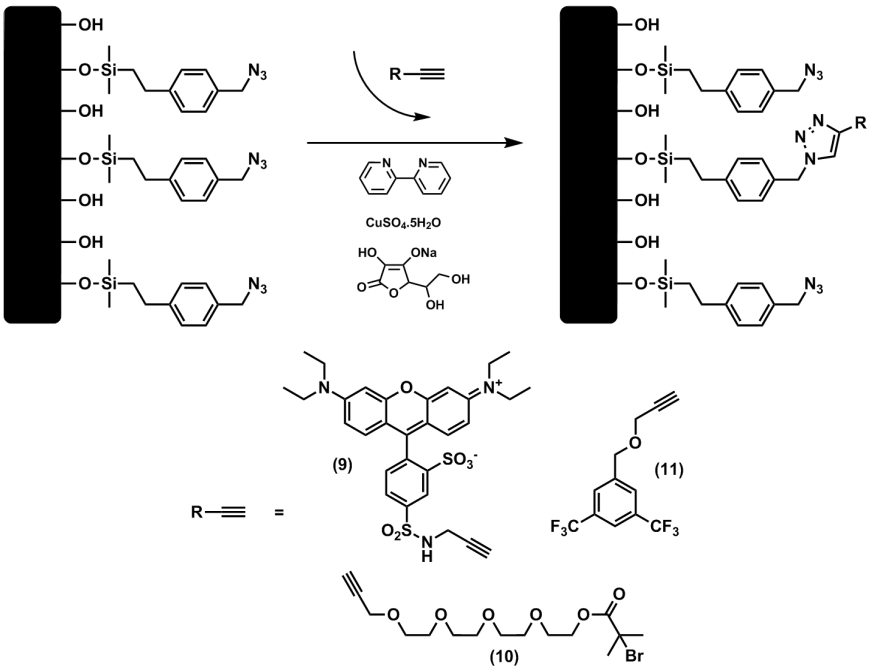

Figure 5.5: In preliminary tests, the catalytic complexes were in solution.

First, a silane bearing a leaving endgroup had to be selected for the preparation of dense SAMs that will be used as the base for the elaboration of azidated surfaces. In the literature, Br-terminated alkylsilanes are often used [56, 108, 110, 124–130] with silane (4) being one of the most used. It was also shown in the thesis of Dr. Peter Hensenne that silane (3) is a good candidate (cf. Figure 6.1 in the Experimental Part on

page 192). In order to determine whether they can be used in this work, they were compared as follows: silanes (3) and (4) were self-assembled on silicon squares according to the standard procedure (Figure 5.6(1)). Then the terminal halogens were substituted by immersion in a saturated solution of NaN_3 in DMF (Figure 5.6(2)). It was shown that a reaction time of 48 h or more is often necessary to reach 100% conversion at room temperature [131]. However, the kinetics is quite fast at the onset of the reaction and a 50% conversion was observed after only 4 hours [125]. As it was anticipated that this step is crucial for the proper functionalization of the substrates, the azidation time was chosen as the parameter to optimize. To determine the advancement of the reaction, XPS could not be used for two reasons: first, halogen atoms are ejected by secondary electrons of low energy under high energy X-ray irradiation preventing the quantification of Cl and Br [132, 133] and second, the unavoidable contamination layer leads to a biased quantification of the carbon content. XRR cannot be used as such because the thickness and the electron density do not vary enough after the azidation step. Indeed, Br has 35 electrons and Cl 17 while N_3^+ has 20. To amplify the signal, the samples were soaked overnight in a solution of the clickable ATRP-initiator (10) (Figure 5.6(3)). This time, the number of electrons should increase by 198 per grafted molecule. By computing the difference between the integrated electron density of each sample after (ζ_g) and before (ζ_g') the click reaction and by dividing this amount with the increase of electrons per alkyne molecule Z, the grafting density of alkyne (10), σ_g, can be obtained: $\sigma_g = (\zeta_g - \zeta_g')/Z$ (Figure 5.7(1)).

For silane (3), the transformation of the Cl in an azide moiety does not change significantly the reflectogram as it was expected. The overnight click reaction with initiator (10) provides a clear increase of thickness and of electron density after 24 h azidation time. The number of molecules grafted per nm^2 is around 1.3. This value is low compared to standard silane layers, but remains large compared to the estimated

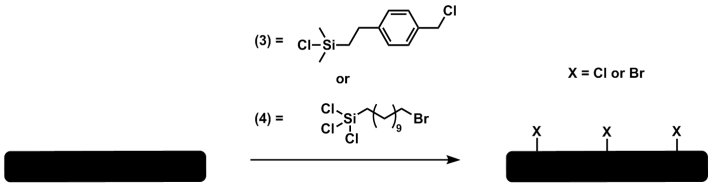

(1) Silanization with (3) or (4)

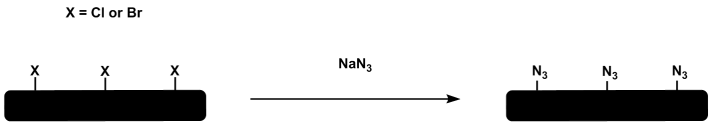

(2) Azidation

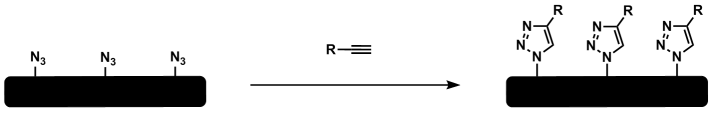

(3) Click

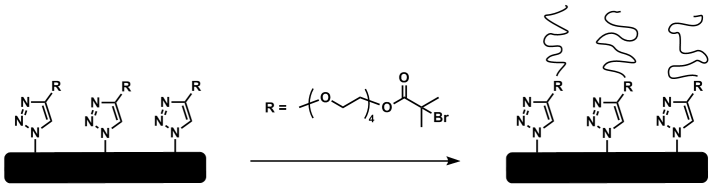

(4) Polymer brush growth

Figure 5.6: Description of the steps involved in the preparation of the samples used in the preliminary study.

grafting density of brushes (around 0.33 chains/nm^2). For shorter azidation times, the grafting densities decrease to 0.25 and 0.45 molecule/nm^2 for 1 h and 3 h azidation time respectively, always for an overnight click reaction.

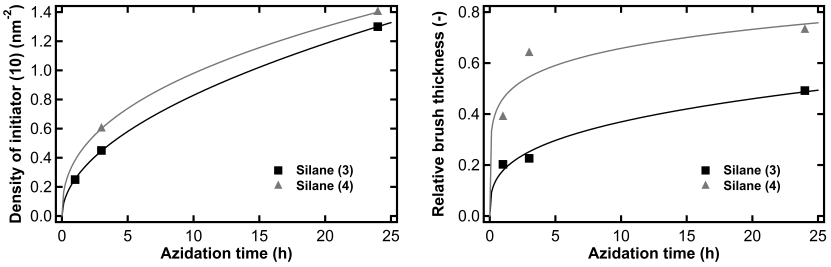

(1) Density of initiator molecules (2) Relative brush thicknesses

Figure 5.7: Density of initiator (10) (left) and relative thicknesses of the subsequent brush (right) as a function of the azidation time measured for two different silanes: silane (3) (■) and silane (4) (▲).

For silane (4), the azidation changes significantly the reflectogram. The layer thickness and electron density decrease. This suggests that partial degradation of the layer may have occured. However, overnight click reaction on these samples succeeds in grafting the initiator. The sample corresponding to a 1 hour azidation showed a problem of roughness, and could not be analyzed reliably. The reaction proceeds similarly to the previous case and good conditions are obtained for 24 h azidation with a grafting density of 1.4 molecule/nm^2, showing that the observed change of thickness did not prevent proper reaction.

Azidation times longer than 24 h led to a more dramatic degradation of the monolayers for both silanes. So here, there is a first indication that the most appropriate azidation time is 24 h which is a good compromise between a high grafting density and a low degradation.

Poly(MEO_2MA) brushes were then grafted from these samples for 2 h (Figure 5.6(4)). The measured brush thicknesses were divided by the thickness of a reference brush grafted from a SAM of silane-initiator (1) (Figure 5.7(2)). For both silanes, a clear increase in the relative thickness is observed with increasing azidation times and it seems that

silane (4) provides thicker brushes. Reference experiments also showed that hardly any growth is observed from pristine silane (3)- or silane (4)-based SAMs.

From this first series of experiments, it can be concluded that both silanes can be employed. SAMs based on silane (4) yields thicker brushes but suffers from apparent degradation during the azidation process. This is why silane (3) was preferred in the following experiments. The click reaction seems very efficient once the azide moiety is properly obtained.

This was confirmed by another experiment where the fluorescent propargyl-sulforhodamine (9) was used. Working with fluorescent molecules has some advantages. Indeed, this allows the characterization of the formed monolayers through Front-Face Fluorimetry and it should allow the imaging of the substrates after the local catalysis experiments through Laser Scanning Confocal Microscopy (LSCM) thanks to the high sensitivity of this instrument (up to single molecule dectection) [134]. In this preliminary study, the azidated substrates were dipped for 60 minutes in a 80 μM solution of (9) in the presence of a copper source and a reducing agent (the concentrations were: (9)/bipy/$CuSO_4 \cdot 5\,H_2O$/ascorbate = 1.2/4.8/4.8/1 $\cdot 10^{-3}$ mmol in H_2O/MeOH = 7.5/7.5 ml). Fluorescent spectra were then recorded for different azidation times (1 h, 2 h and 4 h) and with an excitation wavelength of 566 nm (Figure 5.8).

Again, Figure 5.8 proves that alkyne (9) was successfully grafted on the surfaces. The intensity of the fluorescent signal increases for increasing azidation times which confirms the previous XRR results. Interestingly, a fluorescent signal is observed even for an azidation time as short as 1 h. This means first that the reaction is detectable for assumedly low surface coverages and second that the fluorescence quenching that is inherent to surface immobilization of fluorescent molecules [135–137] is not strong enough to impede this detection even when no particular

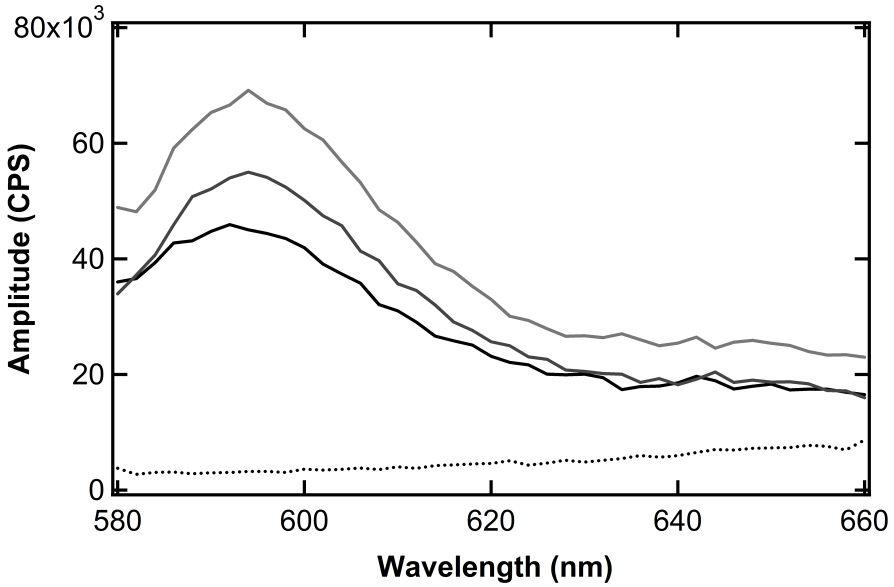

Figure 5.8: Front-Face Fluorimetry spectra obtained for azido-SAMs reacted with alkyne (9) for 60 minutes. Different azidation times are compared: 1 h (black line), 2 h (dark-gray line) and 4 h (light-gray line). The dotted line represents the spectrum obtained for the azido-SAM alone. The excitation wavelength was 566 nm.

caution was taken for the storage of the samples.

The kinetics of the click reaction on azidated silicon substrates was investigated by XPS (Figure 5.9). To this purpose, the propargyl bis(trifluoromethyl)benzene (11) was prepared by Dr. Olivier Schicke. This compound was chosen because it bears 6 fluorine atoms. Indeed, although F is also sensitive to degradation mechanisms as previously discussed (but to a lesser extent compared to Cl and Br), it is attractive for XPS experiments because of its high relative sensitivity factor (fourfold in comparison to C and twofold in comparison to N). The azidated surfaces were then immersed in a 67.5 μM solution of (11) containing ascorbic acid, ligand (12) and $CuSO_4 \cdot 5\,H_2O$ (the concen-

trations were (11)/(12)/$CuSO_4 \cdot 5\,H_2O$/ascorbate = 1/0.1/0.1/0.2 mmol in H_2O/acetone = 7.5/7.5 ml). The conversion of azide molecules to 1,2,3-triazoles was then calculated for 5 reaction times (5, 15, 30, 60 and 120 min) by computing the ratio between the relative XPS intensity of the F_{1s} peak and twice the one of the N_{1s} peak[2] ($F_{1s}/2N_{1s}$) since there are twice as many F as N in a 1,2,3-triazole molecule formed by the cycloaddition of (11) on the azidated surfaces (▲). To study the influence of the ligand and of the copper source, solutions without $CuSO_4 \cdot 5\,H_2O$ (▶) and without both $CuSO_4 \cdot 5\,H_2O$ and ligand (12) (■) were prepared and the process was repeated.

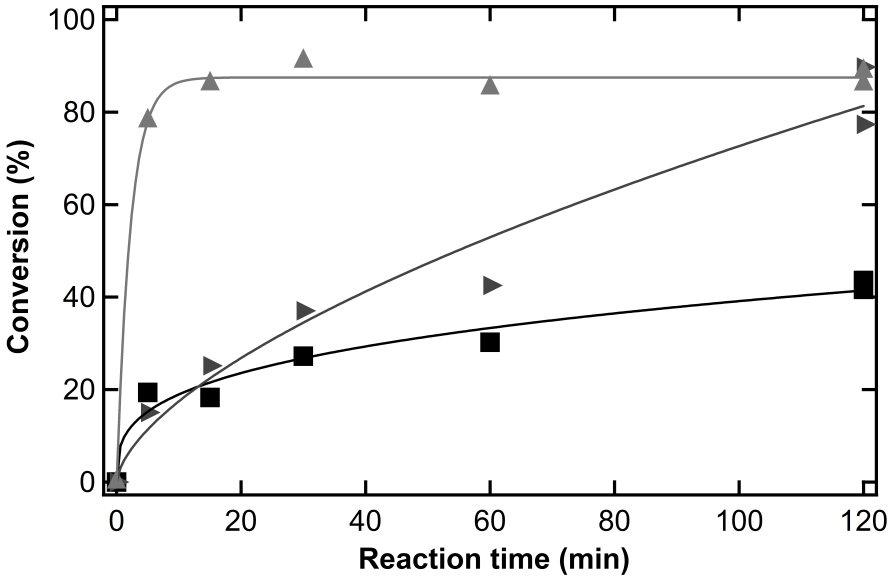

Figure 5.9: Conversion of azide molecules to 1,2,3-triazoles by reaction with alkyne (11). This was calculated from the ratio F/2N obtained by XPS measurements. ■ : Azide-SAM + Alkyne (11); ▶ : Azide-SAM + Alkyne (11) + Ligand (12); ▲ : Azide-SAM + Alkyne (11) + Ligand (12) + $CuSO_4 \cdot 5\,H_2O$. The reaction rate highly increases with the introduction of Cu in the solution.

[2]after application of a correction to take into account the relative sensitivity factors of F and N.

In the absence of the catalytic complex, the reaction is relatively slow. If 20% of the surface functions are converted after 5 minutes, the conversion barely reaches 40% after 2 h of reaction (■). Quite surprizingly, the incorporation of ligand (12) in the reaction mixture increases the kinetics of the reaction and a 80% conversion is obtained after 2 h of reaction (▶). This is still not very well understood. The main result of this experiment comes from the great accelerating effect of the incorporation of $CuSO_4 \cdot 5\,H_2O$ in the solution (▲). Here, the conversion already reaches 80% after only 5 minutes of reaction. This is of course very important in the prospect of the local catalysis experiments.

The last thing that had to be tested is the functionalization of the AFM tips with the catalytic complex. Poly(HEMA) brushes were grafted from Si_3N_4 cantilevers as well as from silicon squares. These brushes were then activated with DSC and DMAP as described in the previous chapter. Ligand (12) was coupled to them by soaking the samples in a solution of (12) in DMF before complexation with $CuSO_4 \cdot 5\,H_2O$ in methanol. Normally, a first indication on the advancement of these reactions could have been given by ellipsometry because of the relatively high amounts of materials that were grafted after each of these steps. However, even if a thickness increase was nearly always observed, the values were not fully reproducible. It was probably due to a random organization of the entangled polymer chains during the rinsing and drying steps. Nevertheless, ellipsometry could give a first hint on the success of the successive reactions.

Since ligand (12) contains nitrogen while poly(HEMA) is only composed of carbon and oxygen, the amide (or amine oxide) formation could be tracked by XPS. The activating agents also contain nitrogen but as seen in the previous chapter, these species are completely removed during the amine-coupling step. This allows the quantitative calculation of the reactive –OH group conversion (at least for the first 10-15 nm at the

surface of the brush). Each HEMA monomer has 5 C and 3 O while ligand (12) has 33 C, 5 O and 4 N. From the XPS spectrum displayed in Figure 5.10(1), C/N and O/N ratios were calculated to be 14.6 and 4.4 respectively. The conversion x can then be estimated with:

$$x_C = \frac{5}{4 \cdot \frac{C}{N} - 33} = 0.20 \quad \text{and} \quad x_O = \frac{3}{4 \cdot \frac{O}{N} - 5} = 0.22 \tag{5.1}$$

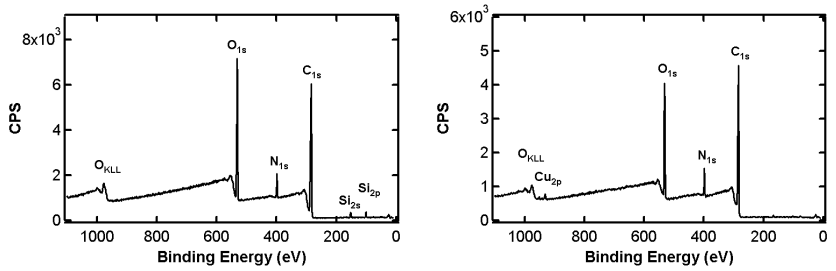

(1) Poly(HEMA) brush + Ligand (12) (2) Poly(MES) brush + Ligand (12) + Cu^{II}

Figure 5.10: XPS survey scans of a poly(HEMA) brush coupled with ligand (12) (left) and of a poly(MES) brush coupled with ligand (12) after complexation with $CuSO_4 \cdot 5\,H_2O$ (right).

The two ratios in equation (5.1) give pretty close values around 20% of conversion. This is not very high but, since ligand (12) is relatively bulky and cannot penetrate deeply inside the dense brush, this conversion is satisfying.

Finally, the complexation of these ligands with $CuSO_4 \cdot 5\,H_2O$ was also monitored by XPS (Figure 5.10(2)). Poly(MES) brushes were used to enhance the Cu_{2p} signal on the survey scan because the conversion of their –COOH functional side groups was slightly more efficient than for the –OH side groups of poly(HEMA). This tends to increase the amount of ligands per unit surface area and thus, the amount of Cu.

However, due to technical considerations[3], poly(HEMA) brushes were preferred for the local catalysis experiments. Nevertheless, since the complexation occurs between the ligand (12) and Cu^{II}, the nature of the underlying polymer brush is of no importance. From Figure 5.10(2), the experimental Cu/N ratio was calculated to be 0.05 while the theoretical ratio is of 0.25 for a 100% complexation. This issues a 20% yield for the complexation of the ligands. Again, this is relatively low but the likely burial of the bipyridine moieties inside the brush can explain this fact. Indeed, the complexation in solution was shown by Dr. Olivier Schicke to be quantitative and to yield nice blue crystals upon solvent evaporation. This experiment allowed the determination of the crystalline structure of the complex by X-Ray Diffraction (XRD) (Figure 5.11).

It was evidenced from this structure that two SO_4 and one H_2O groups intervene in the complexation step.

5.3.2 Local Catalysis

In the preliminary study, all the basic ingredients for the local catalysis experiments were successfully obtained. Experiments in which the catalytic complexes were grafted on AFM tips were then undertaken (Figure 5.12). Propargyl-sulforhodamine (9) was chosen as the alkyne moiety to be grafted for various reasons: it is soluble in a $MeOH/H_2O$ mixture that is well suited for use with the liquid cell of the AFM, the solution is heavily colored in pink which allows the easy monitoring of the solution exchange in the cell and its fluorescent behavior is an added value for the imaging of the obtained patterns.

During a first experiment, the cantilever was swept on the surface

[3] i.e. the lack of control on the polymer thickness and on the general quality of the brush (formation of gels) and the delicate rinsing step due to the high viscosity of the polymerization solution.

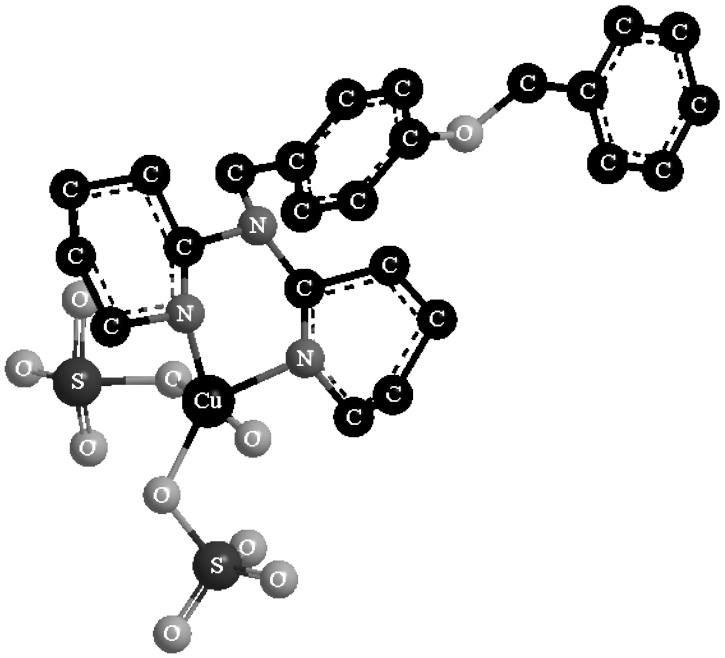

Figure 5.11: Two SO_4 and one H_2O groups intervene in the Cu-ligand (12) complex as highlighted by Dr. Olivier Schicke through X-Ray Diffraction (XRD).

along six vertical lines with different parameters from left to right. Table 5.1 displays these parameters. Two different contact forces were investigated i.e. ~ 9 and 17 nN. These forces can seem a bit large in comparison to forces that are used in nanoshaving lithography, i.e. ~ 5 nN [1] but in order to compare these two series of values, the forces should be divided by the contact area in order to obtain the average pressure that acts on the surface. This contact area between a sphere and a surface can be estimated with the Hertz model:

$$a^3 = \frac{3}{4}\frac{RF \cdot (1-\nu^2)}{E} \tag{5.2}$$

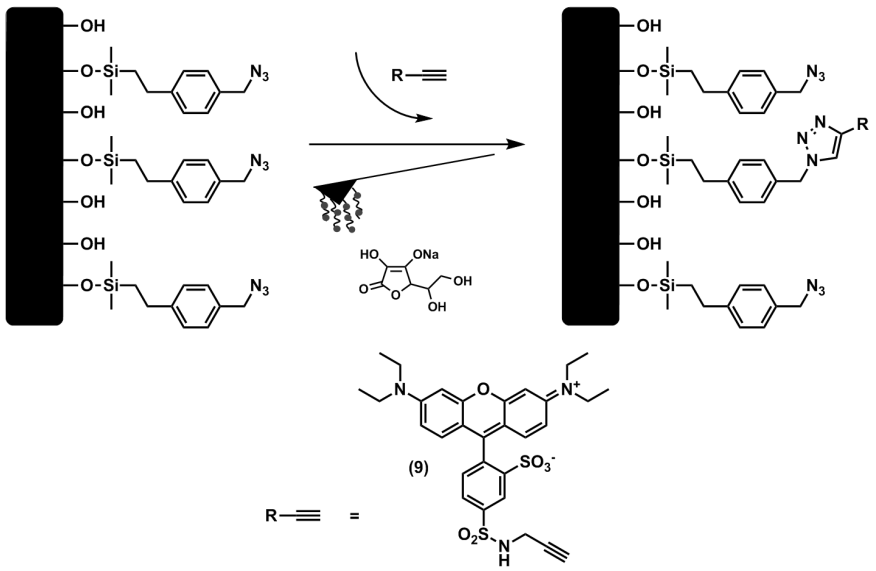

Figure 5.12: In local catalysis experiments, the catalytic complexes were grafted on AFM tips.

where a is the radius of the contact area, R is the radius of the sphere, F is the applied force and ν and E are the Poisson's ratio and the Young's modulus of the elastic material (the brush). In our case, R is the sum between the radius of the tip (~ 30 nm) and the thickness of the brush (~ 50 nm), F is close to 10 nN, ν can be estimated as 0.33 and E as 0.5 GPa because, on the one hand, it can be found in the literature that the Young's modulus of a poly(HEMA) brush in the dry state is 2.6 GPa [138] and, on the other hand, the modulus of a swollen brush is four times lower than the one of the same brush in the collapsed state [139]. Inserting these values in equation (5.2), this gives a contact area of around 300 nm^2 ($a \simeq 10$ nm). The average pressure that is applied by the brush on the surface is thus around 30 MPa[4]

[4]According to our knowledge of the shear modulus of swollen poly(MEO_2MA) brushes extracted from QCM-D experiments [140], the given value for the Young's modulus of swollen poly(HEMA) brushes seems to be overestimated. In that case, the contact area could be larger and this average pressure could be even lower.

which is one order of magnitude lower than the pressure corresponding to the displacement threshold generally observed for a silane SAM during nanoshaving experiments [82]. Indeed, even if the force is lower in these experiments, the tip radius is smaller (~ 10 nm) and the Young's modulus of the SAM is larger (~ 3 GPa) which gives a much smaller contact area and finally a larger pressure. However, in Stoddart's paper [102], a contact force of 300 nN gave the thickest pattern after the lithographic step. This is surprising since it means that the average pressure that was applied on the surface was much larger than the one used in the nanoshaving experiments which were discussed above.

Three different scan speeds were tested i.e. 0.5 μm/s, 2 μm/s and 4 μm/s. These have been chosen according to Stoddart et al. [102] and in agreement with the constraints of the system such as the total duration of the experiment. Indeed, the reaction is quite fast even without any catalyst as shown above. In the preliminary study, the yield of the reaction was close to 20% when the substrate was in contact with the solution for a few tens of minutes. So the parameters were chosen to meet a compromise between the contact time and the quality of the pattern. The lines were around 13 μm-long and separated by 3 μm in order to be easily detected during the characterization step and the time needed for the drawing of the pattern was a bit larger than 1 minute. Obviously, the total duration of the experiment was higher because the lever had to be equilibrated in the reactive solution but this time was always limited to less than 15 minutes.

After the experiment, two lines out of six could be observed with the AFM as shown in Figure 5.13. From these images, some points can be highlighted: first, the lines are not continuous but are formed of what seems to be aggregates; second, these aggregates are randomly distributed all over the surface proving that the reaction occurs also at other places but with a lower kinetics; third, the first line on the left

	Contact Force		Scan Speed
	(V)	(nN)	(μm/s)
Line 1	-1	9	0.5
Line 2	-1	9	2
Line 3	-1	9	4
Line 4	-0.5	17	0.5
Line 5	-0.5	17	2
Line 6	-0.5	17	4

Table 5.1: Parameters for the first local catalysis experiment.

appears thinner than the other which means that the interaction between the tip and the surface changed between these two lines. But this last result also means that these lines are not the result of the deposition of some material from the tip to the substrate, otherwise, the thickest line would have been on the left hand side. It is reasonable to think that the thickest line is Line 4 from Table 5.1 because of the slower scan speed. Line 1 would have also been a good candidate; however, since another line can be seen on its left, this is not possible. It has thus to be assumed that the thin line is Line 3 with the fastest scan speed and the smaller contact force. It is somewhat surprising that this particular line can be seen and not Line 1 or Line 2 that were scanned with a slower speed. This is still not well understood. At this point, it should also be mentioned that the reproducibility of this experiment was not perfect. Indeed, around 50% of similar experiments issued patterned lines while the other 50% did not.

Another interesting point appears when the height profile of the image is analyzed (Figure 5.14). The height of the thickest line was about 6-7 nm while its width was about 50-100 nm. This is of course thicker than the height of a sulforhodamine monolayer. At this point, our best hypothesis is that the reaction is catalyzed when the tip is scanned over the surface and, due to the saturation of the solution, the first grafted

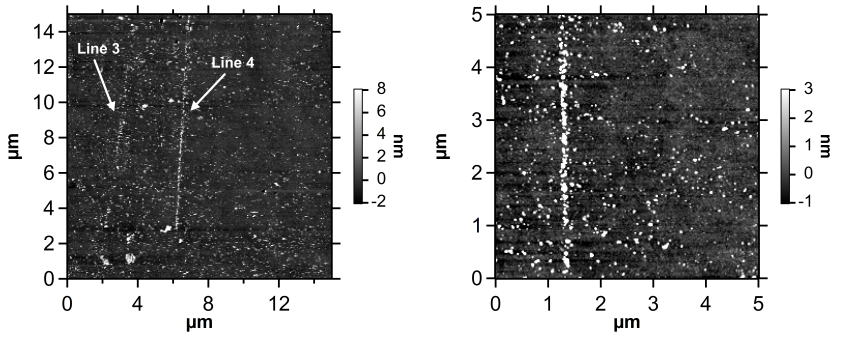

(1) 15 μm × 15 μm image (2) 5 μm × 5 μm image

Figure 5.13: AFM images obtained after the local catalysis experiment in a saturated solution of alkyne (9). Two lines out of six were visible; left: 15 μm-image showing the two lines (4 μm/s and 0.5 μm/s scan speeds) and right: 5 μm-zoom on the thicker line.

molecules serve as nuclei for the crystallization and/or the pi stacking of other sulforhodamine molecules.

The effect of the scan speed on the thickness of the lines was investigated in another series of experiments. The major result of this study is given in Figure 5.15 where the thicknesses of two lines produced during the same experiment are compared. The left line was created with a scan speed of 0.5 μm/s while the right line was produced with a scan speed of 0.25 μm/s. The contact force was around 17 nN in both cases. As can be seen on the height profiles, a huge difference in thickness exists between these two lines. The first one is around 4-6 nm-high while the second one is closer to 20 nm which is 3 to 4 times higher while the scan speed was only decreased by a factor 2. This can have two different but not exclusive explanations: the first one is that, as the tip is scanned slower, the number of anchored molecules increases which leads to a higher number of nuclei to initiate the crystallization. The other explanation is that the brush absorbs some small aggregates which are further transferred to the surface and a larger number of these aggregates is likely to be deposited

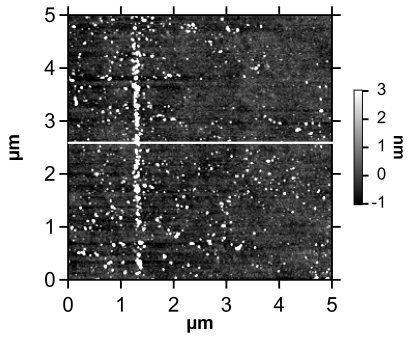

(1) 5 μm × 5 μm image

(2) Height profile

Figure 5.14: Height profile of the thicker catalyzed line. The thickness of this line is around 6-7 nm which is much higher than the thickness of a monolayer of (9).

if the speed is lower.

In order to gain more knowledge on the mechanisms of this local catalysis, a series of tests was undertaken. They are summarized in Table 5.2.

First, the ability of a bare tip to modify the surface in a way that could favor the subsequent crystallization was investigated. So a bare tip was used and the experiment was performed with the same surface and the same solution as before. After this experiment, nothing was

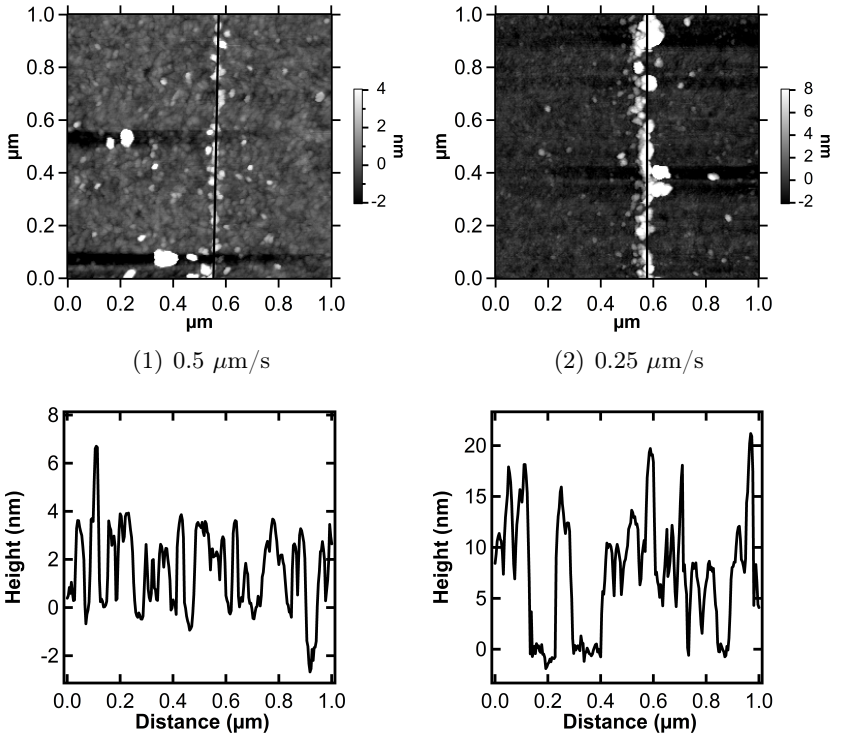

(1) 0.5 μm/s (2) 0.25 μm/s

(3) Height profile at 0.5 μm/s (4) Height profile at 0.25 μm/s

Figure 5.15: Influence of the scan speed on the thickness of the patterned lines for a constant contact force of 10 nN. Left : 0.5 μm/s issuing a 4-6 nm-thick line and right : 0.25 μm/s giving a 20 nm-thick line.

Tests	AFM Tip		Solution		
	Brush	Complex	Solvent	Saturated (9)	Diluted (9)
1				X	
2	X		X		
3	X			X	
4	X	X			X

Table 5.2: Summary of the different tests made to investigate the mechanisms of the local catalysis.

grafted on the surface. Second, the possibility that the brush could be torn off the tip by frictional forces and deposited on the surface during the experiment was considered. In this case, the observed lines would have been made of polymer brush aggregates. This is not very likely given that for typical brushes (50 nm-thick) and tips (30 nm of radius), the volume of the brush in contact with the surface can be estimated by:

$$V_{br} = 2\pi \cdot 30^2 \cdot 50 \text{ nm}^3 = 2.8 \cdot 10^5 \text{ nm}^3 \tag{5.3}$$

while the observed amount of material on the surface for a typical line of dimensions: $L = 13$ μm, $l = 50$ nm and $t = 10$ nm is:

$$V_{mat} = 13 \cdot 10^3 \cdot 50 \cdot 10 \text{ nm}^3/\text{line} = 6.5 \cdot 10^6 \text{ nm}^3/\text{line} \tag{5.4}$$

So for one patterned line, V_{mat} is more than one order of magnitude larger than V_{br}. However, these values could have been underestimated if the polymer brush formed a gel on the tip due to insufficient rinsing or other factors. So, an experiment was carried out where the tip was only coated with a polymer brush and the reactive solution was replaced with the solvent of the reaction. Again, no lines were observed after this test. To see whether the brush could transport some aggregates to the surface and thus produce some lines even in the absence of the catalytic complex, a brush was grafted on the tip and the experiment was realized in a saturated solution of propargyl-sulforhodamine (9). Again, this did not lead to the formation of patterned lines. Finally, a last test was made where the catalytic complex was grafted on the brush but here, the reactive solution was diluted by doubling the amount of solvent. In this case, the solution was not concentrated enough to promote the crystal growth. But it was thought that this crystallization could have

been further initiated by immersing the resulting surface in a saturated solution of (9) for a few hours. However this was not the case.

After all these tests, it could be concluded that the patterned lines are produced by the combination of actions of the catalytic complex and of the brush. This seems to be a two steps phenomenon. The first one involves the catalytic reaction between azides on the surface and alkynes in solution thanks to the catalytic complex grafted on the tip. The second one involves the transport of small fluorophore crystallites by the brush towards this first monolayer and then, due to pi stacking, large aggregates are formed.

The number of sulforhodamine molecules that can react with a particular azide molecule on the surface can be estimated by counting the number of molecules that are located inside a half-sphere centered on this azide molecule and whose radius r can be estimated, assuming a Brownian motion of the molecules, with:

$$r = \sqrt{6Dt} \tag{5.5}$$

where D is the diffusion coefficient and t is the considered time. Here, t is the time during which the azide molecule is in contact with the brush and can be determined by dividing the diameter of the contact area, which was previously determined to be around 20 nm, with the scan speed (0.5 μm/s) yielding a value of 40 ms while D can be estimated with the Stokes-Einstein relation:

$$D = \frac{kT}{3\pi\mu d} \tag{5.6}$$

where k is the Boltzmann constant, T is the temperature, μ is the viscosity of the solution and d is the diameter of the considered molecules. So for small molecules (d = 1 nm) in a water/methanol solution ($\mu = 7.5 \cdot 10^{-4}$ Pa·s) at room temperature, $D \simeq 6 \cdot 10^{-10}$ m^2/s. Injecting these values for t and D in equation (5.5), it comes that $r \simeq 10$ μm. For a concentration of 80 μM, $2{\cdot}10^8$ sulforhodamine molecules are susceptible to react with each azide molecule on the surface provided that this azide molecule is in contact with a catalytic complex and a sulforhodamine molecule during the specific catalytic reaction time.

In addition, the turnover number of the catalyst (TON) was also roughly estimated. The mass of polymer, m_{br} in contact with the surface is $V_{br} \cdot \rho_{br} = 2.82 \cdot 10^{-16}$ g with V_{br} estimated with equation (5.3) and with the mass density of the brush, $\rho_{br} = 1$ g/cm^3. The number of –OH functional groups corresponding to that mass can be obtained by dividing m_{br} with the mass of a monomer yielding around $1.3 \cdot 10^6$ –OH groups. From the aforementioned XPS experiments, 20% of these –OH groups are known to be converted during the coupling with ligand (12) and 20% of these ligands are complexed with Cu. Making the assumption that no Cu is lost during *in situ* reduction from Cu^{II} to Cu^{I}, the number of Cu atoms that are susceptible to catalyze the reaction, n_{Cu}, is then close to $0.2 \cdot 0.2 \cdot 1.3 \cdot 10^6 = 5.2 \cdot 10^4$.
The maximum number of lines that could be patterned during a single experiment was 4. Since the lines were 13 μm-long and around 50 nm-wide, the maximum catalyzed surface area, S_c, was $4 \cdot 13 \cdot 10^3 \cdot 50 = 2.6 \cdot 10^6$ nm^2. XRR experiments showed that 1.3 azido-silanes per nm^2 were converted to 1,2,3-triazoles during the click reaction of (10) for an azidation time of 24 h (Figure 5.7(1) on page 158). This is probably a bit larger than the number of reacted silanes during the local catalysis experiments but as the actual number cannot be obtained, it will be used for this estimation. Then, the number of reacted azido-silanes n_{sil} is given by $2.6 \cdot 10^6 \cdot 1.3 = 3.4 \cdot 10^6$.

The turnover can be calculated by the ratio n_{sil}/n_{Cu}, which issues a TON of 65. This value is quite high for a substrate-to-catalyst ratio, S/C, of around 150 and relatively close to TONs generally observed for heterogeneous catalysis [141]. However, this value remains a very rough approximation.

Finally, some experiments were made to increase the height of the pattern in order to ease its detection by AFM imaging. Initiator (10) was thus used as the alkyne moiety to be patterned on the substrate. After the local catalysis experiment, a poly(HEMA) brush was grown from the resulting lines to "reveal" the pattern in a similar way as the one depicted in Figure 5.6(4) on page 157. However, after this last step, dark zones appeared on the substrate at places where the cantilever was located during the lithography step. XPS measurements were performed to compare these dark zones with the brighter ones. It was evidenced that the silicon in the dark zones was completely oxidized in SiO_x whereas part of the silicon in the bright zones remained in its reduced form. It was then concluded that charge transfer arose between the tip and the substrate during the local catalysis experiment, even when both the substrate and the cantilever were grounded. It is a bit surprising since authors usually observed that the electric field needed to oxidize silicon in a scanning probe oxidation experiment is of the order of 10^9-10^{10} V/m and can only be reached in the region just below the tip for high applied bias (> 5 V) [1, 35].

5.4 Conclusion

In this chapter, the local catalysis of a click reaction thanks to a catalytic complex grafted on an AFM tip was investigated. In a preliminary study, the basic elements for the local catalysis experiments, i.e. the grafting

of azide-moieties on the substrates and the functionalization of AFM tips with copper complexes, were prepared and fully characterized. The optimal azidation time for the preparation of well defined azido-SAMs was shown to be 24 h while 4% of the –OH functional groups inside the brush were converted into Cu-complexes.

Local catalysis experiments were then successfully undertaken. The scan speed was proven to be a determining parameter: the thickness of the patterned lines tripled when the scanning speed was decreased by a factor 2. In every case, the patterned lines were much thicker than the thickness of a monolayer. Different tests indicated that the most likely mechanism for the formation of the patterned lines involves two steps: first, the catalytic reaction between azides on the surface and alkynes in solution with the contribution of the catalytic complexes grafted on the tip and second, the pi stacking of propargyl-sulforhodamine (9) aggregates that are transported by the brush towards this first monolayer.

Finally, the TON was estimated to be 65 which is relatively close to TONs generally observed for heterogeneous catalysis.

References

[1] Xie, X. N.; Chung, H. J.; Sow, C. H.; Wee, A. T. S. *Mater. Sci. Eng., R* **2006**, *54*, 1–48.

[2] Goodberlet, J. G. *Appl. Phys. Lett.* **2000**, *76*, 667–669.

[3] Geissler, M.; Xia, Y. *Adv. Mater.* **2004**, *16*, 1249–1269.

[4] Fujita, J.; Ohnishi, Y.; Ochiai, Y.; Matsui, S. *Appl. Phys. Lett.* **1996**, *68*, 1297–1299.

[5] Cumming, D. R. S.; Thoms, S.; Beaumont, S. P.; Weaver, J. M. R. *Appl. Phys. Lett.* **1996**, *68*, 322–324.

[6] Orloff, J.; Swanson, L. W.; Utlaut, M. *J. Vac. Sci. Technol., B* **1996**, *14*, 3759–3763.

[7] Mackenzie, R. A. D.; Smith, G. D. W. *Nanotechnology* **1990**, *1*, 163.

[8] Chou, S. Y.; Krauss, P. R.; Renstrom, P. J. *Science* **1996**, *272*, 85–87.

[9] Sotomayor Torres, C. M.; Zankovych, S.; Seekamp, J.; Kam, A. P.; Clavijo Cedeno, C.; Hoffmann, T.; Ahopelto, J.; Reuther, F.; Pfeiffer, K.; Bleidiessel, G.; Gruetzner, G.; Maximov, M. V.; Heidari, B. *Mater. Sci. Eng., C* **2003**, *23*, 23–31.

[10] Yu, Z.; Schablitsky, S. J.; Chou, S. Y. *Appl. Phys. Lett.* **1999**, *74*, 2381–2383.

[11] Gates, B. D.; Whitesides, G. M. *J. Am. Chem. Soc.* **2003**, *125*, 14986–14987.

[12] Zhao, X.-M.; Xia, Y.; Whitesides, G. M. *J. Mater. Chem.* **1997**, *7*, 1069–1074.

[13] James, L. W.; et al., *Nanotechnology* **1996**, *7*, 452.

[14] Alom Ruiz, S.; Chen, C. S. *Soft Matter* **2007**, *3*, 168–177.

[15] Quate, C. F. *Surf. Sci.* **1997**, *386*, 259–264.

[16] Snow, E. S.; Campbell, P. M. *Appl. Phys. Lett.* **1994**, *64*, 1932–1934.

[17] Binnig, G.; Rohrer, H.; Gerber, C.; Weibel, E. *Appl. Phys. Lett.* **1982**, *40*, 178–180.

[18] Binnig, G.; Rohrer, H.; Gerber, C.; Weibel, E. *Phys. Rev. Lett.* **1982**, *49*, 57.

[19] Binnig, G.; Quate, C. F.; Gerber, C. *Phys. Rev. Lett.* **1986**, *56*, 930.

[20] Crommie, M. F.; Lutz, C. P.; Eigler, D. M. *Science* **1993**, *262*, 218–220.

[21] Manoharan, H. C.; Lutz, C. P.; Eigler, D. M. *Nature* **2000**, *403*, 512–515.

[22] Heinrich, A. J.; Lutz, C. P.; Gupta, J. A.; Eigler, D. M. *Science* **2002**, *298*, 1381–1387.

[23] Lee, H. J.; Ho, W. *Science* **1999**, *286*, 1719–1722.

[24] Hla, S.-W.; Bartels, L.; Meyer, G.; Rieder, K.-H. *Phys. Rev. Lett.* **2000**, *85*, 2777.

[25] Iwasaki, H.; Yoshinobu, T.; Sudoh, K. *Nanotechnology* **2003**, *14*, R55.

[26] Song, J.; Liu, Z.; Li, C.; Chen, H.; He, H. *Appl. Phys. A: Mater. Sci. Process.* **1998**, *66*, S715–S717.

[27] Zhang, H.-L.; Li, H.-L.; Liu, Z.-F. *Microelectron. Eng.* **2002**, *63*, 381–389.

[28] Wang, X.; Liu, C. *Nano Lett.* **2005**, *5*, 1867–1872.

[29] Kakushima, K.; Watanabe, T.; Shimamoto, K.; Gouda, T.; Ataka, M.; Mimura, H.; Isono, Y.; Hashiguchi, G.; Mihara, Y.; Fujita, H. *Jpn. J. Appl. Phys.* **2004**, *43*, 4041.

[30] Xiaogang, L.; Hua, Z. Scanning Probe Microscopy-Based Nanofabrication for Emerging Applications. In *Modern Research and Educational Topics in Microscopy*; Mendez-Vilas, A., Diaz, J., Eds.; 2007; Vol. 1, pp 770–778.

[31] Garcia, R.; Martinez, R. V.; Martinez, J. *Chem. Soc. Rev.* **2006**, *35*, 29–38.

[32] Kramer, S.; Fuierer, R. R.; Gorman, C. B. *Chem. Rev.* **2003**, *103*, 4367–4418.

[33] Ginger, D. S.; Zhang, H.; Mirkin, C. A. *Angew. Chem., Int. Ed.* **2004**, *43*, 30–45.

[34] Gordon, A. E.; Fayfield, R. T.; Litfin, D. D.; Higman, T. K. *J. Vac. Sci. Technol., B* **1995**, *13*, 2805–2808.

[35] Avouris, P.; Hertel, T.; Martel, R. *Appl. Phys. Lett.* **1997**, *71*, 285–287.

[36] Yasutake, M.; Ejiri, Y.; Hattori, T. *Jpn. J. Appl. Phys.* **1993**, *32*, L1021.

[37] Day, H. C.; Allee, D. R. *Appl. Phys. Lett.* **1993**, *62*, 2691–2693.

[38] Campbell, P. M.; Snow, E. S.; McMarr, P. J. *Appl. Phys. Lett.* **1995**, *66*, 1388–1390.

[39] Xie, X. N.; Chung, H. J.; Xu, H.; Xu, X.; Sow, C. H.; Wee, A. T. S. *J. Am. Chem. Soc.* **2004**, *126*, 7665–7675.

[40] Xie, X. N.; Chung, H. J.; Sow, C. H.; Wee, A. T. S. *Appl. Phys. Lett.* **2004**, *84*, 4914–4916.

[41] Snow, E. S.; Campbell, P. M. *Science* **1995**, *270*, 1639–1641.

[42] Snow, E. S.; Park, D.; Campbell, P. M. *Appl. Phys. Lett.* **1996**, *69*, 269–271.

[43] Tully, D. C.; Wilder, K.; Frechet, J. M. J.; Trimble, A. R.; Quate, C. F. *Adv. Mater.* **1999**, *11*, 314–318.

[44] Sugimura, H.; Takai, O.; Nakagiri, N. *J. Electroanal. Chem.* **1999**, *473*, 230–234.

[45] Benetti, E. M.; Chung, H. J.; Vancso, G. J. *Macromol. Rapid Commun.* **2009**, *30*, 411–417.

[46] Sugimura, H.; Hanji, T.; Hayashi, K.; Takai, O. *Adv. Mater.* **2002**, *14*, 524–526.

[47] Martinez, R. V.; Garcia, R. *Nano Lett.* **2005**, *5*, 1161–1164.

[48] Tello, M.; Garcia, R.; Martin-Gago, J. A.; Martinez, N. F.; Martin-Gonzalez, M. S.; Aballe, L.; Baranov, A.; Gregoratti, L. *Adv. Mater.* **2005**, *17*, 1480–1483.

[49] Hosaka, S.; Koyanagi, H.; Kikukawa, A. *Jpn. J. Appl. Phys.* **1993**, *32*, L464.

[50] Hosaka, S.; Koyanagi, H.; Kikukawa, A.; Maruyama, Y.; Imura, R. *J. Vac. Sci. Technol., B* **1994**, *12*, 1872–1875.

[51] Koyanagi, H.; Hosaka, S.; Imura, R.; Shirai, M. *Appl. Phys. Lett.* **1995**, *67*, 2609–2611.

[52] Calleja, M.; Tello, M.; Anguita, J.; Garcia, F.; Garcia, R. *Appl. Phys. Lett.* **2001**, *79*, 2471–2473.

[53] Li, Y.; Maynor, B. W.; Liu, J. *J. Am. Chem. Soc.* **2001**, *123*, 2105–2106.

[54] Maynor, B. W.; Filocamo, S. F.; Grinstaff, M. W.; Liu, J. *J. Am. Chem. Soc.* **2001**, *124*, 522–523.

[55] Maoz, R.; Cohen, S. R.; Sagiv, J. *Adv. Mater.* **1999**, *11*, 55–61.

[56] Haensch, C.; Hoeppener, S.; Schubert, U. S. *Nanotechnology* **2009**, *20*, 135302.

[57] Bard, A. J.; Unwin, P. R.; Wipf, D. O.; Zhou, F. *AIP Conf. Proc.* **1991**, *241*, 235–247.

[58] Wipf, D. O. Scanning Electrochemical Microscopy. In *Characterization of Materials*; John Wiley and Sons, Inc., 2002.

[59] Ku, S. Y.; Wong, K. T.; Bard, A. J. *J. Am. Chem. Soc.* **2008**, *130*, 2392–2393.

[60] Park, J.-Y.; Yaish, Y.; Brink, M.; Rosenblatt, S.; McEuen, P. L. *Appl. Phys. Lett.* **2002**, *80*, 4446–4448.

[61] Hyon, C. K.; Kojima, A.; Kamimura, T.; Maeda, M.; Matsumoto, K. *Jpn. J. Appl. Phys.* **2005**, *44*, 2056.

[62] Kim, D.-H.; Koo, J.-Y.; Kim, J.-J. *Phys. Rev. B* **2003**, *68*, 113406.

[63] Lyuksyutov, S. F.; Vaia, R. A.; Paramonov, P. B.; Juhl, S.; Waterhouse, L.; Ralich, R. M.; Sigalov, G.; Sancaktar, E. *Nat. Mater.* **2003**, *2*, 468–472.

[64] Kim, J. *Scanning* **2010**, *32*, 320–326.

[65] Chung, H. J.; Xie, X. N.; Sow, C. H.; Bettiol, A. A.; Wee, A. T. S. *Appl. Phys. Lett.* **2006**, *88*, 023116–3.

[66] Xie, X. N.; Chung, H. J.; Sow, C. H.; Bettiol, A. A.; Wee, A. T. S. *Adv. Mater.* **2005**, *17*, 1386–1390.

[67] Xie, X. N.; Chung, H. J.; Sow, C. H.; Adamiak, K.; Wee, A. T. S. *J. Am. Chem. Soc.* **2005**, *127*, 15562–15567.

[68] Crook, R.; Graham, A. C.; Smith, C. G.; Farrer, I.; Beere, H. E.; Ritchie, D. A. *Nature* **2003**, *424*, 751–754.

[69] Barrett, R. C.; Quate, C. F. *J. Appl. Phys.* **1991**, *70*, 2725–2733.

[70] Mesquida, P.; Stemmer, A. *Adv. Mater.* **2001**, *13*, 1395–1398.

[71] Cappella, B.; Sturm, H. *J. Appl. Phys.* **2002**, *91*, 506–512.

[72] Yao, N.; Lun Yeung, K. *Ind. Eng. Chem. Res.* **2008**, *47*, 9195–9200.

[73] Fang, T.-H.; Chang, W.-J.; Weng, C.-I. *Mater. Sci. Eng., A* **2006**, *430*, 332–340.

[74] Filho, H. D. F.; Mauricio, M. H. P.; Ponciano, C. R.; Prioli, R. *Mater. Sci. Eng., B* **2004**, *112*, 194–199.

[75] Hyon, C. K.; Choi, S. C.; Hwang, S. W.; Ahn, D.; Kim, Y.; Kim, E. K. *Appl. Phys. Lett.* **1999**, *75*, 292–294.

[76] Regul, J.; Keyser, U. F.; Paesler, M.; Hohls, F.; Zeitler, U.; Haug, R. J.; Malave, A.; Oesterschulze, E.; Reuter, D.; Wieck, A. D. *Appl. Phys. Lett.* **2002**, *81*, 2023–2025.

[77] Klehn, B.; Kunze, U. *J. Appl. Phys.* **1999**, *85*, 3897–3903.

[78] Kunze, U.; Klehn, B. *Adv. Mater.* **1999**, *11*, 1473–1475.

[79] Chen, Y.-J.; Hsu, J.-H.; Lin, H.-N. *Nanotechnology* **2005**, *16*, 1112.

[80] Xu, S.; Liu, G.-y. *Langmuir* **1997**, *13*, 127–129.

[81] Wadu-Mesthrige, K.; Xu, S.; Amro, N. A.; Liu, G.-y. *Langmuir* **1999**, *15*, 8580–8583.

[82] Liu, G.-Y.; Xu, S.; Qian, Y. *Acc. Chem. Res.* **2000**, *33*, 457–466.

[83] King, W. P.; Kenny, T. W.; Goodson, K. E.; Cross, G.; Despont, M.; Durig, U.; Rothuizen, H.; Binnig, G. K.; Vettiger, P. *Appl. Phys. Lett.* **2001**, *78*, 1300–1302.

[84] Vettiger, P.; Cross, G.; Despont, M.; Drechsler, U.; Durig, U.; Gotsmann, B.; Haberle, W.; Lantz, M.; Rothuizen, H.; Stutz, R.; Binnig, G. *IEEE Trans. Nanotechnol.* **2002**, *1*, 39–55.

[85] Bakbak, S.; Leech, P. J.; Carson, B. E.; Saxena, S.; King, W. P.; Bunz, U. H. F. *Macromolecules* **2006**, *39*, 6793–6795.

[86] Sugimoto, Y.; Abe, M.; Hirayama, S.; Oyabu, N.; Custance, O.; Morita, S. *Nat. Mater.* **2005**, *4*, 156–159.

[87] Ritter, C.; Heyde, M.; Schwarz, U. D.; Rademann, K. *Langmuir* **2002**, *18*, 7798–7803.

[88] Sheehan, P. E.; Lieber, C. M. *Science* **1996**, *272*, 1158–1161.

[89] Roschier, L.; Penttila, J.; Martin, M.; Hakonen, P.; Paalanen, M.; Tapper, U.; Kauppinen, E. I.; Journet, C.; Bernier, P. *Appl. Phys. Lett.* **1999**, *75*, 728–730.

[90] Hu, J.; Zhang, Y.; Gao, H.; Li, M.; Hartmann, U. *Nano Lett.* **2001**, *2*, 55–57.

[91] Ramachandran, T. R.; et al., *Nanotechnology* **1998**, *9*, 237.

[92] Piner, R. D.; Zhu, J.; Xu, F.; Hong, S.; Mirkin, C. A. *Science* **1999**, *283*, 661–663.

[93] Salaita, K.; Wang, Y.; Fragala, J.; Vega, R. A.; Liu, C.; Mirkin, C. A. *Angew. Chem.* **2006**, *118*, 7378–7381.

[94] Ionescu, R. E.; Marks, R. S.; Gheber, L. A. *Nano Lett.* **2003**, *3*, 1639–1642.

[95] Lewis, A.; Kheifetz, Y.; Shambrodt, E.; Radko, A.; Khatchatryan, E.; Sukenik, C. *Appl. Phys. Lett.* **1999**, *75*, 2689–2691.

[96] Maynor, B. W.; Li, Y.; Liu, J. *Langmuir* **2001**, *17*, 2575–2578.

[97] Zapotoczny, S.; Benetti, E. M.; Vancso, G. J. *J. Mater. Chem.* **2007**, *17*, 3293–3296.

[98] Braunschweig, A. B.; Senesi, A. J.; Mirkin, C. A. *J. Am. Chem. Soc.* **2009**, *131*, 922–923.

[99] Long, D.; Unal, K.; Pratt, R. C.; Malkoch, M.; Frommer, J. *Adv. Mater.* **2007**, *19*, 4471–4473.

[100] Liu, X.; Li, Y.; Zheng, Z. *Nanoscale* **2010**, *2*, 2614–2618.

[101] Zhou, X.; Wang, X.; Shen, Y.; Xie, Z.; Zheng, Z. *Angew. Chem., Int. Ed.* **2011**, *50*, 6506–6510.

[102] Paxton, W. F.; Spruell, J. M.; Stoddart, J. F. *J. Am. Chem. Soc.* **2009**, *131*, 6692–6694.

[103] Davis, J. J.; Coleman, K. S.; Busuttil, K. L.; Bagshaw, C. B. *J. Am. Chem. Soc.* **2005**, *127*, 13082–13083.

[104] Blackledge, C.; Engebretson, D. A.; McDonald, J. D. *Langmuir* **2000**, *16*, 8317–8323.

[105] Muller, W. T.; Klein, D. L.; Lee, T.; Clarke, J.; McEuen, P. L.; Schultz, P. G. *Science* **1995**, *268*, 272–273.

[106] Blasdel, L. K.; Banerjee, S.; Wong, S. S. *Langmuir* **2002**, *18*, 5055–5057.

[107] Peter, M.; Li, X.-M.; Huskens, J.; Reinhoudt, D. N. *J. Am. Chem. Soc.* **2004**, *126*, 11684–11690.

[108] Rozkiewicz, D. I.; Janczewski, D.; Verboom, W.; Ravoo, B. J.; Reinhoudt, D. N. *Angew. Chem., Int. Ed.* **2006**, *45*, 5292–5296.

[109] Spruell, J.; Sheriff, B.; Rozkiewicz, D.; Dichtel, W.; Rohde, R.; Reinhoudt, D.; Stoddart, J.; Heath, J. *Angew. Chem., Int. Ed.* **2008**, *47*, 9927–9932.

[110] Gassensmith, J. J.; Erne, P. M.; Paxton, W. F.; Valente, C.; Stoddart, J. F. *Langmuir* **2010**, *27*, 1341–1345.

[111] Ertl, G.; Freund, H.-J. *Physics Today* **1999**, *52*, 32–38.

[112] Berzelius, J. J. *Jahresbericht* **1836**, *15*, 237–243.

[113] Wisniak, J. *The Chemical Educator* **2000**, *5*, 343–350.

[114] List, B. *Chem. Rev.* **2007**, *107*, 5413–5415.

[115] Xu, W.; Kong, J. S.; Yeh, Y.-T. E.; Chen, P. *Nat. Mater.* **2008**, *7*, 992–996.

[116] Costantini, F.; Bula, W. P.; Salvio, R.; Huskens, J.; Gardeniers, H. J. G. E.; Reinhoudt, D. N.; Verboom, W. *J. Am. Chem. Soc.* **2009**, *131*, 1650–1651.

[117] Haber, F. *The Synthesis of Ammonia from its Elements (Nobel Lecture)*, 1920.

[118] Bosch, C. *The development of the chemical high pressure method during the establishment of the new ammonia industry (Nobel Lecture)*, 1932.

[119] Langmuir, I. *Surface chemistry (Nobel Lecture)*, 1932.

[120] Ertl, G. *Reactions at surfaces: from atoms to complexity (Nobel Lecture)*, 2007.

[121] Roberts, M. *Catal. Lett.* **2000**, *67*, 1–4.

[122] Behr, A. Organometallic Compounds and Homogeneous Catalysis. In *Ullmann's Encyclopedia of Industrial Chemistry*; Wiley-VCH Verlag GmbH and Co. KGaA, 2000.

[123] Knozinger, H.; Kochloefl, K. Heterogeneous Catalysis and Solid Catalysts. In *Ullmann's Encyclopedia of Industrial Chemistry*; Wiley-VCH Verlag GmbH and Co. KGaA, 2000.

[124] Lummerstorfer, T.; Hoffmann, H. *J. Phys. Chem. B* **2004**, *108*, 3963–3966.

[125] Fryxell, G. E.; Rieke, P. C.; Wood, L. L.; Engelhard, M. H.; Williford, R. E.; Graff, G. L.; Campbell, A. A.; Wiacek, R. J.; Lee, L.; Halverson, A. *Langmuir* **1996**, *12*, 5064–5075.

[126] Qing, G.; Xiong, H.; Seela, F.; Sun, T. *J. Am. Chem. Soc.* **2010**, *132*, 15228–15232.

[127] Haensch, C.; Hoeppener, S.; Schubert, U. S. *Nanotechnology* **2008**, *19*, 035703.

[128] Haensch, C.; Hoeppener, S.; Schubert, U. S. *Chem. Soc. Rev.* **2010**, *39*, 2323–2334.

[129] London, G.; Carroll, G. T.; Fernandez Landaluce, T.; Pollard, M. M.; Rudolf, P.; Feringa, B. L. *Chem. Commun.* **2009**, 1712–1714.

[130] Prakash, S.; Long, T. M.; Selby, J. C.; Moore, J. S.; Shannon, M. A. *Anal. Chem.* **2006**, *79*, 1661–1667.

[131] Marrani, A. G.; Dalchiele, E. A.; Zanoni, R.; Decker, F.; Cattaruzza, F.; Bonifazi, D.; Prato, M. *Electrochim. Acta* **2008**, *53*, 3903–3909.

[132] Fairbrother, D.; Madey, T.; Perry, C.; Faradzhev, N. *Int. Rev. Phys. Chem.* **2004**, *23*, 289–340.

[133] Sanche, L. *Mass Spectrom. Rev.* **2002**, *21*, 349–369.

[134] Frederich, N.; Bernard, N.; Muls, B.; Hofkens, J.; Habib Jiwan, J.-L.; Jonas, A. M. *Photochem. Photobiol. Sci.* **2008**, *7*, 460–466.

[135] Chance, R. R.; Prock, A.; Silbey, R. Molecular Fluorescence and Energy Transfer Near Interfaces. In *Advances in Chemical Physics*; John Wiley and Sons, Inc., 2007; Vol. 37, pp 1–65.

[136] Clare, T. L.; Clare, B. H.; Nichols, B. M.; Abbott, N. L.; Hamers, R. J. *Langmuir* **2005**, *21*, 6344–6355.

[137] Nie, S.; Chiu, D.; Zare, R. *Science* **1994**, *266*, 1018–1021.

[138] Huang, H.; Chung, J. Y.; Nolte, A. J.; Stafford, C. M. *Chem. Mater.* **2007**, *19*, 6555–6560.

[139] Sui, X.; Chen, Q.; Hempenius, M. A.; Vancso, G. J. *Small* **2011**, *7*, 1440–1447.

[140] Laloyaux, X.; Mathy, B.; Nysten, B.; Jonas, A. M. *Langmuir* **2009**, *26*, 838–847.

[141] Fernandes, A.; Hensenne, P.; Mathy, B.; Guo, W.; Nysten, B.; Jonas, A. M.; Olivier, R. *Chem.–Eur. J. (Accepted for publication)* **2011**.

Chapter 6

Experimental Part

6.1 Materials

6.1.1 Self-Assembled Monolayers on Silicon and Gold

The silanes or thiols monolayers were self-assembled on silicon and gold respectively. Single-side-polished silicon wafers ($\langle 100 \rangle$ orientation) were from ACM (France). The gold surfaces were obtained by coating the silicon surfaces with 20 nm of gold on 2 nm of chromium as the adhesive layer, using BOC Edwards Auto 500 evaporator (U.K.) (base pressure of $2 \cdot 10^{-7}$ mbar; thermal evaporation rate of 0.4 nm/s).

For ATRP, either the silane-initiator (1) or the thiol-initiator (2) were used depending on the nature of the substrate (Figure 6.1). The silane was prepared according to [1] and the thiol was synthesized according to [2]. The solvents (toluene for silanes and ethanol for thiols) were from Acros (USA) and used as received as well as Et_3N which was used to neutralize the HCl molecules formed during the silane-SAM formation.

For the thiol place-exchange reactions, three different thiols were used: $CH_3(CH_2)_{10}SH$ (1-undecanethiol, UDT), $CH_3(CH_2)_{15}SH$ (1-hexadecanethiol, HDT) and $OH(CH_2)_{11}SH$ (11-mercapto-1-undecanol, UDTOH) from Aldrich. These thiols were thought to be quite stable and not likely to exchange during the considered reaction times (typically a few minutes to a few hours).

For the local catalysis experiments, two other silanes were self-assembled on silicon substrates: the chloro(4-(chloromethyl)phenethyl)dimethylsilane (3) and the (11-bromoundecyl)trichlorosilane (4) (ABCR, Germany) (Figure 6.1). Silanes (3) and (4) were selected because of their leaving endgroups that can be substituted with N_3 to yield azido-SAMs.

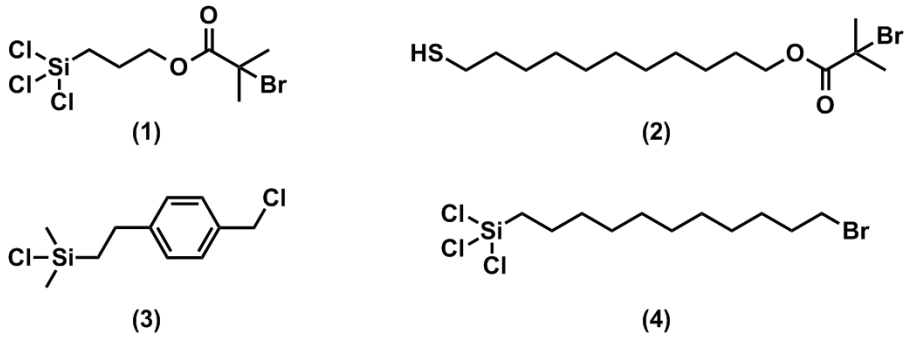

Figure 6.1: Chemical structures of the silanes and thiol used as SAMs: (1) Trichlorosilane-initiator; (2) Thiol-initiator; (3) Chloro(4-(chloromethyl)phenethyl)dimethylsilane; (4) (11-bromoundecyl)trichlorosilane.

6.1.2 Polymer brush growth

ATRP was carried out on different substrates: ⟨100⟩ silicon wafers cut in 1.7 cm^2 squares, these same wafers but covered with gold, glass substrates (optical microscope slides) and AFM cantilevers (either non contact PointProbe cantilevers (Nanosensors, USA) or MLCT-AU V-shaped silicon nitride cantilevers (Bruker, USA)). Organic solvents (ethanol and methanol) were bought from Acros. Deionized water was produced by a Milli-Q Ultrapure purification system (Millipore, USA). Monomers of interest were mono-2-(methacryloyloxy) ethyl succinate (MES) (5), di(ethylene glycol)methyl ether methacrylate (MEO_2MA) (6), the methacrylic acid (MAA)(7) and 2-hydroxyethyl methacrylate (HEMA) (8) (Figure 6.2). Poly(MEO_2MA) is thermoresponsive and exibits a Lower Critical Solution Temperature (LCST) around 27°C in water while poly(MES) and poly(MAA) are pH-responsive. The ligand was 2-2'-bipyridyl, activator was CuCl and deactivator was $CuCl_2$. All these reagents were from Sigma-Aldrich (USA) and used as received.

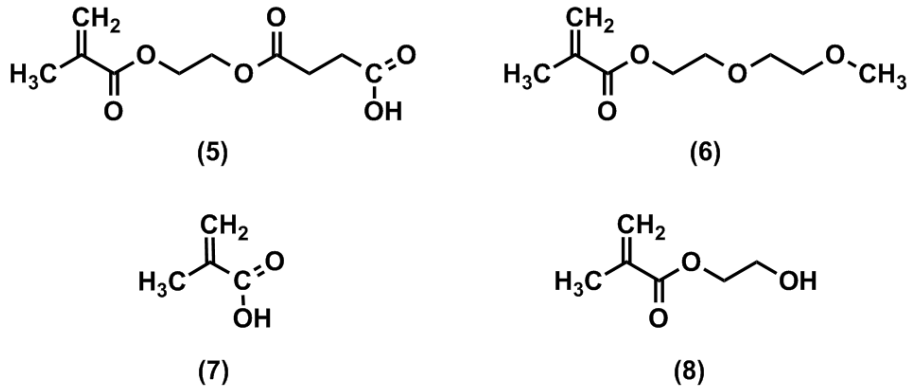

Figure 6.2: Chemical structures of the monomers: (5) mono-2-(methacryloyloxy)ethyl succinate (MES); (6) di(ethylene glycol)methyl ether methacrylate (MEO_2MA); (7) methacrylic acid (MAA); (8) 2-hydroxyethyl methacrylate (HEMA).

6.1.3 Resonance frequency shifts experiments

For the measurement of the kinetics of local reactions with the frequency shift method, PointProbe silicon cantilevers (Figure 6.3) were covered with poly(MAA) brushes. 0.2 M or 0.1 M reactive solutions of N-(3-Dimethylaminopropyl)-N'-ethylcarbodiimide hydrochloride (EDC) and N-Hydroxysuccinimide (NHS) in milli-Q water were prepared. EDC was bought from Sigma-Aldrich and NHS was from Acros.

For the collapse transition temperature (T_{CT}) measurements, these same cantilevers were covered with poly(MEO_2MA). This polymer has an LCST at 27℃. In order to slightly modify the T_{CT}, 0.2 M Na_2SO_4 and 0.1 M NaSCN aqueous solutions were prepared. These two salts were bought from Sigma-Aldrich.

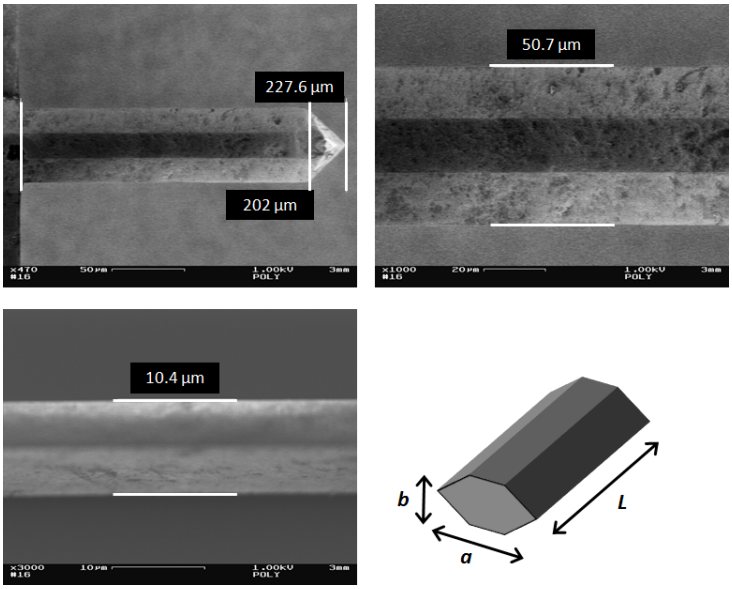

Figure 6.3: SEM images of a non contact PointProbe silicon cantilever.

6.1.4 Deflection experiments

For the measurement of the swelling of pH-responsive polymer brushes with the deflection method, MLCT-AU V-shaped silicon nitride cantilevers (Figure 6.4) were covered with poly(MES) brushes. This polymer was preferred over poly(MAA) because it led to less gel formation on the tip during the polymerization step and thus to less noise in the deflection curves. 50 mM buffer solutions of pH 2, 4, 6.2 and 8 with a 200 mM ionic strength were prepared as follows:

- Phosphate pH 2 buffer: 164 μl (2.4 mmol) of H_3PO_4 and 300 mg (2.5 mmol) of NaH_2PO_4 were dissolved in milli-Q water. Then 1.023 g (25.6 mmol) of NaCl were added and the total volume of the solution was raised to 100 ml by adding water.

- Acetate pH 4 buffer: 229 μl (4 mmol) of CH_3COOH and 123 mg (0.9 mmol) of $CH_3COONa \cdot 3\,H_2O$ were dissolved in milli-Q water. Then 1.114 g (27.9 mmol) of NaCl were added and the total volume of the solution was raised to 100 ml by adding water.

- Phosphate pH 6.2 buffer: 480 mg (4 mmol) of NaH_2PO_4 and 128 mg (0.9 mmol) of Na_2HPO_4 were dissolved in milli-Q water. Then 761 mg (19.0 mmol) of NaCl were added and the total volume of the solution was raised to 100 ml by adding water.

- Phosphate pH 8 buffer: 24 mg (0.2 mmol) of NaH_2PO_4 and 667 mg (4.7 mmol) of Na_2HPO_4 were dissolved in milli-Q water. Then 327 mg (8.2 mmol) of NaCl were added and the total volume of the solution was raised to 100 ml by adding water.

The salts, acidic and basic components were from Fischer (USA).

For the measurement of the kinetics of the "click" reaction, these same cantilevers were covered with poly(HEMA) brushes. This polymer was chosen because of its reactive –OH side groups and of its ease of use (low viscosity, no need to finely adjust the pH of the polymerization solution,...). The alcohol side groups on the brush were activated with a solution of N,N'-Disuccinimidyl carbonate (DSC) and 4-(Dimethylamino)pyridine (DMAP) in DMF. Then they were dipped in a 2-azidoethylamine in CH_2Cl_2 to issue a polymer brush bearing N_3 functionalities. 2-azidoethylamine was prepared according to [3], DSC and DMAP were from Acros, DMF was from Sigma-Aldrich and CH_2Cl_2 was from Fischer.

The reactive solution was prepared by dissolving propargyl-sulforhodamine (9) in a $MeOH/H_2O$ solution (Figure 6.5). To increase the rate of the reaction, L(+)-Ascorbic acid sodium salt, 2-2'-bipyridyl and $CuSO_4 \cdot 5\,H_2O$ were added. Propargyl-sulforhodamine was synthesized

by Dr. Olivier Schicke, bipyridyl and $CuSO_4 \cdot 5\,H_2O$ were bought from Sigma-Aldrich and ascorbate was from Acros.

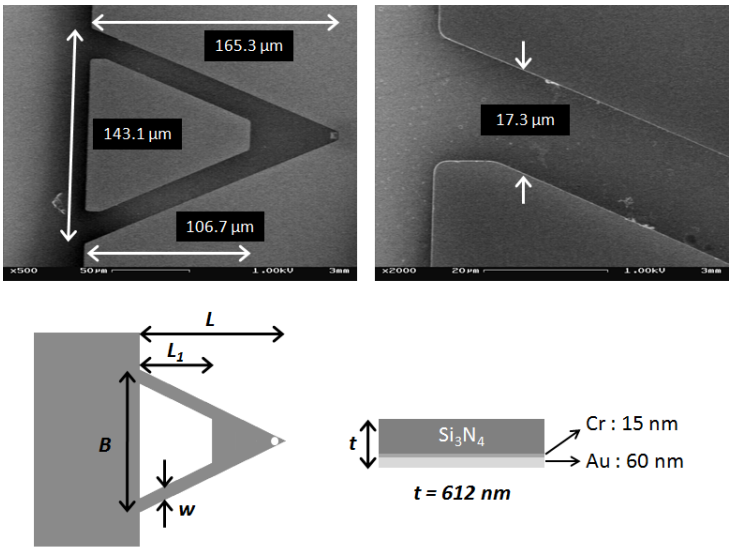

Figure 6.4: SEM images of the V-shaped Si_3N_4 cantilevers.

6.1.5 Local catalysis experiments

For the local catalysis experiments, silanes (3) or (4) were first self-assembled on silicon substrates. A saturated solution of sodium azide (NaN_3) (Acros) in DMF (Sigma-Aldrich) was used to substitute the terminal Cl or Br atoms with N_3. Poly(HEMA) brushes were grafted from V-shaped Si_3N_4 cantilevers and were activated by immersion in a DSC/DMAP solution in DMF before being coupled with the copper-ligand (12) synthesized by Dr. Olivier Schicke and Dr. Peter Hensenne (Figure 6.5). The solvent of this reaction was DMF (Sigma-Aldrich) and the solvents used in the rinsing step were DMF and THF (Acros). Ligand (12) was then complexed with $CuSO_4 \cdot 5\,H_2O$ in methanol. Finally, de-

pending on the experiment, three different alkynes were used: propargyl-sulforhodamine (9), propargyl-TEG-initiator (10) and propargyl-bis(trifluoromethyl)benzene (11) (Figure 6.5). Alkynes (9) and (11) were synthesized by Dr. Olivier Schicke while alkyne (10) was synthesized by Dr. Antony Fernandes.

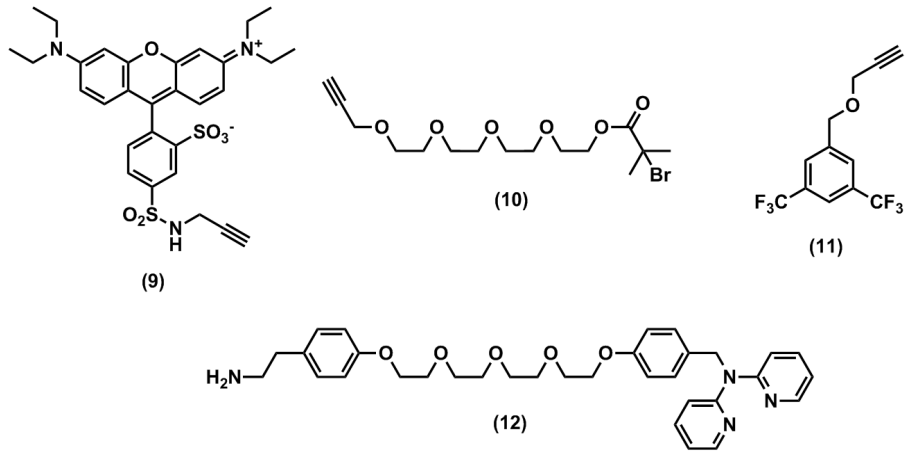

Figure 6.5: Chemical structures of the alkynes and ligand: (9) Propargyl-sulforhodamine; (10) Propargyl-TEG-initiator; (11) Propargyl-bis(trifluoromethyl)benzene; (12) Tyramine ligand.

6.2 Methods

6.2.1 Self-assembled monolayers on silicon and gold

Liquid phase silanization

A silicon wafer (or silicon squares) was immersed in a piranha solution (H_2O_2/H_2SO_4, 1:1 v/v) (Caution! Handle with care, piranha can cause severe burns) to clean it from organic contaminants and to produce

silanol surface groups. After 30 minutes, it was thoroughly rinsed with milli-Q water before being dried under a stream of pure nitrogen. Alternatively, for AFM cantilevers which are more fragile, UV/O_3 irradiation during 30 minutes was preferred to clean and activate their surfaces.

Silanes are very reactive in presence of water. They can dimerize (for monochlorosilanes) or polymerize (for trichlorosilanes). Moreover, silane molecules can be hydrolyzed. The silanization was then processed in a glovebox under dry argon (water content < 0.1 ppm). The wafer was placed in a crystallization dish and covered with 30 ml of toluene. 50 μl of triethylamine were added to neutralize the HCl molecules resulting from the reaction. Finally, a small quantity of silane was taken by capillarity with a Pasteur pipette and injected in the solution. The dish was covered with an aluminum foil and kept in the glovebox overnight. The substrates were then rinsed with methanol and acetone and put under vacuum before use.

Liquid phase thiolization

Gold squares were placed in a crystallization dish. 30 ml of ethanol were poured on them. The thiol was then added dropwise to reach the target concentration (usually, 1 drop) before covering the dish with an aluminum foil. After the desired reaction time, the surfaces were rinsed with ethanol and acetone, dried with N_2 and stored under vacuum.

6.2.2 Polymer brush growth

The monomer was dissolved in a H_2O/MeOH or a H_2O/EtOH solution. For acidic monomers, the pH of the solution was raised to 9 upon addition of NaOH. Then the solution was poured in a Schlenk's flask. Bipyridyl

and $CuCl_2$ were added before sealing the flask with a rubber septum. Nitrogen was then bubbled through a needle to remove the oxygen and the solution was stirred. After 45 minutes, CuCl was added rapidly to avoid its oxidation and the solution was again degassed and stirred during 45 minutes. Typical quantities for all these species are listed in Tables 6.1 to 6.4 for all the monomers used in this study. For copolymer brushes, intermediate quantities were used as shown in Table 6.5.

	Mass (mg)	Vol (ml)	M_w (g/mol)	ρ (g/ml)	# mol (mmol)
Ethanol	-	15	-	0.79	-
Water	-	30	-	1	-
MES (5)	-	18.3	230.21	1.19	95
NaOH	4000	-	40.0	-	100
Bipyridyl	781	-	156.29	-	5
$CuCl_2$	10.8	-	134.45	-	0.08
CuCl	158	-	98.99	-	1.6

Table 6.1: Typical quantities for the ATRP of MES (5).

	Mass (mg)	Vol (ml)	M_w (g/mol)	ρ (g/ml)	# mol (mmol)
Methanol	-	15	-	0.79	-
Water	-	30	-	1	-
MEO_2MA (6)	-	17.5	188.22	1.02	95
Bipyridyl	781	-	156.29	-	5
$CuCl_2$	10.8	-	134.45	-	0.08
CuCl	158	-	98.99	-	1.6

Table 6.2: Typical quantities for the ATRP of MEO_2MA (6).

Aside from that, 5 silicon squares were cut with a diamond tip from a wafer previously silanized with the ATRP initiator and placed in separate small Schlenk's flasks. These were sealed with a septum and degassed by three cycles of vacuum/nitrogen. 4 ml of the solution were then injected in each flask with a syringe through the septa. When the desired

	Mass (mg)	Vol (ml)	M_w (g/mol)	ρ (g/ml)	# mol (mmol)
Methanol	-	15	-	0.79	-
Water	-	30	-	1	-
MAA (7)	-	12.3	86.06	1.01	142.5
NaOH	5400	-	40.0	-	135
Bipyridyl	781	-	156.29	-	5
$CuCl_2$	86	-	134.45	-	0.64
CuCl	158	-	98.99	-	1.6

Table 6.3: Typical quantities for the ATRP of MAA (7).

	Mass (mg)	Vol (ml)	M_w (g/mol)	ρ (g/ml)	# mol (mmol)
Ethanol	-	15	-	0.79	-
Water	-	30	-	1	-
HEMA (8)	-	5.8	130.14	1.07	47.5
Bipyridyl	391	-	156.29	-	2.5
$CuCl_2$	5	-	134.45	-	0.04
CuCl	79	-	98.99	-	0.8

Table 6.4: Typical quantities for the ATRP of HEMA (8).

	Mass (mg)	Vol (ml)	M_w (g/mol)	ρ (g/ml)	# mol (mmol)
Ethanol	-	10	-	0.79	-
Water	-	15	-	1	-
(6) and (7) (total)	-	-	-	-	190
NaOH	var.	-	40.0	-	var.
Bipyridyl	781	-	156.29	-	5
$CuCl_2$	10.8	-	134.45	-	0.08
CuCl	158	-	98.99	-	1.6

Table 6.5: Typical quantities for the ATRP of MAA-*co*-MEO_2MA ("var." means variable).

polymerization time was reached, the silicon squares were removed and rinsed with methanol, water and again methanol before being dried under nitrogen. Figure 6.6 exemplifies the polymer brush growth from a silanized silicon surface in the case of poly(HEMA).

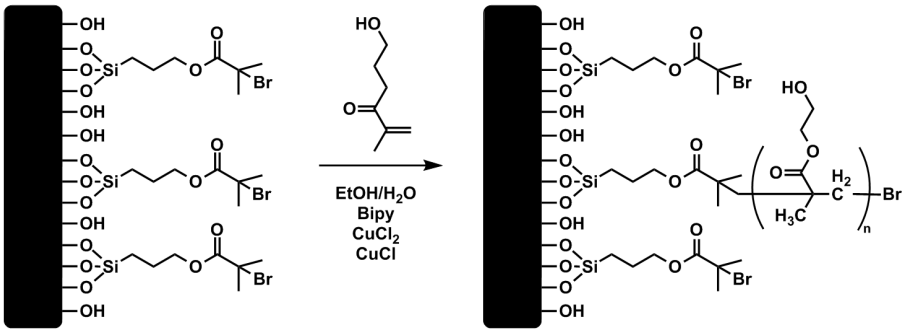

Figure 6.6: Poly(HEMA) brush growth from a silanized silicon wafer with initiator (1).

6.2.3 Resonance frequency shifts experiments

ATRP was carried out on AFM cantilevers as well as on silicon squares in order to have suitable substrates for surface characterization. The AFM cantilevers were handled thanks to a homemade teflon holder (Figure 6.7).

For the measurement of the kinetics of the activation reaction of poly(MAA) brushes with EDC/NHS, the liquid cell of the AFM was filled with water and the functionalized AFM cantilevers were immersed in it for 15 minutes in order to hydrate the brushes and to adjust the position of the laser on the photodiode array. Then, water was replaced with the reactive solution (either a 0.2 M EDC solution or a 0.2 M EDC/0.2 M NHS solution) and resonance frequency curves were recorded every minute until the end of the experiment, i.e. 60 minutes. The for-

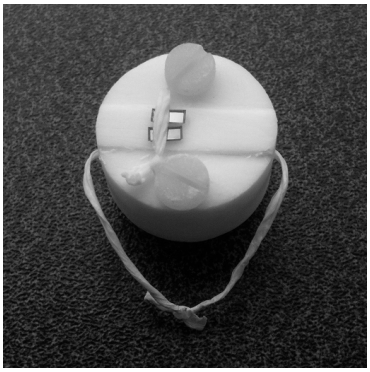

Figure 6.7: Teflon holder for the manipulation of AFM cantilevers.

mation of the activated species is depicted in Figure 6.8 [4–8].

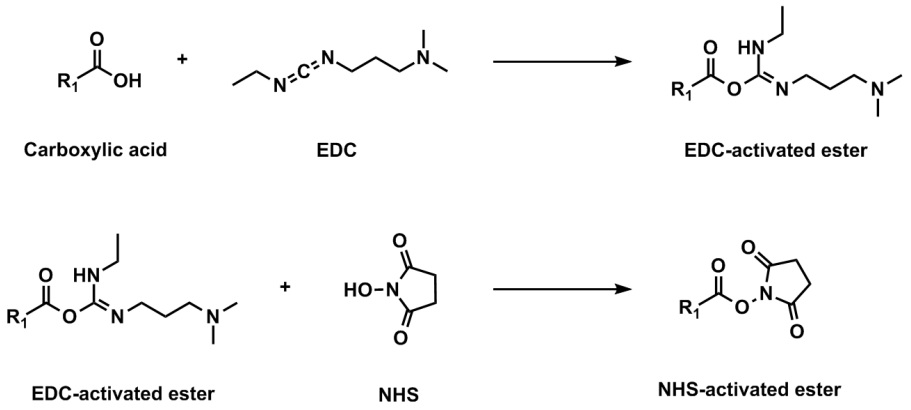

Figure 6.8: The activation reaction of carboxylic acids with EDC and NHS yields to the formation of activated ester intermediates.

For the measurement of the T_{CT} of poly(MEO_2MA) brushes, both QCM-D and AFM measurements were compared. A poly(MEO_2MA) brush was grafted from a quartz sensor which was subsequently placed inside the liquid cell of the microbalance. This cell was fed through a peristaltic pump at a constant flow rate. After 35 minutes of stabilization at 15℃, the liquid inside the cell was heated at a rate of 0.2℃/min up

to 45℃ and the resonance frequency of the sensor was recorded by the built-in software in a continuous fashion. Then, the system was set to stabilize for 35 minutes and the temperature was lowered at the same rate down to 15℃ while still acquiring data. For the AFM experiments, the brush was grafted from a silicon cantilever that was then dipped in the liquid cell of the AFM. This cell was mounted on a Peltier stage for the temperature control of the solution and was fed with a slow but regular flow through a peristaltic pump. After 15 minutes of stabilization, the temperature was ramped up to 38℃ at a rate of 0.5℃/min. Again, the system was allowed to stabilize for 15 minutes and the temperature was then decreased down to 7℃. During both ramps, one resonance frequency curve was recorded every ℃.

All the resonance frequency curves were fitted with the Lorentzian expression for the amplitude of forced damped harmonic oscillators as a function of the excitation frequency ω [9]:

$$A(\omega) = \frac{A_0}{\sqrt{\left(1 - \left(\frac{\omega}{\omega_0}\right)^2\right)^2 + \left(\frac{\omega}{\omega_0 Q}\right)^2}} \tag{6.1}$$

where A_0 is proportional to the amplitude of the excitation force. This equation provides the resonance frequency ω_0 of the lever as well as the quality factor Q of these curves. It appears that the maximum amplitude A_{max} is found for a frequency ω_r usually slightly lower than ω_0. The relation between these two frequencies is given by:

$$\omega_r = \omega_0 \sqrt{1 - \frac{1}{2Q^2}} \tag{6.2}$$

For large Q, this relation becomes $\omega_r = \omega_0$ and the maximum ampli-

tude $A_{max} = A_0 \cdot Q$.

6.2.4 Deflection experiments

Polymer brushes were grafted from gold coated V-shaped Si_3N_4 cantilevers as well as from silicon squares for characterization.

All the experiments were made at constant temperature to avoid thermal drift in the deflection curves. Indeed, it was empirically determined that this thermal drift was ca. 100 nm/°C for bare cantilevers. This came from the fact that they were composed of two relatively thin layers of different materials, i.e. silicon nitride and gold, that have different thermal expansion coefficients (3.3 10^{-6}/°C for Si_3N_4 and 14.2 10^{-6}/°C for Au). This leads to a differential thermal expansion in these two layers when the cantilevers are heated. To release the interfacial stress (or at least part of it), a strain is produced and the cantilevers bend.

Moreover, it was experimentally observed that the level of the liquid inside the cell had to remain constant during the whole analysis. Indeed if the level increased (decreased), an increase (decrease) of the deflection was observed. This was supposedly due to the force that the global upward (downward) motion of the fluid induced on the lever. To reduce this effect, both the inlet and the outlet pipes were connected to the peristaltic pump. Although the same flux was supposed to come in and out of the cell, in practice, that was not always the case and the level of the liquid had to be checked regularly.

For the measurement of the response of a poly(MES) brush in different buffer solutions, this brush was grafted from the Si_3N_4 side of the cantilever. To ease the rinsing step, the viscosity of the solution was decreased by doubling the amount of solvent in comparison to Table 6.1. The cantilever was mounted on the AFM nose and dipped in the liquid

cell. This cell was fed through a peristaltic pump at a constant flow rate. A 6-way valve allowed the selection of the buffer solution injected in the cell. Each solution was put in contact with the cantilever for approximately 20 minutes to let the system equilibrate. The software recorded the deflection signal S of the lever at a frequency of 1 Hz. To avoid thermal drift during the experiment, the temperature was controlled by a Peltier stage and set to 25°C. The measurements were carried out on functionalized cantilevers as well as on bare cantilevers for comparison.

For the measurement of the kinetics of the "click" reaction between an azidated brush and alkyne molecules in solution, poly(HEMA) brushes were grafted from these Si_3N_4 cantilevers. The –OH side groups on the brushes were activated by immersing them overnight in a 0.1 M DSC and 0.1 M DMAP solution in DMF. Then they were reacted overnight with 2-azidoethylamine (50 mM solution in CH_2Cl_2) to issue a polymer brush bearing N_3 functionalities (Figure 6.9).

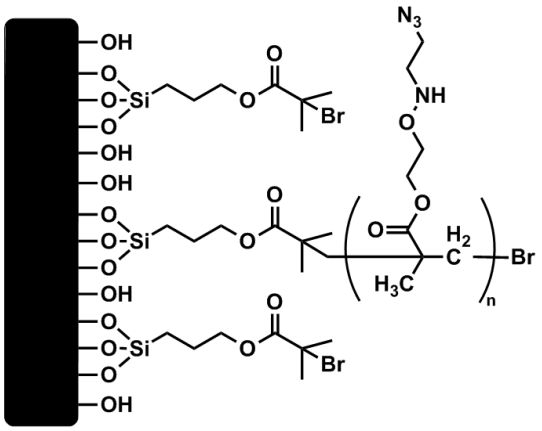

Figure 6.9: The poly(HEMA) brushes grafted from the cantilevers were modified with NaN_3 in order to obtain N_3 pendant groups.

500 ml ($MeOH/H_2O$, 1:1 v/v) of the reactive solution were prepared with 25 mg (80 μM) of propargyl-sulforhodamine (9) and 6.4 mg (64 μM)

of ascorbic acid sodium salt. Before the experiment, 50 ml of this solution were withdrawn and 2.5 mg (320 μM) of 2-2'-bipyridyl as well as 4 mg (320 μM) of $CuSO_4 \cdot 5\,H_2O$ were added. The resulting solution was then filtered and degassed before use.

The cantilever was first allowed to stabilize for 30 minutes in the $MeOH/H_2O$ solution before switching the valve to the reactive solution. Again, the deflection signal was recorded at a frequency of 1 Hz, and the temperature was set at 30°C by a Peltier stage. The measurements were carried out on functionalized cantilevers as well as on bare cantilevers for comparison.

For both series of experiments, the raw data in volts were converted to actual deflections in (nano)meters. This was realized by measuring force curves on a hard substrate. The signal in volts was then related to the vertical displacement of the AFM nose in nanometers in the repulsive region of the force curves. This issued a $\Delta z/S$ ratio of 53 nm/V.

6.2.5 Local catalysis experiments

Surfaces preparation

During the catalysis experiment, the tip was scanned on the substrate. Afterwards, the surface was rinsed and dried before being imaged with the AFM. As the produced drawing were relatively small (ca. 10 μm long lines), it was important to build some landmarks on the surfaces. Our strategy was to use a TEM grid and to reproduce this grid on silicon squares. Therefore, a 100 nm-thick thermal oxide was grown on a silicon wafer (170 minutes at 1000°C under an O_2 flux). Then the wafer was diced into 1 cm^2 squares and a TEM (Transmission Electron Microscopy) grid was stuck on each of these squares with carbon tape. The squares

were then stuck on a sacrificial wafer to ease their manipulation and a 20 nm chromium layer was evaporated on them. TEM grids were stripped off and the substrates were rinsed with acetone to remove the residual carbon tape. The exposed silicon oxide was removed in buffered HF during 95 seconds. Finally, before use, the chromium layer was removed with standard chromium etchant for 5 minutes at a etch rate of 4 nm/s. To remove residual chromium and organic contaminants as well as to produce silanol surface groups, the silicon squares were immersed in a piranha bath during 1 hour (Caution! Handle with care, piranha can cause severe burns). This gave surfaces with a typical RMS roughness of 0.3-0.4 nm. The resulting pattern is shown in Figure 6.10. It is composed of 5x5 arrays of 100 nm-thick silicon oxide squares. Each array is identified with a letter.

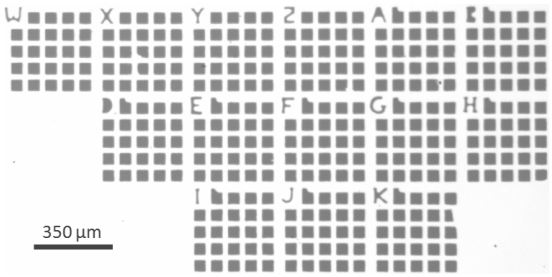

Figure 6.10: The substrates were patterned with TEM grids to form 5x5 arrays of SiO_2 squares identified by a letter.

After this preliminary step, these surfaces were silanized with silanes (3) or (4) (Figure 6.11).

The next step was to substitute the terminal Cl or Br atoms with N_3. A saturated solution of NaN_3 in dry DMF was prepared inside the glovebox. To speed up the dilution of NaN_3, the solution was heated at 50°C and it was stirred for 30 minutes. The silicon squares were placed in the slits of a cylindrical Teflon holder inside a Schlenk's flask and the NaN_3 solution was poured. The reaction took place overnight and the

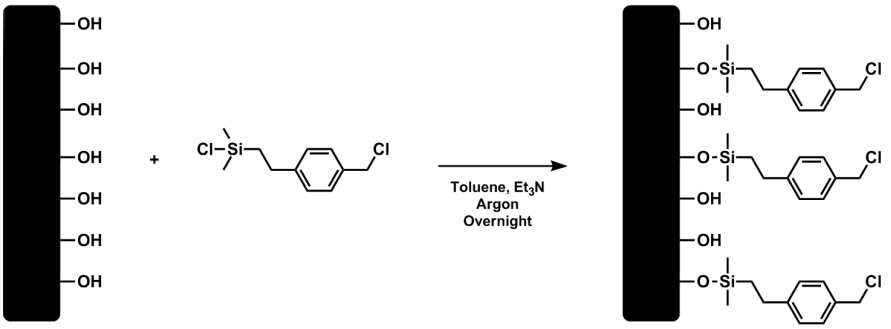

Figure 6.11: Silanization of silicon wafers with silane (3).

wafers were then rinsed with DMF and dried with nitrogen (Figure 6.12).

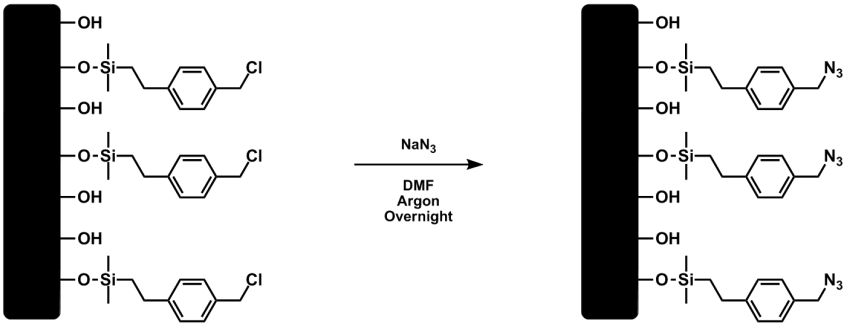

Figure 6.12: S_N2 substitution of the terminal Cl atoms on silane (3) with N_3.

Tips preparation

Catalytic complexes were attached to V-shaped Si_3N_4 cantilevers and to their tips (Figure 6.13). Poly(HEMA) brushes were first grafted from their surface. They were then activated with DSC/DMAP as described above. 75 mg (0.13 mmol) of ligand (12) were dissolved in 10 ml anhydrous DMF under argon. The cantilevers were degassed in a Schlenk's

flask and the solution was injected. After overnight reaction, they were rinsed with THF and DMF and dried with nitrogen. Finally, the cantilevers were immersed in a 0.1 M methanolic solution of $CuSO_4 \cdot 5\,H_2O$ (160 mg in 6 ml) for 3 hours at room temperature. After being rinsed with methanol and water, the cantilevers were put under vacuum before use. Again, these procedures were applied to silicon squares for further characterization.

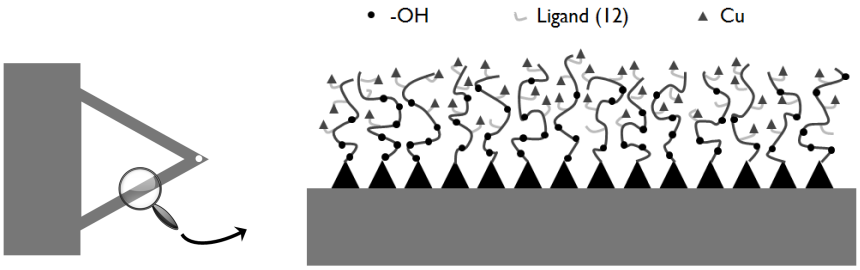

Figure 6.13: The catalytic complex was attached to V-shaped Si_3N_4 cantilevers and to their tips.

Solution preparation

Depending on the alkyne to be reacted on the azide monolayer and on the experiment to be performed (local catalysis or CuAAC on the whole substrate), different solutions were prepared.

Alkynes (9), (10) and (11) were used in preliminary tests where silicon square substrates were functionalized. In this case, the reactive solutions had to contain a ligand and a Cu^{I} source. For alkyne (9), the concentrations were: (9)/bipy/$CuSO_4 \cdot 5\,H_2O$/ascorbate = 1.2/4.8/4.8/1 $\cdot 10^{-3}$ mmol in H_2O/MeOH = 7.5/7.5 ml. The solution was then filtered to remove aggregates larger than 100 nm. For alkyne (10), the concentrations were: (10)/(12)/$CuSO_4 \cdot 5\,H_2O$/ascorbate = 1/0.1/0.1/0.2 mmol

in H_2O/acetone = 7.5/7.5 ml. For alkyne (11), the concentrations were: (11)/bipy/$CuCl_2$/ascorbate = 0.3/0.12/0.12/0.24 mmol in H_2O/MeOH = 7.5/7.5 ml.

Alkyne (9) was used for local catalysis experiments. As previously, a 80 μM solution of (9) in methanol and water (1:1 v/v) was prepared. To reduce Cu^{II} during the reaction, ascorbic acid was added (32 μM). As (9) is not highly soluble in the solvents, the solution was filtered to remove aggregates larger than 100 nm. A saturated solution of (9) was then obtained. The final reaction to be achieved is described in Figure 6.14 where R can be deduced from (9).

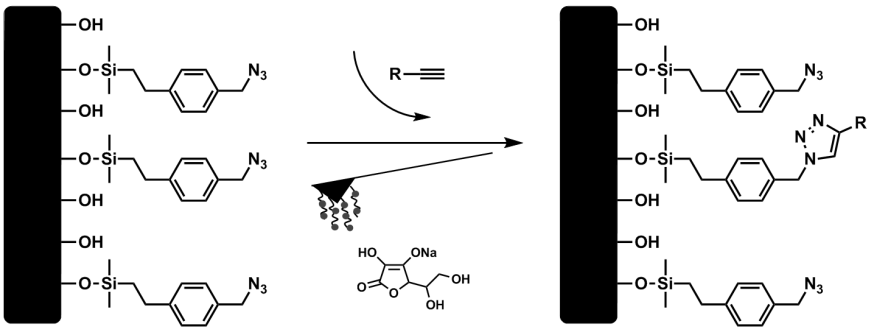

Figure 6.14: Description of the local catalysis of an alkyne-azide cycloaddition reaction with catalytic complexes grafted on an AFM tip.

To realize the local catalysis experiment, the modified lever was mounted on the AFM nose and the azidated patterned surface was fixed on the sample holder. A H_2O/MeOH (1:1 v/v) solution was injected in the liquid cell through the peristaltic pump and the system was allowed to equilibrate for 15 minutes. During this time, AFM images were acquired to determine an appropriate location for the lithography and the pattern was prepared with the built-in script (picolith). The reactive solution was then selected with the 6-way valve and when it arrived in the liquid cell, the lithography was started. Typical values for the scan

speed and the applied force during the lithography were 0.5 μm/s and 17 nN respectively. As soon as the lithography was completed (after 3-4 minutes), the reactive solution was replaced with H_2O/MeOH to rinse the sample. This sample was then dried with a flow of N_2 before being imaged with the AFM.

6.3 Characterization

6.3.1 X-Ray Reflectivity (XRR)

X-ray reflectograms were taken with a two-circle goniometer (Siemens D5000) with 30 cm radius and 0.002 position accuracy (Figure 6.15). X-rays (Cu K_α, $\lambda = 0.15418$ nm) were obtained from a rotating anode (Rigaku, Japan) (a) operated at 40 kV and 300 mA and collimated by a multi-layers mirror (Osmic, Japan) (b). The delivered parallel beam had a 0.0085 angular divergence. After being shaped by a series of slits (c,d), the beam was reflected by the sample (e) which was fixed at the center of the goniometer with an automated procedure using a vertical stage of 1 μm resolution (f) and the reflected intensity was measured by a scintillation detector (h) placed after a filter (g) and a 200 μm receiving slit. The length of the beam was around 0.8 cm and its width was around 40 or 100 μm. Data were scaled by the incident intensity and corrected for beam spillage at very low angles of incidence. The thickness of the organic layer was calculated based on the Patterson function of the reflectogram as detailed elsewhere [10]. To summarize, it was shown that under the approximations of neglecting multiple reflections and refraction and of considering that the wavevector transfer q_z does not change significantly from one medium to the next, the reflectivity $R(q_z)$ can be written as:

$$R(q_z) = \frac{(4\pi r_e)^2}{q_z^4} \left| \int_{-\infty}^{+\infty} \frac{d\rho(z)}{dz} e^{iq_z z} dz \right|^2 \tag{6.3}$$

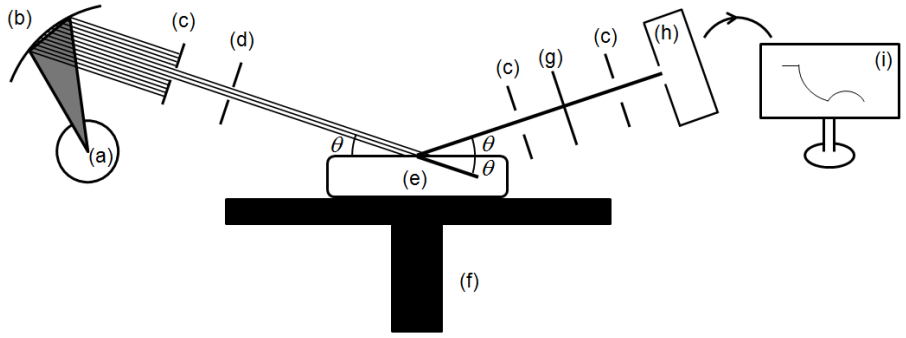

Figure 6.15: Scheme of the XRR apparatus: (a) Rotating anode; (b) Osmic mirror; (c) Slits ; (d) Tunable slit; (e) Sample; (f) Vertical moving stage; (g) Filter; (h) Detector; (i) Computer.

In this equation, $\rho(z)$ is the electron density of the layer as a function of the depth z and r_e is the classical radius of an electron. Then by applying the Wiener-Khinchin theorem:

$$R(q_z) \cdot q_z^4 = (4\pi r_e)^2 \mathcal{F}^{-1}\left(\rho'(z) * \rho'(z)\right) \tag{6.4}$$

$$\text{or} \quad R(q_z) \cdot \left(\frac{\sin\theta}{\lambda}\right)^4 = \left(\frac{r_e}{\pi}\right)^2 \mathcal{F}^{-1}\left(\rho'(z) * \rho'(z)\right) \tag{6.5}$$

So by computing the Fourier transform of the data $R(q_z)$ after multiplication by $(\sin\theta/\lambda)^4$, the pseudo-autocorrelation function of the first derivative of the electron density as a function of the thickness also called the Patterson function was obtained (up to a constant). The abscissas corresponding to the maxima of this function gave the thicknesses of each organic layer [11].

As a very first approximation of the thickness of a monolayer, the fact that the amplitude of the reflected signal exhibits a minimum when the beams coming from the top and bottom interfaces interfere destructively was used (Figure 6.16). This phenomenon can be described by geometric parameters. Indeed, the optical path difference Δl is equal to $\lambda/2$:

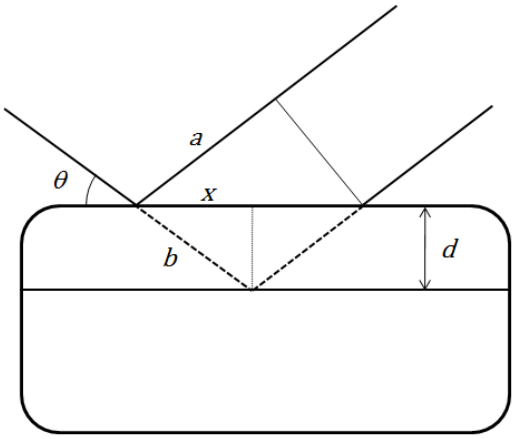

Figure 6.16: There is destructive interference when the optical path difference is equal to $\lambda/2$.

$$\Delta l = 2b - a = \frac{\lambda}{2} \tag{6.6}$$

Moreover, the index of refraction is close to one for small angles. In that case, the angle of refraction is equal to the angle of incidence and equation 6.6 then writes:

$$x = \frac{d}{\tan\theta} \tag{6.7}$$

$$a = 2x\cos\theta \tag{6.8}$$

$$= 2d\frac{\cos^2\theta}{\sin\theta} \tag{6.9}$$

$$b = \frac{d}{\sin\theta} \tag{6.10}$$

$$\Longrightarrow \frac{2d}{\sin\theta} - \frac{2d\cos^2\theta}{\sin\theta} = \frac{\lambda}{2} \tag{6.11}$$

$$\Longrightarrow d = \frac{\pi}{2k_{z,min}} \tag{6.12}$$

with $k_{z,min} = (2\pi/\lambda)\sin\theta_{min}$, being the first minimum of the reflectivity curve.

It was also possible to extract the electron density profile of the organic layer $\rho(z)$ from the data. Therefore, the film had to be modeled as a succession of thin virtual homogeneous layers of zero interfacial roughness, stacked over the silicon substrate of electron density held at 700 electrons/nm^3. The electron density ρ_i of the virtual layers were fittable parameters, whereas their widths w_i were held constant at a single value corresponding to the information content of the XRR curves, $w_i = \pi/(2k_{z,max})$ with $k_{z,max}$ the maximal experimental value of k_{z0}. Typically, $w_i \simeq 0.35$ nm. The absorbance of the virtual layers was set to $5{\cdot}10^{-7}$ nm^{-1}, and the absorbance of the silicon substrate to $1.5{\cdot}10^{-5}$ nm^{-1}. The initial number of virtual layers was set to d_{max}/w_i. From this model of electron density, the film reflectivity was computed using dynamical theory and the chi-square function was minimized with a Marquardt-Levenberg algorithm. In order to avoid numerical problems and unphysical solutions due to the large number of parameters in the final model of the electron density, a regularization technique was applied by adding a smoothing constraint to the chi-square function, as fully described

elsewhere [12]. The grafting densities were obtained from the electron density profiles $\rho(z)$ in the following way. For silane monolayers, the electron density profile of a clean silicon wafer, $\rho_{\mathrm{Si}}(z)$, was subtracted from $\rho(z)$, after horizontal displacement to bring the Si interfaces in coincidence. Then, the area below the resulting profile was computed, giving access to ζ_g, the total number of electrons belonging to grafted molecules, per unit surface. The grafting density was then obtained as $\sigma_g = \zeta_g/Z$, where Z is the number of electrons of the silane molecule, excluding the reactive Cl atoms (because they are removed during the self-assembly). Due to experimental errors, to the small thickness of the silane layers, and to the uncertainty of the lateral shift of one profile versus another, errors of about 20% are to be expected on the values of the grafting densities obtained from the density profiles of the silane monolayers.

6.3.2 Ellipsometry

Ellipsometry is a surface analysis technique used to determine the thickness and the optical parameters of a series of thin layers on a substrate [13, 14]. The principle of this tool is to measure the variations of the polarization of an electromagnetic wave when it interacts with the analyzed sample. When a ray of light falls on a surface with an angle of incidence φ_1, part of it is reflected with the same angle while the other part is refracted with an angle of refraction φ_2 and go through the material. The relation between these angles is the well known Snell's law:

$$N_1 \sin\varphi_1 = N_2 \sin\varphi_2 \tag{6.13}$$

where $N_i = n_i - k_i j$ is the complex index of refraction of material i. n is the index of refraction of the material (dependent on the speed of the

traveling light) and k is coefficient of extinction (dependent on the rate at which the amplitude of the light decreases inside the material). The plane containing the incident, reflected and refracted beams is the "plane of incidence". The electric field associated with the wave can be separated in two components: the component that is perpendicular to the plane, E_p and the parallel component, E_s. Maxwell's equations describe the behavior of these components upon reflection. If only their amplitudes are considered, the ratio between the incident p-wave (s-wave) and the reflected one can be calculated. These ratios are given by the Fresnel's coefficients. Considering an interface between two different materials, they are given by:

$$r_{12}^{p} = \frac{N_2 \cos\varphi_1 - N_1 \cos\varphi_2}{N_2 \cos\varphi_1 + N_1 \cos\varphi_2} \tag{6.14}$$

$$r_{12}^{S} = \frac{N_1 \cos\varphi_1 - N_2 \cos\varphi_2}{N_1 \cos\varphi_1 + N_2 \cos\varphi_2} \tag{6.15}$$

In the case of a thin layer of thickness d, there are two interfaces: air/film and film/substrate. Multiple reflections arise in the film and the reflected beam is the sum of the primary reflected beam and the beams reflected on the second interface as illustrated in Figure 6.17.

In this case, the ratios are given by the total coefficients of reflection:

$$R^{p} = \frac{r_{12}^{p} + r_{23}^{p} \exp(-j2\beta)}{1 + r_{12}^{p} r_{23}^{p} \exp(-j2\beta)} \tag{6.16}$$

$$R^{S} = \frac{r_{12}^{s} + r_{23}^{s} \exp(-j2\beta)}{1 + r_{12}^{s} r_{23}^{s} \exp(-j2\beta)} \tag{6.17}$$

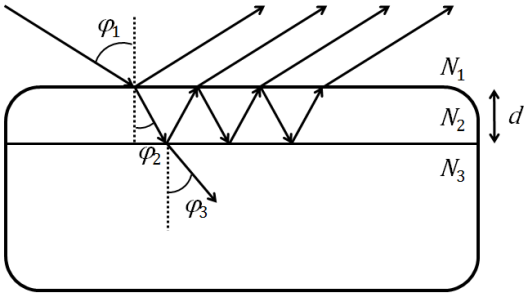

Figure 6.17: The reflected beam is the sum of the beam reflected on the first interface and the beams reflected on the second interface.

where

$$\beta = 2\pi \left(\frac{d}{\lambda}\right) N_2 \cos\varphi_2 \tag{6.18}$$

and is called the "phase thickness".

The parameters Ψ and ρ can now be defined as:

$$\tan\Psi \doteq \frac{|R^P|}{|R^S|} \tag{6.19}$$

$$\rho \doteq \frac{R^P}{R^S} \tag{6.20}$$

As the phase of each component shifts upon reflection, the phase shifts between the p and s components of the incident wave, δ_1, and of the reflected wave, δ_2, have to be defined as well as their difference $\Delta \doteq \delta_1 - \delta_2$. Ψ and ρ are the measured values during the ellipsometric

experiment. Finally, the fundamental equation of ellipsometry writes:

$$\rho = \tan \Psi \cdot e^{j\Delta} \tag{6.21}$$

When a measurement is run for m different wavelengths, $2m$ ellipsometric data sets are obtained. If the sample is composed of p layers of unknown thicknesses, $(2m + 1) \cdot p$ parameters have to be calculated (n_i and k_i for each λ and thickness). There are thus more unknowns than equations. To bypass this issue, a model which approximates $n_i(\lambda)$ and $k_i(\lambda)$ has to be used.

Brush thicknesses were measured with a Uvisel spectroscopic ellipsometry (Horiba-Jobin-Yvon, France) at an angle of incidence of 70° and wavelengths ranging from 400 to 850 nm with a 25 nm step. Depending on the substrate, different models were created for the determination of the brush thickness. In the case of silicon wafer, the model comprised three layers: the silicon substrate itself, the native silicon oxide (fixed at 15 Å) and the organic layer. For the QCM-D sensors, the model had four layers: gold, titanium, silicon oxide, and the organic layer. The optical parameters of the inorganic layers came from data by D.E. Aspnes [15, 16]. The ellipsometric data for the organic layer were fitted by the DeltaPsy 2 software of the apparatus with the Cauchy model. This model approximates the complex index of refraction $n(\lambda)$ with:

$$n(\lambda) = n_0 + \frac{n_1}{\lambda^2} + \frac{n_2}{\lambda^4} \tag{6.22}$$

and the extinction coefficient $k(\lambda)$ is neglected. This model is only valid for materials that are transparent at the considered wavelengths. It has the advantages of being quite simple and to contain only three parame-

ters which facilitates the numeric optimization. This model worked well for brushes thinner than 70 to 80 nm. For larger thicknesses, the fit was less accurate and another model, more complex, had to be used. One of the more satisfying models is the "classical" one. It is given by:.

$$\widetilde{\varepsilon}(\omega) = \varepsilon_\infty + \underbrace{\frac{(\varepsilon_s - \varepsilon_\infty)\omega_t^2}{\omega_t^2 - \omega + j\Gamma_0\omega}}_{\text{Single oscillator}} + \overbrace{\frac{\omega_p^2}{-\omega^2 + j\Gamma_D\omega}}^{\text{Drude's model}} + \underbrace{\sum_{i=1}^{2} \frac{f_i\omega_{0i}^2}{\omega_{0i}^2 - \omega^2 + j\Gamma_i\omega}}_{\text{Double oscillator}} \tag{6.23}$$

In this expression, ε_x are the dielectric constants of the oscillators x considered in the model, ω_x are their resonance frequencies and Γ_x, their damping coefficients. This model includes 12 coefficients that have to be computed to minimize the error function between experimental and theoretical curves. This is suitable as far as they are independent from each other [13, 17]. The measurements were carried out three times at different spots on the substrate. The evaluated ellipsometric thickness of the polymer brushes was compared to the thickness measured by XRR: both measurements generally agreed to within less than 10%.

6.3.3 X-Ray Photoelectron Spectroscopy (XPS)

X-Ray Photoelectron Spectroscopy (XPS) is a quantitative analysis technique that gives chemical information about the surface of a material [18–20]. Its basic principle is to send an X-ray beam on a sample and to collect the produced electrons. An energy analyzer measures the kinetic energy of these electrons which allows the determination of their binding energy. As this energy is different for each orbital of each atom, the atom they originate from can be determined.

When photons go through a material, three different inelastic phenomena can occur: Compton diffusion, production of e^-/e^+ pairs and photoelectric effect. For electrons of higher energy ($\varepsilon > 10$ MeV), the pair production is dominant. In this case, the energy from the incident photon is converted into both e^- and e^+. The latter has a very short lifetime and annihilates by colliding with an electron, producing two photons of 511 keV travelling in opposite directions. For electrons of intermediate energy (10 MeV $> \varepsilon >$ 500 keV), Compton diffusion is the more likely phenomenon. Here, the photon gives part of its energy to an electron. The electron is then excited and the photon continues its way with a deviated trajectory. Finally, for smaller photon energies ($\varepsilon <$ 500 keV), the photoelectric effect predominates. All the photon energy is absorbed by an electron and, if this energy is sufficient, it is ejected from the material. Its kinetics energy can be calculated with:

$$E_{kin} = h\nu - E_b - W_f \tag{6.24}$$

where $h\nu$ is the photon energy, E_b is the binding energy of the electron and W_f is the work function which is the difference between the energy of vacuum and the Fermi level.

Although photons can penetrate deeply in matter (a few μm for keV photons), emitted electrons come from a much smaller thickness. Indeed, once they are freed, they collide elastically or inelastically with other electrons from the sample. The average distance that an electron can cover before undergoing an elastic (λ_e) or inelastic (λ_i) collision is called the mean free path. In a typical experiment, one cares only about λ_i for the quantitative analysis in XPS. The intensity of the electronic current decreases as a function of the depth as:

$$I = I_0 e^{-\frac{x}{\lambda_i}} \tag{6.25}$$

From this equation, we can calculate that more than 95% of the electronic current comes from a thickness $d = 3\lambda_i \sin\varphi$ with φ the angle between the analyzer axis and the sample surface (Figure 6.18).

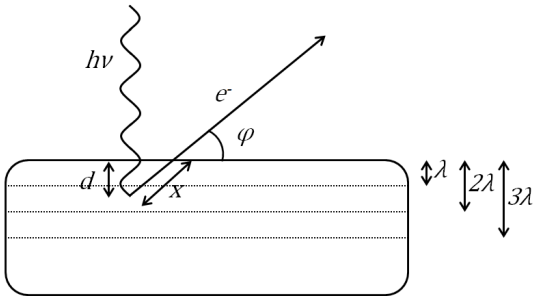

Figure 6.18: 95% of the electronic current comes from a thickness $d = 3\lambda_i \sin\varphi$.

The inelastic mean free path of a polymer lies around 20 Å. The depth of information is thus smaller than 10 nm. In order to avoid contamination of the sample and to increase the mean free path of the electrons inside the spectrometer, the analysis has to be carried out in Ultra High Vacuum ($p < 10^{-8}$ mbar).

XPS data were obtained with a SSX 100/206 spectrometer (1988) from Surface Science Instruments (USA). The monochromatized and microfocused Al K_α source (a) issued photons with a 1486.7 eV energy in the analysis chamber under a pressure of $2 \cdot 10^{-9}$ mbar. After collision of the photons with the sample (b) (elliptical spot size: 1.7 × 1 mm^2), the emitted electrons were focused (c) towards a hemispherical energy analyzer (d) with a constant pass energy of 50 eV (for elemental spectra) or 150 eV (for survey scans). Due to the potential difference between the

two plates of the analyzer, only the electrons having their energy close to the pass energy could go through. Then a multichannel photomultiplier (e) amplified the signal with a gain of 10^8, signal that was finally recorded by a computer (f) (Figure 6.19).

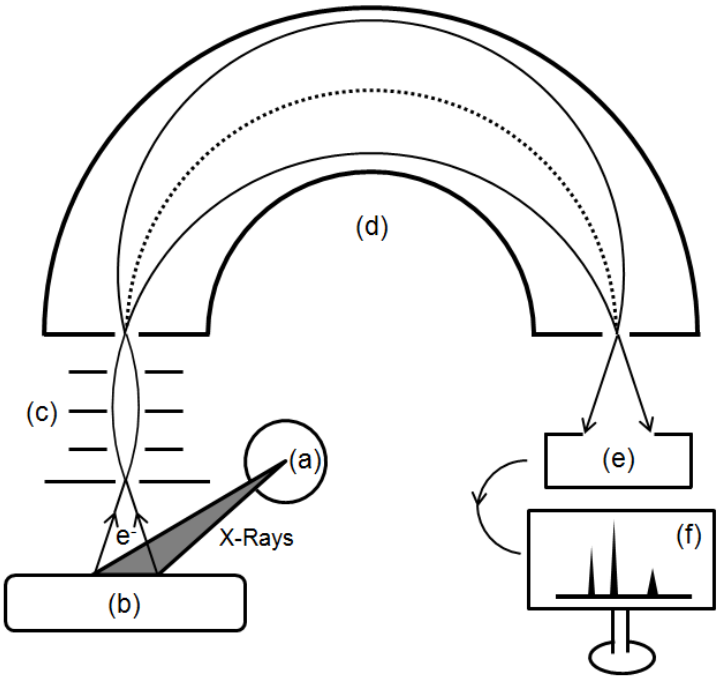

Figure 6.19: Scheme of the XPS apparatus: (a) Rotating anode; (b) Sample; (c) Electronic lenses; (d) Energy analyzer; (e) Multichannel photomultiplier; (f) Computer.

The major interest of this technique is its capacity to provide a quantitative information about the elementary composition of the surface under study. In order to sort this information, a model that takes into account every involved aspects is needed. This model is called the three-step model: 1. the production of photoelectrons, 2. their transport and 3. their detection:

$$dI_A = \underbrace{I_x(\gamma)T(\Omega, E_A)D(E_P)A(\alpha)\Delta\Omega}_{\text{Step 3}} \underbrace{N\chi_A \frac{d\sigma_x}{d\Omega}}_{\text{Step 1}} \underbrace{\exp\left[\frac{-z}{\lambda(E_A)\cos\alpha}\right]}_{\text{Step 2}} dz \tag{6.26}$$

In this equation,

- I_A is the photoelectron flux coming from atoms A,
- $I_x(\gamma)$ is the X-ray flux on the sample,
- γ is the angle between the X-ray beam and the analyzed electron beam,
- $T(\Omega, E_A)$ is the transmission function for the instrument, the direction Ω and electrons with kinetic energy E_A,
- $D(E_P)$ is the detector efficiency according to the pass energy,
- $A(\alpha) = A_0/\cos\alpha$ with A_0 the analyzed area for a take-off angle $\alpha = 0$,
- $\Delta\Omega$ is the admission angle of the analyzer,
- N is the atomic density of the material,
- χ_A is the atomic fraction of atoms A in the sample,
- $\frac{d\sigma_x}{d\Omega}$ is the differential cross section for the photoelectric effect and
- $\lambda_i(E_A)$ is the inelastic mean free path of photoelectrons having a kinetic energy $= E_A$.

This equation is rather complete but does not take into account elastic scattering, attenuation in the medium, reflexion and refraction of

the X-rays inside the material and supposes that the surface is of infinite length and atomically flat. Every component of equation (6.26) are either measured during the experiment or tabulated and the atomic composition of the sample can then be calculated.

Besides this elementary quantification, XPS offers the possibility to analyze the chemical composition of the sample. Indeed, the binding energy of an electron is dependent on the bonds that its corresponding atom makes with surrounding atoms and on their electronegativity. The values of these "chemical shifts" are tabulated for many common compounds.

6.3.4 Fourier Transform Infrared Spectrometry (FTIR)

When photons enter a material, a series of phenomena can occur depending on their wavelength λ. When λ lies in the infrared spectrum, their energy can be transfered to the molecules constituting the material and be converted into vibrational energy. This is basically the working principle of Fourier Transform Infrared Spectroscopy (FTIR). The different vibrational energy states are quantified. So, in order to be absorbed, the energy of the incident photon has to match the transition energy from one level to another in the target sample. Molecular vibrations can be very complex. Indeed, a molecule containing N atoms has $3N$ degrees of freedom. Three of them represent translational motion in the three directions of space (x, y and z) and three represent rotational motion around these three axis. There is then $3N-6$ degrees of freedom devoted to vibrational motion. This is a maximum value. Indeed, there can only be a transition if the dipolar moment of the molecule changes during the vibration. If the molecule has some elements of symmetry, some modes can be degenerated or forbidden. For instance, linear molecules have only 2 rotational modes since a rotation around the molecular axis

does not induce a movement of their atoms and they thus have $3N - 5$ vibrational modes. For a diatomic molecule, $N = 2$ and there is then $6 - 5 = 1$ vibrational mode allowed (stretching) while for ethylene, $N = 6$ and there are $18 - 6 = 12$ vibrational modes. Figure 6.20 presents the 6 different modes of a terminal CH_2 group.

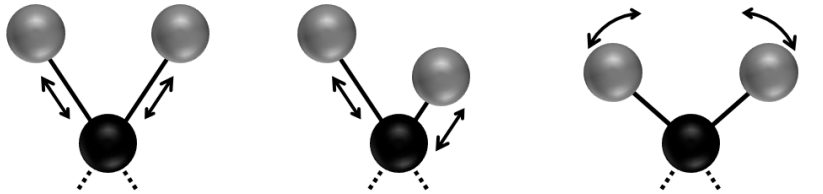

(1) Symmetric stretching (2) Asymmetric stretching (3) Scissoring

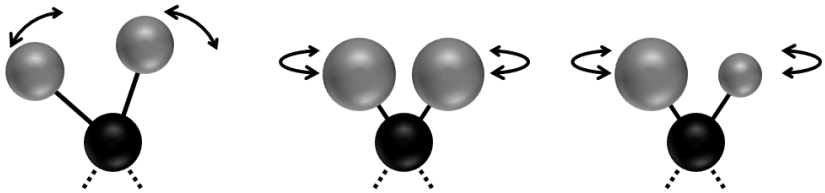

(4) Rocking (5) Wagging (6) Twisting

Figure 6.20: Each CH_2 moiety of ethylene has 6 vibrational degrees of freedom.

Each vibrational mode can be described by a potential function known as the Morse potential shown by the black line in Figure 6.21 as a function of the distance between atoms. For small energies, this potential can be approximated by the harmonic oscillator (Hooke's law) shown by the gray line in Figure 6.21. In this model, the atoms vibrate around a constant equilibrium position at a certain characteristic frequency ν_i for each mode i. The vibrational energy states V_{iv} can be calculated by:

$$V_{iv} = h\nu_i \left(v_i + \frac{1}{2} \right) \tag{6.27}$$

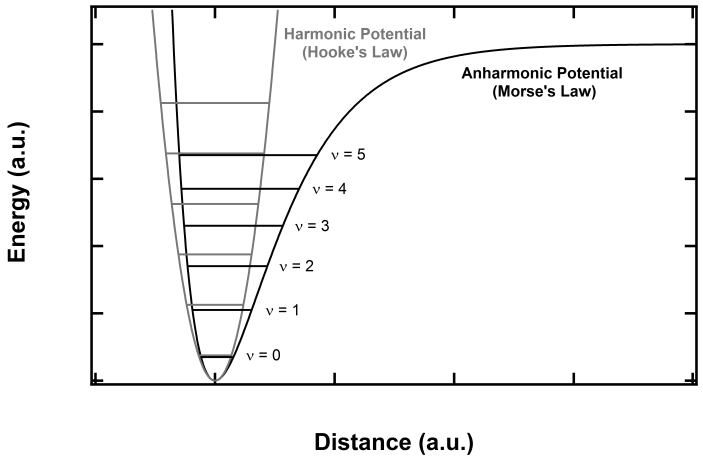

Figure 6.21: Morse potential model for the potential energy of a diatomic molecule (black line) and the harmonic oscillator approximation (gray line). When the energy of the molecule increases, the mean distance between atoms increases as well and the permitted energy levels become closer from each other.

In this equation, h is the Plank's constant and v_i, the quantum number associated with the i^{th} mode. When energy increases, deviation from the harmonic potential becomes important and the vibrational energy states have to be described using the anharmonic Morse potential. The vibrational energy states can be rewritten to a first approximation by:

$$V_{iv} = h\nu_i \left(v_i + \frac{1}{2} \right) + h\nu_i x_i \left(v_i + \frac{1}{2} \right)^2 \tag{6.28}$$

where x_i is the anharmonic constant [21].

An FTIR experiment consists thus in bombarding a sample with infrared photons of varying wavelength and measuring the transmitted intensity. The different peaks in the spectrum correspond to molecular vibrations which gives an insight into the composition of the sample.

In this work, FTIR spectra were obtained with a Thermo Nicolet Nexus 870 spectrometer (Thermo Scientific, USA) operated at a wavenumber ranging between 4000 and 400 cm^{-1} with a 8 cm^{-1} resolution and 128 passes. The analysis chamber was filled with nitrogen and the absorbance was recorded. Acidic samples were immersed into water for 10 minutes then in a $Na_2CO_3/Na(CO_3)_2$ buffer solution (pH = 10) to equilibrate the carboxylic acid functional groups. To protonate the samples, they were dipped into a HCl solution at pH = 3 for 30 minutes.

6.3.5 Atomic Force Microscopy (AFM)

The Atomic Force Microscope (AFM) monitors the interaction between a sharp tip (radius of curvature ca. 10 nm) at the end of a cantilever (a) and the surface of a sample (e) while it is scanned over it [9, 22, 23]. Typically, the deflection of the cantilever or the oscillation amplitude are measured using a laser spot (c) that is reflected from the apex of the cantilever towards a position sensitive detector (PSD) (d) connected to a computer (f) but other techniques exist. The precise x, y and z adjustments are made through piezoelectric crystals (b) that drive the cantilever and/or the sample (Figure 6.22).

In the absence of external forces, the probe-surface interaction can be approximated by a Lennard-Jones potential. When the tip approaches the sample, the terminal atoms of the tip and atoms on the surface attract due to long range interactions such as Van der Waals forces. Then

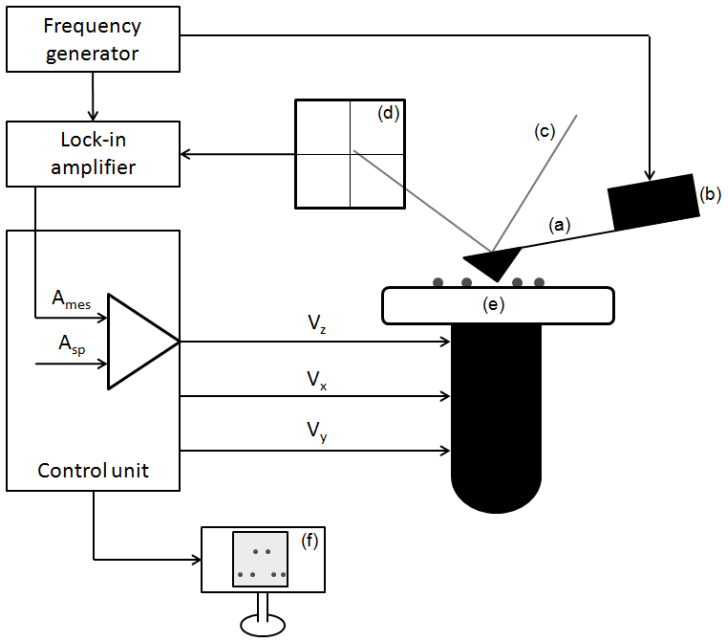

Figure 6.22: Working principle of the AFM: (a) Cantilever; (b) Piezoelectric bimorph; (c) Laser; (d) Array of photodiodes; (e) Sample; (f) Computer

when the distance decreases, atoms repel each other due to electrostatic repulsion between atomic cores. Other forces can intervene such as capillary forces, adhesion forces, electrostatic forces, magnetic forces, etc. This allows the AFM to be operated according to two kinds of modes: the static modes (contact) and the dynamic modes (non-contact or intermittent contact) (Figure 6.23):

1. Static modes

   Here, the tip-surface interaction is in the repulsive region (Figure 6.23). Two working modes exist: the constant interaction mode and the constant height mode. In constant interaction, which is the most used mode, a feedback loop adjusts the tip-sample distance to

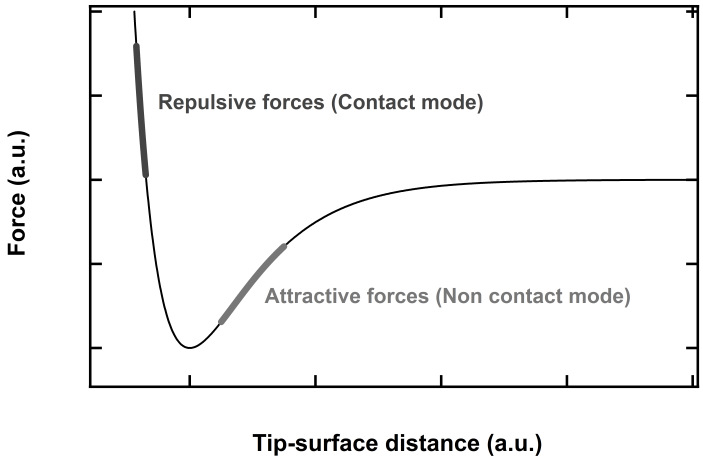

Figure 6.23: When the tip approaches the sample, the terminal atoms of the tip and atoms on the surface attract due to long range interactions such as Van der Waals forces. Then when the distance decreases, atoms repel each other due to electrostatic repulsion between atomic cores. This allows the AFM to be operated according to two modes (non-contact or intermittent contact modes and contact modes).

maintain a constant interaction between the tip and the sample. The recorded data are the vertical sample displacements needed to maintain this constant interaction. This allows imaging rough substrates but at a quite slow rate due to the need of a feedback loop. In constant height, the tip is scanned over the sample and the tip-sample distance remains the same during the whole experiment. In this case, the interaction (the cantilever deflection) is recorded. This mode allows a fast scanning of the surface but it is not suited for rough sample because of the risk that the tip collides with the surface.

Contact mode is not suited for soft samples due to the high pressures that the tip applies on the surface (10 to 500 GPa). Moreover, the tip is rapidly contaminated and can be damaged. This is why dynamic modes are often preferred.

2. Dynamic modes

Dynamic modes are based on the fact that the resonance frequency of a cantilever varies when a force acts on the tip. The relation between the resonance angular frequency ω and the force F is given by:

$$\omega = \omega_0 \sqrt{1 - \frac{1}{k}\frac{\partial F}{\partial z}} \tag{6.29}$$

There exist basically two major dynamic modes: the frequency modulated AFM (FM-AFM) [24] and the amplitude modulated AFM (AM-AFM) [25, 26]. In FM-AFM, the cantilever is constantly driven with a fixed amplitude at its resonance frequency which depends on the tip-sample distance as shown in equation (6.29). The spatial dependence of the shift between the measured resonance frequency and the resonance frequency of the free lever is recorded and used to reconstruct the image. In AM-AFM, the cantilever is oscillated at a constant frequency, f_{IC}, generally slightly lower than the free resonance frequency, f_0. A feedback loop maintains a constant oscillation amplitude by playing on the tip-sample distance (Figure 6.24). The image is then constructed by plotting the feedback signal during the scan.

FM-AFM is well suited for experiments in UHV (Ultra High Vacuum) where the quality factor, Q, is high while AM-AFM is generally used for measurements in air or in liquids where Q is lower. In most cases, the tip does not touch the sample in FM-AFM (non-contact AFM (NC-AFM)) whereas the tip gently touches the sample at the bottom of its oscillation motion in AM-AFM (intermittent contact AFM (IC-AFM)). Nevertheless, it was shown that FM-AFM can be used in the repulsive region as well and that AM-AFM can be used in non-contact [9].

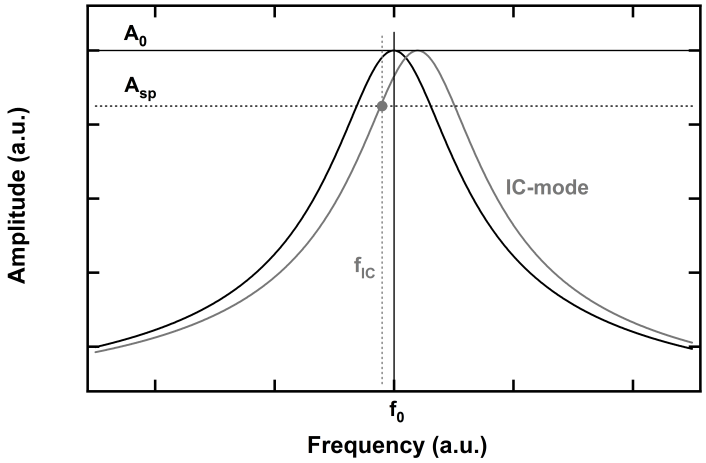

Figure 6.24: In AM-AFM, the cantilever is oscillated at a frequency slightly lower than its resonance frequency. The amplitude of the vibrations is maintained at a constant value A_{sp} thanks to a feedback loop.

Here, AFM experiments were performed using a PicoPlus microscope (Agilent Technologies, USA) equipped with a 100-μm scanner. The images were acquired in the intermittent contact mode (amplitude modulated AFM, AM-AFM) at ambient temperature using the acoustic excitation mode of the microscope. Noncontact silicon PointProbes (Nanosensors) were used. These probes had resonance frequencies around 165 kHz and an integrated tip with a typical apex radius of curvature smaller than 10 nm. These same probes were used for the resonance frequency shifts experiments. MLCT V-shaped silicon nitride cantilever arrays (Bruker) were used for deflection as well as for local catalysis experiments. The selected probes had a spring constant of 0.3 N/m and were coated on one side with a 60 nm thick layer of gold by the intermediary of a 15 nm-thick layer of chromium.

The analysis of the images and of the resonance and deflection curves was performed using home-made procedures developed under the Igor

Pro software (Wavemetrics, USA). The images were flattened to correct for the scanner bow and the fact that the sample surface could not be perfectly parallel to the scanning plane. This was done by subtracting a second- or third-order average surface from the raw images.

For more details about AFM-based experiments (frequency shifts measurements, deflection measurements, local catalysis), please refer to the appropriate sections.

6.3.6 Quartz Crystal Microbalance with Dissipation Monitoring (QCM-D)

The Quartz Crystal Microbalance with Dissipation Monitoring (QCM-D) measurements were performed in water with a Q-Sense E4 microbalance. The AT-cut quartz crystal sensor of 14 mm diameter was oscillating at its fundamental frequency (5 MHz). All overtones were acquired, although the third overtone was generally selected for analysis. The thickness of the silicon oxide layer covering the sensor was evaluated by ellipsometry on five different sensors to be 23 ± 2.5 nm. The quartz sensor was mounted in a flow module with one side exposed to the solution. The module temperature was maintained with a precision of 0.02℃. Data collection was realized in dynamic mode. Before starting the measurements, the samples were equilibrated with the solution during 35 minutes at 15℃. The temperature was ramped at 0.2℃/min while continuously acquiring data in a given solution. The QCM-D data were collected between 15 and 45℃ due to instrumental limitations. Because of the presence of a small hysteresis resulting from the large time constant needed for the stabilization of the QCM-D setup [27] the frequency shift (Δf) and dissipation shift (ΔD) curves obtained upon heating and cooling were slightly different.

QCM-D was used here to follow the temperature dependence of the hydration and dehydration process of the bulk of the polymer brush. By applying a proper oscillating voltage, the QCM-D quartz sensor was made to vibrate at its resonance frequency f_1 and odd overtones f_n (n=1, 3, 5,...). After the application of the oscillating excitation, the damping of the vibration was monitored during the relaxation period of the sensor, giving access to the dissipation factor D that is defined as $D = (\tau\pi f_1)^{-1}$ where τ is the time constant for the amplitude decay after switching off the power source [28, 29]. The deposition of extra material on the sensor surface (e.g. by grafting a polymer brush), changes the resonance frequency. If the layer is thin, rigid, uniform enough, and in vacuum, then the frequency shift (Δf) can be related to the absorbed mass by the Sauerbrey equation [30]:

$$\Delta m = -C\frac{\Delta f}{n} \tag{6.30}$$

where Δm is the sensed mass per piezoelectrically active area, C is a constant depending on the sensor parameters (17.7 ng/(cm^2 · Hz) in our case), and n is the overtone number. Most of the time, the fundamental resonance frequency f_1 is noisy because of energy trapping or piezoelectric stiffening [31]. Therefore, the third overtone f_3 was generally selected here. When the sensor is immersed in a fluid and/or if the deposited layer is viscoelastic, as is the case here, the Sauerbrey equation breaks down. The response of a piezoelectric sensor covered by a viscoelastic layer immersed in a bulk liquid was proposed some time ago [29, 32–34] as reviewed recently [35]. Assuming that the swollen brush can be modeled as a single average homogeneous layer, the frequency shift with respect to the bare sensor, Δf, and dissipation factor shift, ΔD, can be linked to the temperature-dependent thickness $h_{\mathrm{br}}(T)$, density $\rho_{\mathrm{br}}(T)$, shear viscosity $\eta_{\mathrm{br}}(T)$, and shear modulus $\mu_{\mathrm{br}}(T)$ of the polymer brush as follows:

$$\Delta f(T) \approx C_f \left[\frac{\eta_{\mathrm{L}}(T)}{\delta_{\mathrm{L}}(T)} + h_{\mathrm{br}}(T)\rho_{\mathrm{br}}(T)\omega - 2h_{\mathrm{br}}(T) \left(\frac{\eta_{\mathrm{L}}(T)}{\delta_{\mathrm{L}}(T)} \right)^2 \frac{\eta_{\mathrm{br}}(T)\omega^2}{\mu_{\mathrm{br}}^2(T) + \eta_{\mathrm{br}}^2(T)\omega^2} \right] \tag{6.31}$$

$$\Delta D(T) \approx C_D \left[\frac{\eta_{\mathrm{L}}(T)}{\delta_{\mathrm{L}}(T)} + 2h_{\mathrm{br}}(T) \left(\frac{\eta_{\mathrm{L}}(T)}{\delta_{\mathrm{L}}(T)} \right)^2 \frac{\mu_{\mathrm{br}}(T)\omega}{\mu_{\mathrm{br}}^2(T) + \eta_{\mathrm{br}}^2(T)\omega^2} \right] \tag{6.32}$$

where $\omega = 2\pi f_n$. The constants $C_f = -(2\pi\rho_s h_s)^{-1}$ and $C_D = 2\pi f_n \rho_s h_s$, where h_s is the thickness of the quartz crystal and ρ_s is its density, can be determined easily and are considered to be temperature-independent under our conditions. $\delta_{\mathrm{L}}(T) = [2\eta_{\mathrm{L}}(T)/\rho_{\mathrm{L}}(T)\omega]^{1/2}$ is the water viscous penetration depth with $\rho_{\mathrm{L}}(T)$ the temperature-dependent water density and $\eta_{\mathrm{L}}(T)$ is the water viscosity as a function of the temperature. More details about the determination of all these parameters are given in [27].

6.3.7 Front-Face Fluorimetry (FFF)

The fluorescence spectra of the films were acquired with a Fluorolog-3 spectrofluorometer (Horiba-Jobin Yvon SPEX system from Instrument S.A., USA) in the front face (FF) mode with an excitation wavelength (λ_{ex}) of 566 nm. Excitation and emission slits with a nominal band-pass of 4 nm, a PMT voltage of 1000 V and no polarizer were used.

6.3.8 Scanning Electron Microscopy (SEM)

Scanning Electron Microscopy (SEM) images were obtained using a LEO 982 Field emission scanning electron microscope (FE-SEM, Carl Zeiss SMT GmbH, Germany). The typical used accelerating voltage was 1 kV.

References

[1] Husseman, M.; Malmstrom, E. E.; McNamara, M.; Mate, M.; Mecerreyes, D.; Benoit, D. G.; Hedrick, J. L.; Mansky, P.; Huang, E.; Russell, T. P.; Hawker, C. J. *Macromolecules* **1999**, *32*, 1424–1431.

[2] Jones, D. M.; Brown, A. A.; Huck, W. T. S. *Langmuir* **2002**, *18*, 1265–1269.

[3] Angelos, S.; Yang, Y.-W.; Patel, K.; Stoddart, J. F.; Zink, J. I. *Angew. Chem., Int. Ed.* **2008**, *47*, 2222–2226.

[4] Ligaj, M.; Jasnowska, J.; Musial, W. G.; Filipiak, M. *Electrochim. Acta* **2006**, *51*, 5193–5198.

[5] Tengvall, P.; Jansson, E.; Askendal, A.; Thomsen, P.; Gretzer, C. *Colloids and Surfaces B: Biointerfaces* **2003**, *28*, 261–272.

[6] Wissink, M. J. B.; Beernink, R.; Pieper, J. S.; Poot, A. A.; Engbers, G. H. M.; Beugeling, T.; van Aken, W. G.; Feijen, J. *Biomaterials* **2001**, *22*, 151–163.

[7] Lahiri, J.; Isaacs, L.; Tien, J.; Whitesides, G. *Anal. Chem.* **1999**, *71*, 777–790.

[8] Richert, L.; Boulmedais, F.; Lavalle, P.; Mutterer, J.; Ferreux, E.; Decher, G.; Schaaf, P.; Voegel, J.; Picart, C. *Biomacromolecules* **2004**, *5*, 284–294.

[9] Garcia, R.; Perez, R. *Surf. Sci. Rep.* **2002**, *47*, 197–301.

[10] Russell, T. *Materials Science Reports* **1990**, *5*, 171–271.

[11] Daillant, J.; Gibaud, A. *X-ray and Neutron Reflectivity : Principles and Applications*; Springer: Berlin / Heidelberg, 1999; Vol. 770.

[12] Arys, X.; Laschewsky, A.; Jonas, A. M. *Macromolecules* **2001**, *34*, 3318–3330.

[13] Tompkins, H. G. *A user's guide to ellipsometry*; Academic Press: Boston, 1993.

[14] Tompkins, H. G.; McGahan, W. A. *Spectroscopic ellipsometry and reflectometry a user's guide*; Wiley: New York, 1999.

[15] Aspnes, D. E.; Studna, A. A. *Phys. Rev. B* **1983**, *27*, 985.

[16] Aspnes, D. E.; Theeten, J. B. *J. Appl. Phys.* **1979**, *50*, 4928–4935.

[17] Matyjaszewski, K.; Dong, H.; Jakubowski, W.; Pietrasik, J.; Kusumo, A. *Langmuir* **2007**, *23*, 4528–4531.

[18] Briggs, D.; Seah, M. *Practical surface analysis by Auger and X-ray photoelectron spectroscopy*; John Wiley and Sons Ltd: Chichester, UK, 1983; Vol. 1.

[19] Feldman, L.; Mayner, J.; Adams, F. *Fundamentals of surface and thin film analysis*; Elsevier: Amsterdam, 1986.

[20] Ibach, H. *Electron Spectroscopy for Surface Analysis*; Topics in Current Physics; Springer-Verlag: Berlin, 1977.

[21] Griffiths, P. R.; De Haseth, J. A. *Fourier Transform Infrared Spectrometry*, 2nd ed.; Wiley Interscience: New York, 2007; Vol. 83.

[22] Giessibl, F. J. *Reviews of Modern Physics* **2003**, *75*, 949.

[23] Bhushan, B.; Marti, O. Scanning Probe Microscopy – Principle of Operation, Instrumentation, and Probes. In *Springer Handbook of Nanotechnology*; Bhushan, B., Ed.; Springer Berlin Heidelberg, 2007; pp 591–636.

[24] Albrecht, T. R.; Grutter, P.; Horne, D.; Rugar, D. *J. Appl. Phys.* **1991**, *69*, 668–673.

[25] Martin, Y.; Williams, C. C.; Wickramasinghe, H. K. *J. Appl. Phys.* **1987**, *61*, 4723–4729.

[26] Zhong, Q.; Inniss, D.; Kjoller, K.; Elings, V. B. *Surf. Sci.* **1993**, *290*, L688–L692.

[27] Laloyaux, X.; Mathy, B.; Nysten, B.; Jonas, A. M. *Langmuir* **2009**, *26*, 838–847.

[28] Zhang, Y.; Du, B.; Chen, X.; Ma, H. *Anal. Chem.* **2008**, *81*, 642–648.

[29] Voinova, M. V.; Rodahl, M.; Jonson, M.; Kasemo, B. *Phys. Scr.* **1999**, 391.

[30] Sauerbrey, G. *Z. Phys. A: Hadrons Nucl.* **1959**, *155*, 206–222.

[31] Diethelm, J. *Macromol. Chem. Phys.* **1999**, *200*, 501–516.

[32] Domack, A.; Prucker, O.; Ruhe, J.; Johannsmann, D. *Phys. Rev. E* **1997**, *56*, 680.

[33] Nakamoto, T.; Moriizumi, T. *Jpn. J. Appl. Phys.* **1990**, *29*, 963.

[34] Granstaff, V. E.; Martin, S. J. *J. Appl. Phys.* **1994**, *75*, 1319–1329.

[35] Johannsmann, D. *Phys. Chem. Chem. Phys.* **2008**, *10*, 4516–4534.

Chapter 7

General Conclusions and Perspectives

In the framework of building the constitutive elements of a nanofactory, this thesis had two main objectives: first, the development of probes that could locally measure the kinetics of reactions arising in the nanoreactors and the diffusion of the formed products and second, the fabrication of a tool that could locally alter the kinetics of reactions taking place inside the reactors or favor a reaction between molecules on the surface of the nanofactory and molecules in solution. In both cases, the strategy was to use AFM cantilevers and tips as probes or catalytic triggers because they are cheap, commercially available, can be precisely positioned and have proven to be efficient sensors or tools for nanolithography. In order to further increase their sensitivity, polymer brushes were grafted from their surfaces. Indeed, due to their high grafting densities, they provide a high amount of reactive functional groups per unit surface area.

In the first part of this thesis, the growth kinetics of polymer brushes grafted from solid surfaces by ATRP was investigated. Two substrates were considered: gold and silicon. To proceed with the polymerization these substrates had to be functionalized with thiol-initiators (for gold) or silane-initiators (for silicon). However, since thiol-based SAMs are relatively unstable, especially regarding place-exchange reactions, the silane-on-silicon system was preferred. Then, the parameters of the polymerization were optimized for two monomers, MEO_2MA and MAA, in order to rapidly achieve thick brushes with a good control. This optimization study was not undertaken for the two other monomers used in this thesis (MES and HEMA) and as a consequence, the control of their polymerization was not ideal. For future studies based on these brushes, increased efforts should be done in finding more appropriate sets of parameters if a good control is desired which was not the case here. Finally, the copolymerization of MEO_2MA and MAA was studied. The ratio of each moiety in the copolymer was shown to be rather different from the ratio in the feed solution because of the larger reactivity ratio

of MEO_2MA as compared to MAA.

In the second part, the realization of the first objective was tackled. To locally measure the kinetics of a reaction with AFM cantilevers, two methods were considered: a dynamic method where the grafted mass is quantified by following the resonance frequency shifts of the cantilever upon absorption of molecules and a static method where the variation of the surface stress induced by the selective absorption of molecules on only one side of the cantilever is monitored by evaluating the change of its deflection state.

It was shown that the first method is not the best one for measurements in a liquid medium with AFM cantilevers because of coupling effects between the cantilever oscillations and the surrounding liquid. However, some interesting results were found for the determination of the kinetics of the activation reaction of poly(MAA) brushes and of the collapse transition temperature of thermoresponsive poly(MEO_2MA) brushes. First, a decrease of the resonance frequency of AFM cantilevers grafted with poly(MAA) brushes was observed upon their immersion in a reactive solution of EDC or EDC/NHS. The conversion of the reactive side groups inside the polymer brushes was estimated. For a thin polymer brush immersed in a EDC/NHS solution, the conversion was close to 1 after one hour while it was only 0.3 for a thick polymer brush after a 1 hour-immersion in a EDC solution. This was explained by a higher reactivity of the EDC/NHS couple compared to EDC alone and by the larger proportion of accessible reactive groups inside the thin brush compared to the thick one. Second, variations in the resonance frequency of cantilevers grafted with poly(MEO_2MA) brushes were observed upon heating or cooling the salt solutions in which they were dipped. The slopes of the resulting curves showed variations in the expected ranges of temperatures which were previously determined by QCM-D measurements.

The second method was found to be promising for the fabrication

of liquid-operated sensors. Indeed, pH-sensors were made by grafting pH-responsive polymer brushes from one side of flexible AFM cantilevers. The deflection of these cantilevers decreased when lowering the pH of the solution from 8 to 2. The final observed deflection was around 600 nm which corresponds to a surface stress difference of around 600 mN/m. This phenomenon was proven to be reversible. However, when attempting to measure the kinetics of a click reaction between azide-functionalized brushes and alkyne molecules in solution, this method seemed to lack of sensitivity.

It is thus very important to try to increase the sensitivity of such systems in a future work. The key parameter to achieve this appears to be the accessibility of the reactive side groups inside the brush. Smaller molecules could penetrate deeper down to the bottom of the brush but the change in mass or in the surface stress of the cantilever would maybe not be sufficient enough to have a strong impact on its resonance frequency or on its deflection state. An alternative would be to decrease the grafting density of the brush as well as its thickness. In this case, the conversion of the reactive side groups would increase. This can be done by silanizing the cantilevers with the initiator in the vapor phase in the presence of an inactive silane. This silane has to be quite similar to the initiator in order for them to mix in the vapor phase and to self-assemble randomly on the surface instead of forming patches. Then, an optimization work would be necessary to find the protocol that would lead to the maximum grafted amount of target molecules inside the brush after a given reaction time. It is believed that a 50% more diluted brush with a thickness of around 10 nm would give a satisfactory sensitivity.

The last part dealt with the second objective, i.e. the local catalysis of a surface reaction. An AFM tip was covered with a reactive brush hosting Cu-complexes in order to locally catalyze a CuAAC reaction between azido-functionalized surfaces and alkyne molecules in solution. The steps yielding these levers as well as the functionalized surfaces were

fully characterized. Patterns of propargyl-sulforhodamine (9) were successfully drawn. Their thickness was greater than a monolayer of (9) and inversely proportional to the scan speed while the contact force did not seem to play a role on it at least for the experimented values. This fact combined with other various tests indicated that the mechanism of the pattern formation involves the combined action of the catalytic complexes and the brush. The complexes allow the formation of a first monolayer and small aggregates absorbed in the brush are stacked on it during the scan yielding thick crystals.

To be 100% sure that the patterned lines are actually composed of propargyl-sulforodamine (9) crystals, confocal microscopy images should have been taken. This could not be done in this thesis because the confocal microscope available at UCL was optimized for biological samples and did not offer enough sensitivity for surface samples. A collaboration with the group of Prof. Hofkens from KULeuven was considered because their system was specifically designed for this kind of samples. However, this project could not take shape because of technical problems. Then, it would be interesting to add another "color" in the patterns to test the feasibility of multiple successive reactions with different kinds of molecules on the same substrate. This could be done for instance by using already-available propargyl-fluoresceine. Another interesting idea would be to use functionalized quantum dots since their emission wavelength depends on their size. Moreover, due to their relatively large diameter (from 5 to 50 nm) it would allow an easier characterization of the patterns through AFM imaging.

Finely tuning the spacial arrangement of polymer brushes was proven to have a huge impact on some specific properties such as the collapse transition temperature of thermoresponsive brushes [1] and on the extent at which the brushes are swollen for a given set of experimental parameters [2]. Then, locally catalyzing click reactions with an ATRP initiator should lead to the very precise positioning of the subsequent brushes and hopefully with a better resolution than the one obtained in a recent

work using DNL [3]. Moreover, growing brushes from patterns of initiators would be useful as a revealing step for their easy characterization by AFM due to the thickness increase. First experiments showed that interactions between the tip and the substrate, maybe charge transfer, provoked some artifacts after the polymerization step. It is believed that using a conductive substrate such as aluminum (which can be silanized as well), would solve that issue. In the long term, other kinds of reactions could be investigated such as the metathesis of olefines that is catalyzed by metals such as ruthenium. Olefin metathesis is a reaction in which two olefins are involved. The alkene double bonds are cleaved to form a cyclobutane and finally, a statistical redistribution of the substituents occurs. For example, an alkene-terminated silane could be grafted on a silicon substrate, a modified version of alkyne (9) with a double bond instead of a triple one could be in solution and AFM tips could be grafted with a ruthenium alkylidene catalyst such as those presented in [4]. This kind of reactions is interesting because the ruthenium catalysts are highly efficient and supposed to be very stable [5].

Anyway, a new project has already been written on the basis of this thesis to develop a better understanding of the local catalysis process. In this project, different substrates will be investigated such as a mica substrate covered with an azide-terminated catecholic monolayer obtained by the azidation of a 4-(bromomethyl)benzene-1,2-diol monolayer. The AFM tips will be prepared according to three different methods:

1. Carboxylic groups will be generated on AFM tip apexes by applying an appropriate bias voltage on octadecyltrichlorosilane-coated AFM probes and will be used as binding agents to directly adsorb metal ions.

2. Copper ligands will be grafted on AFM tips using a silane or a catechol coupled to a bipyridine ligand.

3. The same methodology as the one used in this thesis will be fol-

lowed (catalytic complexes grafted on AFM tips by the intermediate of reactive polymer brushes).

The alkyne that will be used is the ATRP-initiator (10) in order to investigate the responsive behavior of the subsequent brushes depending on their state of confinement. The effect of the scan speed on the extent of the reaction will also be investigated and the kinetic data will be compared to the case of identical reactions led in solution.

References

[1] Jonas, A. M.; Hu, Z.; Glinel, K.; Huck, W. T. S. *Nano Lett.* **2008**, *8*, 3819–3824.

[2] Liu, X.; Li, Y.; Zheng, Z. *Nanoscale* **2010**, *2*, 2614–2618.

[3] Zhou, X.; Wang, X.; Shen, Y.; Xie, Z.; Zheng, Z. *Angew. Chem., Int. Ed.* **2011**, *50*, 6506–6510.

[4] Dragutan, I.; Dragutan, V.; Filip, P. *Arkivoc* **2005**, *10*, 105–129.

[5] Scholl, M.; Ding, S.; Lee, C. W.; Grubbs, R. H. *Org. Lett.* **1999**, *1*, 953–956.